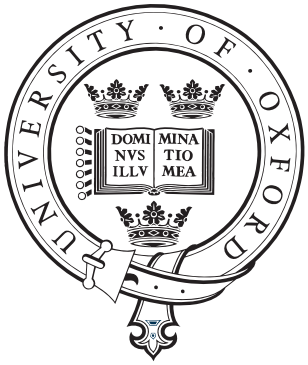
Pulsed squeezed light: characterization and applications

Gil Triginer Garcés
Merton College, Oxford



Submitted for the degree of Doctor of Philosophy
Trinity Term 2019

Supervised by
Prof. Ian A. Walmsley

Clarendon Laboratory
University of Oxford
United Kingdom

Pulsed squeezed light: characterization and applications

Gil Triginer Garcés
Merton College, Oxford

Submitted for the degree of Doctor of Philosophy
Trinity Term 2019

Abstract

Squeezed light is expected to enable new quantum metrology and quantum computation applications, but the very high degree of experimental control required in practice places severe demands on the physical devices used to generate it. As ultrafast squeezed light sources are reaching an unprecedented degree of brightness and modal control, there is a strong interest in developing methods for their experimental characterization and theoretical understanding. In this thesis, we demonstrate both a new application and a new characterization technique for pulsed squeezed light.

In the first part of the thesis, we present a new metrological application of pulsed squeezed light: quantum-enhanced label-free nonlinear microscopy. Stimulated emission microscopy (SEM) is a state-of-the-art pump-probe microscopy technique whose sensitivity is ultimately limited by shot noise in the probe beam. We propose to overcome this fundamental limitation by using a sub-Poissonian probe generated via optical parametric amplification. We demonstrate an intensity-squeezed sub-picosecond pulsed probe, and a simple stimulated emission microscope. Using this squeezed probe, sub-Poissonian statistics are observed in the SEM signal. After this proof-of-principle experiment, we aim to provide an improved design for a source of intensity-squeezed light. First, we develop a theoretical framework to simulate the photon statistics of a general sub-Poissonian source, considering pulsed and focused pump and seed fields in a unified spatio-temporal description. Next, we use this framework to suggest possible improvements to our previous squeezed probe.

In the second part of this thesis, we provide new theoretical and experimental tools to analyze the high gain regime of pulsed spontaneous parametric down-conversion (SPDC). We study a waveguided source capable of generating twin-beams with tens of photons in a single spatio-temporal mode. We develop a framework to efficiently simulate SPDC for an arbitrary nonlinear gain, including the effect of parasitic nonlinearities such as self-phase modulation (SPM) of the pump and cross-phase modulation (XPM) between pump and twin-beams. We experimentally characterize our source using a new technique based on stimulated difference-frequency generation (DFG). In a type-II down-conversion process, we measure the frequency generation produced not only in the orthogonal polarization to the seeding beam, but also in its same polarization, which we interpret as cascaded difference-frequency generation. We argue that the additional information obtained in this measurement allows for a self-referenced estimation of the squeezing gain. Using these measurements, we accurately fit our theoretical model, revealing that, in the high gain regime, parasitic nonlinearities strongly affect the spectral structure of the twin-beams. We propose a simple strategy to reduce the impact of these nonlinearities on the modal structure of SPDC.

Acknowledgements

Many people have helped and supported me during my DPhil, both in the lab and outside of it. I thank my supervisor, Prof. Ian Walmsley, without whom this research would not have been possible. Thank you for creating the very special place that is the Ultrafast Group, and for welcoming me into it. I am also very grateful to Merton College and La Caixa for their generous support, going the extra mile to turn a DPhil into a formative experience beyond the academic. During the last four years I have been very lucky to receive guidance from a brilliant set of people: Steven Kolthammer directed my first steps in Oxford, and his scientific intuition and rigour remain an inspiration to this day. I am very grateful to Prof. Morgan Mitchell for inviting me to visit his group at ICFO, which made my doctorate experience so much richer. I would like to thank Prof. John Sipe for the theoretical thoroughness with which he has contributed to some of the work in this thesis. I also want to thank Raj Patel for his invaluable work coordinating the lab towards the end of my DPhil.

Most of what I know about quantum optics I have learnt from the people that I have worked with. I owe so much to Mihai Vidrighin, who began as a mentor and became a friend. I look forward to meeting again in the mountains in Romania! From Helen Chrzanowski I received, in addition to a hard experiment, an incredible amount of support both in and out of the lab. Her work lay the foundation for the experiment reported in the first part of this thesis. I would also like to thank the post-docs with whom I have striven to squeeze light: with Anna Marchant, we brought much needed order to the experiment; Valerian Thiel

turned both theory and setup inside out, which helped hugely; finally, Shakib Daryanoosh took up the torch. I should also mention the fruitful transatlantic collaboration with Nicolás Quesada, which enriched my understanding of high-gain PDC. Although I won't be able to name all the people in the Ultrafast group that have made my work days (and nights) so much more enjoyable, a few special mentions are necessary: Thomas H., Tom P., Alex, Georg, Adrian, Joelle, Chris M., and Santi, thank you! I also want to take this opportunity to thank my colleagues who have taken the time to read this thesis and provide me with very useful feedback: Bryn Bell, Valerian Thiel, Helen Chrzanowski and Raj Patel.

A special thank you goes to the people that have made my life these last years about much more than my research. To my London friends, who gave me the excuse to take the occasional break from Oxford. To Laia, a cousin at home who became a friend abroad. To Axel, Nacho, Adri, Kiko and Joan, for your lasting friendship. To the Tercero del Agua family, who made me feel at home from the start. To my little family in Oxford: Esther, with whom I discovered the other side of Oxford, and who I plan to lure back to Barcelona; Cris, whose brief stay left a mark; Alvaro, half philosopher but still half physicist; Javi, an infinite optimism reservoir; Miren, an infinite source of creative entropy; and Pablo, who has made me grow as a person and whose friendship I treasure. Another special thank you to Marcello, who made me discover a new sensibility and whose lovely day-to-day company I will miss.

To my parents, Gil and Anna, and my sister, Blanca, thank you for your unconditional support, your love and your caring. You have always encouraged me to pursue my interests, and with your trust have given me the confidence to go through the most challenging moments. I also want to thank all my grandparents: they have been an example of personal integrity as well as of intellectual curiosity and independence.

Finally, I want to thank you, Julia. You have shared in my highs and lows throughout the last four years and, just by that, have made a world of difference. Now that I close this chapter I can only look forward to the future. I dedicate this thesis to you.

Author's publications

Journal publications

1. G. Triginer[†], M.D. Vidrighin[†], A. Eckstein, N. Quesada, M. Moore, W.S. Kolthammer, J. Sipe, I.A. Walmsley, *Understanding high-gain twin beam sources using cascaded stimulated emission*, pending submission

2. N. Quesada [†], G. Triginer [†], M.D. Vidrighin [†], J. Sipe, *Efficient simulation of high-gain twin-beam generation in waveguides*, https://arxiv.org/abs/1907.01958, pending submission

3. J. Renema, A. Menssen, W.R. Clements, G. Triginer, W.S. Kolthammer, I.A. Walmsley, *Efficient classical algorithm for boson sampling with partially distinguishable photons*, Phys. Rev. Lett. 120, 220502 (2018)

[†] equal contributions

Conference oral presentations

G. Triginer, M.D. Vidrighin, N. Quesada, W.S. Koltahmmer, I.A. Walmsley, *Complete description of high-gain twin-beam generation via a cascaded nonlinearity*, Quantum Optics IX, Cartagena de Indias (2018)

J. Renema, R. Garcia-Patron, V. Schesnovich, A. Menssen, W. Clements, G. Triginer, W.S. Kolthammer, I.A. Walmsley, P.W.H. Pinkse, *The hardness of boson sampling under imperfections*, Quantum Technology International Conference, Paris (2018)

G. Triginer, M.D. Vidrighin, A. Eckstein, M. Moore, W.S. Kolthammer, I.A. Walmsley, *Experimental characterization of a broadband multimode squeezed light source in the high-gain regime*, CLEO Europe, Munich (2017)

Conference posters

G. Triginer, M.D. Vidrighin, N. Quesada, W.S. Kolthammer, I.A. Walmsley, *A complete description of a bright broadband twin-beam source using cascaded difference-frequency generation*, QCUMbEr conference, Oxford (2018)

G. Triginer, M.D. Vidrighin, W.S. Kolthammer, I.A. Walmsley. *Characterization of a pulsed two-mode squeezing source with classical measurements*, YQUIS conference, ICFO, Barcelona (2016)

In preparation

G. Triginer, V. Thiel, H. Chrzanowski, A. Marchant, S. Daryanoosh , I.A. Walmsley, *Quantum enhanced stimulated emission microscopy*

G. Triginer, V. Thiel, I.A. Walmsley, *Design of optimized sources of pulsed sub-Poissonian light*

Contents

Acknowledgements **iii**

Author's publications **v**

List of Figures **xi**

List of Tables **xiv**

List of abbreviations **xv**

List of symbols **xvi**

Introduction and basic concepts **1**

1 Introduction **2**

1.1 Thesis outline 3

1.2 Basic concepts and notation 6

1.2.1 Quantum optics 6

1.2.2 Ultrafast linear optics 17

1.2.3 Non-linear optics 29

1.2.4 Ultrafast nonlinear quantum optics 35

I Quantum enhanced stimulated emission microscopy 49

2 A proposal for quantum-enhanced ultrafast stimulated emission microscopy 50

2.1 Quantum metrology in biology 50
2.2 Stimulated emission microscopy (SEM) 53
2.3 Quantum enhancement of SEM 56
2.4 Squeezing coherent states: the degenerate parametric amplifier 62
2.4.1 Losses 67
2.4.2 The connection between intensity and quadrature squeezing 69
2.5 Experimental design 72
2.5.1 A sketch of the experiment: the need for pulsed and focused beams . . 72
2.5.2 Quantum noise in a pulsed optical field 74
2.5.3 Squeezing pulsed beams 77
2.5.4 Squeezing focused beams 82
2.6 Experimental demonstration 84
2.6.1 Sub-Poissonian light source 84
2.6.2 Experimental demonstration of SEM 94
2.6.3 Towards quantum-enhanced SEM 97
2.7 Summary and outlook 99

3 Simulating and designing pulsed sub-Poissonian light sources 101

3.1 Motivation 101
3.2 Hamiltonian description of optical parametric amplification 103
3.3 Heisenberg spectral input-output relations 107
3.3.1 Perturbative expansion of the spectral input-output relations 108
3.3.2 Non-perturbative input-output relations: Takagi factorization 109
3.3.3 Squeezing pulsed coherent states 111
3.3.4 Limits of pulsed intensity squeezing 114
3.4 Heisenberg spatial input-output relations 121
3.4.1 Separation of transverse directions 123
3.4.2 Ordinary axis input-output relations: no walk-off 126

3.4.3 Extraordinary axis input-output relations: spatial walk-off 133
3.5 Heisenberg spatio-temporal input-output relations 135
3.5.1 The origin of space-time coupling 136
3.5.2 Spatio-temporal modal decomposition 140
3.5.3 Output photon statistics 142
3.5.4 Space-time coupling limits squeezing 144
3.6 An improved design 146
3.7 Summary and outlook 150

II High gain broadband twin-beam generation 151

4 Simulating twin-beam generation in the high-gain regime 152
4.1 Motivation 152
4.2 Efficient modelling of waveguided type-II PDC in the high-gain regime 155
4.2.1 Field quantization 155
4.2.2 Expansion fields in a waveguide 156
4.2.3 The nonlinear interaction 160
4.2.4 Dynamics of the fields 162
4.2.5 Solving the equations of motion 167
4.2.6 Commutation relations and modal structure 171
4.3 A simple example 173
4.4 Summary and outlook 178

5 Understanding high-gain twin-beam generation through cascaded stimulated emission tomography 180
5.1 Cascaded stimulated emission tomography 180
5.1.1 All spectral transfer functions from cascaded stimulated emission . . . 182
5.1.2 Self-referenced measurement of squeezing strength 184
5.1.3 The need for a model-based approach 186
5.2 Experimental demonstration 187
5.2.1 Parametric down-conversion source 187

5.2.2 Stimulated emission measurements 189
5.2.3 Results 191
5.2.4 Discussion 204
5.2.5 Summary and outlook 207

III Conclusions and outlook **209**

6 Conclusions and outlook **210**

Bibliography **213**

A Locking on deamplification: generating the error signal **222**

B Taylor expansion of the transverse momentum mismatch **223**

C The nonlinear coefficients **225**

List of Figures

1.1 Coordinate system in an anisotropic uniaxial crystal 26
1.2 Factorable vs non-factorable JSA 44

2.1 Stimulated emission microscopy 55
2.2 Types of squeezed states 60
2.3 Enhancing gain estimation with squeezed coherent states 61
2.4 Squeezing transformation on a coherent state 65
2.5 Phase-dependent intensity amplification and Fano factor 66
2.6 Beamsplitter model of linear loss 68
2.7 Sketch of the experiment 73
2.8 Shot noise in a pulsed laser 76
2.9 Temporally inhomogeneous deamplification/squeezing 79
2.10 Spatially inhomogeneous deamplification 83
2.11 Sub-Poissonian light source experimental setup 85
2.12 Amplification/deamplification fringes 88
2.13 Locking to deamplification 89
2.14 Intensity squeezing measurements 93
2.15 Stimulated emission microscopy setup 95
2.16 SEM measurement with sub-Poissonian light 98

3.1 Type-I PDC joint spectral amplitude 116
3.2 Choice of pulse lengths 117

3.3 Tolerance of squeezing to pulse delay . . . 118
3.4 Maximum crystal length (temporal walk-off) . . . 120
3.5 Joint angular amplitudes . . . 127
3.6 Choice of beam waists. Intensity gain . . . 128
3.7 Choice of beam waists. Fano factor . . . 129
3.8 Maximum crystal length (beam divergence) . . . 131
3.9 Tolerance of squeezing to focal point offset. Intensity gain . . . 132
3.10 Tolerance of squeezing to focal point offset. Fano factor . . . 132
3.11 Joint angular amplitudes. Pump walk-off . . . 134
3.12 Maximum crystal length (spatial walk-off) . . . 136
3.13 Phase-matching space-time coupling . . . 139
3.14 2D broadband modes. No pump walk-off . . . 142
3.15 2D broadband modes. Pump walk-off . . . 142
3.16 Space-time correlated deamplification . . . 145
3.17 Effect of phase-matching space-time coupling on squeezing . . . 146

4.1 Time-ordering corrections to the JSA shape . . . 176
4.2 Time ordering corrections to the amplitudes of the squeezing parameters . . . 177
4.3 Same-mode transfer function . . . 178

5.1 Cascaded stimulated emission tomography . . . 182
5.2 Experimental setup . . . 189
5.3 Stimulated emission spectrum interpolation . . . 190
5.4 Low gain results . . . 192
5.5 Pump spectrum . . . 192
5.6 Phase-matching characterization . . . 196
5.7 Effect of XPM on the same-mode TFs . . . 199
5.8 High-gain results . . . 199
5.9 Effect of pump spectral phase on same-mode TFs . . . 201
5.10 Ratio between direct and cascaded stimulated emission . . . 203
5.11 Fitting error . . . 204
5.12 Inferred brightness and purity . . . 205

5.13 Improvement by pre-chirping the pump 208

List of Tables

2.1 SEM fitting parameters 99

List of abbreviations

Abbreviation	Description
APD	avalanche photodiode
AR	anti-reflection
a.u.	arbitrary units
BBO	barium borate
BiBO	bismuth triborate
BS	beam splitter
CW	continuous wave
DFG	difference-frequency generation
FHWM	full width at half maximum
HWP	half-wave plate
JA	joint amplitude
JAA	joint angular amplitude
JSA	joint spectral amplitude
JSI	joint spectral intensity
KTP	potassium titanyl phosphate
LO	local oscillator
OPA	optical parametric amplifier
OPO	optical parametric oscillator
OSA	optical spectrum analyzer
PBS	polarizing beam-splitter
PID	proportional-integral-derivative
PDC	parametric down-conversion
PSD	power spectral density
RF	radio-frequency
SA	spectrum analyzer
SEM	stimulated emission microscopy
SET	stimulated emission tomography
SFG	sum-frequency generation
SHG	second-harmonic generation
SNR	signal to noise ratio
SPDC	spontaneous parametric down-conversion
SPM	self phase modulation
TF	transfer function
XPM	cross phase modulation

List of symbols

Symbol	Description
$\propto$	proportional to
$\sim$	similar to
$\langle \cdot \rangle$	mean value
$\mathrm{var}(\,\cdot\,)$	variance
$\delta_{i,j}$	Kronecker delta
$\delta(\cdot)$	Dirac delta
$\hat{\cdot}$	operator
$[\cdot\,,\cdot]$	commutator
†	Hermite conjugation
$*$	complex conjugation
∂_μ	partial differentiation with respect to μ
∇	nabla differential operator
i	imaginary unit
e	base of natural logarithm
$\hbar$	reduced Planck constant
c	speed of light
ϵ_0	vacuum permittivity
μ_0	vacuum permeability
t	time
$\mathbf{r}$	position vector
$\boldsymbol{\rho}$	transverse position vector
$\mathbf{k}$	wavevector
$\mathbf{q}$	transverse wavevector

Part

Introduction and basic concepts

Chapter 1

Introduction

Light has played a crucial role in the history of quantum physics. The first hint at the incompleteness of classical mechanics was contained in the solution to the black-body spectrum problem proposed in 1900 by Max Planck, which required the seemingly strange assumption that light must be emitted and absorbed in packets of energy. Soon afterwards, in 1905, Einstein consolidated the concept of light quanta by using them to explain experimental data from the photoelectric effect [1]. Light played a central part again in the landmark experimental demonstrations of Bell nonlocality in the 70s and 80s [2,3], and since then quantum optical setups have been fruitful testbeds to validate different fundamental features of quantum theory (e.g. contextuality [4]). A major research effort is currently being made towards preparing and manipulating large quantum systems, whose evolution cannot be simulated by current classical computers. Nonclassical light offers a promising, although experimentally challenging, avenue to prepare and measure large quantum states [5]. Analogously to alternative candidate platforms, the scaling up of quantum optical setups is challenged by the extremely fine experimental control required by this enterprise. Indeed,

it seems that mastering optical engineering will be the prerequisite to achieving substantial fundamental advances with nonclassical light.

Besides its fundamental interest, quantum optics is also at the center of the current program to leverage quantum effects in order to build technology with unprecedented capabilities. Optical quantum random number generation [6] and cryptography [7] are mature, currently commercialized technologies. Optical quantum computation and metrology [8] have seen great advances since their inception, but currently require an improved optical control in order to become widespread technologies. Again, the success of optical quantum technologies hinges on the availability of highly controllable optical devices, as well as of complete and reliable optical characterization techniques.

In this thesis we tackle the challenge of designing and characterizing pulsed sources of nonclassical light in two different contexts. In our first project, we consider a new application of intensity-squeezed light to a biologically relevant metrology problem. In our second project, we address the problem of building and characterizing a source of pulsed twin beams operating in the high gain regime of parametric down-conversion.

1.1 Thesis outline

This thesis is divided into an Introduction, two main Parts, corresponding to the two distinct projects mentioned above, and a Conclusion. Each Part contains one or more Chapters, which are numbered consecutively. In Section 1.1 of the Introduction (Chapter 1), we provide the thesis outline. In Section 1.2, we define some basic concepts and notation used throughout the thesis. More specific background on each of the two projects is provided at the beginning of the relevant chapters.

The first part (Part I) contains the work done in relation to a novel use of nonclassical light to aid in a biological metrology problem. We propose to improve a state of the art label-free non-linear microscopy technique called stimulated emission microscopy by using bright intensity-squeezed states of light as optical probes.

In Chapter 2 we lay out our proposal to achieve quantum-enhanced stimulated emission microscopy. We begin the chapter with a presentation of stimulated emission microscopy, and a rationale to use sub-Poissonian light to improve its sensitivity. We then provide a design of a source based on optical parametric amplification of a coherent seed. Finally, we present our experimental results and assess the limitations of the current experimental setup. We conclude that an improved design for our sub-Poissonian light source is necessary, for which we require a more detailed model of the parametric amplification process than was available to us at the time of the experiment.

In Chapter 3, we develop a theoretical framework to model the photon statistics obtained by phase-sensitive amplification of pulsed and focused coherent states in an optical parametric amplifier. We analyze the spatio-temporal structure of parametric amplification, first considering spatial and temporal degrees of freedom of the interacting beams separately, and finally considering an integrated spatio-temporal description. This modelling framework allows us to quantify the effect that different optical propagation phenomena have on the achievable squeezing. Finally, we use this insight to propose an improved design for a sub-Poissonian light source.

The second part (Part II) contains the work done in relation to the generation and characterization of twin-beams in the high-gain regime of parametric down-conversion.

In Chapter 4 we present a new theoretical framework to efficiently simulate the emission

of waveguided high-gain pulsed twin-beam sources. This framework admits an arbitrarily high parametric gain, and includes parasitic nonlinear phenomena such as self-phase modulation and cross-phase modulation of the pump field. The addition of these phenomena is motivated by the experiments reported in Chapter 5. We begin the chapter by presenting the equations of motion obeyed by the interacting fields in a waveguided parametric down-conversion process, in the presence of parasitic nonlinearities, under a small set of assumptions. We then solve these differential equations, obtaining a non-iterative solution for a simple case. Finally, we illustrate the usefulness of our framework by computing the high-gain joint spectral amplitude of a twin-beam source.

In Chapter 5 we demonstrate a general experimental framework to characterize broadband twin-beam sources in the high-gain regime. In the first place, we introduce cascaded stimulated emission tomography (SET), a technique which generalizes previous seeded measurements of pulsed twin-beam sources: one polarization of a pulsed, type-II PDC source is seeded with a narrowband field, and the broadband light generated in both output polarizations is measured. We show that the redundancy offered by this measurement allows for the self-referenced inference of the PDC interaction strength, and also provides information about the spectral phase of the biphoton joint spectral amplitude. Using the information offered by cascaded SET, together with a small number of complementary measurements, we fit the theoretical model of twin-beam generation provided in Chapter 4. With this fitted theoretical model we can interpret several features of the spectral data, assigning them to parasitic nonlinearities besides PDC. Moreover, we use this fitted model to identify limitations of the current source design, and to explore new designs which overcome these shortcomings.

1.2 Basic concepts and notation

In this section we present some basic theoretical tools used throughout this thesis. We assume that the reader is familiar with the formalism of quantum mechanics, as well as with classical electromagnetism. Here, we begin with a brief presentation of quantum optics, which will serve as background for the rest of the thesis. We then provide a summary of ultrafast linear optics, reviewing some key phenomena related to the propagation of ultrafast optical pulses in dielectric media. The concepts presented here will be relevant throughout the thesis, and the notation that we introduce will be extensively used in Chapter 3. Next, we give a brief presentation of nonlinear optics, noting its relevance both as a means to generate non-classical quantum states of light, and as a tool for classical optical engineering. Finally, we focus on the quantum applications of nonlinear optics, using broadband parametric down conversion as a paradigmatical example.

1.2.1 Quantum optics

Quantum optics is the quantum theory of light and its interaction with matter, and provides a single description which accounts for the wave-like and particle-like phenomena exhibited by the electromagnetic field. A quantum field theory can be obtained from its classical counterpart through a Hamiltonian quantization procedure. This procedure consists in providing a Hamiltonian that is numerically equal to the energy of the system, as well as a set of commutation relations for the field amplitudes. These commutation relations should be specified such that we can apply the Heisenberg equation of motion to the field amplitudes and successfully retrieve the classical equations of motion.

Choice of fundamental fields

The classical evolution of optical fields in charge and current free, non-magnetic media such as we consider in this thesis is given by the simplified Maxwell equations

$$\frac{\partial}{\partial t}\mathbf{B} = -\nabla \times \mathbf{E}, \tag{1.1}$$

$$\frac{\partial}{\partial t}\mathbf{D} = \nabla \times (\mathbf{B}/\mu_0), \tag{1.2}$$

$$\nabla \cdot \mathbf{D} = 0, \tag{1.3}$$

$$\nabla \cdot \mathbf{B} = 0, \tag{1.4}$$

where μ_0 is the vacuum permeability and the displacement and electric fields are linked by the constitutive relation

$$\mathbf{D} = \epsilon_0 \mathbf{E} + \mathbf{P}. \tag{1.5}$$

It is common practice to adopt the electric field as a fundamental field, writing the polarization $\mathbf{P}$ as a function of $\mathbf{E}$. This, however, has been shown to be incompatible with a consistent Hamiltonian quantization procedure whenever the polarization is a non-linear function of $\mathbf{E}$[9,10]. A simple argument runs as follows[10]: choosing $\mathbf{E}$ as the fundamental field, we express it as a linear superposition of creation and annihilation operators: $\mathbf{E} = \mathrm{poly}_1(a_\sigma, a_\sigma^\dagger)$, where σ labels bosonic operators fulfilling $[a_\sigma, a_{\sigma'}^\dagger] = \delta_{\sigma,\sigma'}$, and poly_M is shorthand for a polynomial of order M. We also assume that $\mathbf{B} = \mathrm{poly}_1(a_\sigma, a_\sigma^\dagger)$, since we are considering a non-magnetic material. Writing the nonlinear electric polarization as a

power series of order N in the electric field, $\mathbf{P} = \text{poly}_N(a_\sigma, a_\sigma^\dagger\sigma)$, the Hamiltonian will be a polynomial of order $N+1$[10] in the bosonic operators: $H = \text{poly}_{N+1}(a_\sigma, a_\sigma^\dagger)$. Now, using the Heisenberg equation of motion to compute the temporal evolution of the magnetic field, we find

$$\partial_t \mathbf{B} = [\mathbf{B}, H]/(i\hbar) = [\text{poly}_1(a_\sigma, a_\sigma^\dagger), \text{poly}_{N+1}(a_\sigma, a_\sigma^\dagger)] = \text{poly}_N(a_\sigma, a_\sigma^\dagger), \tag{1.6}$$

clearly contradicting the Maxwell-Faraday equation (1.1), which states that the time derivative of the magnetic field is linear in the electric field, and thus a linear combination of bosonic operators. This contradiction does not occur if we choose the electric displacement field, **D**, as our fundamental field. Moreover, working with **D** guarantees that our fields fulfill Gauss' Law (Eq. 1.3), which greatly simplifies calculations. This is not true for the electric field, **E**, in non-homogeneous dielectric structures.

Given our choice of fields and neglecting material dispersion and absorption, we write the polarization in a dielectric material as a series of the form

$$P_i = \Gamma^{(1)}_{ij} D_j + \Gamma^{(2)}_{ijk} D_j\, D_k + \dots \tag{1.7}$$

where summation over repeated indices is implied. The linear coefficients $\Gamma^{(1)}_{ij}$ can be simply related to the usual linear susceptibilities, $\chi^{(1)}_{ij}$, as[10]

$$1 - \Gamma^{(1)}_{ij} = (1 + \chi^{(1)}_{ij})^{-1} \tag{1.8}$$

To include the effect of material dispersion, the definition of the polarization has to be

generalized to represent a response function of the form

$$P_i(t) = \int \mathrm{d}s \; \Gamma_{ij}^{(1)}(t-s) D_j(s) + ..., \tag{1.9}$$

accounting for a frequency-dependent response of the material. Denoting the Fourier transform of a temporal function as

$$f(\omega) = \mathcal{F}\{f(t)\} = \int \frac{\mathrm{d}t}{\sqrt{2\pi}} e^{i\omega t} f(t), \tag{1.10}$$

this response is expressed in the frequency domain in terms of a simple transfer function

$$P_i(\omega) = \Gamma_{ij}^{(1)}(\omega) D_j(\omega) + ... \tag{1.11}$$

Field quantization in vacuum

Here we will proceed to apply a quantization procedure to an optical field in the vacuum. From classic electromagnetism arguments[11], we can write the energy density of the electromagnetic field as

$$\mathcal{H} = \int \mathbf{H} \cdot \mathrm{d}\mathbf{B} + \mathbf{E} \cdot \mathrm{d}\mathbf{D} \tag{1.12}$$

which, given the constitutive relation Eq. 1.5 and the expansion of the polarization in terms of the displacement field in vacuum Eq. 1.77, yields

$$\mathcal{H}_{\mathrm{vac}} = \frac{\mathbf{B}^2}{2\mu_0} + \frac{\mathbf{D}^2}{2\epsilon_0} \tag{1.13}$$

with the Hamiltonian H given by the integral over space of this energy density. It has been shown in[12,13] that the commutation relations that recover Maxwell's equations for the operators $\mathbf{D}$ and $\mathbf{B}$ using the Hamiltonian given above are

$$[\hat{D}_j(\mathbf{r}), \hat{B}_l(\mathbf{r}')] = i\hbar\,\epsilon_{jlm}\,\frac{\partial}{\partial r_m}\delta(\mathbf{r}-\mathbf{r}'), \tag{1.14}$$

$$[\hat{D}_j(\mathbf{r}), \hat{D}_l(\mathbf{r})] = [\hat{B}_j(\mathbf{r}), \hat{B}_l(\mathbf{r}')] = 0. \tag{1.15}$$

where ϵ_{jlm} is the Levi-Civita symbol and $\{j, l, m\}$ label Cartesian coordinates.

To recover a more familiar expression for the field commutators, we expand the $\mathbf{D}$ and $\mathbf{B}$ fields in the basis of the harmonic solutions of the linear Maxwell equations. Assuming linearly polarized fields in vacuum, said solutions are the plane waves in orthogonal polarizations

$$\hat{D}(\mathbf{r}, t) = \int \mathrm{d}\mathbf{r}\,\sqrt{\frac{\hbar\omega\epsilon_0}{2\pi V}}\,e^{i(\mathbf{k}\cdot\mathbf{r}-\omega t)}\;\hat{a}(\mathbf{k}) + \mathrm{h.c} \tag{1.16}$$

$$\hat{B}(\mathbf{r}, t) = i\int \mathrm{d}\mathbf{r}\,\sqrt{\frac{\hbar\omega\mu_0}{2\pi V}}\,e^{i(\mathbf{k}\cdot\mathbf{r}-\omega t)}\;\hat{a}(\mathbf{k}) + \mathrm{h.c} \tag{1.17}$$

with the dispersion relation $|\mathbf{k}| = \omega/c$, where V is a quantization volume. The amplitude $\hat{a}(\mathbf{k})$, now considered a quantum operator, can be written in terms of the magnetic and displacement fields (also quantum operators). Doing so, we find that $\hat{a}(\mathbf{k})$ and $\hat{a}^\dagger(\mathbf{k}')$ satisfy the bosonic commutation relations[14]

$$[\hat{a}(\mathbf{k}), \hat{a}^\dagger(\mathbf{k}')] = \delta(\mathbf{k}-\mathbf{k}') \tag{1.18}$$

$$[\hat{a}(\mathbf{k}), \hat{a}(\mathbf{k}')] = [\hat{a}^\dagger(\mathbf{k}), \hat{a}^\dagger(\mathbf{k}')] = 0 \tag{1.19}$$

which identifies them as creation and annihilation operators. Moreover, the free evolution Hamiltonian can be re-written in terms of these operators, yielding the familiar expression

$$H_{\text{vac}} = \int \mathrm{d}\mathbf{k}\, \hbar\omega \left(\hat{a}^\dagger(\mathbf{k})\hat{a}(\mathbf{k}) + \frac{1}{2}\right) \tag{1.20}$$

Quantizing the electromagnetic field in a general nonlinear, absorptive and dispersive medium has been the subject of much work[9,13,15–18]. A considerable difficulty is met when trying to quantize the fields in a dispersive medium: while the dispersive character of the medium requires $\mathbf{P}$ to depend on $\mathbf{D}$ at possibly all previous times (Eq. (1.9)), the Hamiltonian is by definition a state functional and therefore can only involve dynamical variables at a single time (the present). This is solved in[16] by introducing additional auxiliary harmonic oscillators representing the dielectric medium, which are coupled in a frequency-dependent way to the electromagnetic field. Here we will not delve into this question, but will only mention that the usual quantization of the electromagnetic field holds in the dispersive case, provided that the right normalization of the fields is used.

Simple states and observables

We will now concentrate on a single monochromatic mode of the electromagnetic field, described by the bosonic operators $(a, a^\dagger)$, where we drop the label $\mathbf{k}$. Using the commutation relation $[\hat{a}, \hat{a}^\dagger] = 1$, we can compute some simple observables of the field. For convenience, we will set the reduced Planck constant to unit ($\hbar = 1$). The operator

$$\hat{n} = \hat{a}^\dagger\hat{a} \tag{1.21}$$

is the photon number operator, as its eigenvalues correspond to those of the free-evolution Hamiltonian, rescaled by the photon energy. The eigenvectors of the photon number operator, $|n\rangle$ are called Fock states, and define a complete basis for the state of the electromagnetic field in this mode. The creation and annihilation operators receive their name from the way that they act on the Fock states, by either adding or removing a photon:

$$\hat{a}^\dagger|n\rangle = \sqrt{n+1}\ |n+1\rangle \quad , \quad \hat{a}|n\rangle = \sqrt{n}\ |n-1\rangle \quad , \quad \hat{a}\ |0\rangle = 0, \tag{1.22}$$

where the Fock state $|0\rangle$ is called the vacuum state.

Combining the creation and annihilation operators we can construct two observables,

$$\hat{X} = \frac{\hat{a}+\hat{a}^\dagger}{2} \quad , \quad \hat{P} = \frac{\hat{a}-\hat{a}^\dagger}{2i}, \tag{1.23}$$

called the field quadratures. These correspond to the sine and cosine components of a monochromatic electromagnetic field, and are canonically conjugate observables with a commutator $[\hat{X}, \hat{P}] = i$, analogously to the position and momentum of a harmonic oscillator. While the vacuum state exhibits a zero mean and variance of the photon number operator, $\langle 0|\hat{n}|0\rangle = 0$ and $\langle 0|\hat{n}^2|0\rangle = 0$, the same is not true for the quadrature operators. The quadratures of the vacuum state have a zero mean $\langle 0|\hat{X}|0\rangle = \langle 0|\hat{P}|0\rangle = 0$, but a non-zero variance, as the Heisenberg uncertainty principle requires that

$$\mathrm{var}(\hat{X})\mathrm{var}(\hat{P}) \geq |\frac{i}{2}[\hat{X}, \hat{P}]|^2 = 1/4. \tag{1.24}$$

In particular, defining the rotated quadrature

$$\hat{X}_\theta = \frac{e^{i\theta}\hat{a}^\dagger + e^{-i\theta}\hat{a}}{2}, \tag{1.25}$$

the vacuum state is a minimum uncertainty state with $\mathrm{var}(\hat{X}_\theta) = 1/2$ for all phases θ.

Simple transformations

In the Heisenbeg picture of quantum mechanics, the evolution of the quantum state due to a given Hamiltonian is expressed as a transformation of the field bosonic operators. We will now calculate the effect of some simple Hamiltonians.

Let us first consider the displacement Hamiltonian,

$$\hat{H}_{\mathrm{disp}}(\alpha) = i\hbar\,\alpha\,\hat{a}^\dagger + \mathrm{h.c.} \tag{1.26}$$

Applying the Heisenberg equation of motion, we find that $\hat{H}_{\mathrm{disp}}(\alpha)$ generates the following evolution of the annihilation operators:

$$\begin{aligned} \partial_t\,\hat{a}(t) &= -\frac{1}{i\hbar}[\hat{H}, \hat{a}(t)] = \alpha, \\ \Rightarrow \hat{a}(t) &= \hat{a}(0) + \alpha\,t \end{aligned} \tag{1.27}$$

which we identify as a displacement. Thus, the unitary operation $\hat{D}(\alpha) = \exp(\alpha\,\hat{a}^\dagger - h.c)$ is called the displacement operator, as it generates the transformation

$$\hat{D}(\alpha)^\dagger\,\hat{a}\,\hat{D}(\alpha) = \hat{a} + \alpha. \tag{1.28}$$

The state that we obtain by acting on the vacuum state with the displacement operator is called a coherent state

$$|\alpha\rangle = \hat{D}(\alpha)\,|0\rangle, \tag{1.29}$$

which, like the vacuum state, is a minimum uncertainty state with $\mathrm{var}(\hat{X}_\theta) = 1/2$ for all phases of the rotated quadrature $\hat{X}_\theta$.

A second important mode transformation is that describing a four-port beam-splitter. This ubiquitous unitary transformation describes not only the effect of semi-transparent optical elements, but rather a very general class of linear mode-mixing interactions such as polarization splitting in a polarizing beam-splitter (PBS), sum-frequency generation in a quantum pulse gate[19] or light-matter interaction in a warm-vapor quantum memory[20]. The effect of a beam-splitter on two input modes represented by the bosonic operators $\hat{a}_1$ and $\hat{a}_2$ is

$$\begin{aligned} \hat{a}_1 &\to \sqrt{T}\,\hat{a}_1 + \sqrt{1-T}\,e^{i\phi_1}\,\hat{a}_2 \\ \hat{a}_2 &\to \sqrt{1-T}\,e^{i\phi_2}\,\hat{a}_1 - \sqrt{T}\,e^{i(\phi_1+\phi_2)}\,\hat{a}_2 \end{aligned} \tag{1.30}$$

where T is the fraction of input photons that are transmitted, $1-T$ is the fraction of input photons that are reflected in the beam-splitter, and ϕ_1, ϕ_2 are two free phases.

Finally, a central transformation in this thesis is that generated by the (in general two-mode) squeezing Hamiltonian,

$$\hat{H}_{\mathrm{sq}} = -i\frac{\xi}{2}\,\hat{a}_1^\dagger\,\hat{a}_2^\dagger + \mathrm{h.c.} \tag{1.31}$$

where ξ is a complex number referred to as the squeezing parameter. The evolution of the

bosonic operators that this Hamiltonian generates is

$$\begin{aligned}\partial_t\,\hat{a}_1(t) &= \frac{i}{\hbar}[\hat{H}_{\rm sq},\hat{a}_1(t)] = -\xi\,\hat{a}_2^\dagger(t)\\ \partial_t\,\hat{a}_2^\dagger(t) &= \frac{i}{\hbar}[\hat{H}_{\rm sq},\hat{a}_2^\dagger(t)] = -\xi^*\,\hat{a}_1(t)\end{aligned} \tag{1.32}$$

$$\begin{aligned}\Rightarrow \hat{a}_1(t) &= \cosh(r)\,\hat{a}_1(0) - e^{i\theta}\sinh(r)\,\hat{a}_2^\dagger(0)\\ \Rightarrow \hat{a}_2^\dagger(t) &= \cosh(r)\,\hat{a}_2^\dagger(0) - e^{i\theta}\,\sinh(r)\hat{a}_1(0)\end{aligned}$$

where we have decomposed the product $\xi\,t$ into its magnitude and phase, $\xi\,t = r\,e^{i\theta}$. In the degenerate case in which the two modes coupled by this Hamiltonian are the same ($\hat{a}_1 = \hat{a}_2 = \hat{a}$), and assuming a real ξ, the quadrature operators are transformed in the following way:

$$\hat{X}(t) = \hat{X}(0)\exp(-r) \quad , \quad \hat{P}(t) = \hat{P}(0)\exp(r), \tag{1.33}$$

where the $\hat{X}$ quadrature has been squeezed and the $\hat{P}$ quadrature antisqueezed. In the non-degenerate case ($\hat{a}_1 \neq \hat{a}_2$), the two-mode squeezing Hamiltonian generates correlations between the two modes. Defining the sum of the $\hat{X}$ quadratures $\hat{X}_+(t) = \hat{X}_1(t) + \hat{X}_2(t)$, and the difference of the $\hat{P}$ quadratures $\hat{P}_-(t) = \hat{P}_1(t) - \hat{P}_2(t)$, the two-mode squeezing Hamiltonian generates the transformation

$$\hat{X}_+(t) = \hat{X}_+(0)\exp(-r) \quad , \quad \hat{P}_-(t) = P_-(0)\exp(-r) \tag{1.34}$$

For a squeezing parameter tending to infinity $r \to \infty$, a measurement of one quadrature of the first mode yielding $\hat{X}_1 = x_1$ ($\hat{P}_1 = p_1$), immediately implies that the outcome of an

analogous measurement on the second mode would yield, $\hat{X}_2 = -x_1$ ($\hat{P}_2 = p_1$), regardless of the physical locations of these modes. This form of correlation was discussed by Einstein, Podolsky and Rosen in 1935[21], and unveiled one of the most characteristic features of quantum mechanics: non-locality.

In particular, the two-mode squeezing Hamiltonian applied on vacuum creates perfect photon-number correlations between the two-modes that it acts on[22]:

$$\exp(-i\,\hat{H}_{\rm sq}t)|0,0\rangle = \cosh^{-1}(r)\sum_{n=0}^{\infty}\Big[-\exp^{i\theta}\tanh(r)\Big]^n|n,n\rangle \tag{1.35}$$

In the low-squeezing limit, the state generated in this interaction is well approximated as a sum of the vacuum and two-photon components, $|\psi\rangle \approx |0,0\rangle + r\,\exp(i\theta)\,|1,1\rangle$. This state has been used to herald the generation of a single photon in one mode upon detection of a photon in the other mode[23]. In the high-gain regime, where more than a single pair of photons is created on average, a pair of optical modes in this quantum state are referred to as twin-beams. The description and characterization of such twin-beams will be the focus of Chapters 4 and 5.

Broadband modes

The monochromatic modes that we have considered until now are sometimes not well suited to describe the quantum properties of pulses of light. For instance, the light generated by a pulsed mode-locked laser consists of a superposition of plane waves of different frequencies. Assuming propagation in the z direction, such that $k_z(\omega) = \omega/c$ is the wavenumber of a plane wave of frequency ω, it is useful to define an annihilation operator that acts on a

superposition of frequencies as

$$\hat{A} = \int d\omega\, f(\omega)\, \hat{a}(\omega), \tag{1.36}$$

where $\hat{a}(\omega)$ are the monochromatic annihilation operators introduced earlier, and $f(\omega)$ is a frequency dependent amplitude. If $\int d\omega |f(\omega)|^2 = 1$, the broadband creation and annihilation operators fulfill the usual bosonic commutation relations, $[\hat{A}, \hat{A}^\dagger] = 1$. A coherent pulse of light with a spectral amplitude $f(\omega)$ can thus be written simply as a displaced vacuum, where the displacement is effected on the corresponding broadband mode

$$|\alpha_{f(\omega)}\rangle = \exp(\alpha\, \hat{A}^\dagger - \text{h.c})\, |0\rangle \tag{1.37}$$

Similarly, a single photon in a superposition of frequencies is suscinctly expressed as a broadband annihilation operator applied on the vacuum state:

$$|1_{f(\omega)}\rangle = \hat{A}^\dagger\, |0\rangle \tag{1.38}$$

1.2.2 Ultrafast linear optics

In this thesis we will deal with pulses of light propagating in dielectric materials. The linear propagation of these pulses (i.e. the evolution of the fields neglecting the nonlinear medium polarization) has a great influence on the classical and quantum properties of the light that we can generate. We will here recall some basic notions about linear propagation of light in dielectric media, providing basic notation for the following chapters.

The linear propagation of light in a dielectric medium is given by Maxwell's equations,

from which we can write the general wave equation

$$\frac{\partial^2}{\partial t^2}\mathbf{D} + \epsilon_0\, c^2\, \nabla \times \nabla \times \mathbf{E} = 0 \tag{1.39}$$

with $c = (\epsilon_0\, \mu_0)^{-1/2}$, and where we assume that the material polarization is a linear combination of the electric displacement at different times,

$$P_i(t) = \int \mathrm{d}s\; \Gamma^{(1)}_{ij}(t-s) D_j(s). \tag{1.40}$$

This deceivingly simple-looking equation can describe a large variety of physical phenomena, depending on the specific relation between the electric field and the electric displacement. In what follows we will unpack some of these phenomena.

Material dispersion

We begin by considering the linear propagation of a pulse in an isotropic, homogeneous linear medium. This is a good description of optical elements made of amorphous materials, such as glass lenses or prisms. It is also a good approximation of the propagation of linearly polarized beams in birefringent crystals, as long as the polarization of the beam is aligned with one of the optical axes of the crystal.

In homogeneous and isotropic media, we can omit the vectorial nature of $\Gamma^{(1)}_{ij}$, as well as its spatial dependence. Then, in the frequency domain, the electric field is suscinctly written as a function of the displacement field:

$$\mathbf{E}(\omega) = \frac{1 - \Gamma^{(1)}(\omega)}{\epsilon_0}\mathbf{D}(\omega) = \frac{1}{\epsilon_0\; \epsilon_r(\omega)}\mathbf{D}(\omega) \tag{1.41}$$

where $\Gamma^{(1)}(\omega)$ is the Fourier transform of $\Gamma^{(1)}(t)$ and $\epsilon_r(\omega)$ is the usual frequency-dependent relative permittivity of the dielectric. Due to the linearity of Maxwell's equations, the propagation of any temporal waveform (pulse) can be expressed as a superposition of monochromatic harmonic solutions:

$$\mathbf{D}(\mathbf{r},t) = \int \frac{\mathrm{d}\omega}{\sqrt{2\pi}}\ \tilde{\mathbf{D}}^{(+)}(\mathbf{r},\omega)\ e^{-i\omega t} + \tilde{\mathbf{D}}^{(-)}(\mathbf{r},\omega)\ e^{i\omega t} \tag{1.42}$$

where we have separated the solutions into a positive and a negative frequency component, fulfilling $\tilde{\mathbf{D}}^{(+)} = (\tilde{\mathbf{D}}^{(-)})^*$. These harmonic solutions obey the Helmholtz equation

$$\nabla^2\tilde{\mathbf{D}}^{(+)} + k^2(\omega)\tilde{\mathbf{D}}^{(+)} = 0 \tag{1.43}$$

where $k(\omega) = \omega\, n(\omega)/c$ is the frequency-dependent wavenumber and $n(\omega) = \sqrt{\epsilon_r(\omega)}$ is the frequency-dependent refractive index.

We will first consider the plane-wave solution of this equation, assuming that the field varies only in one direction and neglecting its transverse confinement. This will allow us to focus on the temporal aspects of wave propagation in a dispersive medium. The positive-frequency component of a plane wave propagating in the z direction is written:

$$\tilde{\mathbf{D}}^{(+)}(\mathbf{r},\omega) = A(\omega)\ e^{ik(\omega)z}\mathbf{a} \tag{1.44}$$

where $\mathbf{a}$ is a transverse unit vector (contained in the x-y plane) in order to satisfy Gauss' Law, and $A(\omega)$ is the field spectral amplitude.

Let us briefly lay out some notation regarding the spectral amplitude of optical pulses.

Our fundamental light source will be a mode-locked laser that generates trains of phase-coherent pulses at fixed repetition rate. The spectral amplitude of such a laser is a frequency comb, but it is often useful to disregard the individual frequency lines and consider only their spectral envelope. While many mode locked lasers generate pulses with a temporal profile close to a sech^2 shape, we will now approximate them as Gaussian pulses with a spectral amplitude

$$A_{\mathrm{gauss}}(\omega) = A_0 \exp\Big(- (\omega - \omega_0)^2 \tau^2 \Big) \tag{1.45}$$

where we define an optical carrier frequency, ω_0, linked to the usual carrier wavelength in vacuum through $\lambda_0 = 2\pi c/\omega_0$. The width parameter τ corresponds to the standard deviation of the intensity (absolute square) of the pulse temporal amplitude

$$A_{\mathrm{gauss}}(t) = (2\tau^2)^{-1/2} \ \exp\Big(- \frac{t^2}{4\tau^2} + i\,\omega_0 t \Big). \tag{1.46}$$

This width can be related to the more usual full width at half maximum of the temporal intensity of the pulses (FWHM_τ) through

$$\mathrm{FWHM}_\tau = 2\sqrt{2\ln 2}\,\tau \tag{1.47}$$

It is also convenient to express this width in terms of wavelength, as measured in an optical spectrum analyzer (OSA). The intensity FWHM of the spectrum in units of wavelength is

$$\mathrm{FWHM}_\lambda = \lambda_0^2\,\sqrt{2\ln 2}/(2\pi\, c\,\tau) \tag{1.48}$$

Now that we have introduced some basic notation, we can consider the spatial propaga-

tion of such a temporal pulse in a dielectric material. Given that the bandwidth of optical pulses is typically very small compared to ω_0, it is convenient to expand their wavenumber into a Taylor expansion around the carrier:

$$k(\omega) \;=\; k(\omega_0+\Omega) \;\approx\; k(\omega_0) + \frac{\partial k(\omega)}{\partial \omega}\Big|_{\omega_0}\Omega + \frac{1}{2}\frac{\partial^2 k(\omega)}{\partial \omega^2}\Big|_{\omega_0}\Omega^2 + .. \tag{1.49}$$

where we denote the frequency detuning from the carrier frequency as $\Omega = \omega - \omega_0$. Even for ultrafast pulses, it is often sufficient to keep only up to the quadratic term in Ω in order to guarantee a good approximation. The first term of this expansion is proportional to the speed at which the carrier propagates, also called the phase velocity v_{ph}:

$$v_{\mathrm{ph}} = \frac{\omega_0}{k(\omega_0)} = \frac{c}{n(\omega_0)} \tag{1.50}$$

The second term in Eq. (1.49) gives the speed at which the pulse envelope propagates, called the group velocity v_{g}:

$$v_{\mathrm{g}}(\omega_0) = \Big(\frac{\partial k(\omega)}{\partial \omega}\Big|_{\omega_0}\Big)^{-1} = c\,\Big(n(\omega_0) + \frac{\partial n}{\partial \omega}\Big|_{\omega_0}\omega_0\Big)^{-1} \tag{1.51}$$

The group velocity is generally different from the phase velocity in a dielectric medium. Most materials exhibit a refractive index that increases with frequency, a behaviour called *normal dispersion*. In these materials, the group velocity of a pulse is slower than its phase velocity.

Finally, the third term is related to group velocity dispersion (GVD). It describes a group velocity that varies monotonically as a function of frequency. In pulses with a broad

enough spectrum, this leads to chirped pulses: the higher frequencies will move to the beginning/end of the pulse depending on the sign of the GVD. There are two related but different quantities used in the literature to describe this phenomenon. The quantity that arises naturally from our Taylor expansion is referred to simply as GVD, and it can be seen as the derivative of the inverse group velocity with respect to the angular frequency :

$$\mathrm{GVD}(\omega_0) = \frac{\partial^2 k(\omega)}{\partial \omega^2}\Big|_{\omega_0} = \frac{\partial}{\partial \omega}\left(\frac{1}{v_g(\omega)}\right)\Big|_{\omega_0}. \tag{1.52}$$

In the context of ultrafast optical pulses, this quantity is naturally given in units of $\mathrm{fs}^2/\mathrm{mm}$. An alternative definition, used in the context of optical fiber communications, is given by the differential delay experienced as a function of wavelength, per distance travelled in the medium. This is referred to as the dispersion parameter

$$\mathrm{D}_\lambda = -\frac{2\pi c}{\lambda^2}\mathrm{GVD} \tag{1.53}$$

and is typically given in units of ps/(nm km).

Gaussian beams

Real optical beams are not plane waves: they do not extend infinitely in space, but are confined in the transverse direction. Still, laser beams mostly propagate in one direction, with little variation of their transverse profile. Under this condition, known as the paraxial approximation (see a detailed account in [24,25]), the fields will be approximately orthogonal to the principal direction of propagation (e.g. here they lie in the x-y plane), while having a finite transverse extension. Assuming a transverse linearly polarized field, we can capture

its transverse spatial dependence writing the field as a superposition of plane waves with different transverse wavevectors

$$\tilde{D}^{(+)}(\boldsymbol{\rho}, z, \omega) = \int \frac{\mathrm{d}\mathbf{q}}{2\pi}\, e^{-i\mathbf{q}\cdot\boldsymbol{\rho}}\, \tilde{D}_q^{(+)}(\mathbf{q}, z, \omega) \tag{1.54}$$

$$\tilde{D}_q^{(+)}(\mathbf{q}, z, \omega) = \int \frac{\mathrm{d}\boldsymbol{\rho}}{2\pi}\, e^{i\mathbf{q}\cdot\boldsymbol{\rho}}\, \tilde{D}^{(+)}(\boldsymbol{\rho}, z, \omega) \tag{1.55}$$

where we have defined the transverse coordinates $\boldsymbol{\rho} = (x, y)$.

Let us now compute the evolution of an optical field with a finite transverse profile in a homogeneous and isotropic dielectric medium. Introducing the transverse plane wave expansion (Eq. 1.54) into the Helmholtz equation that describes such a medium, Eq. (1.43), we obtain a differential equation for the transverse plane wave amplitudes

$$\Big(\frac{\partial^2}{\partial z^2} + k^2(\omega) - |\mathbf{q}|^2\Big)\tilde{D}_q^{(+)}(\mathbf{q}, z, \omega) = 0, \tag{1.56}$$

which has a solution

$$\tilde{D}_q^{(+)}(\mathbf{q}, z, \omega) = \tilde{D}_q^{(+)}(\mathbf{q}, 0, \omega)\, e^{ik_z(\mathbf{q},\omega)z} \tag{1.57}$$

with

$$k_z(\mathbf{q}, \omega) = \sqrt{k^2(\omega) - |\mathbf{q}|^2}. \tag{1.58}$$

Given an initial transverse profile at $z = 0$, we can find the spatial profile of the beam at any position z by computing the transverse plane wave decomposition of the initial profile (1.55), applying the solution that we found (1.57) and computing the inverse transformation (1.54).

A particularly useful beam transverse profile, due to its analytical tractability, is that of

a Gaussian beam. We write a Gaussian beam with a flat phase at $z = 0$ as

$$\tilde{D}^{(+)}_{\text{gauss}}(\boldsymbol{\rho}, z = 0, \omega) = A_0 \exp\Big(- \frac{|\boldsymbol{\rho}|^2}{4w_0^2}\Big) \tag{1.59}$$

where w_0 is the standard deviation of the intensity spatial profile. It is often more convenient to refer to the full width at half maximum of the intensity profile (FWHM_ρ), which is related to w_0 through

$$\text{FWHM}_\rho = 2\sqrt{2\ln 2}\, w_0. \tag{1.60}$$

We can obtain the transverse plane wave representation of the beam at any position z by appying (1.55) and (1.57)

$$\tilde{D}^{(+)}_{q,\text{gauss}}(\mathbf{q}, z, \omega) = 2\, w_0^2\, A_0 \;\exp\Big(- |\mathbf{q}|^2 \; w_0^2\Big) \exp\Big(iz\,(k(\omega) - \frac{|\mathbf{q}|^2}{2k(\omega)})\Big), \tag{1.61}$$

where we have used the fact that, in the paraxial approximation, we can assume that the transverse components of the wavevector will be much smaller than the wavenumber, allowing us to Taylor expand the longitudinal wavevector as

$$k_z(\mathbf{q}, \omega) \approx k(\omega) - \frac{|\mathbf{q}|^2}{2k(\omega)} \tag{1.62}$$

The more familiar spatial distribution of a Gaussian beam can be obtained by transforming Eq. (1.61) back to the spatial domain, which yields

$$\tilde{D}^{(+)}_{\text{gauss}}(\mathbf{r}, \omega) = \frac{A_0}{2}\frac{w_0}{w(z)} \exp\Big(- \frac{|\boldsymbol{\rho}|^2}{4w(z)^2}\Big) \exp\Big(i\,(k(\omega)z + k(\omega)\frac{|\boldsymbol{\rho}|^2}{2R(z)} + \phi(z)\Big) \tag{1.63}$$

with a position-dependent beam waist, phase-front curvature and Guoy phase, respectively

$$w(z) = w_0\sqrt{1+\left(\frac{z}{z_R}\right)^2} \quad , \quad R(z) = z\left(1+\left(\frac{z_R}{z}\right)^2\right) \quad , \quad \phi(z) = \arctan\left(\frac{z}{z_R}\right) \tag{1.64}$$

where we have defined the Rayleigh range

$$z_R = 2\,k(\omega)\,w_0^2 \tag{1.65}$$

Anisotropic media — Refractive indices in a uniaxial crystal

Many of the crystals relevant to quantum optics experiments, e.g. barium borate (BBO), are not isotropic. The relation between the electric displacement and the polarization in them depends on the direction of the fields. In general, this means that the full $\Gamma^{(1)}_{ij}$ tensor has to be considered in equation 1.11, although simplifications can be made. Given that we have assumed a non-magnetic material, the symmetry $\Gamma^{(1)}_{ij} = \Gamma^{(1)}_{ji}$ is implied. This allows us to find an xyz frame of reference, which we will call the *principal axes*, where the tensor $\Gamma^{(1)}_{ij}(\omega)$ is a diagonal 3x3 matrix. From the diagonal elements of this matrix, and analogously to the derivation in [26], we can define the three *principal indices of refraction*

$$n_j(\omega) = \sqrt{1-\Gamma^{(1)}_{jj}(\omega)} \tag{1.66}$$

where now the index j refers to a coordinate in this rotated coordinate system, and $\Gamma^{(1)}_{jj}$ is the diagonal of the rotated matrix. It is customary to classify optical crystals according to the number of different principal refractive indices that they have. A crystal where two of the principal refractive indices are equal (e.g. $n_x = n_y$) is called a uniaxial crystal. The

refractive index that is repeated is referred to as the ordinary refractive index (n_o), and the different refractive index is called extraordinary (n_e). The direction associated to the extraordinary refractive is also called the optical axis of the crystal. A crystal where all three refractive indices are different is called a *biaxial* crystal. For simplicity, here we will only consider uniaxial crystals. An extensive treatment of anisotropic beam propagation including biaxial crystals is found in [27].

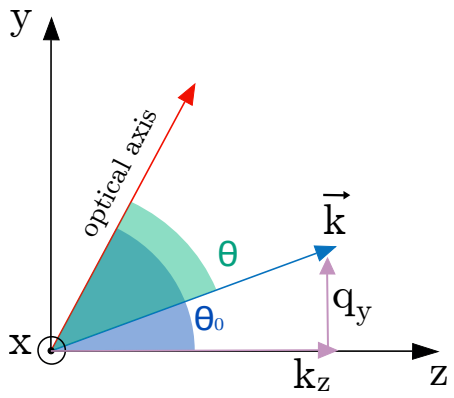


Figure 1.1: Coordinate system in an anisotropic uniaxial crystal. The angle between the optical axis and the main propagation direction, z, is denoted as θ_0. Any plane wave is characterized by the angle θ with respect to the optical axis at which it propagates.

A wave polarized along the jth principal axis of a crystal will propagate as if it was in a homogeneous medium with a refractive index n_j. But what happens to a beam with an arbitrary polarization? As explained in [26], a plane wave propagating in an arbitrary direction is a solution of the anisotropic Helmholtz equation, but it has two possible values for its wavevector, one for each of two orthogonal polarizations. Consider a plane wave propagating along the z direction in a uniaxial crystal with its optical axis contained in the $y-z$ plane (see figure 1.1). If the wave is polarized along x (one of the two ordinary axes), its wavenumber will be given by the usual dielectric dispersion relation $k(\omega) = \omega n_o(\omega)/c$. An orthogonally polarized wave (polarized along y), however, has a polarization that is not

along either of the principal axes. In a slight abuse of notation, this component will be referred to as the extraordinarily polarized wave, or e-wave, despite not having a polarization completely aligned with the extraordinary principal axis. Denoting the angle between the light wavevector and the optical axis as θ , the refractive index experienced by this component is[27]

$$n_{\text{ext}}^2(\omega,\theta) = \Big(\frac{\sin^2\theta}{n_e^2(\omega)} + \frac{\cos^2\theta}{n_o^2(\omega)}\Big)^{-1} \tag{1.67}$$

Spatial walk-off

An important consequence of crystal anisotropy is that a beam polarized along a direction that is not aligned with either of the principal axes experiences spatial walk-off. We will here consider a simple picture of this phenomenon in a uniaxial crystal. In the paraxial regime, all the plane waves that compose an arbitrary beam profile will propagate in very similar directions (i.e. at small angles from z in our convention). Defining the angle between the optical axis and z as θ_0, we can write the angle between the wavevector of any plane wave and the optical axis as

$$\theta = \theta_0 + \arcsin(\frac{q_y}{k_{\text{e}}(\omega,\theta)}) \approx \theta_0 + \frac{q_y}{k_{\text{e}}(\omega,\theta_0)} \tag{1.68}$$

where q_y is the transverse wavenumber in the direction of the optical axis. Then, due to the angular dependence of the extraordinary refractive index (1.67), there is an angular dependence of the wavenumber which can be expressed implicitly as a dependence on q_y,

$$k_{\text{e}}(\omega,q_y) = \frac{\omega\ n_{\text{ext}}(\omega,q_y)}{c}. \tag{1.69}$$

Now, recalling the transverse plane wave expansion introduced earlier (Eq. (1.54)), we can find the differential equation that the transverse plane wave amplitudes have to satisfy:

$$\Big(\frac{\partial^2}{\partial z^2} + k^2(\omega, q_y) - |\mathbf{q}|^2\Big)\tilde{D}_q^{(+)}(\mathbf{q}, z, \omega) = 0, \tag{1.70}$$

where now we have made it explicit that the wavenumber depends on the transverse propagation direction. We solve this differential equation analogously to Eq. (1.57), finding that the propagating plane wave is written

$$\tilde{D}_q^{(+)}(\mathbf{q}, z, \omega) = \tilde{D}_q^{(+)}(\mathbf{q}, 0, \omega)\ \exp(ik_z(\mathbf{q},\, \omega)z), \tag{1.71}$$

where the longitudinal wavevector k_z now has the form

$$k_z(\omega, \mathbf{q}) = \sqrt{k_\mathrm{e}(\omega, q_y)^2 - |\mathbf{q}|^2}\ \approx\ k_\mathrm{e}(\omega, q_y) - \frac{|\mathbf{q}|^2}{2k_\mathrm{e}(\omega, q_y)}. \tag{1.72}$$

Let us now consider the propagation of a harmonic wave of frequency ω_0, with a confined spatial profile, in such an anisotropic medium. The spatial profile of the propagating wave at any position z can be expressed as a function of its profile at the origin

$$\tilde{D}^{(+)}(\boldsymbol{\rho}, z, \omega_0) = \int \frac{\mathrm{d}\mathbf{q}}{2\pi}\ \exp(-i\mathbf{q}\cdot\boldsymbol{\rho})\ \tilde{D}_q^{(+)}(\mathbf{q}, 0, \omega_0)\ \exp(ik_z(\mathbf{q}, \omega_0)z) \tag{1.73}$$

where we assume the angular dependence of the longitudinal wavenumber given in (1.72). In the paraxial approximation, this longitudinal wavenumber can be Taylor expanded to

first order in θ, the angle between the wavevector and the optical axis, obtaining

$$k_z(\omega_0, \theta) \approx k_z(\omega_0, \theta_0) + \frac{\partial k_z(\omega_0, \theta)}{\partial \theta}\Big|_{\theta_0} (\theta - \theta_0) \tag{1.74}$$

where we are implying the relation between propagation angle and transverse wavenumber given in (1.68) . We can finally compute the spatial distribution of the propagating wave under these approximations:

$$\tilde{D}^{(+)}(x, y, z, \omega_0) = \exp(ik_{z0}\, z)\ \tilde{D}^{(+)}(x,\, y + \rho_{\mathrm{wo}} z,\, 0,\, \omega_0) \tag{1.75}$$

where we have defined the central wavenumber $k_{z0} = k_z(\omega_0, \theta_0)$, as well as the walk-off angle

$$\rho_{\mathrm{wo}} = \frac{\partial k_z(\omega_0, \theta)}{\partial \theta}\Big|_{\theta_0} \frac{1}{k_{\mathrm{e}}(\omega_0, \theta_0)} = \frac{\partial n_{\mathrm{ext}}(\omega_0, \theta)}{\partial \theta}\Big|_{\theta_0} \frac{1}{n_{\mathrm{ext}}(\omega_0, \theta_0)} \tag{1.76}$$

Thus, we identify that the second term of the expansion of k_z, linear in q_y, introduces a walk-off of the beam spatial profile as it propagates. The slope of the walk off is typically in the order of the milliradians.

1.2.3 Non-linear optics

Non-linear optics are a central tool for quantum optics, allowing for instance to implement the the squeezing Hamiltonian introduced earlier. In a nonlinear medium, the material polarization can be a nonlinear function of the electric displacement, giving rise to the high

order terms of the power series

$$P_i = \Gamma^{(1)}_{ij} D_j + \Gamma^{(2)}_{ijk} D_j D_k + ... \tag{1.77}$$

In a non-centrosymmetric material, the coefficient multiplying the quadratic term of the series will be non-zero, and it can be related to the usual quadratic susceptibility via

$$\Gamma^{(2)}_{ijk} = \frac{\chi^{(2)}_{ijk}}{\epsilon_0 \; n^6_{\text{typ}}}, \tag{1.78}$$

where we neglect the effects of material dispersion in the nonlinear Hamiltonian, and take n_{typ} to be an index of refraction at some "typical" wavelength [13] (e.g. the harmonic mean of the refractive indices of the three fields involved in the process).

This second order nonlinearity mediates interactions between three optical fields of different frequencies. Consider two plane waves of different frequencies, ω_1 and ω_2 propagating along the z direction in a nonlinear medium, such that the displacement field is written

$$D(z,t) = D_1 \exp[i(z\, k(\omega_1) - \omega_1\, t)] + D_2 \exp[i(z\, k(\omega_2) - \omega_2\, t]) + \text{c.c} \tag{1.79}$$

where, for simplicity, we are assuming scalar fields in a homogeneous isotropic medium, and the dispersion relation is simply $k(\omega) = \omega\, n(\omega)$. The non-linear polarization generated by

these waves has the form

$$P_{\mathrm{NL}}(z,t) \propto D_1^2 + D_2^2 + D_1^2\cos(2\,k_1\,z - 2\,\omega_1 t) + D_2^2\cos(2\,k_2\,z - 2\,\omega_2 t) \\ + 2\,D_1\,D_2\cos([k_1+k_2]\,z - [\omega_1+\omega_2]t) + 2\,D_1\,D_2\cos([k_1-k_2]\,z - [\omega_1-\omega_2]t) \tag{1.80}$$

The first two terms correspond to optical rectification [28], and the next two correspond to second harmonic generation [29] (SHG) by each of the two input fields. The fifth and sixth terms correspond respectively to sum frequency generation (SFG) and difference-frequency generation (DFG). In the context of a quadratic nonlinear optical process, we refer to the field with highest frequency as the pump, and to the two low-frequency fields as signal and idler. In the particle picture of nonlinear optics, these processes correspond to the creation or annihilation of photons of different energies, mediated by the material nonlinearity. In a SFG process, for instance, two photons with energies $\hbar\omega_1$ and $\hbar\omega_2$ are combined into a photon with energy $\hbar(\omega_1+\omega_2)$, ensuring energy conservation.

It must be noted that, in order to observe efficient frequency conversion processes, the new frequencies generated throughout the medium must interfere constructively. In a dispersive medium, this condition is not obtained by default. Considering the spatial dependence of the material polarization in a SFG process, for instance, we see that the nonlinear polarization that gives rise to SFG has a phase $\phi_{\mathrm{SGH}} = (k(\omega_1)+k(\omega_2))\,z$. The difference between this phase and that of the electromagnetic wave propagating at the sum frequency is known as the phase-mismatch, $\Delta k\,z = (k(\omega_1)+k(\omega_2)-k(\omega_1+\omega_2))\,z$. Therefore, the nonlinear polarization and the new generated frequency will get out of phase every $\Delta z_{\mathrm{deph}} = \pi/\Delta k$, preventing the constructive build-up at the sum frequency. The phase-matching condition,

$\Delta k = 0$, can be achieved for instance, by compensating for linear dispersion using the birefringence of the nonlinear medium. An alternative way of achieving constructive interference of the new frequencies is by flipping the sign of the nonlinear susceptibility periodically every Δz_{deph} which is called periodic poling[30].

Broadband second harmonic generation

Second harmonic generation is a common technique to obtain a high frequency pump to drive parametric processes. In particular, we use SHG to generate a pulsed pump in Chapter 2. Let us now provide a brief description of this process, noting that ultrafast SHG is a broad topic in its own, which we will not discuss in all its complexity here. Find a complete analysis of this topic in[24]. As a matter of convenience, in this section we will use the electric field instead of the displacement in our calculations. This is not problematic given that we are not relying on a canonical quantization approach, but instead will use classical wave equations.

We start from the classical nonlinear wave equation

$$\nabla^2 \boldsymbol{E} - \omega_0 \epsilon \frac{\partial^2 \boldsymbol{E}}{\partial t^2} = \mu_0 \frac{\partial^2 \boldsymbol{P}_{\text{NL}}}{\partial t^2}, \tag{1.81}$$

where P_{NL} is the second order nonlinear polarization caused by the input electric field. Let us assume linearly polarized plane waves propagating along the z direction, and let us also decompose the electric field into a component with frequencies close to the fundamental, $E_\omega(t)$, and a second harmonic component, $E_{2\omega}(t)$. The Fourier expansion of the electric

fields and the nonlinear polarization are written

$$E_\omega(z,t) = \int_0^\infty \tfrac{d\omega}{\sqrt{2\pi}}\ \mathcal{E}_\omega(\omega)\ \exp\Big(-i(\omega\, t - k_\omega(\omega)z)\Big) + \text{c.c} \tag{1.82}$$

$$E_{2\omega}(z,t) = \int_0^\infty \tfrac{d\Omega}{\sqrt{2\pi}}\ \mathcal{E}_{2\omega}(\Omega)\ \exp\Big(-i(\Omega\, t - k_{2\omega}(\Omega)z)\Big) + \text{c.c} \tag{1.83}$$

$$P_{\text{NL}}(z,t) = \int_0^\infty \tfrac{d\omega}{\sqrt{2\pi}}\ \mathcal{P}_{\text{NL}}(z,\omega)\ \exp(-i\omega\, t) + \text{c.c} \tag{1.84}$$

The nonlinear polarization responsible for SHG is given by $P_{\text{NL}}(t) = 2\,\epsilon_0\, d_{\text{eff}}\, E^2_\omega(t)$. Substituting the Fourier expansion of the polarization in Eq. 1.81, and making the slowly varying envelope approximation, we arrive to the linear differential equation for the envelope of the harmonic field

$$\frac{\partial \mathcal{E}_{2\omega}(\Omega)}{\partial z} = i\frac{\omega_0 d_{\text{eff}}}{n_{2\omega}c}\int_0^\infty d\omega' \mathcal{E}_\omega(\omega')\mathcal{E}_\omega(\Omega-\omega')\exp(-i\Delta k\, z), \tag{1.85}$$

where we have defined the phase mismatch

$$\Delta k = k_{2\omega}(\Omega) - k_\omega(\omega') - k_\omega(\Omega-\omega') \tag{1.86}$$

Also, we have defined an effective nonlinearity, d_{eff}, as well as the central frequency of the fundamental field, ω_0, and the refractive index for the central frequency of the second harmonic, $n_{2\omega}$.

Assuming that the fundamental field is undepleted throughout the interaction, we can integrate this differential equation and find the envelope of the second harmonic at the end

of the interaction

$$\mathcal{E}_{2\omega}(L,\Omega) = i\frac{\omega_0 d_{\text{eff}}}{n_{2\omega}c}\int_0^\infty d\omega'\,\mathcal{E}_\omega(\omega')\mathcal{E}_\omega(\Omega-\omega')\Big[L\exp(-i\frac{\Delta k\,L}{2})\ \text{sinc}(\frac{\Delta k\,L}{2})\Big] \tag{1.87}$$

We see that, whereas the nonlinear polarization is proportional to the square of the fundamental field (the convolution of the field with itself in the frequency domain), this is not the whole story with the generated second harmonic. An additional term containing the phase-mismatch modifies the spectral structure of the harmonic light. To identify the dominant effect of this extra term, we expand the phase-mismatch to first order in optical frequency which, assuming phase matching for the central frequency, ω_0, is written

$$\Delta k(\Omega) \approx \Big[\frac{\partial k_{2\omega}}{\partial\omega}\Big|_{2\omega_0} - \frac{\partial k_\omega}{\partial\omega}\Big|_{\omega_0}\Big](\Omega - 2\omega_0) \tag{1.88}$$

The dependence of the phase mismatch term only on Ω shows that its main effect is to act as a filter that limits the bandwidth of the fundamental beam that can be efficiently upconverted. In addition, the complex exponential in the term introduces a non-flat spectral phase on the second harmonic.

A practical corollary of this result is that we identify the longest SHG crystal that we can use while still efficiently doubling all the frequencies in the fundamental pulse. The condition under which the thin crystal approximation is valid is roughly expressed as $\Delta k(\Omega_{\text{BW}})\,L < 1$, where Ω_{BW} is the bandwidth of the fundamental. This has a simple interpretation: given a Fourier limited fundamental pulse with a duration Δt, this condition corresponds to finding the length of crystal over which two pulses of duration Δt but travelling respectively at the pump and signal group velocities will walk-off from each other.

1.2.4 Ultrafast nonlinear quantum optics

In this thesis we will be mainly interested in the DFG term of the nonlinear polarization. In Chapters 2 and 3 we will use a DFG process driven by a strong pump pulse of central frequency $\bar{\omega}_{\mathrm{p}}$, and seeded by a weak signal pulse of central frequency $\bar{\omega}_{\mathrm{s}} = \bar{\omega}_{\mathrm{p}}/2$. This situation receives the name of optical parametric amplification (OPA), as the DFG term of the material polarization oscillates at the same frequency as the input seed ($\bar{\omega}_{\mathrm{DFG}} = \bar{\omega}_{\mathrm{p}} - \bar{\omega}_{\mathrm{s}} = \bar{\omega}_{\mathrm{s}}$), and thus appears as an amplification (or deamplification, depending on the phase) of the seed. As we will see in Chapter 2, the photon statistics of this amplified/deamplified seed correspond to those of a coherent squeezed state, which we leverage for metrological purposes.

In Chapters 4 and 5, we use a DFG process where the signal and idler fields are unseeded, but where the pump mode is populated with a strong field. Classically, Eq. (1.80) tells us that no DFG should occur in this situation, since the the nonlinear polarization contains the product of the pump and the signal field amplitudes, the latter being zero. However, the quantum fluctuations in the signal/idler mode are sufficient to seed the parametric process, allowing for the spontaneous decay of a high-energy pump photon into a pair of low-energy signal and idler photons. This process receives the name of spontaneous parametric down-conversion (SPDC).

Hamiltonian description of PDC / DFG

In order to convey the quantum properties of the light generated via a nonlinear optical process, the interacting optical fields have to be treated as quantum operators rather than classical amplitudes. In this context, it is common to compute the quantum properties

of the optical field after a nonlinear interaction by using a Hamiltonian description of the process. Once the appropriate interaction Hamiltonian has been found, this can be used to compute the state of the output optical field using the Schrödinger equation, or to compute the transformed observables that describe the field using the Heisenberg equation. Here we will illustrate this procedure by computing the quantum state generated in a low-gain broadband PDC process. In Chapter 3 we will extend the concepts introduced here in order to account for the complete spatio-temporal structure of the a DFG process. In Chapter 4 we will extend the Hamiltonian description of a broadband PDC process to the high-gain regime, where some of the assumptions that we make here break down.

The Hamiltonian that describes three-wave-mixing via a second order nonlinearity is [10]

$$\hat{\mathrm{H}}_{3\mathrm{WM}} = -\frac{1}{3\epsilon_0}\Gamma^{(2)}_{ijk}\int_{V_I} \mathrm{d}\mathbf{r}\, \hat{D}_i(\mathbf{r})\, \hat{D}_j(\mathbf{r})\, \hat{D}_k(\mathbf{r}), \tag{1.89}$$

where summation over cartesian indices i, j, k is implied. The integration of the interaction energy density extends only over the interaction volume V_I, which is the space occupied by the nonlinear crystal. We expand the displacement field as a sum of a broadband pump field whose frequency is labeled by ω_p, and two signal and idler fields with frequencies much lower than those of the pump, denoted ω_s and ω_i. Now we apply the slowly-varying envelope approximation, realizing that the only components of the interaction picture Hamiltonian that oscillate slowly in time, and therefore do not average to zero, are

$$\hat{\mathrm{H}}_{\mathrm{int}}(t) = -\frac{\Gamma^{(2)}}{3\epsilon_0}\int_{V_I} \mathrm{d}\mathbf{r}\ \tilde{D}^{(+)}_{\mathrm{p}}(\mathbf{r},\omega_p)\tilde{D}^{(-)}_{\mathrm{s}}(\mathbf{r},\omega_s)\tilde{D}^{(-)}_{\mathrm{i}}(\mathbf{r},\omega_i)\exp\Big((\omega_s+\omega_i-\omega_p)t\Big)\ +\ \mathrm{h.c} \tag{1.90}$$

where we have assumed that there is only one triplet of pump/signal/idler polarizations

coupled by the $\Gamma^{(2)}_{ijk}$ tensor. We have ommitted the spatial sub-indices in the fields, and substituted them for the latin indices $\{\mathrm{s},\mathrm{i},\mathrm{p}\}$ denoting the relevant polarization for each field. The element of the nonlinear tensor that couples the three fields is simply written as $\Gamma^{(2)}$ for notational simplicity.

In a general bulk crystal, and assuming paraxial beams, the interacting fields can be written in a plane wave expansion with wavevectors that follow the dispersion relations introduced in section 1.2.2. The pump field will be assumed to be in a coherent state of sufficient amplitude that its quantum noise properties can be ignored and it can be described only by its mean coherent amplitude

$$\tilde{D}^{(+)}_{\mathrm{p}}(\mathbf{r},\omega_{\mathrm{p}}) = \gamma_{\mathrm{p}} \int \mathrm{d}^2\mathbf{q}\,\mathrm{d}\omega \exp\Big(i[\mathbf{q}\cdot\boldsymbol{\rho} + k_{\mathrm{p},z}(\omega,\mathbf{q})z]\Big)\ \alpha_{\mathrm{p}}(\mathbf{q},\omega) \tag{1.91}$$

where γ_{p} is a normalization constant and $\alpha_{\mathrm{p}}(\mathbf{q}_{\mathrm{p}},\omega_{\mathrm{p}})$ is a function with units of $\sqrt{\text{photon number}}$ that obeys

$$\int \mathrm{d}\mathbf{q}_{\mathrm{p}}\ \mathrm{d}\omega_{\mathrm{p}}\ |\alpha_{\mathrm{p}}(\mathbf{q}_{\mathrm{p}},\omega_{\mathrm{p}})|^2 = N_{\mathrm{p}} \tag{1.92}$$

where N_{p} is the number of photons contained in a pump pulse. The longitudinal wavenumber of the pump, $k_{\mathrm{p},z}(\omega,\mathbf{q})$, depends on the transverse wavenumber $\mathbf{q}$ through the dispersion relations introduced in Sec. 1.2.2, thus allowing us to accommodate the effect of transverse propagation.

The signal and idler fields are also expressed in a plane-wave decomposition, where the plane wave amplitudes are substituted by annihilation operators (Eq.(1.16))

$$\tilde{D}^{(+)}_{j}(\mathbf{r},\omega_j) = \gamma_j \int \mathrm{d}^2\mathbf{q}\,\mathrm{d}\omega \exp\Big(i[\mathbf{q}\cdot\boldsymbol{\rho} + k_{j,z}(\omega,\mathbf{q})z]\Big)\ \hat{a}_j(\mathbf{q},\omega) \tag{1.93}$$

with $j \in \{\mathrm{s}, \mathrm{i}\}$, and where we have defined γ_j as the appropriate normalization constant and $k_{j,z}(\mathbf{q}, \omega)$ as the appropriate longitudinal wavenumber. The signal and idler bosonic operators obey the commutation relations

$$[\hat{a}_j(\mathbf{q}, \omega), \hat{a}^\dagger_{j'}(\mathbf{q}', \omega')] = \delta(\mathbf{q} - \mathbf{q}')\delta(\omega - \omega')\delta_{j,j'} \tag{1.94}$$

$$[\hat{a}_j(\mathbf{q}, \omega), \hat{a}_{j'}(\mathbf{q}', \omega')] = [\hat{a}^\dagger_j(\mathbf{q}, \omega), \hat{a}^\dagger_{j'}(\mathbf{q}', \omega')] = 0 \tag{1.95}$$

The interaction Hamiltonian can thus be written in terms of these plane-wave expansions

$$\hat{\mathrm{H}}_{\mathrm{int}}(t) = -g' \int_{V_I} \mathrm{d}\mathbf{r} \int \mathrm{d}\mathbf{q}_\mathrm{p}\, \mathrm{d}\mathbf{q}_\mathrm{s}\, \mathrm{d}\mathbf{q}_\mathrm{i}\, \mathrm{d}\omega_\mathrm{p}\, \mathrm{d}\omega_\mathrm{s}\, \mathrm{d}\omega_\mathrm{i}\ \alpha_\mathrm{p}(\mathbf{q}_p, \omega_p)\ \hat{a}^\dagger_\mathrm{s}(\mathbf{q}_\mathrm{s}, \omega_\mathrm{s})\ \hat{a}^\dagger_\mathrm{i}(\mathbf{q}_\mathrm{i}, \omega_\mathrm{i}) \tag{1.96}$$

$$\times \exp\Big(i(\mathbf{q}_\mathrm{p} - \mathbf{q}_\mathrm{s} - \mathbf{q}_\mathrm{i}) \cdot \boldsymbol{\rho} + i(k_{\mathrm{p},z} - k_{\mathrm{s},z} - k_{\mathrm{i},z})z - i(\omega_\mathrm{p} - \omega_\mathrm{s} - \omega_\mathrm{i})t\Big) + \mathrm{h.c} \tag{1.97}$$

where we have absorbed all the constant prefactors into a gain coefficient g'.

Perturbative solution of PDC (DFG)

The unitary operation that connects the state of the signal and idler fields before and after the nonlinear interaction is found by integrating the Schrodinger equation in the interaction picture. This unitary operator is formally written

$$\hat{U}_{\mathrm{int}} = \mathcal{T} \exp\Big(-\frac{i}{\hbar}\int_{-\infty}^{+\infty} \mathrm{d}t\ \hat{\mathrm{H}}_{\mathrm{int}}(t)\Big) \tag{1.98}$$

where $\mathcal{T}$ is the time-ordering operator. Given that the interaction Hamiltonian is time varying, the exact solution of this operator is hard to obtain, which leads to the use of perturbative expansions. While a Dyson power series has been used extensively in photon

pair generation applications[23,31], the Magnus expansion[32,33] is a more natural choice in our case. The Magnus expansion approximates the solution of the Schrodinger equation as an exponential whose argument is developed in a power series. This is a desirable feature in our analysis, in which it will be convenient to work in the Heisenberg picture: in this picture, the exponential form of the unitary operator guarantees simple transformations of the field operators. The first order Magnus expansion coincides exactly with the first term of the equivalent Dyson series, yielding

$$\hat{U}_{\text{int}} \approx \exp\Big(-\frac{i}{\hbar}\int_{-\infty}^{+\infty} \mathrm{d}t\ \hat{\mathrm{H}}_{\text{int}}(t)\Big) \tag{1.99}$$

where we note that the time ordering operator has been ommited. This is an approximation that is valid only in the low gain regime, whereas more terms would have to be added in the exponent as the parametric gain is increased[33]. In that situation, the difference between a Dyson and Magnus series would become more apparent, as the former would be written as a sum of exponential operators, whereas the latter would retain the form of a single exponential operator.

At this point it is convenient to define the generator of this unitary operator, which in a slight abuse of notation we will denote as

$$\hat{\mathrm{H}}_{\text{int}} = -\frac{i}{\hbar}\int_{-\infty}^{+\infty} \mathrm{d}t\ \hat{\mathrm{H}}_{\text{int}}(t), \tag{1.100}$$

distinguishing it from the time-dependent Hamiltonian by the absence of a temporal dependence in the notation. The generator $\hat{\mathrm{H}}_{\text{int}}$ has until now been expressed in terms of the spatial and temporal integrals of products of three plane waves. We can now carry out the

integration over all the interaction space and time. The transverse dimensions of the beams are assumed to be much smaller than the nonlinear crystal where the interaction is taking place, and therefore we can extend the integration over transverse coordinates $\boldsymbol{\rho}$ from $-\infty$ to $+\infty$. The integral over z, however, has to be considered over a finite length of crystal, which we denote as extending from $z = -L/2$ to $z = L/2$. Evaluating these integrals, as well as the integration over time, we obtain

$$\begin{aligned}\hat{\mathrm{H}}_{\mathrm{int}} = g \int \mathrm{d}\mathbf{q}_{\mathrm{p}}\, \mathrm{d}\mathbf{q}_{\mathrm{s}}\, \mathrm{d}\mathbf{q}_{\mathrm{i}}\, \mathrm{d}\omega_{\mathrm{p}}\, \mathrm{d}\omega_{\mathrm{s}}\, \mathrm{d}\omega_{\mathrm{i}}\ \alpha_{\mathrm{p}}(\mathbf{q}_{\mathrm{p}}, \omega_p)\ \hat{a}^{\dagger}_{\mathrm{s}}(\mathbf{q}_{\mathrm{s}}, \omega_{\mathrm{s}})\ \hat{a}^{\dagger}_{\mathrm{i}}(\mathbf{q}_{\mathrm{i}}, \omega_{\mathrm{i}}) \\ \times\ \delta(\Delta\mathbf{q})\ \delta(\Delta\omega)\ \mathrm{sinc}(\frac{L}{2}\Delta k_z) + \mathrm{h.c}\end{aligned} \tag{1.101}$$

where $\Delta\mathbf{q} = \mathbf{q}_{\mathrm{p}} - \mathbf{q}_{\mathrm{s}} - \mathbf{q}_{\mathrm{i}}$, $\Delta\omega = \omega_{\mathrm{p}} - \omega_{\mathrm{s}} - \omega_{\mathrm{i}}$ and $\Delta k_z = k_{\mathrm{p},z} - k_{\mathrm{s},z} - k_{\mathrm{i},z}$. We have absorbed all the constant prefactors into the gain parameter

$$g = -i\, g'(2\pi)^4 L/\hbar. \tag{1.102}$$

We evaluate the two delta functions that appear in Eq.1.101 by integrating over the pump frequency and transverse wavevector, yielding

$$\hat{\mathrm{H}}_{\mathrm{int}} = g \int \mathrm{d}\mathbf{q}_{\mathrm{s}}\, \mathrm{d}\mathbf{q}_{\mathrm{i}}\, \mathrm{d}\omega_{\mathrm{s}}\, \mathrm{d}\omega_{\mathrm{i}}\ \alpha_{\mathrm{p}}(\mathbf{q}_s + \mathbf{q}_i, \omega_s + \omega_i)\, \mathrm{sinc}\Big(\frac{L}{2}\Delta k_z\Big)\ \hat{a}^{\dagger}_{\mathrm{s}}(\mathbf{q}_{\mathrm{s}}, \omega_{\mathrm{s}})\ \hat{a}^{\dagger}_{\mathrm{i}}(\mathbf{q}_{\mathrm{i}}, \omega_{\mathrm{i}}) + \mathrm{h.c} \tag{1.103}$$

It is important to remember that Δk_z contains the longitudinal wavevector of the pump, which is related to both ω_{p} and $\mathbf{q}_{\mathrm{p}}$. In the following, one should remember to carry out the substitution $\mathbf{q}_{\mathrm{p}} = \mathbf{q}_{\mathrm{s}} + \mathbf{q}_{\mathrm{i}}$ and $\omega_{\mathrm{p}} = \omega_{\mathrm{s}} + \omega_{\mathrm{i}}$ wherever Δk_z appears.

It is also important to keep in mind that this Hamiltonian is applied in the interaction

picture, yielding the unitary transformation $\hat{U}_{\rm int} = \exp(-\frac{i}{\hbar}\hat{H}_{\rm int})$. In order to recover the transformation between the input and output fields (Schrodinger picture), the additional phases corresponding to linear propagation need to be included, such that the unitary transformation connecting the fields at the two ends of the waveguide becomes $\hat{U} = \exp(-\frac{i}{\hbar}\hat{H})$ with

$$\hat{H} = g \int \mathrm{d}\mathbf{q}_{\rm s}\, \mathrm{d}\mathbf{q}_{\rm i}\, \mathrm{d}\omega_{\rm s}\, \mathrm{d}\omega_{\rm i}\ \alpha_{\rm p}(\mathbf{q}_s + \mathbf{q}_i, \omega_s + \omega_i)\, \mathrm{sinc}\Big(\frac{L}{2}\Delta k_z\Big)\ \exp\Big(i\,\frac{L}{2}\Delta k_z\Big) \hat{a}^\dagger_{\rm s}(\mathbf{q}_{\rm s}, \omega_{\rm s})\ \hat{a}^\dagger_{\rm i}(\mathbf{q}_{\rm i}, \omega_{\rm i}) + \mathrm{h.c} \tag{1.104}$$

A simple example: broadband photon-pair generation

The generator $\mathrm{H}_{\rm int}$ couples the signal and idler modes in a way reminiscent of the two-mode squeezing unitary operation. However, a general DFG process does not couple a single pair of signal and idler modes, but rather a continuum labelled by their frequency and transverse wavevector. Moreover, the strength of this coupling is, in general, not uniform over all frequencies and wavevectors, but can show correlations due to energy conservation and momentum conservation (phase matching). Let us now illustrate a paradigmatic consequence of this correlated coupling: the quantum state of the photon pairs emitted in a broadband SPDC process is not simply $|\psi\rangle = |0,0\rangle + r\,|1_{\rm s}, 1_{\rm i}\rangle$, where r is a coupling strength (1.35). Instead, photons are emitted at different angles and with different frequencies, which might be correlated in order to conserve energy and momentum. This has important consequences in heralded single photon generation.

Let us consider a simple situation where the transverse dependence of the field wavevectors can be neglected. The longitudinal wavenumbers of the fields are simply $k_{z,j}(\omega) = \omega\, n_j(\omega)$

where $j \in \{\mathrm{s}, \mathrm{i}, \mathrm{p}\}$ label the signal, idler and pump modes, and the refractive index for each mode can be different depending on its polarization. The unitary transformation that describes the PDC process is then

$$\hat{U}_{\mathrm{int}} = \exp\Big(g \int \mathrm{d}\omega_{\mathrm{s}}\, \mathrm{d}\omega_{\mathrm{i}}\, \mathrm{JSA}(\omega_{\mathrm{s}}, \omega_{\mathrm{i}})\, \hat{a}_{\mathrm{s}}^{\dagger}(\omega_{\mathrm{s}})\, \hat{a}_{\mathrm{i}}^{\dagger}(\omega_{\mathrm{i}}) + \mathrm{h.c}\Big) \tag{1.105}$$

where we have simplified the notation to ommit the transverse wavevector dependence, and we have introduced the perturbative *joint spectral amplitude* (JSA), which can be expressed as a product of the pump function, α_{p}, and a phase-matching function ϕ_{pm}

$$\begin{aligned} \mathrm{JSA}(\omega_{\mathrm{s}}, \omega_{\mathrm{i}}) &= \alpha_{\mathrm{p}}(\omega_{\mathrm{s}} + \omega_{\mathrm{i}})\, \phi_{\mathrm{pm}}(\omega_{\mathrm{s}}, \omega_{\mathrm{i}}) \\ \phi_{\mathrm{pm}}(\omega_{\mathrm{s}}, \omega_{\mathrm{i}}) &= \mathrm{sinc}\Big(\frac{L}{2}\Delta k_z(\omega_{\mathrm{s}}, \omega_{\mathrm{i}})\Big) \end{aligned} \tag{1.106}$$

with $\Delta k_z(\omega_{\mathrm{s}}, \omega_{\mathrm{i}}) = (\omega_{\mathrm{s}} + \omega_{\mathrm{i}})\, n_{\mathrm{p}}(\omega_{\mathrm{s}} + \omega_{\mathrm{i}}) - \omega_{\mathrm{s}}\, n_{\mathrm{s}}(\omega_{\mathrm{s}}) - \omega_{\mathrm{i}}\, n_{\mathrm{i}}(\omega_{\mathrm{i}})$.

Assuming a weak enough pump that at most a single photon pair is emitted at any time, the quantum state of the signal and idler modes can be expressed as the first order Taylor expansion of the PDC unitary applied on the vacuum state

$$|\psi\rangle = \hat{U}_{\mathrm{int}}|0,0\rangle \approx |0,0\rangle + g \int \mathrm{d}\omega_{\mathrm{s}}\, \mathrm{d}\omega_{\mathrm{i}}\, \mathrm{JSA}(\omega_{\mathrm{s}}, \omega_{\mathrm{i}})\, \hat{a}_{\mathrm{s}}^{\dagger}(\omega_{\mathrm{s}})\, \hat{a}_{\mathrm{i}}^{\dagger}(\omega_{\mathrm{i}})\, |0,0\rangle \tag{1.107}$$

This state describes a situation where a pair of photons is emitted probabilistically, and where the probability of observing a particular combination of signal and idler frequencies in a detection event is given by the *joint spectral intensity*

$$\mathrm{JSI}(\omega_{\mathrm{s}}, \omega_{\mathrm{i}}) = |\langle 0,0|\hat{a}_{\mathrm{s}}(\omega_{\mathrm{s}})\hat{a}_{\mathrm{i}}(\omega_{\mathrm{i}})|\psi\rangle|^2 = |\mathrm{JSA}(\omega_{\mathrm{s}}, \omega_{\mathrm{i}})|^2 \tag{1.108}$$

With this in mind, it is apparent that the pump function enforces energy conservation in the photon generation process, as it prevents the sum of the energies of the downconverted photons from being greater that the energy of a pump photon. In an SPDC process driven by a pulsed pump, the pump function $\alpha_{\mathrm{p}}(\omega_{\mathrm{p}})$ is non-zero for a broad range of frequencies. In consequence, the frequency anticorrelation that it imposes on the downconverted photons is not strict: the sum of their energies need only be within the bandwidth of the pump field. Analogously, the phase-matching function enforces momentum conservation. Again, this constraint is not strict: the momentum mismatch Δk_z is only restricted to be smaller than the inverse of the crystal length, L.

The interplay between these two restrictions shapes the spectral structure of the emitted photon pairs. Assuming a combination of pump, signal and idler central frequencies ($\bar{\omega}_{\mathrm{p}}$, $\bar{\omega}_{\mathrm{s}}$ and $\bar{\omega}_{\mathrm{i}}$) fulfilling energy and momentum conservation, $\bar{\omega}_{\mathrm{s}} + \bar{\omega}_{\mathrm{i}} = \bar{\omega}_{\mathrm{p}}$ and $\Delta k_z(\bar{\omega}_{\mathrm{s}}, \bar{\omega}_{\mathrm{i}}) = 0$), we perform a Taylor expansion of Δk_z up to first order in the signal and idler frequencies, obtaining

$$\Delta k_z(\Omega_{\mathrm{s}}, \Omega_{\mathrm{i}}) \approx v_{\mathrm{s}}\,\Omega_{\mathrm{s}} + v_{\mathrm{i}}\,\Omega_{\mathrm{i}} - v_{\mathrm{p}}\,(\Omega_{\mathrm{s}} + \Omega_{\mathrm{i}}) \tag{1.109}$$

where we have defined the signal/idler detunings $\Omega_j = \omega_j - \bar{\omega}_j$, as well as their group velocities $v_j = \partial_\omega k_j(\omega)|_{\bar{\omega}_j}$ for $j \in \{\mathrm{s}, \mathrm{i}\}$, and also the pump group velocity $v_{\mathrm{p}} = \partial_\omega k_{\mathrm{p}}(\omega)|_{\bar{\omega}_{\mathrm{s}}+\bar{\omega}_{\mathrm{i}}}$. The absolute value of the phase matching function is then a 'sinc' function with its maximum along the line where its argument is zero, which occurs for $\Omega_{\mathrm{i}} = \Omega_{\mathrm{s}} \tan(\theta_{\mathrm{pm}})$ with

$$\tan(\theta_{\mathrm{pm}}) = -\frac{v_{\mathrm{s}}^{-1} - v_{\mathrm{p}}^{-1}}{v_{\mathrm{i}}^{-1} - v_{\mathrm{p}}^{-1}} \tag{1.110}$$

It is worth noting that, unlike the pump function, which always has a slope of $-45°$, the

phase matching function can have a positive slope if the group velocity of the pump is between those of the signal and idler, $v_s < v_p < v_i$ or $v_i < v_p < v_s$. As illustrated in Fig 1.2, while a phase-matching function with a negative slope necessarily leads to a JSA with frequency anticorrelations, a positive θ_{pm} allows for a JSA with no frequency correlations to be obtained.

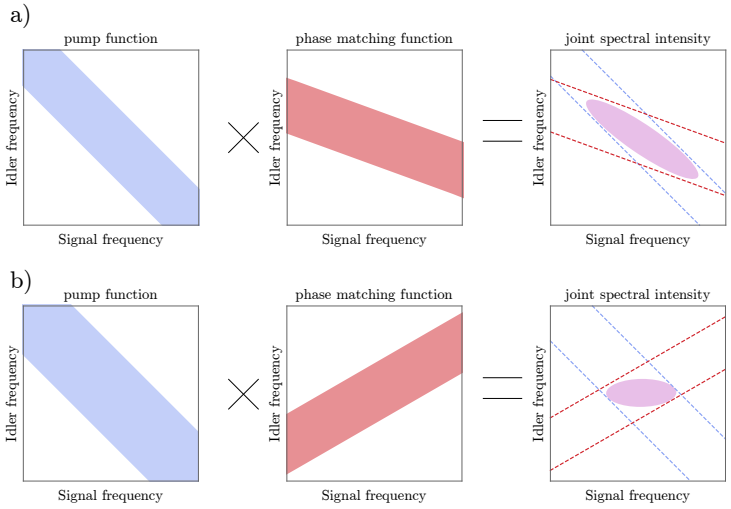


Figure 1.2: The JSA is the product of a pump function (energy conservation) and a phase-matching function (momentum conservation). While a phase matching function with a negative slope always yields a JSA with frequency correlations (a), a positive θ_{pm} can yield an uncorrelated JSA (b).

Schmidt mode decomposition

The unitary transformation realized in a broadband PDC (DFG) process is naturally interpreted in terms of its Schmidt decomposition (equivalently, the Bloch-Messiah decomposition of the Bogoliubov transformation in the Heisenberg picture) [34–38]. The Schmidt decomposition defines a set of modes that are only coupled pairwise in the PDC transformation. Considering again a situation where transverse propagation can be neglected, we find that PDC is fully described by its two-dimensional joint spectral amplitude, $\mathrm{JSA}(\omega_s, \omega_i)$. Defining the discretized JSA, $\mathbf{M}_{\mathrm{JSA}}$, where we assume a sufficiently small discretization

step, we can always use singular value decomposition (SVD) to factor this matrix into the product

$$\mathbf{M}_{\mathrm{JSA}} = \mathbf{U}\,\mathbf{D}\,\mathbf{W}^{\dagger} \tag{1.111}$$

where $\mathbf{U}$ and $\mathbf{W}$ are unitary matrices, and $\mathbf{D}$ is a diagonal matrix with real, non-negative coefficients. This decomposition can be cast back in terms of continuous functions

$$\mathrm{JSA}(\omega_{\mathrm{s}}, \omega_{\mathrm{i}}) = \sum_{k} r_k\, \rho_{\mathrm{s}}^{(k)}(\omega_{\mathrm{s}})\, \rho_{\mathrm{i}}^{(k)}(\omega_{\mathrm{i}}) \tag{1.112}$$

where $\{\rho_{\mathrm{s/i}}^{(k)}\}$, called the signal/idler Schmidt modes, correspond to the rows of $\mathbf{U}$ and $\mathbf{W}$ respectively, and thus form a complete and orthonormal basis. The coefficients r_k correspond to the elements of $\boldsymbol{D}$, and they are called Schmidt values.

This decomposition allows us to simplify computations of the state evolution generated by the PDC unitary transformation. Annihilation operators can be defined for the Schmidt modes as

$$\hat{A}_{\mathrm{s/i}}^{(k)} = \int \mathrm{d}\omega\, [\rho_{\mathrm{s/i}}^{(k)}(\omega)]^{*}\, \hat{a}_{\mathrm{s(i)}}(\omega), \tag{1.113}$$

which follow the usual bosonic commutation relations $[\hat{A}_j^{(k)}, \hat{A}_j^{(k')\dagger}] = \delta_{k,k'}$. Using the orthonormality of the Schmidt modes, the PDC unitary transformation can be simplified to

$$\hat{U}_{\mathrm{int}} = \exp\Big(\sum_{l} r_k\, \hat{A}_{\mathrm{s}}^{(k)\dagger}\, \hat{A}_{\mathrm{i}}^{(k)\dagger} + \mathrm{h.c}\Big) = \prod_{k} \exp\Big(r_k\, \hat{A}_{\mathrm{s}}^{(k)\dagger}\, \hat{A}_{\mathrm{i}}^{(k)\dagger} + \mathrm{h.c}\Big) \tag{1.114}$$

This expression shows that a broadband PDC transformation can always be expressed as a product of two-mode squeezing transformations applied on suitably defined broadband modes. The PDC transformation can also be expressed in the Heisenberg picture, where the

broadband bosonic operators evolve independently, following the usual two-mode squeezing transformation

$$\hat{A}_{\mathrm{s}}^{(k)} \to \hat{A}_{\mathrm{s}}^{(k)} \cosh(r_k) + \hat{A}_{\mathrm{i}}^{(k)\dagger} \sinh(r_k) \tag{1.115}$$

$$\hat{A}_{\mathrm{i}}^{(k)} \to \hat{A}_{\mathrm{i}}^{(k)} \cosh(r_k) + \hat{A}_{\mathrm{s}}^{(k)\dagger} \sinh(r_k) \tag{1.116}$$

Decomposing PDC into single-mode squeezers: Takagi factorization

In the context of pulsed squeezing generation, unlike in the context of photon-pair or twin-beam generation, a straightforward Schmidt decomposition is not the most useful description available. As explained above, in a Schmidt decomposition, the PDC transformation is expressed as a product of independent *two-mode* squeezers, where the Schmidt modes for the signal and idler, $\rho_{\mathrm{s/i}}^{(k)}$, are, in general, different.

In the context of squeezing generation, on the contrary, it is desirable to decompose the PDC transformation as a product of *single mode* squeezers of the form

$$\hat{U}_{\mathrm{int}} = \prod_k \exp\left(r_k \, [\hat{A}^{(k)\dagger}]^2 + \mathrm{h.c}\right) \tag{1.117}$$

where the set of annihilation operators $\{\hat{A}^{(k)}\}$ defines an orthonormal basis, and r_l are real and positive squeezing parameters. Given this form of U_{int}, each broadband mode evolves according to the single-mode squeezing transformation

$$\hat{A}^{(k)} \to \hat{A}^{(k)} \cosh(r_k) + \hat{A}^{(k)\dagger} \sinh(r_k) \tag{1.118}$$

which yields well-known photon and quadrature statistics for the output state in the kth

broadband mode, especially when the input is a Gaussian state (e.g. vacuum or coherent state).

We can achieve the decomposition presented in Eq. (1.117) analogously to how, in the previous section, we decomposed a PDC unitary as a product of two-mode squeezers using SVD, with the difference that now we require that the signal and idler photons have the same polarization (type-0 or type-I PDC), as well as to be able to find the symmetric decomposition of the joint spectral amplitude

$$\mathrm{JSA}(\omega, \omega') = \sum_k r_k \, \phi^{(k)}(\omega) \, \phi^{(k)}(\omega'), \tag{1.119}$$

where we have dropped the distinction between signal and idler. The equivalent matrix factorization problem is

$$\mathbf{M}_{\mathrm{JSA}} = \mathbf{U} \, \mathbf{\Lambda} \, \mathbf{U}^T, \tag{1.120}$$

where $\mathbf{M}_{\mathrm{JSA}}$ is the discretized JSA, $\mathbf{U}$ is a unitary matrix whose rows correspond to the broadband modes $\phi^{(k)}$, and $\mathbf{\Lambda}$ is a diagonal matrix with real non-negative elements corresponding to the squeezing parameters, r_k. This decomposition, known as a Takagi factorization, is known to exists if $\boldsymbol{M}_{\mathrm{JSA}}$ is a square, complex, symmetric matrix.

It has been found [39] that the Takagi factorization of a matrix can be computed directly from its SVD, which allows us to take advantage of readily available computer routines that efficiently calculate SVD decompositions. In the first place, let

$$\mathbf{M}_{\mathrm{JSA}} = \mathbf{W} \, \mathbf{\Lambda} \, \mathbf{V}^\dagger \tag{1.121}$$

be the SVD of $\mathbf{M}_{\text{JSA}}$, such that $\mathbf{W}$ and $\mathbf{V}$ are unitary matrices and $\mathbf{\Lambda} \geq 0$ is a real diagonal matrix. Then, the Takagi factorization can be computed from this decomposition as

$$\mathbf{M}_{\text{JSA}} = \mathbf{U}\mathbf{\Lambda}\mathbf{U}^T \tag{1.122}$$

where

$$\mathbf{U} = \mathbf{W}(\mathbf{W}^\dagger\mathbf{V}^*)^{1/2}. \tag{1.123}$$

Here † indicates conjugate transpose, while * indicates conjugation.

Part I

Quantum enhanced stimulated emission microscopy

Chapter 2

A proposal for quantum-enhanced ultrafast stimulated emission microscopy

2.1 Quantum metrology in biology

The scientific method relies heavily on our ability to perform accurate and repeatable measurements of physical quantities. A physical measurement is paradigmatically modelled as a coupling between a probing meter and a system under study, after which one or more physical parameters of the system are encoded in the state of the meter. Subsequently, an experimenter can obtain information about the physical parameters of interest by destructively measuring the probing meter. However, the information that they will obtain can be imperfect: any uncertainty about the initial state of the meter will lead to a derived uncertainty about the inferred physical parameters. A measurement setup can be carefully designed and characterized in order to avoid such an imperfect information transfer, but an obstacle remains: the probing meter is ultimately described as a quantum mechanical

object and, as such, its initial state cannot be defined with arbitrary precision. This leaves us with the bleak conclusion that quantum mechanics sets an ultimate limit to the precision of any measurement.

Luckily, quantum mechanics also provides a workaround. While the Heisenberg uncertainty principle does preclude the simultaneous precise measurement of two or more non-commuting observables, it does not require that all observables be equally uncertain. It is possible to prepare a meter in such a state that the quantum fluctuations in the observable that encodes useful information are reduced, at the expense of incurring in increased fluctuations in an experimentally less relevant observable. In a seminal paper [40], Caves proposed to use such non-classical states of light to improve the precision of optical interferometric measurements, pioneering the field that is now known as quantum metrology [41]. In time, the field has grown to apply quantum-enhanced measurements to a variety of problems including spectroscopy [42], magnetometry [43], imaging [44] and even biological measurements [45].

In this work we are concerned with the application of quantum metrology techniques to biological measurements. A sustained interest in making precise observations of cells and biomolecules has driven a continuous improvement of optical imaging and sensing techniques. As we understand more about the nature of light, we design more sophisticated optical devices such as confocal, phase contrast and fluorescence microscopes. It is natural to ask the question: can biological measurements also benefit from the application of quantum metrology techniques?

A number of light-based, quantum-enhanced techniques for biological sensing have been proposed in recent years. In 2009, entangled-photon-pair optical coherence tomography was first demonstrated [46]. After that, many proposals followed. Amongst others we find:

protein concentration measurements using NOON states[47], measurements of the diffusion of nanoparticles in a cell using a bright amplitude-squeezed local oscillator[48,49] and a twin-beam enhanced wide field microscope[50]. These proposals take advantage of different properties of non-classical states of light, which in turn translate into improvements of different figures of merit of the measurements with respect to classical schemes.

One often-quoted advantage of quantum-enhanced biological sensing is that it allows for a lower light intensity to be used in an optical measurements without trading off sensitivity. Reducing optical brightness can be useful to prevent cell damage through optical heating and photochemical effects[45]. One can argue that experiments involving bright squeezed states address this consideration more directly than those using few-photon probes which, by their low-energy nature, can hardly damage a biological sample regardless of whether they achieve a quantum enhancement. A related but different argument in favor of quantum-enhanced techniques is that they can allow for an improvement of the *maximum achievable* sensitivity of a measurement, as opposed to the sensitivity per photon. This scenario is found when, for some reason, there is a maximum achievable signal amplitude, such that measurements can only be improved by reducing the readout noise. This is precisely the case in single-molecule sensing[45], where the signal to be measured can only achieve a limited amplitude due to the fact that there is a single emitter. In contrast, studies of bigger objects, such as cells, are typically not limited by instrument sensitivity[45], but rather by external causes such as cell-to-cell variation.

2.2 Stimulated emission microscopy (SEM)

In this work we identify a biological measurement that, following the criteria just mentioned, can benefit from the use of a non-classical optical probe. In short, we propose to improve a state of the art non-linear microscopy technique called stimulated emission microscopy [51] by using squeezed states of light as optical probes. Non-linear microscopes can go beyond the fundamental limitations of linear absorption imaging by exploiting the nonlinear optical response of the sample. Fluorescence microscopy, for instance, uses the fact that certain proteins, when optically excited, re-emmit light at a wavelength longer than that of the excitation, which allows us to separate the scattered and incident fields by wavelength. Chemically attaching such fluorescent proteins to a biological system of interest, it is possible to obtain an image of the fluorescence emitted in the target structure. This technique offers a better contrast than a regular absorption image, as the background excitation light is removed using optical filters. Moreover, a resolution beyond the Rayleigh limit can be obtained due to the quadratic scaling of the process on the field amplitude.

One shortcoming of fluorescence microscopy, however, is that it is not always practical or possible to label a biological structure with a fluorescent protein. This is exemplified in experiments that study the motion and interaction of a biomolecule in a medium. Attaching a fluorescent protein to the molecule of interest can modify its motility or chemical reactivity [45], thus undermining the experiment. In such cases it is usually preferred to use label-less methods, like conventional absorption microscopy, giving up the enhanced contrast provided by fluorescence.

Label-free nonlinear microscopy techniques aim to achieve a similar contrast enhancement as that obtained through fluorescence microscopy, while avoiding the use of fluorescent

label proteins. Stimulated emission microscopy, introduced by Min et al.[51], is one such label-free technique. There are many biological systems which absorb light strongly at a particular wavelength (i.e. they are chromophores) but which do not fluoresce strongly due to the existence of predominant non-radiative decay paths (i.e. they are not fluorophores). In these cases, Min et al. propose to use the phenomenon of stimulated emission to enhance the radiative decay over the non-radiative relaxation, thus making the first detectable.

The principle of operation of SEM is illustrated in Fig. 2.1: after exciting a collection of chromophores with an *excitation beam*, a second *stimulation beam* of lower frequency is used to promote the reemission of energy in the form of light. This light is emitted in the mode of the stimulation beam, therefore appearing as a small amplification of this (see Fig. 2.1.b).

In the non-saturating condition, where few chromophores are excited, the population in the excited level (level 2 in Fig. 2.1.a) is linearly proportional to the intensity of the excitation beam[51],

$$N_2 \propto N_0 \, I_{\mathrm{E}} \, \sigma_{\mathrm{abs}[0\to1]}/S \tag{2.1}$$

where N_0 is the population in the ground energy level (see Fig. 2.1.a), I_{E} is the intensity of the excitation beam, $\sigma_{\mathrm{abs}[0\to1]}$ is the absorption cross-section and S is the area of the excitation beam at its beam waist. If the stimulation is also done in the non-saturating regime, the number of stimulated photons is also proportional to the stimulation beam intensity, I_{S}, as well as to the number of excited molecules, N_2, yielding

$$\Delta I_{\mathrm{S}} \propto N_0 \, I_{\mathrm{E}} \, I_{\mathrm{S}} \, (\sigma_{\mathrm{abs}[0\to1]}/S)/(\sigma_{\mathrm{stim}[2\to3]}/S) \tag{2.2}$$

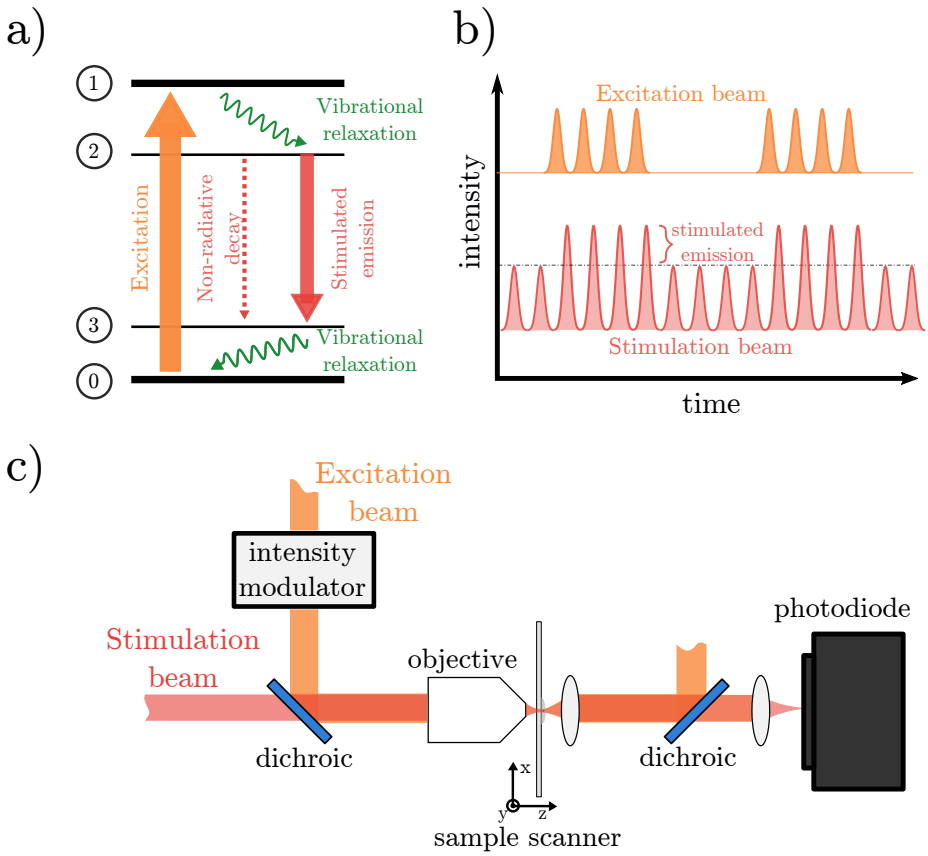


Figure 2.1: a) Energy level describing the enhancement of radiative decay by stimulated emission. b) The stimulation beam gets amplified only when the modulated excitation beam is present. c)Sketch of a SEM experimental setup.

where $\sigma_{\text{stim}[2\to3]}$ is the cross-section of stimulated emission. Therefore we see that the small amplification, ΔI_S, is proportional to the density of chromophores in the illuminated region. Given the nonlinear nature of this process, it is common to enhance its efficieny by using sub-picosecond excitation and stimulation pulses, thus increasing the intensities of the interacting fields.

An image of the density of the sample can be obtained by scanning the positions of the excitation and stimulation beams, or else by directly scanning the sample on a nano-stage (see Fig. 2.1).c. The spatial resolution obtained in SEM is in principle a factor of two better than that of fluorescent microscopy, due to the interaction volume being given by

the overlap of the excitation and stimulation beams. Moreover, the technique is inherently capable of doing three-dimensional optical sectioning of the region at the focci of the beams due to the nonlinear dependence of the signal on the beam intensities.

However, in experiments where few chromophores are being imaged, the amplification of the stimulation beam is so small that it can easily be buried in the low frequency technical noise of the laser and electronics [51]. Luckily, the pump-probe structure of the measurement allows for a straightforward mitigation technique: given that stimulation emission can only occur when the excitation beam is present, it is possible to introduce a modulation in the stimulated emission gain by modulating the intensity of the excitation beam (see Fig. 2.1.b). Shifting the modulated signal up in frequency, e.g. by a few MHz, the predominantly low-frequency technical noise of the laser and electronics is avoided [52]. The high-frequency signal can then be picked up using either a phase-locked-loop (PLL) or an electronic spectrum analyzer.

In summary, SEM has a number of advantages with respect to absorption and fluorescence microscopy. First, it enhances the contrast of the former without using the label fluorescent proteins required in the later. Second, it provides a better spatial resolution than fluorescence or absorption imaging. Third, it allows for a modulation of the SEM signal by modulating the excitation beam, therefore avoiding technical noise.

2.3 Quantum enhancement of SEM

Despite improving the signal to noise ratio (SNR) of SEM by avoiding the low-frequency technical noise, the wideband quantum fluctuations in the stimulation beam, known as shot noise, still set a fundamental limit to the sensitivity of the measurement. In the original SEM

paper[51], they reported that shot noise in the stimulation beam sets a smallest resolvable signal corresponding to the emission from 5 molecules of crystal violet (a dye) in focus. In this thesis we propose to overcome this limitation using the tools of quantum metrology.

The light produced by a laser is, to a very good approximation, in a coherent state. We can express a coherent state in a single optical mode as a displaced vacuum state (see Eq.(1.29)), such that the Heisenberg picture annihilation operator corresponding to that optical mode is

$$\hat{a_{\mathrm{s}}} = \hat{a}_{\mathrm{v}} + \alpha_{\mathrm{s}}, \tag{2.3}$$

where a_{v} is an annihilation operator refered to the vacuum state and α_{s} is a complex displacement. The quadratures of the field can be suscinctly written in vectorial form as

$$\hat{\mathbf{X}}_{\mathrm{s}} = \hat{\mathbf{X}}_{\mathrm{v}} + \mathbf{x}_0 \tag{2.4}$$

where $\mathbf{x_0} = (\mathrm{Re}\{\alpha\}, \mathrm{Im}\{\alpha\})$ is a displacement vector and $\hat{\mathbf{X}}_{\mathrm{s}} = (\hat{X}_{\mathrm{s}}, \hat{P}_{\mathrm{s}})$ and $\hat{\mathbf{X}}_{\mathrm{v}} = (\hat{X}_{\mathrm{v}}, \hat{P}_{\mathrm{v}})$ are vectors containing the two orthogonal quadratures defined in Eq.(1.23), respectively computed from the coherent state bosonic operators, $\hat{a}_{\mathrm{s}}$, and the vacuum state bosonic operators, $\hat{a}_{\mathrm{v}}$.

The process of stimulated emission gain in the non-saturating condition (Eq. (2.2)) can be modeled as phase-insensitive linear amplifier. This is the simplest type of amplifier that exists, where the output mean quadratures are just a re-scaled version of the input mean quadratures,

$$\mathbf{x_0}^{\mathrm{out}} = G_{\mathrm{SE}}\, \mathbf{x_0}, \tag{2.5}$$

G_{SE} being the stimulated emission gain parameter. It is known that, in order to maintain the

bosonic commutation relations of the electromagnetic field, a minimum amount of excess noise has to be introduced during the amplification process. A phase-insensitive linear amplifier adds an uncorrelated noise to each quadrature with a variance[53]

$$\sigma^2_{\text{excess}} = \sigma^2_{\text{X(P)}} \, |1 - G^{-1}_{\text{SE}}|. \tag{2.6}$$

where $\sigma_{X(P)}$ is the standard deviation in that quadrature due to shot noise. In the limit of very high amplification the excess noise is equal to the initial quantum fluctuations, therefore doubling the initial noise. However, for the very small amplification that we are considering in SEM, the added excess noise is negligible and we can write simply

$$\hat{\mathbf{X}}^{\text{out}} \approx G_{\text{SE}} \, \hat{\mathbf{X}} \tag{2.7}$$

Our goal consists essentially in estimating the small gain parameter G_{SE}, from which the chromophore density can be inferred. The amplified field is measured with a photodetector, which produces a photocurrent proportional to the intensity of the field,

$$\hat{\text{I}} = \eta_{\text{d}} \, |\hat{\mathbf{X}}^{\text{out}}|^2, \tag{2.8}$$

where η_{d} is the ratio between absorbed photons and emitted electrons in the detector. The measured current is compared to a calibrated "no-amplification current", and an estimator for G_{SE} is obtained. However, the presence of quantum uncertainty in the photocurrent, i.e. shot noise, leads to a derived uncertainty in the amplification that we infer from a single measurement. It can easily be seen that the first and second moments of the photocurrent

generated by the amplified field are

$$\langle \hat{\mathrm{I}} \rangle = \eta_{\mathrm{d}} G_{\mathrm{SE}}^2 |\mathbf{x_0}|^2 \quad , \quad \mathrm{var}(\hat{\mathrm{I}}) = 2\,\eta_{\mathrm{d}}^2 G_{\mathrm{SE}}^4 |\mathbf{x_0}|^2, \tag{2.9}$$

We can build the estimator for the stimulated emission gain by taking the ratio between the photocurrent in the presence of stimulated emission and the calibrated no-amplification photocurrent

$$\hat{\Gamma} = \hat{I}/I_0 \tag{2.10}$$

where $I_0 = \eta|\boldsymbol{\alpha_0}|^2$ is the no-amplification photocurrent. The first and second moments of the stimulated emission gain estimator are

$$\langle \hat{\Gamma} \rangle = G_{\mathrm{SE}}^2 \quad , \quad \mathrm{var}(\hat{\Gamma}) = 2\,G_{\mathrm{SE}}^4/|\mathbf{x_0}|^2, \tag{2.11}$$

where we see that it is possible to improve the SNR of the measurement by increasing the intensity of the stimulation beam, although at the cost of risking damaging the chromophores that are being imaged.

In this thesis we propose to improve the SNR of this measurement, instead, by using an amplitude-squeezed stimulation beam. Informally speaking for the moment (find a rigorous explanation in [54]), a squeezed state of light is a Gaussian state in which the quantum uncertainty associated to one quadrature is smaller than the minimum symmetric uncertainty found in a coherent state. This quadrature is said to be *squeezed*. In order to fulfill the Heisenberg uncertainty principle, the conjugate quadrature must be *antisqueezed*: it must have an uncertainty greater than that found in a coherent state. A squeezed state with a zero

mean is called a squeezed vacuum (see Fig. 2.2.a), while a squeezed state with a non-zero mean, given by a displacement vector $\boldsymbol{x}_0$, is called a squeezed coherent state (see Fig. 2.2.a and b). Unlike in a squeezed vacuum, where the choice of squeezed quadrature corresponds to a simple global phase, a coherent squeezed state presents a non-trivial phase: the relative phase between $\mathbf{x_0}$ and the squeezed quadrature. This phase can be seen informally as the angle that the squeezed uncertainty ellipse makes with the line that goes from the ellipse to the phase-space origin.

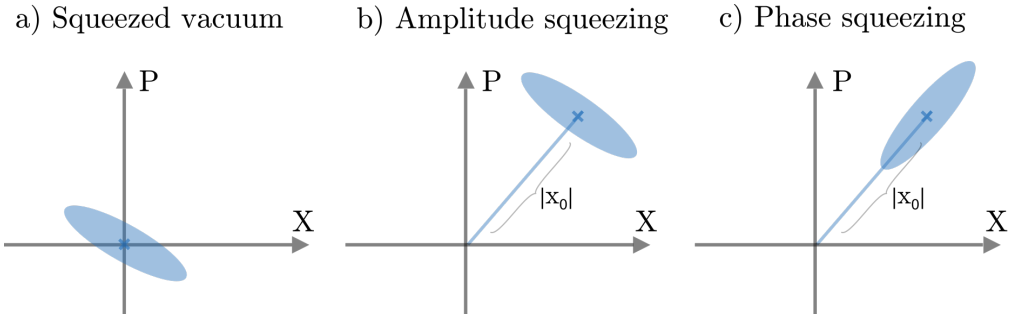


Figure 2.2: Different types of squeezed states. a) Squeezed vacuum has a zero mean and asymmetric quadrature fluctuations. b) An amplitude squeezed coherent state is displaced from the phase-space origin and its quadrature fluctuations are squeezed in the radial direction. c) A phase-squeezed coherent state is displaced from the origin, and its quadrature fluctuations are squeezed in the angular direction.

There are two extreme cases regarding the relative phase between the coherent amplitude and the squeezed quadrature. The first case is a state where the squeezing and displacement occur in the same quadrature (see Fig. 2.2.b). In a polar coordinate representation, the radial (amplitude) coordinate of an amplitude-squeezed state appears squeezed, while its angular (phase) coordinate is antisqueezed. These are the so-called amplitude-squeezed states. In contrast, a state where the squeezing and displacement occur in orthogonal quadratures (see Fig. 2.2.c) is called a phase-squeezed state. In this case, the radial coordinate of a polar representation is antisqueezed, while the angular coordinate (phase) appears squeezed.

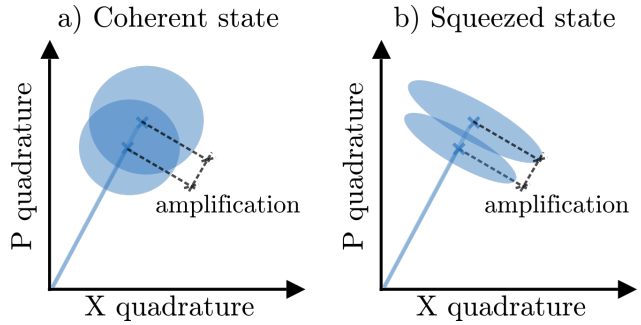


Figure 2.3: a) Estimating a small gain in a coherent state is hindered by quantum uncertainty. b) The gain estimation in an amplitude-squeezed state is improved because the overlap between the original and amplified quadrature distributions is smaller.

The parameter estimation problem posed by SEM can be improved by using amplitude-squeezed coherent states. An intuitive graphical explanation for why this is the case is found in Fig. 2.3 : given that we want to distinguish states with coherent amplitudes of slightly different magnitudes, it is advantageous to squeeze the quantum fluctuations in the radial direction, diminishing their overlap and making them more distinguishable. As we will show in the next section, this enhancement is due to the fact that an amplitude-squeezed state has lower intensity fluctuations (shot noise) than an equivalent coherent state with the same amplitude. This allows for a more precise estimation of the intensity of the amplified probe (Eq. (2.9)) from which the stimulated emission gain is estimated. It is important to note that, if we were trying to estimate a parameter encoded in the phase of the optical probe, an amplitude-squeezed state would give worse results than a coherent state with the same coherent amplitude, as its phase fluctuations are antisqueezed.

2.4 Squeezing coherent states: the degenerate parametric amplifier

We have laid out our proposal to improve SEM by using an amplitude-squeezed stimulation beam. The obvious question now is: how do you prepare such a state of light? It has long been known that nonlinear optics provides a mechanism for this task: the optical parametric amplifier (OPA)[54–56]. Here we will briefly review some standard results and notation, showing that a squeezed coherent state can be prepared through the phase-sensitive amplification of a monochromatic coherent state in an idealized narrowband OPA. This is presented only in order to illustrate the fundamental ideas behind amplitude squeezing, leaving the realistic modelling of a multimode ultrafast OPA for Chapter 3. The notation presented here follows mostly[57] and[58], with some straightforward modifications.

Consider the schematic DFG effective Hamiltonian in the interaction picture, coupling three monochromatic plane-wave fields (one pump and two degenerate signal fields) through a second order nonlinearity (see Sec. 1.2.4). This interaction corresponds to the well-known single mode squeezing transformation

$$\hat{S}(\xi) = \exp\left(\frac{1}{2}\left(\xi^* \hat{a}_\mathrm{s}^2 - \xi\,(\hat{a}_\mathrm{s}^\dagger)^2\right)\right) \tag{2.12}$$

with a squeezing parameter $\xi = 2\,g\,\alpha_\mathrm{p}$, where α_p is the coherent amplitude of the macroscopic pump, g is a gain parameter proportional to the second order susceptibility of the crystal, as well as the crystal length, and we have assumed that the pump oscillates at twice the frequency of the signal field, $\omega_\mathrm{p} = 2\,\omega_\mathrm{s}$. The signal field is described by the annihilation operator $\hat{a}_\mathrm{s}$, which fullfills the bosonic commutation relations $[\hat{a}_\mathrm{s}\,, \hat{a}_\mathrm{s}^\dagger] = 1$ and

$[\hat{a}_{\rm s}, \hat{a}_{\rm s}] = [\hat{a}_{\rm s}^\dagger, \hat{a}_{\rm s}^\dagger] = 0$.

In the Heisenberg picture, this evolution causes the following transformation of the signal annihilation operator

$$\hat{S}^\dagger \, \hat{a}_{\rm s} \, \hat{S} = \cosh(r) \, \hat{a}_{\rm s} - \sinh(r) e^{i\theta_{\rm p}} \hat{a}_{\rm s}^\dagger \tag{2.13}$$

where we have separated the squeezing parameter into its modulus and phase, $\xi = r \, e^{i\theta_{\rm p}}$. When this Hamitonian is applied to a signal field in the vacuum state, the state of the resulting field will be a squeezed vacum. This state is characterized by a non-zero mean photon number (spontaneous emission), as well as by a phase-dependent quadrature variance. But what is the state generated by applying this Hamiltonian to a coherent state? The predictable answer is: a squeezed coherent state. Despite this terminology, it is worth noting that an OPA does more to an input coherent state than just redistributing the quantum fluctuations of its field quadratures. Like the name suggests, an OPA amplifies (or deamplifies) a coherent state, both its mean and its fluctuations, depending on its phase.

Recalling that an initial coherent state can be expressed as a displaced vacuum (1.29), the state generated by amplifying a coherent state in a degenerate OPA is obtained by acting on the vacuum successively with the displacement operator, $\hat{D}(\alpha_{\rm s})$, followed by the single mode squeezing operator $\hat{S}(\xi)$:

$$|\alpha_{\rm s}, \xi\rangle = \hat{S}(\xi) \, \hat{D}(\alpha_{\rm s}) \, |0\rangle \tag{2.14}$$

and the transformation of the signal annihilation operator due to the chained effect of the

two operators is

$$\hat{a}_{\rm out} = \hat{D}(\alpha_{\rm s})^{\dagger}\, \hat{S}(\xi)^{\dagger}\, \hat{a}_{\rm s}\, \hat{S}(\xi)\, \hat{D}(\alpha_{\rm s}) = \cosh(r)(\hat{a} + \alpha_{\rm s}) - \sinh(r) e^{i\theta}(\hat{a}^{\dagger} + \alpha_{\rm s}^{*}) \tag{2.15}$$

with $\xi = r\, e^{i\theta}$. It is convenient to use the phase of the pump as a reference, setting $\theta_{\rm p} = 0$, and to define the phase of the input coherent state with respect to this. Then, the quadratures of the amplified signal field, defined in terms of its creation and annihilation operators, are

$$\hat{X}_{\rm out} \quad = (\hat{a}_{\rm out} + \hat{a}_{\rm out}^{\dagger}) \,/\, 2 = e^{-r}\ (\hat{X}_{\rm v} + {\rm Re}\{\alpha_{\rm s}\}) \tag{2.16}$$

$$\hat{P}_{\rm out} \quad = (\hat{a}_{\rm out} - \hat{a}_{\rm out}^{\dagger}) \,/\, (2\, i) = e^{r}\ (\hat{P}_{\rm v} + {\rm Im}\{\alpha_{\rm s}\}) \tag{2.17}$$

where we recall that $\hat{X}_{\rm v}$ and $\hat{P}_{\rm v}$ are the quadrature operators referred to the vacuum state.

This transformation can be seen as composed of two successive steps: first, the quadratures are displaced to the position $\mathbf{x_0} = ({\rm Re}\{\alpha_{\rm s}\}, {\rm Im}\{\alpha_{\rm s}\})$. Subsequently, the entire quadrature space is stretched (squeezed in one direction, antisqueezed in the other) by a factor of $\exp(\pm r)$. It is worth noting that, as shown in Fig. 2.4, the squeezing transformation affects not only the fluctuations of the displaced vacuum, but also its mean. Depending on the phase of the input coherent state, its mean will be amplified or deamplified due to the squeezing transformation. Moreover, as seen in Fig. 2.4 this dependence maps also to the direction of the fluctuation squeezing: if a coherent state gets deamplified it also gets amplitude-squeezed. On the contrary, if it is amplified it will also be phase-squeezed.

In our proposal, we are interested in measuring the intensity (photon number) of the stimulation beam rather than its quadratures. Using an amplitude-squeezed coherent state,

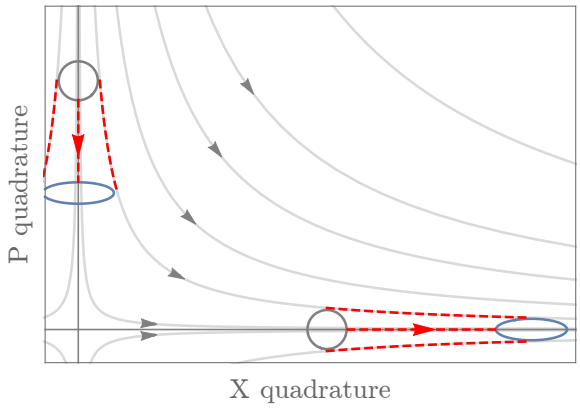


Figure 2.4: The single mode squeezing transformation stretches the phase space. If a coherent state gets deamplified it is simultaneously amplitude-squeezed, while if it is amplified it gets phase-squeezed.

we intend to reduce the intensity fluctuations (shot noise) for a given mean intensity. We can show that DFG achieves this by comparing the first and second order moments of the intensity (photon number) operator for a squeezed coherent state. The mean and variance of the photon number are, respectively

$$\begin{aligned}\langle \hat{n}_{\text{out}} \rangle &= \langle \alpha_{\text{s}}, \xi | \hat{a}^{\dagger}_{\text{out}} \, \hat{a}_{\text{out}} | \alpha_{\text{s}}, \xi \rangle \\ &= \text{Re}\{\alpha_{\text{s}}\}^2 \, e^{-2r} + \text{Im}\{\alpha_{\text{s}}\}^2 \, e^{2r} + \sinh^2(r)\end{aligned} \tag{2.18}$$

$$\begin{aligned}\text{var}(\hat{n}_{\text{out}}) &= \langle \alpha_{\text{s}}, \xi | \Delta \hat{n}^2_{\text{out}} | \alpha_{\text{s}}, \xi \rangle \\ &= \text{Re}\{\alpha_{\text{s}}\}^2 \, e^{-4r} + \text{Im}\{\alpha_{\text{s}}\}^2 \, e^{4r} + 2\sinh^2(r)\cosh^2(r)\end{aligned} \tag{2.19}$$

where we have defined $\Delta \hat{n}_{\text{out}} = \hat{a}^{\dagger}_{\text{out}} \, \hat{a}_{\text{out}} - \langle \hat{n}_{\text{out}} \rangle$.

We identify that the two first terms in the mean intensity, Eq. (2.18), correspond to the mean photon number of the input coherent state, $n_0 = |\alpha_{\text{s}}|^2$, amplified or deamplified depending on its phase. The last term, which arises only due to the bosonic commutation

relations of the creation and annihilation opearators, corresponds to the mean number of photons created by spontaneous emission. Neglecting the spontaneous emission when n_0 is large, the ratio between the intensity before and after amplification has a very simple form. Expressing the complex amplitude of the input coherent state as $\alpha_s = |\alpha_s| \exp(i\,\theta_s)$, we can write the intensity amplification parameter as

$$G = \frac{\langle \hat{n}_{out} \rangle}{n_0} \approx \cos^2(\theta_s)\, e^{-2r} + \sin^2(\theta_s)\, e^{2r} \tag{2.20}$$

Now we turn our attention to the intensity noise properties of a squeezed coherent state. The single-mode OPA transformation amplifies (deamplifies) not only the mean photon number of the input coherent state, but also its fluctuations. The ratio between the variance and the mean of the output photon number, often referred to as the intensity Fano factor, quantifies the sensitivity with which a measurement of the output field intensity can be performed.

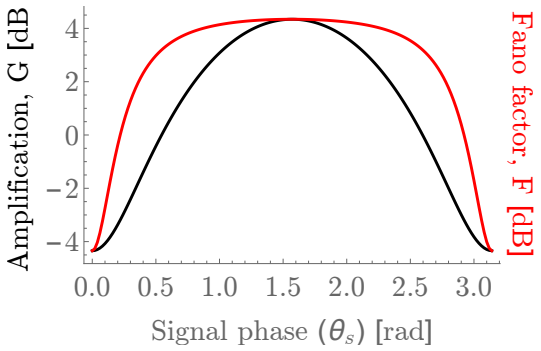


Figure 2.5: The amplification (deamplification) of the intensity mean and variance of a coherent state are respectively quantified by the intensity gain, G, and the intensity Fano factor, F. These attain the same value at their extremes, but not for intermediate phases. The difference is larger for higher squeezing parameters.

We can easily see that the Fano factor for a coherent state is equal to one by setting $r = 0$ in Eq.(2.18) and (2.19). This unit ratio, characteristic of the Poissonian photon statistics of

a coherent state, sets the "classical limit" that we aim to overcome. Any state of light whose Fano factor is lower than one can thus be referred to as sub-Poissonian. For the squeezed coherent states that we generate using an OPA, assuming that we can neglect spontaneous emission, the intensity Fano factor is

$$\mathrm{F} = \frac{\mathrm{var}(\hat{n}_{\mathrm{out}})}{\langle \hat{n}_{\mathrm{out}} \rangle} \approx \frac{\cos^2(\theta_{\mathrm{s}})e^{-4r} + \sin^2(\theta_{\mathrm{s}})e^{4r}}{\cos^2(\theta_{\mathrm{s}})e^{-2r} + \sin^2(\theta_{\mathrm{s}})e^{2r}}, \tag{2.21}$$

which can take values lower than one (squeezing), or higher (antisqueezing), depending on the phase of the input coherent state. It is worth noting that the maximum squeezing, attained for $\theta_{\mathrm{s}} = 0$, coincides with the value of the maximum deamplification, obtained at the same phase. In the same way, the maximum antisqueezing and amplification are also equal. However, this coincidence does not occur away from these optima, with the discrepancy being larger for higher values of the squeezing parameter. In Fig. 2.5 we show an example of this behaviour, where it is apparent that squeezing shows a higher sensitivity to phase fluctuations than intensity deamplification. Nevertheless, the correspondence between deamplification and squeezing at the optima suggests a straightforward strategy when experimentally attempting to maximize squeezing: tune the phase of the input coherent state to maximize deamplification, squeezing should follow.

2.4.1 Losses

It is well known that optical losses hinder the generation of squeezed light. Quantum correlations are broken when photons are scattered randomly, causing a reduction of the degree of squeezing. It is common to model linear losses in a single optical mode as scattering in a fictitious beamsplitter[59], identifying two of the ports (1 and 2 in Fig. 2.6) with

the optical field before and after loss, while the other two ports (3 and 4) are identified respectively as input and output "loss ports". The output loss port will carry the fraction of light that is scattered in the loss process, while the input loss port will be simply in the vacuum state.

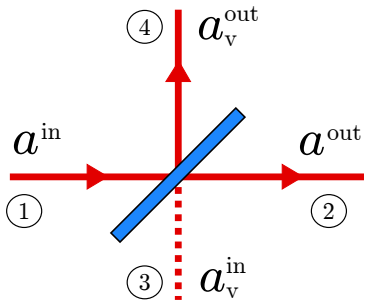


Figure 2.6: The effect of linear losses on a single optical mode can be modelled as a fictitious beamsplitter. As the input optical field is attenuated, vacuum fluctuations from the empty input port of the beamsplitter are coupled to it.

Using the beamsplitter transformation in the Heisenberg picture

$$\hat{a}^{\mathrm{out}} = \sqrt{\eta_{\mathrm{loss}}}\ \hat{a}^{\mathrm{in}} + \sqrt{1-\eta_{\mathrm{loss}}}\ \hat{a}_{\mathrm{in}}^{\mathrm{v}}, \tag{2.22}$$

where η_{loss} is the fraction of photons that are not lost, the annihilation operators $\hat{a}^{\mathrm{in}}$ and $\hat{a}^{\mathrm{out}}$ correspond to the optical field before and after loss and $\hat{a}_{\mathrm{in}}^{\mathrm{v}}$ corresponds to the input loss port in the vacuum state (see Fig. 2.6) , we find that the moments of the photon number at the input and output of the "loss beamsplitter" are related through

$$\langle \hat{n}^{\mathrm{out}} \rangle = \eta_{\mathrm{loss}}\ \langle \hat{n}^{\mathrm{in}} \rangle \tag{2.23}$$

$$\mathrm{var}(\hat{n}^{\mathrm{out}}) = \eta_{\mathrm{loss}}^2\ \mathrm{var}(\hat{n}^{\mathrm{in}}) + \eta_{\mathrm{loss}}\ (1-\eta_{\mathrm{loss}}) \langle \hat{n}^{\mathrm{in}} \rangle \tag{2.24}$$

where $\hat{n}^{\text{in/out}} = (\hat{a}^{\text{in/out}})^{\dagger}\hat{a}^{\text{in/out}}$ and we have used the fact that the input loss port (port 3) is in the vacuum state and that its bosonic operators commute with the bosonic operators in port 1. Using these relations we find that the intensity Fano factors of the fields before and after the losses are related through the simple expression

$$F^{\text{out}} = F^{\text{in}}\ \eta_{\text{loss}} + (1 - \eta_{\text{loss}}), \tag{2.25}$$

showing that, as the losses increase, the intensity squeezing parameter is degraded and approaches the classical limit of one. The relations shown here are easily generalized to a multimode case, provided that these modes are uncorrelated and that the losses affect each mode independently.

2.4.2 The connection between intensity and quadrature squeezing

There exists an extensive literature studying the generation of squeezed vacuum and its measurement through homodyne detection. In contrast, the topic of intensity squeezing in an OPA has received comparatively little attention. It is worth pointing out that there is a strong connection between the two, as this will allow us to tap from the squeezed-vacuum literature when designing our optical parametric amplifier. Although the parallelism is only exact in the single mode case, we will find that it is a good rule of thumb to begin designing a sub-Poissonian source of light using the insights gained in squeezed vacuum generation experiments.

Let us begin by providing a very schematic description of a homodyne detection scheme. More details can be found in [58]. In homodyne detection, the signal field to be measured, often prepared in a few-photon state, is sent into one port of a 50/50 beam-splitter (BS). A

local oscillator (LO) field prepared in a coherent state with a macroscopic amplitude is sent to the other input port of the BS. This coherent state can be described by the complex coherent amplitude β_{LO}, which corresponds to a displacement in the spatio-temporal mode occupied by the LO. The signal field can be decomposed in a basis of broadband optical modes, and an annihilation operator $\hat{b}_{\mathrm{s}}$ can be assigned to the spatio-temporal mode matching that of the coherent LO (save for their being in different ports in the BS). We find that the optical fields in the output ports of the BS are then described by the annihilation operators

$$\hat{b}_{\mathrm{out},1} = \sqrt{\frac{1}{2}}(\hat{b}_{\mathrm{s}} + \beta_{\mathrm{LO}}) \qquad \hat{b}_{\mathrm{out},2} = \sqrt{\frac{1}{2}}(\hat{b}_{\mathrm{s}} - \beta_{\mathrm{LO}}) \tag{2.26}$$

Detecting the intensity in each port with two balanced photodetectors, and subtracting them electronically, we obtain a current-difference signal

$$\Delta\hat{I} = \eta_{\mathrm{BD}} \left|\beta_{\mathrm{LO}}\right| \hat{X}^{\mathrm{s}}_{\phi_{\mathrm{LO}}} \tag{2.27}$$

where $\hat{X}^{\mathrm{s}}_{\theta_{\mathrm{LO}}} = \hat{b}^{\dagger}_{\mathrm{s}}\, e^{i\theta_{\mathrm{LO}}} + \hat{b}_{\mathrm{s}}\, e^{-i\theta_{\mathrm{LO}}}$ is a rotated quadrature of the signal optical field, and we have defined the phase of the LO complex amplitude as $\theta_{\mathrm{LO}} = \arg(\beta_{\mathrm{LO}})$, as well as a proportionality constant η_{BD} describing the response of the balanced photodetectors.

Now we can compare the quadrature squeezing measured through homodyne detection in a vacuum-seeded OPA with the intensity squeezing measured through direct detection in a coherent-state-seeded OPA. We can compute the Heisenberg picture quadrature operators corresponding to the output of a vacuum-seeded parametric amplifier by applying Eq.(2.17) and making the coherent amplitude at its input equal to zero. These quadratures are then measured through homodyne detection (Eq. (2.27)), leading to an intensity-difference signal

with a zero-mean and a variance that is squeezed or antisqueezed depending on the phase of the local oscillator:

$$\mathrm{var}(\Delta\hat{I}) = \langle \Delta\hat{I}^2 \rangle = 2\,\eta_{\mathrm{BD}}^2\,|\beta_{\mathrm{LO}}|^2\,(e^{-2r}\cos^2(\phi_{\mathrm{LO}}) + e^{2r}\sin^2(\phi_{\mathrm{LO}})) \tag{2.28}$$

where we have used the fact that the quadratures of a vacuum state are uncorrelated and each has a variance equal to one half. Normalizing the measured variance to that obtained for a non-squeezed vacuum ($r = 0$), we obtain a measure of quadrature squeezing:

$$s = \frac{\mathrm{var}(\Delta\hat{I})}{\mathrm{var}(\Delta\hat{I})|_{r=0}} = e^{-2r}\cos^2(\theta_{\mathrm{LO}}) + e^{2r}\sin^2(\theta_{\mathrm{LO}}) \tag{2.29}$$

We can now compare the intensity Fano parameter of a squeezed coherent state generated in an OPA (Eq. (2.21)) with the quadrature squeezing/antisqueezing of a squeezed vacuum produced in the same OPA (Eq. (2.29)). These two quantities are equal at their extrema, for maximum squeezing and antisqueezing. This parallelism motivates our informal corollary that we can often inform sub-Poissonian light source design using the literature on squeezed vacuum generation. It will be seen that this parallelism breaks down when modelling a multimode scenario, a question that we will tackle extensively in Chapter 3.

2.5 Experimental design

2.5.1 A sketch of the experiment: the need for pulsed and focused beams

In the last sections we have presented the elements that make up our proposal: we want to improve a stimulated emission microscope by reducing the quantum fluctuations in the intensity of its pulsed stimulation beam. This can be achieved by deamplifying an initial coherent state in a phase-sensitive OPA, which simultaneously reduces its intensity fluctuations below the coherent shot noise level. Now it is time to make this proposal more concrete, considering some practical details about the physical implementation of a real stimulated emission microscope. In doing so, we want to highlight a somewhat obvious point: while the single-mode model of an OPA that we have presented in the previous sections has provided us with much useful intuition, our experiment cannot be described by such a simple picture. Far from the monochromatic plane-wave description that we have used until now, the stimulation beam involved in our SEM experiment will be pulsed with sub-picosecond pulses and will have a finite transverse profile. As will be seen, this imposes additional considerations in the design of an appropriate OPA.

Let us begin by describing our implementation of an SEM experiment (see Fig.2.7), as it is this application that will demand certain specifications from our intensity-squeezed stimulation beam. In order to isolate the basic physics of the problem, and due to practical constraints, in this first demonstration we will only consider a bare-bones version of a practical SEM experiment. In the first place, we will not deal with the practical problems of scanning a sample to obtain an SEM image, but instead will consider a uni-pixel

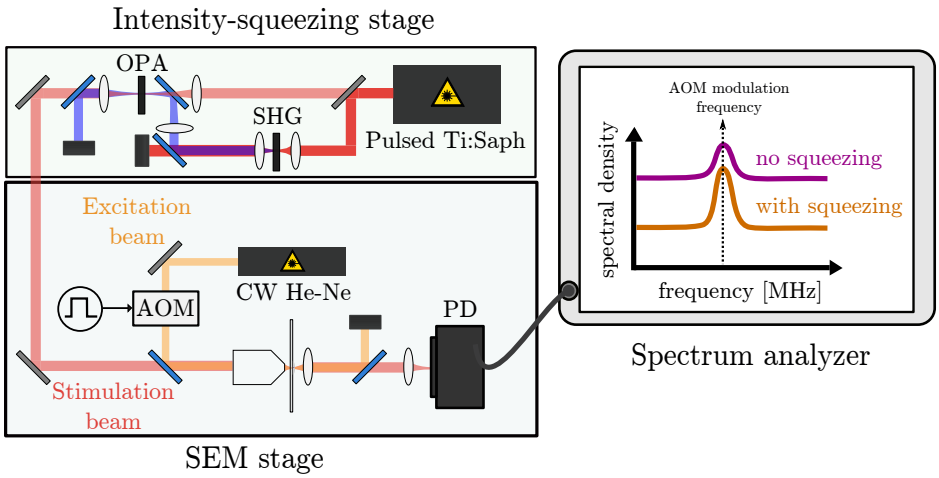


Figure 2.7: Sketch of the experiment. A pulsed sub-Poissonian beam is generated by phase-sensitive deamplification of a sub-picosecond pulsed Ti:Sapph laser. This beam is used as the "stimulation beam" in a simplified stimulated emission microscope.

measurement of a static sample. In second place, while the original SEM proposal[51] used sub-picosecond beams for both excitation and stimulation beams, in this demonstration we will use a continuous-wave (CW) excitation beam. This simplifies the experimental setup, forgoing the need to synchronize the excitation and stimulation pulses, while maintaining the core physics of the problem. As a test sample for the microscope we will use a diluted sample of a dye called Brilliant Blue FCF, which we choose because it absorbs strongly at the wavelength of an available excitation He-Ne laser ($\lambda_{\text{He-Ne}} = 632.8$ nm). The light used to stimulate the SEM sample will be obtained from a sub-picosecond modelocked Ti:Saph laser, with a central wavelength of 820 nm, chosen to be well outside of the absorption spectrum of the dye sample. Unlike with the excitation light, we do not make the simplification of using a CW field for this beam, as we aim to demonstrate the feasibility of generating ultrafast bright pulses with sub-shot noise intensity fluctuations. Our Ti:Saph laser outputs a train of 190-fs long pulses with a maximum energy of 40 nJ per puse, at a repetition rate of 80 MHz.

2.5.2 Quantum noise in a pulsed optical field

While until now we have carried our discussion of optical quantum noise assuming monochromatic beams, we note that our experiment differs from that model in that it uses trains of ultrafast optical pulses. Therefore, we must extend our picture of quantum noise to a broadband model that can describe the noise in such a pulsed field. Following [60], we quantize a broadband electromagnetic field propagating in a single spatial mode, and assuming negligible dispersion, by assigning each frequency a creation operator, $\hat{a}(\omega)$, which fulfill the commutation relations

$$[\hat{a}(\omega), \hat{a}^\dagger(\omega')] = \delta(\omega, \omega') \tag{2.30}$$

$$[\hat{a}(\omega), \hat{a}(\omega')] = [\hat{a}^\dagger(\omega), \hat{a}^\dagger(\omega')] = 0 \tag{2.31}$$

The time-varying intensity measured at a photodiode is given by the normally-ordered Poynting vector

$$\hat{n}(t) = \frac{\hbar\omega_0}{2\pi S} \int \mathrm{d}\omega \, \mathrm{d}\omega' \, \hat{a}^\dagger(\omega) \, \hat{a}(\omega') \exp(-i(\omega - \omega')t) \tag{2.32}$$

where S is a quantization area and ω_0 is the central frequency of the detected optical field. In our experiment, we will be concerned with the power spectral density (PSD) of the diode photocurrent, as measured with an electronic spectrum analyzer (SA). Defining the Fourier transform of the time-varying Poynting vector

$$\hat{S}(\Omega) = \frac{1}{\sqrt{2\pi}} \int \mathrm{d}t \, \hat{n}(t) \, \exp(-i\Omega t), \tag{2.33}$$

where we note that Ω is an "analysis frequency" in the radio-frequency (RF) range, we find that the PSD of the diode photocurrent is

$$\mathrm{PSD_i}(\Omega) = \eta_\mathrm{d} \langle |\hat{S}(\Omega)|^2 \rangle = \eta_\mathrm{d} \langle \hat{S}(\Omega)\, \hat{S}(-\Omega) \rangle \tag{2.34}$$

where η_d is a constant describing the ratio between light absorbed and current output. Note that we are making the simplification of assuming a photodiode with a flat frequency response, as we will only be interested in the low frequencies of the detected signal. The second equality in Eq. (2.34) is due to the fact that the time-domain Poynting vector is real. Doing a bit of algebra, and applying the commutation relations in Eq. (2.30), we find that the PSD of the diode photocurrent can be expressed as

$$\mathrm{PSD_i}(\Omega) = \langle \eta_\mathrm{d} \Big(: \hat{S}(\Omega)^2 : + \int \mathrm{d}\Omega\, \hat{S}(\Omega) \Big) \rangle \tag{2.35}$$

where the colons around $\hat{S}(\Omega)^2$ denote normal ordering of the creation and annihilation operators. Now, a pulsed coherent state, $|\alpha(\omega)\rangle$, can be represented in the Heisenberg picture by applying a frequency-dependent displacement to the vacuum:

$$\hat{a}(\omega) = \alpha(\omega) + \hat{a}_\mathrm{v}(\omega) \tag{2.36}$$

where $\hat{a}_\mathrm{v}(\omega)$ is the annihilation operator referred to the vacuum and $\alpha(\omega)$ is the frequency-dependent coherent amplitude. Expressing the PSD of the diode photocurrent in terms of

these Heisenberg-picture operators yields

$$\begin{aligned} \mathrm{PSD_i}(\Omega) &= \eta_\mathrm{d}\Big([\int \mathrm{d}\omega\, \alpha(\omega+\Omega)^*\, \alpha(\omega)]^2 + \int \mathrm{d}\omega\, |\alpha(\omega)|^2\Big) \\ &= \eta_\mathrm{d}\Big([\int \mathrm{d}\omega\, \alpha(\omega+\Omega)^*\, \alpha(\omega)]^2 + N_0\Big) \end{aligned} \tag{2.37}$$

We identify that the first term in the rhs of Eq. (2.37) corresponds to the autocorrelation of $\alpha(\omega)$, and the second term in the rhs corresponds to a frequency-independent (white) noise with a spectral amplitude equal to the mean photon number in $|\alpha(\omega)\rangle$, which we denote as N_0.

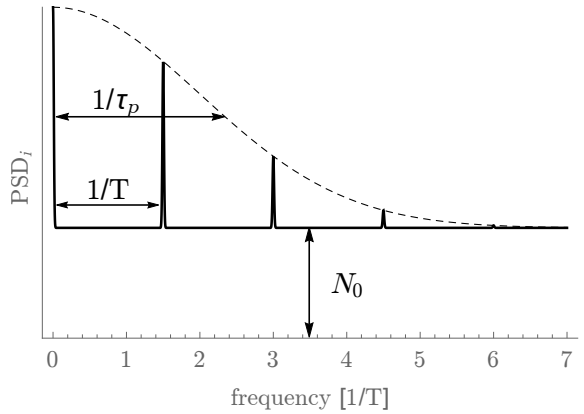


Figure 2.8: The PSD of the photocurrent generated by a train of optical pulses has peaks separated by the repetition rate of the laser, which are modulated by an envelope given by the Fourier transform of the pulse temporal shape. The quantum fluctuations of the optical intensity add a constant noise background with an amplitude proportional to the energy of a pulse.

The spectral amplitude corresponding to a train of pulses is a frequency-comb of the form

$$\alpha(\omega) = \sum_m A_0(\omega-\omega_0)\, \delta(\omega-\omega_0+\frac{2\pi\, m}{T}) \tag{2.38}$$

where $A_0(\omega)$ is the base-band Fourier transform of the pulse temporal envelopes, ω_0 is the frequency of the optical carrier, and T is the period between pulses. This frequency comb

yields a detected photocurrent PSD like the one shown in Fig. 2.8. The spectral peaks are separated by the repetition rate of the laser, which in our experiment is 80 MHz. The envelope of the PSD has a bandwidth of the order of $1/\tau_{\mathrm{p}}$, where τ_{p} is the temporal duration of the transform-limited optical pulses (this bandwidth is artificially small in Fig. 2.8). In addition to the frequency peaks at the repetition rate of the laser, the photocurrent PSD also has a flat background, which we have identified as shot noise. In our experiment, we intend to reduce this flat noise background, without reducing the amplitude of the frequency peaks, by using a pulsed squeezed coherent beam.

2.5.3 Squeezing pulsed beams

As we have advanced earlier, in order to obtain intensity squeezing in the stimulation beam, this has to be deamplified in a phase-sensitive three-wave-mixing process, where it will play the role of the sub-harmonic *signal* field. However, now that we consider squeezing a pulsed signal instead of the plane-wave monochromatic field introduced in Sec. 2.4, it is natural to ask what form the pump beam should take. Given the parallelism between squeezed-vacuum generation and sub-Poissonian light generation that we have mentioned earlier (section 2.4.2), we initially guided our design of a proof-of-principle experiment using insights taken from the pulsed squeezed-vacuum literature. It will be seen later that, while this provided us with a good basis from which to begin, our initial picture of pulsed OPA turned out to be too simple. Let us for the moment introduce the principles that guided our experimental demonstration. In Chapter 3 we provide a more complete theoretical analysis of a seeded OPA, pointing out possible limitations, and guiding a future design.

Pulse durations

A natural first consideration regarding the pulsed nature of the signal field is: if the signal pulses are delivered at a rate of 80 MHz and have a duration of only 200 fs, the fraction of the time occupied by a pulse is less than 10^{-4} in one. This precludes the possibility of using a CW pump in a travelling-wave configuration, given that only a minuscule fraction of its power would be used to deamplify the signal pulses. The question arises: can we use a pulsed pump in order to employ its power efficiently? Indeed, some of the first experiments producing squeezed vacuum involved short pump pulses, used to enhance the effective optical nonlinearity in a travelling-wave configuration [61–64].

Let us now analyze what are the conditions required from the pump and signal pulses, such that squeezing can be achieved. Let us consider a slab of quadratic nonlinear material in which a signal and pump pulses travel along the z direction, omitting for the moment any transverse propagation effects. Given that the carrier frequency of the pump is twice that of the signal, these two fields are coupled through the quadratic nonlinearity. In a dispersionless material, where the two pulses would travel together along the entire crystal, a simple condition is required from their respective durations: in order to optimize squeezing, the pulse length of the signal (local oscillator) must be shorter than that of the pump [65]. This is an intuitive requirement given that, if the seed pulse is longer than the pump, its temporal wings will not participate in the nonlinear interaction and therefore will not be squeezed.

In a seeded OPA, the effect of imperfect mode overlap is double: the part of the pulse that is overlapped with the pump is simultaneously deamplified and squeezed (see Fig.2.9.a). Let us coarsely estimate the degree to which squeezing deteriorates if this condition is not

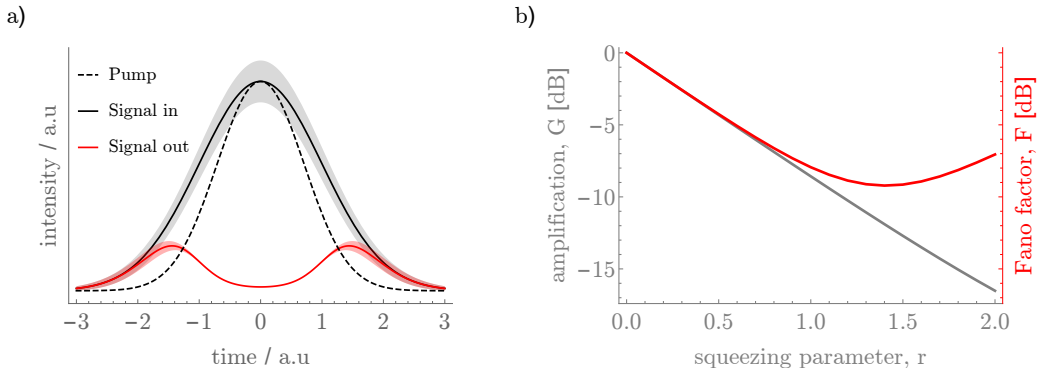


Figure 2.9: a) Illustration of deamplification and squeezing of a signal pulse longer than the pump. The solid lines represent the mean of the optical intensity, and the shade around them represents the standard deviation of its fluctuations. The wings of the pulse experience less deamplification and squeezing than its center. b)As the pump power is increased, the Fano factor of the total intensity does not decrease monotonically. Here the pump and signal pulses are Gaussian, with $\sigma_{\mathrm{s}} = \sigma_{\mathrm{p}}\sqrt{2}$. This corresponds to a field overlap of $\eta_{\mathrm{OL}} = 0.97$.

fulfilled. Considering a certain overlap between the pump and signal field amplitudes, η_{o}, only a fraction η_{o}^2 of the intensity of the pulse experiences deamplification and squeezing, whereas a fraction $(1-\eta_{\mathrm{OL}})^2$ remains unchanged. Assuming that the overlapping part is uniformly deamplified and squeezed, following the single mode OPA model (Eq. (2.20) and (2.21)), we can calculate the intensity Fano factor after the interaction:

$$F_{\mathrm{out}} = \frac{\mathrm{var}(n_{\mathrm{out}})}{\langle n_{\mathrm{out}}\rangle} = \frac{e^{-4r}\,\eta_{OL}^2 + (1-\eta_{OL})^2}{e^{-2r}\,\eta_{OL}^2 + (1-\eta_{OL})^2} \tag{2.39}$$

This estimation, despite being only qualitative, highlights an important difference between quadrature and intensity squeezing. Whereas the observed quadrature squeezing increases monotonically with the squeezing parameter r, regardless of the overlap between the LO and the squeezed mode, this is not the case in intensity squeezing (see Fig.2.9.b).

The problems with using SHG to generate the pump A common method to obtain a phase-stable train of pump pulses with the same repetition rate as the signal pulses is to generate both using the same laser, obtaining the pump through SHG of the fundamental beam in a quadratic nonlinear crystal. In this work we used this scheme due to its experimental simplicity (see Fig. 2.7): the light output by the high-power Ti:Sapph laser is separated into a weak beam, which will be used as the signal, and an intense beam headed for a frequency doubling crystal. The generated second-harmonic pump light is separated from the remaining fundamental by means of optical filters, and subsequently combined with the signal in a dichroic mirror. Now, the co-propagating signal and pump, which have been appropriately synchronized by matching their path lengths, are focused into a second nonlinear crystal, which implements an OPA.

While this is a simple and effective arrangement, it is worth noting that it implies a fundamental limitation. Given the quadratic dependence of SHG on the fundamental amplitude, the second harmonic pulses will be shorter than the fundamental pulses (i.e. assuming a short nonlinear crystal such that dispersion can be neglected. See Sec. 1.2.3 for more details). In particular, assuming fundamental pulses with a Gaussian temporal profile, the second harmonic pulses will also be Gaussian with a temporal constant smaller than the first by a factor of $\sqrt{2}$. According to the discussion above, having a pump that is shorter than the signal inevitably reduces squeezing. To quantify this effect, we use the coarse model that we presented in Eq.(2.39), taking $\eta_{\mathrm{OL}} = 0.97$ as the field amplitude overlap integral between two Gaussian pulses with width constants differing by a factor of $\sqrt{2}$. As seen in Fig. 2.9.b, we find that the temporal mismatch is not expected to degrade the intensity Fano factor significantly below 6 dB of squeezing. However, the effect becomes stronger

beyond this point, limiting the absolute achievable intensity squeezing to $\sim$ 12 dB.

Angle phase-matching

The nonlinear crystals in which OPA takes place are not dispersionless media. The refractive indices experienced by the signal and pump fields, whose carrier frequencies are separated by an octave, are in general different. This leads to a dephasing between the two beams as they propagate along the crystal. Given that parametric amplification is phase-dependent, this dephasing leads to an alternation between amplification and deamplification processes, which cancel each other. Efficient optical parametric amplification (deamplification) requires a phase-matching condition to be fulfilled: the refractive indices experienced by the pump and seed fields must be equal in order to prevent dephasing as they propagate. In our experiment, we choose a simple method to achieve phase-matching: using the birefringence of BBO, we find the propagation angle for which the refractive indices for an e-polarized pump and an o-polarized signal (type-I interaction) are the same (see Sec. 1.2.2 for background on birefringent propagation). Using the Sellmeier equations of BBO, we find that the propagation angle with respect to the crystal optical axis for which this condition is achieved is $\theta_0 = 29°$. It is worth noting that the phase-matching condition required for degenerate OPA is the same required for SHG. This provides a simple way of aligning the orientation of the crystal for efficient OPA by maximizing SHG when only the signal beam is sent into the crystal. The advantages of using angle phase-matching are that we can use common and relatively inexpensive nonlinear crystals, as well as having a simpler experimental setup than that involved in other approaches, such as temperature phase-matching.

Crystal length: temporal walk-of

Dispersion in the crystal leads to an additional effect to consider: temporal walk-off. The signal and pump pulses travel along the crystal at different group velocities, such that two initially overlapping pulses will walk-off from each other after a long enough propagation length. The implication on the design of the OPA is that we should use a crystal shorter than the propagation length that it takes the pulses to walk-off. Evaluating the group velocity of the signal and pump in BBO ($v_s = 0.594\,c$ and $v_p = 0.574\,c$ respectively), we find that the length of crystal for which their temporal overlap decays by a factor of two is $L_{max} = 800\,\mu m$. The crystal used in our experiment was 300 μm long, ensuring that the temporal walk-off between the pulses is small.

2.5.4 Squeezing focused beams

In a bulk crystal travelling-wave OPA, the pump and signal beams are focused into the interaction region, enhancing their intensities and increasing the efficiency of the process. The fact that the interacting beams are confined in the transverse direction supposes an additional departure from the plane-wave model introduced in Sec. 2.4. We will here discuss the design considerations derived from this.

In the first place, it has been noted that, in a travelling-wave OPA where the beams diverge substantially during the interaction, a mixing of the amplified and deamplied quadratures can occur[66–68]. If the phase fronts of the pump and signal beams do not remain parallel as they travel through the nonlinear medium, their quadratures will rotate with respect to each other as they propagate, leading alternation between amplification and deamplification. This would seem to suggest that the optimum configuration is to operate

under the Boyd-Kleinman condition[69], where the waist of the pump is made smaller than that of the signal by a factor of $\sqrt{2}$ to ensure that their phase-fronts remain parallel as they diverge.

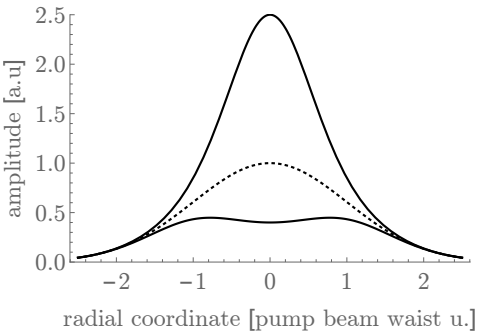


Figure 2.10: Spatially inhomogeneous deamplification. The solid lines show the spatial profile of the amplified (peaked) and deamplified (dipped) quadratures. The original spatial profile is shown in a dotted line for reference.

However, this choice of beam waists seems to contradict another principle that we set when we discussed the choice of pulse durations (Sec. 2.5.3): the pump field should overlap with all of the signal field in order to avoid having non-deamplified sections that limit the achievable squeezing. In addition, using a pump beam smaller than the signal leads to an intrinsic limitation in the high-gain regime through the phenomenon of gain-induced diffraction[66]: the shape of the signal beam profile for the amplified and deamplified quadratures will be both non-Gaussian, but different (see Fig.2.10). These two distorted beam profiles will diffract differently even if the initial beam waists had been chosen to satisfy the Boyd-Kleinman condition, which again leads to a mixing of amplification and deamplification. It has been found that, if the unpertubed signal and pump beams satisfy the Boyd-Kleinman configuration, the limit in the amount of achievable quadrature squeezing due to gain-induced diffraction is 6 dB[66].

A compromise between these two seemingly opposing principles, i.e matching the phase-

fronts of the interacting beams and using a pump beam that homogeneously covers all of the signal spatial profile, must be seeked. One way of making the effect of beam divergence small, despite the possibly non-matched phase-fronts, is to make the Rayleigh length of the interacting beams much longer than half the length of the nonlinear crystal. In a previous study [70,71] it was experimentally concluded that optimal squeezing could be achieved by setting the beam waist of the pump to be a factor of $\sqrt{2}$ larger than that of the signal, while keeping the confocal length of the beams much larger than the length of the nonlinear crystal. Here we adopt this same strategy: focusing the signal down to a beam waist (defined as the standard deviation of the spatial intensity profile) of $W_{\mathrm{s}} = 40\,\mu$m, and the pump down to $W_{\mathrm{p}} = 60\,\mu$m, we obtain a Rayleigh length for the signal and pump of respectively $z_{\mathrm{s}} = 10$ mm and $z_{\mathrm{p}} = 40$ mm. These are almost three orders of magnitude larger than the $150\,\mu$m half-length of our BBO crystal, ensuring that beam divergence is kept small.

2.6 Experimental demonstration

In this section we report on our experimental demonstration of a quantum-enhanced SEM experiment. For clarity of exposition, we will divide the description of our setup into two blocks: first we will discuss the sub-Poissonian light source, and then we will describe the SEM microscope. After detailing the main experimental challenges involved in each block, we will report on our measurement of SEM with an intensity-squeezed probe.

2.6.1 Sub-Poissonian light source

The core component in this experiment is a source of intensity-squeezed bright ultrafast pulses, which will be used as a stimulation beam in the SEM setup. While pulsed sub-

Poissonian light has been produced before[68], to our knowledge this is the first demonstration of such optical states using sub-picosecond pulses. This represents a reduction by three orders of magnitude in pulse duration with respect to previous experiments, entering a regime of ultrafast optics where this problem has not been investigated before.

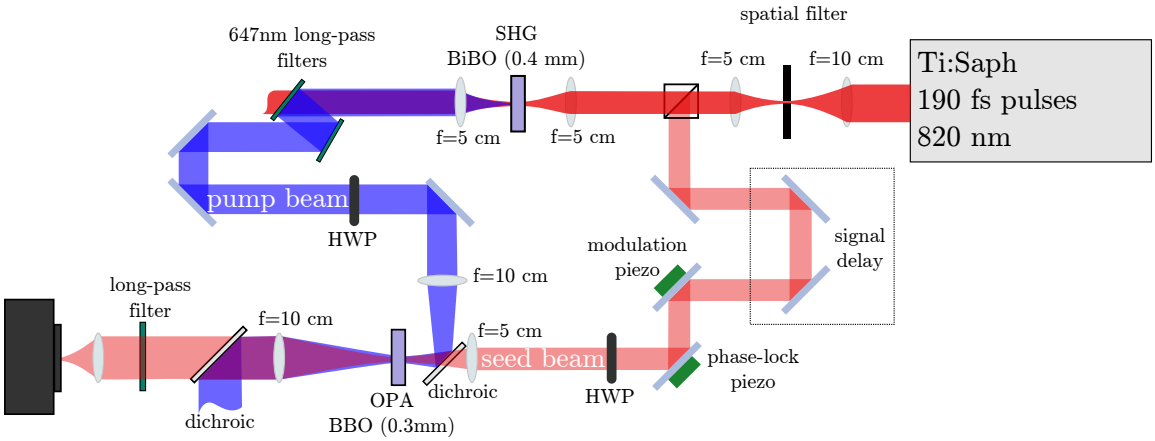


Figure 2.11: Sub-Poissonian light source experimental setup

The experimental setup

The basic structure of our source is shown in Fig 2.11. It follows the typical configuration mentioned earlier: a fundamental laser beam is split into a weak signal field and a strong pump generated through SHG. These are then recombined in a second nonlinear crystal where the signal field undergoes parametric deamplification. The OPA consists in a 300 μm-long BBO crystal, chosen due to the considerations listed in Sec. 2.5.

Our fundamental laser source is an ultrafast Ti:Sapphire laser (Coherent Chameleon) generating a train of 190-fs long pulses at a central wavelength of 820 nm, with a repetition rate of 80 MHz and a maximum average power of 3 W. The spectral phase of these pulses was measured using a pulse characterization device (APE LX spider), ensuring that they

are indeed Fourier transform limited. The laser is initially spatially filtered, obtaining a collimated Gaussian profile with a beam waist of 1 mm.

Let us first follow the path of the pump beam. The 410 nm pump is produced via SHG in a 400 μm-long bismuth triborate (BiBO) crystal. The fundamental beam is focused down to a waist of 20 μm into the BiBO crystal, achieving efficient conversion without incurring into significant elipticity of the second harmonic due to the relatively small walk-off angle of the crystal (20 mrad [72]). The fundamental beam and second harmonic are separated using two long-pass filters (Semrock 647 nm EdgeBasic long-pass) placed next to each other such that the pump is reflected multiple times off the filters. After four reflections, the 810 nm fundamental is attenuated by a factor of 10^{-20}, ensuring the spectral purity of the pump. We obtain a maximum average pump power of 550 mW using 2 W of 820 nm fundamental.

Next, we want the high-power pump to interact with the weak signal beam that we initially split off. In order to make the pump and signal pulses overlap temporally, the optical path lengths of the two are matched, first by coarsely matching the distances that the beams travel, and then obtaining the fine tuning using a μm-resolution delay stage in the signal path. Two piezo-controlled mirrors, about which more will be said later, are used to adjust the relative phase between the pump and signal. To combine the signal and pump in the OPA crystal, while controlling their beam-waists separately, these are first focused using independent lenses and then combined in a dichroic mirror (Semrock Brightline 660nm edge dichroic). As we have mentioned earlier, the lenses are chosen to obtain beam waist of $W_\mathrm{s} = 40\,\mu$m for the signal, and $W_\mathrm{p} = 60\,\mu$m for the pump, achieving a compromise between spatial overlap and phase-front matching.

Parametric amplification

A careful alignment of the signal and pump, as well as of the crystal, is necessary to obtain parametric amplification. The two fields must overlap as they propagate through the nonlinear medium, which has to be located at the focus of the beams. The orientation of the crystal has to be adjusted to provide degenerate type-I phase matching, and the polarizations of the beams must be set accordingly. This task is greatly simplified by splitting the process in two steps. First, blocking the pump and increasing the signal power, the crystal is aligned to maximize the amount of SHG generated by the signal. This is a good starting point given that the conditions that optimize the generation of signal-SHG (i.e. phase-matching angle and beam focused at the crystal) are the same required for OPA. In second place, the pump beam has to be overlapped with the signal, both spatially and temporally. Instead of attempting this directly, it is useful to first align the pump with the signal-SHG as a proxy. These two beams can be simultaneously coupled into a single-mode fiber (spatial overlap) and sent to an optical spectrum analyzer (OSA) to look for spectral interference fringes when they are temporally overlapped. Attaining this condition indirectly ensures that the signal and pump will be overlapped.

Now we are ready to observe parametric amplification/deamplification of the weak signal. Measuring the phase-sensitive amplification of the mean intensity of the signal will provide an indication that, according to our model of an OPA, its quantum fluctuations should be reduced as well. We send a strong pump (> 50 mW) and a weak signal (~ 1 mW) into the BBO crystal, and separate the outcoming beams using a low-loss dichroic mirror (Layertech separator 109433). The direction of energy transfer in an OPA (i.e. from signal to pump or the other way round) depends on the relative phase between the two beams,

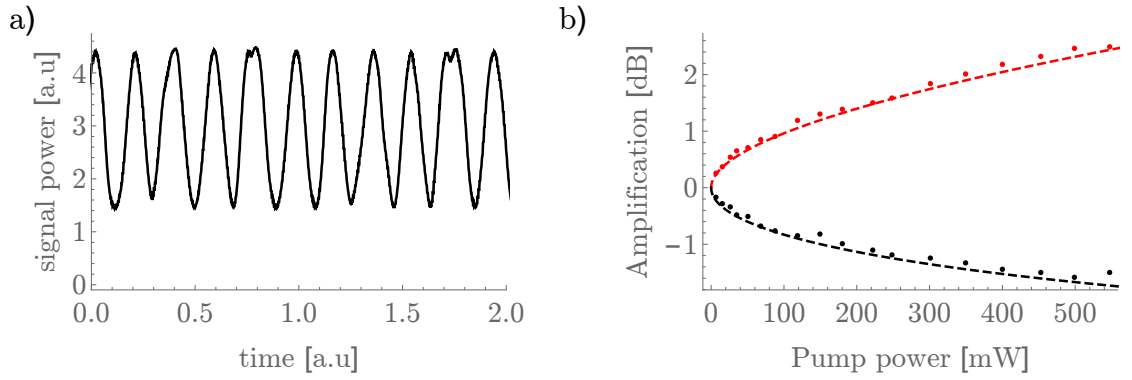


Figure 2.12: a) Amplification/deamplification fringes as the signal phase is scanned linearly. b) Maximum amplification (red) and deamplification(black) as a function of pump power. The data is fitted with a simple model considering imperfect overlap between the pump and signal.

which we scan using a piezo-controlled mirror (labelled "phase-lock piezo" in Fig. 2.11). Using a photodiode to measure the power of the output signal, we observe that this oscillates from maximum amplification to maximum deamplification as we scan the signal phase (see Fig. 2.12).a. We align the pump and signal beams to maximize the contrast of these "amplification fringes", indicating an optimum nonlinear interaction. Considering a generic non-unit overlap (e.g. spatial, temporal, polarization) between the signal beam and the mode that gets uniformly deamplified, η_{OL}, the amplified/deamplified output power in the signal should be [73]

$$\mathrm{P_{out}} = \eta_{\mathrm{OL}} \exp(\pm\alpha\sqrt{\mathrm{P_p}})\, P_{\mathrm{in}} + (1-\eta_{\mathrm{OL}})P_{\mathrm{in}} \tag{2.40}$$

where $P_{\mathrm{in/out}}$ is the average power of the input/output signal beam, P_{p} is the average power of the pump, and α is a fitting constant. In Fig. 2.12.b we show the values of these extrema in our experiment, taken for a range of pump powers up to 550 mW. The dashed lines correspond to a fit of Eq. 2.40 using only the low-power data in order to avoid phenomena

like gain-induced diffraction. The overlap parameter has been fitted to $\eta_{\mathrm{OL}} = 0.58$.

Locking on deamplification

The relative phase between the pump and signal fluctuates continuously even when we are not scanning it with a piezo. These chaotic fluctuations originate from a variety of causes, with a predominant contribution from the air currents in the laboratory. In consequence, a free-running OPA process jumps from amplification to deamplification in a random fashion, yielding the output signal light unfit for any practical application.

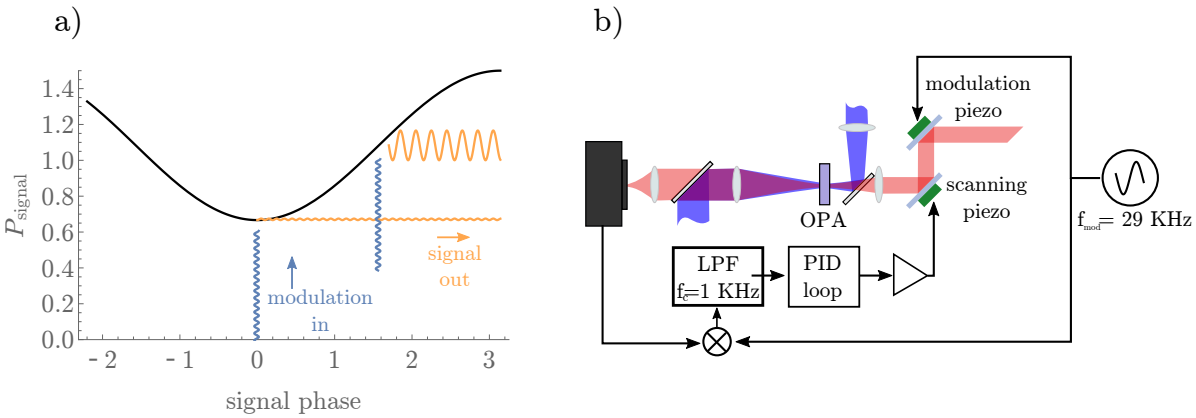


Figure 2.13: Locking to deamplification. a) We introduce a small modulation of the signal phase, which is transferred to the signal output power through the phase-dependent amplification process. This signal can be demodulated electronically and is monotonic at the point of maximum deamplification. b) Electronics used to lock the OPA to deamplification.

To lock the relative phase between the pump and signal fields, in order to consistently obtain deamplification of the latter, we implement a feedback system that reads the unstable output signal power and compensates for the random fluctuations of the phase using a piezo-controlled mirror. We should note that locking to a minimum of the signal power (i.e. maximum deamplification), is not a trivial task given that, at its minimum, the output signal power does not depend monotonically on therelative phase between the pump and

signal fields. Therefore, the output signal power cannot be used directly as an error signal to a proportional-integral-derivative (PID) loop, and additional processing has to be done. As illustrated in Fig. 2.13, we can add a small modulation to the input signal phase, $\theta_{\mathrm{s}} = \theta_{\mathrm{s},0} + s(t) = \theta_{\mathrm{s},0} + \delta \sin(2\pi f_{\mathrm{mod}} t)$, where δ is a small amplitude. This phase modulation is translated into an amplitude modulation of the output signal power through the phase-sensitive amplification process, $\mathrm{P}_{\mathrm{out}}(\theta_{\mathrm{s},0}+s(t))$,which can be electronically demodulated (i.e. multiplied with a sinusoidal local oscillator of frequency f_{mod} and then low-pass filtered, see Fig. 2.13). As shown in Appendix A, the demodulated signal is proportional to the derivative of $P_{\mathrm{s,out}}$ with respect to the signal phase,

$$P_{f_{\mathrm{mod}}} \propto \partial_x P_{\mathrm{out}}(\theta_{\mathrm{s},0} + x). \tag{2.41}$$

This processed signal is monotonic at the point of maximum deamplification of P_{out}, and can therefore be used as the error signal in a PID loop. In our experiment, we modulate the phase of the signal field using an independent piezo-controlled mirror, driven with the low-amplitude sinusoidal output of a waveform generator (Tektronix AFG 3022). The output of the photodiode that detects the signal field power is then mixed with a phase-locked "copy" of the modulation signal, and the product is low-pass filtered (Thorlabs EF110) and used as the error signal of a PID loop (New Focus LB1005). The output of the PID loop is then sent to high voltage amplifier (Thorlabs MDT694B), and the amplified signal is fed to a second piezo-controlled mirror to compensate for the phase fluctuations ("phase-lock piezo"). Using this scheme, we are able to robustly lock the phase of the signal field to maximum amplification or deamplification (depending on the setting of the PID loop).

Direct detection of sub-Poissonian noise

A key task in our experiment is to achieve shot-noise-limited detection of the SEM stimulation beam. This requires a photodiode with a high quantum efficiency, low noise and fairly large detection bandwidth. The reason why we need a large bandwidth is that, while we do not need to resolve each optical pulse separately, we still modulate the SEM signal at a high frequency (> 2 MHz) in order to avoid technical noise. In our experiment we use a Hamamatsu S5971 silicon PIN photodiode, with 85% quantum efficiency at 820 nm and a bandwidth of 100 MHz, reverse-biased at 30 V. The output current is amplified by a custom-made low-noise transimpedance amplifier, previously high-pass filtered to avoid saturation of the amplifier by the DC component of the signal. This scheme yields a clearance of 12 dB between the shot noise and electronic noise in a frequency band from 2 MHz to 10 MHz with an average signal power of $P\text{in} = 2$ mW. In addition, this electronic board contains a second circuit where the current from the photodiode is independently amplified with no high-pass filtering occurring. This DC output gives us a direct measurement of the signal power, which we use as an alignment monitor, as well as a way to obtain a large signal proportional to the amplification/deamplification in the OPA, which we use in our locking system.

Using this photodiode we can measure the intensity fluctuations of our deamplified signal beam, which we know should be reduced with respect to those of a coherent state of the same mean power. We quantify the degree of intensity squeezing in the following way: locking the phase of the signal to achieve deamplification in the OPA, we measure the high-frequency output signal noise in an electrical spectrum analyzer (SA), Keysight PXA N9030A. Tuning the SA to a central frequency where technical noise is negligible (e.g. 4 MHz), and using a

small frequency range(100 KHz), together with a large resolution bandwidth (1 KHz) and low video bandwidth (10 Hz), we acquire and average a total of 100 noise power traces. Next, we proceed to measure the noise of a reference coherent state by blocking the pump beam that drives the OPA. Given that the mean power of the signal changes when it ceases to be deamplified, this has to be compensated to be the same as that of the deamplified beam. Once this is done, a second batch of 100 traces are taken with the SA, comparing their average to that measured with the deamplified signal. The difference between these two traces, i.e. the difference between the noise power of the deamplified beam and that of a reference coherent state, corresponds to the Fano factor of the intensity-squeezed signal beam.

It is worth noting that, if we had two balanced photodiodes with the required specifications, the Fano factor could be measured more conveniently by dividing the beam in a 50/50 beam-splitter and detecting the intensity in each port. In this configuration, the fluctuations of the intensity-squeezed beam can be measured from the sum of the photocurrents, while their difference would have fluctuations corresponding to those in our reference coherent state.

In the same way that we measured the amplification/deamplification of the signal as we scanned the pump power (see Fig. 2.12), we measure the degree of intensity squeezing for different pumps. However, this time we are faced with an unexpected outcome: as shown in Fig. 2.14, the degree of intensity squeezing that we measure is much smaller than the classical deamplification of the mean. While there are many reasons why the measured squeezing can be smaller than deamplification of the mean, the discrepancy that we observe is difficult to explain using a simple model.

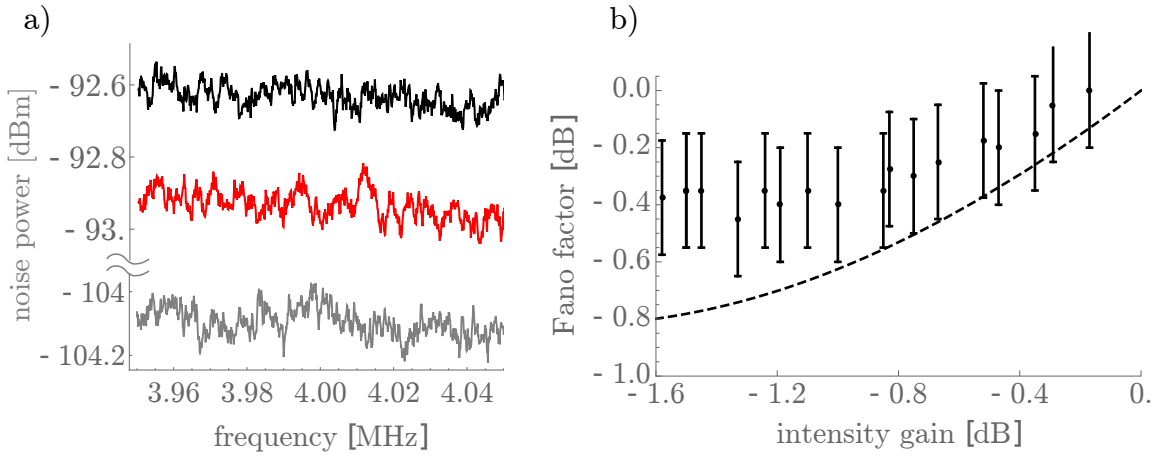


Figure 2.14: a) Spectral power of the shot noise measured with no deamplification (black) and a deamplified signal (red). The bottom (gray) line corresponds to the electronic noise. b) Dots - Measured intensity Fano factor as a function of the mean intensity deamplification. The noise squeezing is much smaller than the mean intensity deamplification, and it saturates early on. Dashed line - A simple model including the experimentally measured linear loss and the imperfect overlap between the pump and signal, as extracted from classical amplification/deamplification, cannot account for the reduced squeezing

In first place, we need to account for the reduction of squeezing due to linear losses after the OPA which, as explained in Sec. 2.4.1, break the quantum correlations responsible for squeezing. We separate the sources of loss into two components: the propagation efficiency from the OPA to the photodiode, η_{p}, and the detection efficiency of the detector, η_{d}. The first is measured using a bright coherent beam and a powermeter, obtaining $\eta_{\mathrm{p}} = 0.94$. The second is taken from the specifications of the photodiode, $\eta_{\mathrm{d}} = 0.85$. While these two inefficiencies indeed reduce the observable squeezing, they do not explain the observed data on their own. In particular, the effect of linear loss (see Eq. (2.25)) does not explain the curbing of the intensity Fano factor observed in Fig. 2.14. We can make some progress by including the effect of an imperfect overlap between the pump and signal fields. We recall that the intensity Fano factor of a signal beam imperfectly overlapped with the pump can be coarsely estimated using Eq. (2.39), which considers that the overlapped fraction is

deamplified and squeezed homogeneoulsy, while the non-overlapped fraction stays the same. We use $\eta_{\mathrm{OL}} = 0.58$, the overlap coefficient that we obtained from the dependence of classical amplification/deamplification on the pump power (see Sec. 2.6.1).

Taking into account both the effect of linear losses (Eq. (2.25)) and of imperfect overlap (Eq. (2.39)), we predict the correspondence between Fano factor and classical deamplification shown in Fig. 2.14. While it qualitatively agrees with the measured data at low gains, the disagreement that we observe at high gains makes us think that a more accurate model of our OPA is required to understand its limited performance. As anticipated by our simple model of imperfect overlap (Eq. (2.39)), we expect that the existence of multiple optical modes (e.g. different spatial or temporal profiles) being squeezed inhomogeneously might lead to a reduction of the directly measurable intensity squeezing. In Chapter 3 we develop such a model.

2.6.2 Experimental demonstration of SEM

Let us now move on to describing our implementation of the second building block of our proposal: a stimulated emission microscopy setup. As we have mentioned in Sec. 2.5.1, this implementation will involve the minimum complexity necessary to test the physics of a quantum-enhanced SEM. The basic experimental configuration, illustrated in Fig. 2.15, is as follows: a homogenous sample of a dye called Brilliant Blue FCF is illuminated with a continuous-wave HeNe laser ($\lambda_{\mathrm{HeNe}} = 633$ nm). Due to the strong absorption peak of Brilliant Blue close to λ_{HeNe}, a large number of molecules in the dye get excited. Simultaneously, our pulsed Ti:Sapph laser ($\lambda_{\mathrm{Ti:Sapph}} = 820$nm), which we are not squeezing at this point, is shone onto the same sample. While the Ti:Sapph light is not absorbed by Brilliant

Blue, it still acts as a stimulation field, promoting the release of energy from the excited dye molecules in the form of light at this wavelength. The energy that is incoherently transferred from the excitation to the stimulation beam should show as a small amplification of the later.

In order to resolve this amplification signal, which is small compared to the technical noise at low frequencies, the stimulated emission interaction is modulated in time by turning the excitation HeNe laser on and off periodically at a frequency above the technical noise bandwidth (> 2MHz). To achieve this fast switching, which is out of reach of a mechanical shutter, we send the HeNe beam into an acousto-optic modulator (Gooch&Housego) whose Bragg grating is turned on and off following a high-frequency (4 MHz) square pulse train. The first diffraction order, which becomes pulsed at the AOM modulation frequency, is then allowed through an iris in order to completely isolate it from unwanted scattered light, and then sent towards the sample.

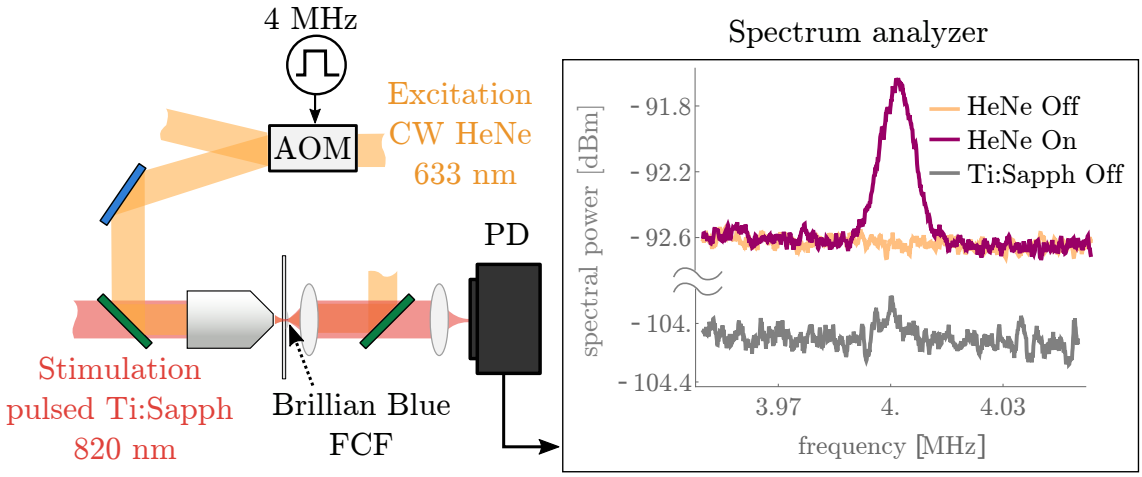


Figure 2.15: Stimulated emission microscopy setup. The periodic amplification of the stimulation beam ($P_s = 2.5$ mW) due to the temporally modulated excitation beam ($P_e = 30\mu$W) is measured with a spectrum analyzer. A peak at the modulation frequency appears over the shot noise when the excitation beam is turned on. When the stimulation beam is turned off only the electronic noise remains, verifying that this peak is due to stimulated emission and not experimental imperfections.

The excitation and stimulation beams are combined in a dichroic mirror (Semrock FF670-SDi01) and focused into the dye sample using an achromatic objective (20X Olympus Plan Achromat), both achieving a beam waist of approximately 50 μm. The high intensities of the beams in the region of the sample where they overlap allow for their efficient interaction. After collimating the two output beams with a lens, the excitation HeNe is removed using a combination of a long-pass filter (Semrock EdgeBasic 785 nm) and band-pass filter (Semrock 830 nm MaxLine, tilted for transmission at 820 nm). In order to detect the time-modulated amplification of the outcoming stimulation beam, we send this into a photodiode and measure the generated photocurrent using a spectrum analyzer. A peak of the spectral density at the AOM modulation frequency signals the presence of stimulated emission (see Fig. 2.15). We check that this peak disappears when either the excitation or stimulation beams are blocked, verifying that this signal is not caused by experimental imperfections such as leakage from the HeNe laser or electronic pick up noise. In this demonstration we only perform a static measurement of a homogeneous sample, obtaining as a result a single amplitude of the gain peak. A natural follow-up experiment would record the amplitude of this peak while scanning an inhomogeneous sample across the probe lasers. Given the dependence of the SEM signal on the density of excitable molecules, an image of the sample would be obtained.

However, we observe an unforseen phenomenon: the amplitude of the stimulated emission peak decays exponentially over time, with a time constant that becomes smaller as we increase the power of the excitation beam. This effect, refered to in the literature as photobleaching[74], occurs due to chemical alterations of the dye caused by the absorbption of light, which progressively make it unable to undergo stimulated emission. Nevertheless,

the damage does not seem to be permanent, as the SEM signal reappears after a recovery period with the excitation beam blocked. We conclude that it is necessary to operate the microscope using a power of the HeNe beam smaller than 100μW, which yields a long enough decay constant ($>$ 2 minutes) to allow experiments to be done consistently. We must note that, despite this mitigation measure, the existence of photobleaching will still pose an experimental difficulty in experiments that require long integration times.

2.6.3 Towards quantum-enhanced SEM

Having built an SEM setup and a compatible source of sub-Poissonian light, it is now time to bring the two together. As illustrated in Fig. 2.7, we deamplify of our Ti:Sapph laser in an OPA (see Sec. 2.6.1 for details), and use the resulting sub-Poissonian field as a stimulation beam for the SEM experiment. In first place, we verify that the intensity squeezing is not lost due to the non-unit transmission efficiency of the microscope objective and the dye sample ($\eta_{\text{microscope}} = 0.75$), obtaining a maximum measurable squeezing of 0.3 dB. The next step is to compare the SEM signal obtained with this intensity-squeezed probe with that obtained with a coherent probe of the same mean intensity. We expect to improve the SNR of the measurement by decreasing the intensity fluctuations in the stimulation beam.

In Fig. 2.16 we show the result of such a measurement. The average power of the stimulation beam was set to $P_s = 2$mW, ensuring shot noise limited detection, and the average power of the excitation HeNe beam was kept to 30μW in order to avoid excessive photobleaching. However, the long integration time required to resolve the difference between squeezed and non-squeezed noise ($>$ 1 min) caused the SEM signal to decay significantly during the measurement. In order to avoid this decay, we resorted to slowly scanning the

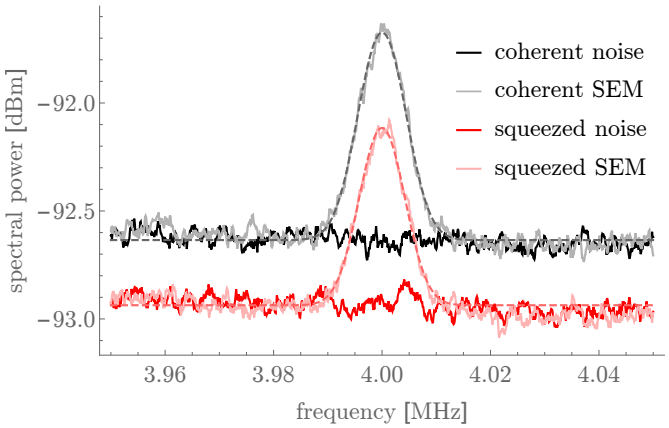


Figure 2.16: SEM signal with a coherent stimulation beam (gray) and an intensity-squeezed stimulation beam (pink). The shot noise of the probe in the absence of excitation of the dye is also shown. The SEM signals are fitted to a Gaussian model to obtain their SNR.

position of the sample (which is assumed to be homogeneous) during the measurement, thus continuously measuring non-photobleached areas.

The result of this measurement is difficult to interpret: while the intensity noise of the squeezed probe is clearly reduced compared to its coherent analog, the amplitude of the SEM signal also appears to be smaller. We quantify the change in SNR by fitting these traces to the following simple Gaussian model:

$$S(f) = N_0 + A_{\mathrm{SEM}} \exp(-\frac{(f - f_{\mathrm{AOM}})^2}{2\sigma_{\mathrm{SEM}}^2}) \tag{2.42}$$

where N_0 is the flatbackground due to electronic and shot noise, and an SEM signal at the AOM modulation frequency, f_{AOM}, and with a Gaussian envelope. The amplitude of the SEM signal, A_{SEM}, is a function of the intensity of the excitation and stimulation beams, as well as of the sample density, and its bandwidth, σ_{SEM} is just given by the resolution bandwidth of the spectrum analyzer. The parameters of the fits corresponding to a squeezed and coherent probes, shown in Fig. 2.16, are listed in Table 2.1. We see that, while the

shot noise is reduced in the squeezed case by a factor of 0.3 dB, the signal amplitude is also reduced by a factor of more than 1 dB. This behaviour could be due either to a systematic error in the measurement procedure (the experiment was repeated three times with the same result), or to an unaccounted for physical mechanism.

Table 2.1: SEM fitting parameters

	coherent	**squeezed**
N_0 [dBm]	-92.6	-92.9
A_{SEM} [dBm]	-98.7	-99.8

2.7 Summary and outlook

In this chapter we have proposed a quantum-enhanced label-free nonlinear microscopy technique: we suggest to overcome the fundamental sensitivity limit of stimulated emission microscopy by using an intensity squeezed stimulation beam. In order to achieve that, we have demonstrated a source of bright intensity squeezed sub-picosecond optical pulses, with the temporal and spatial mode specifications required by SEM. The lowest Fano factor achieved by our source is F = −0.4 dB, signaling inequivocal sub-Poissonian photon statistics. We have integrated our sub-Poissonian light source into an operating SEM setup, showing that intensity squeezing is maintained after the microscope optics. However, in preliminary experiments we have observed that the amplitude of the SEM signal is systematically reduced when we employ an intensity-squeezed probe. This decrease of the SEM signal, whose causes are yet unknown and will be the subject of future experiments, has prevented us from demonstrating a quantum enhancement in the measurement. These preliminary results prompt us to improve on the design of our sub-Poissonian light source, as its modest performance has been a limiting factor in the experiment. In Chapter 3 we introduce

a framework to simulate the photon statistics obtained from the parametric deamplification of a pulsed an focused seed, and use it to analyze the limitations of our initial design. The insight obtained from these simulations allows us to then propose a design for an improved source.

Chapter 3

Simulating and designing pulsed sub-Poissonian light sources

3.1 Motivation

The modest degree of intensity squeezing that we achieved with the OPA design implemented in the previous chapter has been a limiting factor in our endeavor to observe quantum-enhanced SEM. We would like to know what the causes reducing the OPA performance have been, and what can be done to improve on the current design. While a lot of work has been devoted over the years to describing squeezing in an OPA, most of it has considered specific cases in which some degrees of freedom of the interacting beams can be neglected. On the one hand, most accounts of pulsed squeezing have assumed that the beams are confined in a waveguide or have otherwise simplified the analysis to a single spatial dimension [36,65,75,76]. On the other hand, those analyses that consider the spatial structure of squeezed light have until recently limited their scope to a monochromatic pump beam [44,77,78]. There

are some exceptions that have considered the non-factorable spatio-temporal structure of PDC[79,80], but these have largely studied photon-pair generation and have not directly analysed the photon statistics of a pulsed coherent seed deamplified in an ultrafast OPA. More generally, the available literature focuses mostly on the generation of squeezed vacuum and its characterization through homodyne detection, and the question of direct detection of squeezed coherent states, although studied in some regimes[68,81], has received comparatively little attention.

In this section we develop a theoretical framework to model the photon statistics obtained by phase-sensitive amplification of pulsed and focused coherent states in an optical parametric amplifier. We analyze the spatio-temporal structure of parametric amplification, first considering spatial and temporal degrees of freedom of the interacting beams separately, and finally joining them into a single, more general spatio-temporal description. Drawing from Schmidt decomposition techniques, we develop a modelling framework which accommodates either description (spatial, temporal or spatio-temporal) using the same mathematical and computational tools. Thanks to the shared concepts and methods employed in the analysis of apparently different descriptions, we can draw general rules and intuitions that translate well from one to another.

Using this modelling framework we are able to quantify the effect that different propagation phenomena have on the achievable intensity squeezing. The usefulness of this unified framework is illustrated by the range of phenomena that we have been able to simulate: we consider temporal walk-off of the pump and seed pulses due to group velocity mismatch, spatial walk-off of the pump beam in a critically-phase-matched crystal, divergence of the interacting beams within a long nonlinear crystal, spatio-temporal coupling in the phase-

matching condition due to crystal birefringence, among other phenomena. At the end of the chapter, we use the insight obtained from these simulations to propose an improved design for a sub-Poissonian light source.

3.2 Hamiltonian description of optical parametric amplification

In our modelling of OPA, we will draw heavily from theoretical tools that have their origin in the study of spontaneous PDC. In fact, a single-pass OPA can be described by applying the same PDC transformation that we introduced in section 1.2.4 to an input coherent state, instead of vacuum

$$|\psi\rangle_{\text{out}} = \hat{U}_{\text{PDC}} |\alpha\rangle_{\text{in}} \tag{3.1}$$

where $|\alpha\rangle_{\text{in}}$ is a coherent state and U_{PDC} is the appropriate unitary operation to describe PDC (DFG). Here we will derive the form of U_{PDC} for the pulsed and focused type-I DFG process used in the last chapter. We will consider the interaction between two focused ultrafast pulses (signal and pump) in a slab of material with a quadratic nonlinearity (e.g. BBO). The interacting pump and signal fields have orthogonal polarizations (type-I interaction), and an efficient interaction is achieved by angle phase-matching (critical phase-matching). While the following derivation is easily generalizable to other experimental parameters, the simulations that we present here assume the particular parameters of the experimental setup in chapter 2 (e.g. dispersion characteristics of BBO).

Let us begin by briefly recalling some basic concepts regarding the Hamiltonian description of a DFG process (see section 1.2.4). The OPA interaction in a crystal with a quadratic

susceptibility is mediated by the three-wave-mixing Hamiltonian (Eq. (1.89)). We can expand the interacting fields as a sum of macroscopic, high-frequency coherent pump, and two microscopic, low-frequency signal and idler fields. We are considering a type-I downconversion process, where an e-polarized pump photon decays into two o-polarized photons. Given the polarization degeneracy of these downconverted photons, we will not distinguish between signal and idler photons, but just refer to the low-frequency field as the *signal*.

In a bulk crystal, the interacting fields are naturally expanded in terms of plane waves. Analogously to equations (1.91) and (1.93), the positive-frequency components of the pump and signal displacement fields are written respectively

$$\tilde{D}_{\mathrm{p}}^{(+)}(\mathbf{r},\omega) = \gamma_e \int \mathrm{d}^2\mathbf{q}\,\mathrm{d}\omega \exp\Big(i[\mathbf{q}\cdot\boldsymbol{\rho} + k_{e,z}(\omega,\mathbf{q})z]\Big)\ \alpha_{\mathrm{p}}(\mathbf{q},\omega) \tag{3.2}$$

$$\tilde{D}_{\mathrm{s}}^{(+)}(\mathbf{r},\omega) = \gamma_o \int \mathrm{d}^2\mathbf{q}\,\mathrm{d}\omega \exp\Big(i[\mathbf{q}\cdot\boldsymbol{\rho} + k_{o,z}(\omega,\mathbf{q})z]\Big)\ a(\mathbf{q},\omega) \tag{3.3}$$

where we use the same conventions as in sections 1.2.2 and 1.2.4. The prefactors γ_e and γ_o are normalization constants. The pump is described by its coherent amplitude α_{p}, which is normalized according to equation (1.92), and $k_{e,z}$ is its longitudinal wavenumber, where e stands for its e-polarization. We are considering parametric amplification in BBO, which is a birefringent uniaxial crystal. Therefore, the refractive index experienced by the e-polarized pump plane-waves depends not only on their frequency, but also on their propagation direction. Using the same coordinate frame of reference presented in Figure 1.1 to describe propagation in a uniaxial crystal, the longitudinal wavenumber for pump plane waves (e-waves) is written

$$k_{e,z}(\omega,\mathbf{q}) = \sqrt{k_{\mathrm{e}}^2(\omega,\theta) - |\mathbf{q}|^2} \tag{3.4}$$

where

$$k_{\mathrm{e}}(\omega,\theta) = \omega\, n_{\mathrm{ext}}(\omega,\theta)/c \tag{3.5}$$

is the wavenumber of an e-wave of frequency ω, which propagates at an angle θ with respect to the optical axis of the uniaxial crystal. We recall that the refractive index experienced by such a wave is (1.67)

$$n_{\mathrm{ext}}(\omega,\theta) = \Big(\frac{\sin^2\theta}{n_e^2(\omega)} + \frac{\cos^2\theta}{n_o^2(\omega)}\Big)^{-1} \tag{3.6}$$

where n_e and n_o are the refractive indices along the two principal axes of the crystal. The angle θ has been defined as contained in the y-z plane and is equal to θ_0 for propagation along z. In the paraxial approximation, $\theta \approx \theta_0 + q_y/k_{\mathrm{p0}}$, where q_y is the y component of the transverse wavevector $\mathbf{q}$, and we have defined the pump central wavenumber $k_{\mathrm{p0}} = k_e(\omega_{\mathrm{p0}},\theta_0)$ and the pump central frequency ω_{p0}.

The signal field is an o-wave, so its longitudinal wavenumber is simply

$$k_{o,z}(\omega,\mathbf{q}) = \sqrt{k_{\mathrm{o}}^2(\omega) - |\mathbf{q}|^2} \tag{3.7}$$

where

$$k_{\mathrm{o}}(\omega) = \omega\, n_o(\omega)/c. \tag{3.8}$$

The state of the signal fields is described by the bosonic operators $a(\mathbf{q},\omega)$, which obey the

commutation relations

$$[\hat{a}(\mathbf{q},\omega),\hat{a}^\dagger(\mathbf{q}',\omega')] = \delta(\mathbf{q}-\mathbf{q}')\,\delta(\omega-\omega') \tag{3.9}$$

$$[\hat{a}(\mathbf{q},\omega),\hat{a}(\mathbf{q}',\omega')] = [\hat{a}^\dagger(\mathbf{q},\omega),\hat{a}^\dagger(\mathbf{q}',\omega')] = 0 \tag{3.10}$$

We assume that the optical axis of the crystal is tilted such that phase-matching along the z direction is achieved for a pump with central frequency $\omega_{\mathrm{p}0}$ and a signal with central frequency $\omega_{\mathrm{s}0} = \omega_{\mathrm{p}0}/2$ such that

$$k_{e,z}(\omega_{\mathrm{p}0},\mathbf{q}=0) - 2\,k_{o,z}(\omega_{\mathrm{s}0},\mathbf{q}=0) = 0 \tag{3.11}$$

Keeping only the terms of the three-wave-mixing Hamiltonian that oscillate slowly, and performing a spatial and temporal integration over the interaction region and interaction time in a way analogous to section 1.2.4, we find that a perturbative expansion (Magnus expansion) of the unitary transformation implemented by the OPA is given by

$$\hat{U} = \exp(\hat{\mathrm{H}}_{\mathrm{int}}) \tag{3.12}$$

where the argument of the exponential is the interaction picture Hamiltonian

$$\hat{\mathrm{H}}_{\mathrm{int}} = g\int \mathrm{d}\mathbf{q}\,\mathrm{d}\mathbf{q}'\,\mathrm{d}\omega\,\mathrm{d}\omega'\,\Psi(\omega,\mathbf{q},\omega',\mathbf{q}')\,\hat{a}^\dagger(\mathbf{q},\omega)\;\hat{a}^\dagger(\mathbf{q}',\omega') + \mathrm{h.c} \tag{3.13}$$

We denote the frequencies and transverse wavevectors of the two signal fields involved in the quadratic interaction as $\omega,\mathbf{q}$ and $\omega',\mathbf{q}'$ respectively. Here, g is a dimensionless gain parameter proportional to the crystal length, L, and, analogously to the joint spectral

amplitude defined in section 1.2.4, we have defined a six-dimensional *joint amplitude* (JA)

$$\Psi(\omega,\, \mathbf{q},\, \omega',\, \mathbf{q}') = \alpha_{\mathrm{p}}(\mathbf{q}+\mathbf{q}', \omega+\omega')\,\mathrm{sinc}\Big(\frac{L}{2}\Delta k_z\Big) \tag{3.14}$$

where we have defined the momentum mismatch

$$\Delta k_z(\omega,\, \mathbf{q},\, \omega',\, \mathbf{q}') = k_{e,z}(\omega+\omega', \mathbf{q}+\mathbf{q}') - k_{o,z}(\omega, \mathbf{q}) - k_{o,z}(\omega', \mathbf{q}') \tag{3.15}$$

3.3 Heisenberg spectral input-output relations

To introduce the main ideas that will allow us to compute the evolution of a coherent state in an OPA, let us begin by considering a simple case where we neglect the effect of transverse propagation. Let us say, without further explanation for the moment, that this approximation is valid when the JA can be factored into a product of a function that depends solely on the field frequencies, and a second function that depends only on the field transverse wavevectors. In this scenario we write the input and output signal fields as

$$\begin{aligned}\tilde{D}^{(+)}_{\mathrm{in/out}}(\omega) &= \tilde{D}^{(+)}_{\mathrm{s}}(z_{\mathrm{in/out}},\, \mathbf{q}=0,\, \omega) \\ &= \gamma_o \int \mathrm{d}\omega \exp\Big(i\, k_{o,z}(\omega)\, z_{\mathrm{in/out}}\Big)\; \hat{a}_{\mathrm{in/out}}(\omega)\end{aligned} \tag{3.16}$$

with $z_{\mathrm{in}} = -L/2$ and $z_{\mathrm{out}} = L/2$, and where we are implying $\mathbf{q}_{\mathrm{s}} = \mathbf{q}_{\mathrm{i}} = 0$ in the longitudinal wavenumbers $k_{o,z}(\omega)$, and in the input/output bosonic mode operators, $\hat{a}_{\mathrm{in/out}}(\omega)$. We simplify the notation for the OPA unitary operation, neglecting its transverse wavevector dependence

$$\hat{U} = \exp\Big(g \int \mathrm{d}\omega\, \mathrm{d}\omega'\, f(\omega,\omega')\, \hat{a}^{\dagger}_{\mathrm{in}}(\omega)\hat{a}^{\dagger}_{\mathrm{in}}(\omega') + \mathrm{h.c}\Big) \tag{3.17}$$

where we have arrived at the two-dimensional joint spectral amplitude, $f(\omega,\omega')$, as the particular case of the six-dimensional joint amplitude, $\Psi(\omega,\,\mathbf{q},\,\omega',\,\mathbf{q}')$, where transverse propagation is neglected,

$$f(\omega,\omega') = \Psi(\omega,\,\mathbf{q}=0,\,\omega',\,\mathbf{q}'=0) \tag{3.18}$$

The input and output annihilation operators are then related by the Heisenberg picture input-output relations[36]

$$\hat{a}_{\text{out}}(\omega) = \hat{U}^{\dagger}\,\hat{a}_{\text{in}}(\omega)\,\hat{U} \tag{3.19a}$$

$$= \int \mathrm{d}\omega'\, C(\omega,\omega')\,\hat{a}_{\text{in}}(\omega') + \int \mathrm{d}\omega'\, S(\omega,\omega')\,\hat{a}^{\dagger}_{\text{in}}(\omega') \tag{3.19b}$$

where the transfer functions $C(\omega,\omega')$ and $S(\omega,\omega')$ define a Bogoliubov transformation of the input bosonic operators.

3.3.1 Perturbative expansion of the spectral input-output relations

The transfer functions $C(\omega,\omega')$ and $S(\omega,\omega')$ can be perturbatively calculated from the JSA by applying the formula[82]

$$e^{\hat{A}}\,\hat{B}\,e^{-\hat{A}} = \hat{B} + [\hat{A},\hat{B}] + \frac{1}{2!}[\hat{A},[\hat{A},\hat{B}]] + ... \tag{3.20}$$

to equation (3.19a), where $\hat{A} = -g\int d\omega\,\mathrm{d}\omega'\, f(\omega,\omega')\,\hat{a}^{\dagger}_{\text{in}}(\omega)\,\hat{a}^{\dagger}_{\text{in}}(\omega') + \text{h.c}$ and $\hat{B} = \hat{a}_{\text{in}}(\omega)$. Keeping only the first three terms of the expansion, and using the commutation relations in

Eq. (3.10), we obtain the perturbative input-output relations

$$\hat{a}_{\mathrm{out}}(\omega) \approx \int \mathrm{d}\omega'\, \tilde{C}(\omega,\omega')\, \hat{a}_{\mathrm{in}}(\omega') + \int \mathrm{d}\omega'\, \tilde{S}(\omega,\omega')\, \hat{a}^{\dagger}_{\mathrm{in}}(\omega') \tag{3.21}$$

where $\tilde{C}(\omega,\omega')$ and $\tilde{S}(\omega,\omega')$ are the perturbative transfer functions, given in terms of the JSA as

$$\tilde{S}(\omega,\omega') = g\Big(f(\omega,\omega') + f(\omega',\omega)\Big) \tag{3.22}$$

$$\tilde{C}(\omega,\omega') = \delta(\omega,\omega') + g^2 \int \mathrm{d}\omega'' f^*(\omega,\omega'')\tilde{S}(\omega',\omega'') + f^*(\omega'',\omega)\tilde{S}(\omega',\omega'') \tag{3.23}$$

This expansion is valid for small values of the gain parameter g, as subsequent components of the expansion (3.20) involve higher powers of g and can be neglected.

3.3.2 Non-perturbative input-output relations: Takagi factorization

A solution of the input-output transformation beyond the perturbative expansion presented above can be found by moving from the basis of monochromatic mode operators to a convenient broadband operator basis. Given that $f(\omega,\omega')$ is symmetric to the exchange of ω and ω' (see Eq. (3.14) and (3.15)), it is amenable to being decomposed using a Takagi factorization. We recall (see section 1.2.4) that the Takagi factorization is a particular case of singular value decomposition in which the basis functions that diagonalize $f(\omega,\omega')$ are symmetric

$$f(\omega,\omega') = \sum_k r_k\, \phi^{(k)}(\omega)\phi^{(k)}(\omega') \tag{3.24}$$

where $\{r_k\}$ are real and positive coefficients, and the set of broadband mode functions $\{\phi^{(k)}(\omega)\}$ forms an orthonormal basis. We can define the broadband mode operators

$$\hat{A}_{\rm in}^{(k)} = \int \mathrm{d}\omega' \, [\phi^{(k)}(\omega')]^* \, \hat{a}_{\rm in}(\omega') \tag{3.25}$$

which fulfill the standard bosonic commutation relations, $[\hat{A}^{(k)}, \hat{A}_{\rm in}^{(k')\dagger}] = \delta_{k,k'}$ and $[\hat{A}_{\rm in}^{(k)}, \hat{A}_{\rm in}^{(k')}] = [\hat{A}_{\rm in}^{(k)\dagger}, \hat{A}_{\rm in}^{(k')\dagger}] = 0$. Using the orthonormality of $\{\phi^{(k)}\}$, the unitary operation implemented by the OPA can be expressed simply as a product of independent single-mode squeezers

$$\hat{U} = \prod_k \exp\left(g\, r_k \, (\hat{A}_{\rm in}^{(k)\dagger})^2 + \text{h.c}\right) \tag{3.26}$$

such that the Heisenberg evolution of each broadband mode operator under the unitary transformation is simply

$$\hat{A}_{\rm out}^{(k)} = \hat{U}^\dagger \, \hat{A}_{\rm in}^{(k)} \, \hat{U} = \cosh(g\, r_k) \, \hat{A}_{\rm in}^{(k)} + \sinh(g\, r_k) \, \hat{A}_{\rm in}^{(k)\dagger} \tag{3.27}$$

Now we can use these solutions to compute the input-output relations for the monochromatic mode operators. Given the completeness of the basis $\{\phi^{(k)}\}$, the input monochromatic operators can be expressed as $\hat{a}_{\rm in}(\omega) = \sum_k \phi^{(k)}(\omega) \, \hat{A}_{\rm in}^{(k)}$. The output monochromatic mode operators can then be written as a sum over the evolved broadband operators

$$\hat{a}_{\rm out}(\omega) = \sum_k \phi^{(k)}(\omega) \, \hat{U}^\dagger \hat{A}_{\rm in}^{(k)} \hat{U} \tag{3.28a}$$

$$= \sum_k \phi^{(k)}(\omega) \, (\cosh(g\, r_k) \, \hat{A}_{\rm in}^{(k)} + \sinh(g\, r_k) \, \hat{A}_{\rm in}^{(k)\dagger}) \tag{3.28b}$$

where their independent evolution is granted by the diagonal form of U in this basis. We

can re-cast this equation in its integral form using the definition of the input broadband mode operators, which yields the input-output relation of equation 3.19b with

$$C(\omega,\omega') = \sum_k \phi^{(k)}(\omega)\ \phi^{(k)}(\omega')\ \cosh(g\, r_k) \tag{3.29}$$

$$S(\omega,\omega') = \sum_k \phi^{(k)}(\omega)\ \phi^{(k)}(\omega')\ \sinh(g\, r_k) \tag{3.30}$$

3.3.3 Squeezing pulsed coherent states

The input-output relations found above describe the transformation that the OPA effects on its input signal field. If the input signal is in a vacuum state, the output of the OPA will be a multimode squeezed vacuum. However, we are interested in simulating an OPA seeded with a pulsed coherent state. This coherent input is expressed in the Heisenberg picture as a displaced vacuum

$$\hat{a}_{\mathrm{in}}(\omega) = \hat{a}_{\mathrm{v}}(\omega) + \alpha_{\mathrm{in}}(\omega) \tag{3.31}$$

where $\hat{a}_{\mathrm{v}}(\omega)$ are annihilation operators acting on monochromatic vacua and, according to the definition given in equation (3.16), $\alpha_{\mathrm{in}}(\omega)$ corresponds to the spectral amplitude of the seed at the center of the nonlinear crystal. To compute the output state of the signal field, we can decompose its input monochromatic mode operators in the basis $\{\phi^{(k)}\}$ that diagonalizes the OPA interaction

$$\hat{a}_{\mathrm{in}}(\omega) = \textstyle\sum_k \phi^{(k)}(\omega)\, (\hat{A}^{(k)}_{\mathrm{v}} + c^{(k)}_{\mathrm{in}}) \tag{3.32}$$

where we have defined the broadband mode operators and broadband coherent amplitudes

$$\hat{A}_{\mathrm{v}}^{(k)} = \int \mathrm{d}\omega \, [\phi^{(k)}(\omega)]^* \, \hat{a}_{\mathrm{v}}(\omega) \tag{3.33}$$

$$c_{\mathrm{in}}^{(k)} = \int \mathrm{d}\omega \, [\phi^{(k)}(\omega)]^* \, \alpha_{\mathrm{in}}(\omega), \tag{3.34}$$

We find the ouput mode operators analogously to equation (3.28b): each of the input broadband mode operators, $\hat{A}_{\mathrm{v}}^{(k)}$, as well as the broadband coherent amplitudes, $c_{\mathrm{in}}^{(k)}$, evolve independently under a single-mode squeezing Hamiltonian. This can be conveniently written in terms of field quadratures. We define two quadratures for each broadband field operator,

$$\hat{X}_{\mathrm{v}}^{(k)} = (\hat{A}_{\mathrm{v}}^{(k)} + \hat{A}_{\mathrm{v}}^{(k)\dagger})/2, \tag{3.35}$$

$$\hat{P}_{\mathrm{v}}^{(k)} = (\hat{A}_{\mathrm{v}}^{(k)} - \hat{A}_{\mathrm{v}}^{(k)\dagger})/(2\,i), \tag{3.36}$$

whose statistical moments correspond to having independent vacuum states in each broadband mode

$$\langle \hat{X}_{\mathrm{v}}^{(k)} \hat{X}_{\mathrm{v}}^{(k')} \rangle = \langle \hat{P}_{\mathrm{v}}^{(k)} \hat{P}_{\mathrm{v}}^{(k')} \rangle = \delta_{k,k'} \tag{3.37}$$

$$\langle \hat{X}_{\mathrm{v}}^{(k)} \hat{P}_{\mathrm{v}}^{(k')} \rangle = \langle \hat{P}_{\mathrm{v}}^{(k)} \hat{X}_{\mathrm{v}}^{(k')} \rangle = 0. \tag{3.38}$$

Using the quadrature operators defined above, we can write the output monochromatic mode operators suscinctly as

$$\hat{a}_{\mathrm{out}}(\omega) = \sum_k \phi_k(\omega) \Big(\exp(-g\, r_k) \, (\mathrm{Re}\{c_k\} + \hat{X}_{\mathrm{v}}^{(k)} + i \, \exp(g\, r_k) \, (\mathrm{Im}\{c_k\} + \hat{P}_{\mathrm{v}}^{(k)} \Big) \tag{3.39}$$

making it apparent that the output of the OPA corresponds to a superposition of squeezed coherent states (see section 2.4) in the orthogonal broadband frequency modes $\{\phi^{(k)}(\omega)\}$. Given the orthogonality of $\{\phi^{(k)}\}$, the output photon statistics are easily computed. Omitting spontaneous emission, the mean of the frequency-resolved input/output photon number is

$$\left\langle \hat{n}_{\text{in/out}}(\omega) \right\rangle = \left\langle \hat{a}^{\dagger}_{\text{in/out}}(\omega)\, \hat{a}_{\text{in/out}}(\omega) \right\rangle = \Big| \sum_{k} c^{(k)}_{\text{in/out}}\, \phi^{(k)}(\omega) \Big|^2 \tag{3.40}$$

where we have defined the output coherent amplitude for the kth broadband mode

$$c^{(k)}_{\text{out}} = \exp(-g\, r_k)\, \text{Re}\{c^{(k)}_{\text{in}}\} + i\, \exp(g\, r_k)\, \text{Im}\{c^{(k)}_{\text{in}}\} \tag{3.41}$$

In addition, we compute the variance of the frequency-resolved output photon number

$$\begin{aligned} \text{var}\big(\hat{n}_{\text{out}}(\omega)\big) &= \left\langle\, (\hat{a}^{\dagger}_{\text{out}}(\omega)\hat{a}_{\text{out}}(\omega))^2 - \hat{n}^2_{\text{out}}(\omega)\, \right\rangle \\ &= \Big| \sum_{k} \phi^{(k)}(\omega) \Big(\exp(-\, g\, r_k)\, \text{Re}\{c^{(k)}_{\text{out}}\} + i\, \exp(\, g\, r_k)\, \text{Im}\{c^{(k)}_{\text{out}}\} \Big) \Big|^2 \end{aligned} \tag{3.42}$$

while the variance of the input beam is simply $\text{var}\big(\hat{n}_{\text{in}}(\omega)\big) = \langle \hat{n}_{\text{in}}(\omega) \rangle$.

Sometimes it will be more intuitive to work with the temporal representation of the optical pulses instead of with their frequency representation. We define the input/output temporal annihilation operators straightforwardly

$$\hat{a}_{\text{in/out}}(t) = \int \text{d}\omega\, \exp(i\, \omega t)\, \hat{a}_{\text{in/out}}(\omega) \tag{3.43}$$

and compute the temporally resolved output mean photon number

$$\langle \hat{n}_{\mathrm{in/out}}(t) \rangle = \langle \hat{a}^{\dagger}_{\mathrm{in/out}}(t)\, \hat{a}_{\mathrm{in/out}}(t) \rangle = \Big| \sum_k c^{(k)}_{\mathrm{in/out}}\ \phi^{(k)}(t) \Big|^2 \tag{3.44}$$

where we have defined the temporal brodband mode functions

$$\phi^{(k)}(t) = \int \mathrm{d}\omega\, \phi^{(k)}(\omega)\ \exp(i\,\omega t) \tag{3.45}$$

The temporally-resolved output photon number variance is computed analogously to Eq. (3.42), finding

$$\mathrm{var}\big(\hat{n}_{\mathrm{out}}(t)\big) = \Big| \sum_k \phi^{(k)}(t) \Big(\exp(-\,g\,r_k)\,\mathrm{Re}\{c^{(k)}_{\mathrm{out}}\} + i\ \exp(\,g\,r_k)\,\mathrm{Im}\{c^{(k)}_{\mathrm{out}}\} \Big) \Big|^2 \tag{3.46}$$

and the variance of the temporally-resolved input photon number is $\mathrm{var}(\hat{n}_{\mathrm{in}}(t)) = \langle n_{\mathrm{in}}(t) \rangle$.

3.3.4 Limits of pulsed intensity squeezing

Let us now apply this framework to simulate the type-I process that we implemented in our experiment. In first place we will compute the JSA of the interaction, which we simplify by considering that the dominant dispersion terms in the phase-matching functions are only linear and quadratic. Doing a Taylor expansion of the longitudinal momentum mismatch, Δk_z, up to second order in the signal frequencies yields [36]

$$\Delta k_z = (\Omega + \Omega')(\frac{1}{v_e} - \frac{1}{v_o}) + \frac{1}{2}(\Omega + \Omega')^2 \beta_{2,e} - \frac{1}{2}(\Omega^2 + \Omega'^2)\beta_{2,o} \tag{3.47}$$

where we have defined the detunings $\Omega = \omega - \omega_{s,0}$ and $\Omega' = \omega' - \omega_{s,0}$. We have also defined the group velocities

$$v_o = (\partial_\omega k_{\rm o}(\omega)|_{\omega_{\rm s0}})^{-1} \quad , \quad v_e = (\partial_\omega k_{\rm e}(\omega,\theta_0)|_{\omega_{\rm p0}})^{-1} \tag{3.48}$$

as well as the group velocity dispersion parameters

$$\beta_{2,o} = \partial^2_\omega\, k_{\rm o}(\omega)|_{\omega_{\rm s0}} \quad , \quad \beta_{2,e} = \partial^2_\omega\, k_{\rm e}(\omega,\theta_0)|_{\omega_{\rm p0}} \tag{3.49}$$

To further simplify the JSA, we assume a Fourier-limited pump with a Gaussian spectral amplitude

$$\alpha_{\rm p}(\omega) = \sqrt[4]{\frac{2N_{\rm p}^2\,\tau_{\rm p}^2}{\pi}}\exp\Big(-\tau_{\rm p}^2\,(\omega-\omega_{\rm p,0})^2\Big) \tag{3.50}$$

where $N_{\rm p}$ is the pump photon number, $\tau_{\rm p}$ is the standard deviation of the temporal pulse intensity, and $\omega_{\rm p0}$ is the pump central frequency. We can now compute the JSA corresponding to our BBO crystal ($L = 300\mu$m) using equations (3.14) and (3.50). In Fig. 3.1 we show the JSA expected for our source, decomposed in its constituent pump and phase matching functions.

We will now proceed to compute the photon statistics of a seed beam after it has evolved due to the OPA transformation. We will consider Fourier-limited Gaussian seed pulses, possibly delayed from the pump

$$\alpha_{\rm in}(\omega) = \sqrt[4]{\frac{2N_{\rm s}^2\,\tau_{\rm s}^2}{\pi}}\exp\Big(-\tau_{\rm s}^2\,(\omega_{\rm s}-\omega_{\rm s,0})^2\Big)\,\exp\Big(i\,t_0\,(\omega-\omega_{\rm s0})\Big) \tag{3.51}$$

where $N_{\rm s}$ is the seed photon number, $\tau_{\rm s}$ is the standard deviation of the temporal pulse

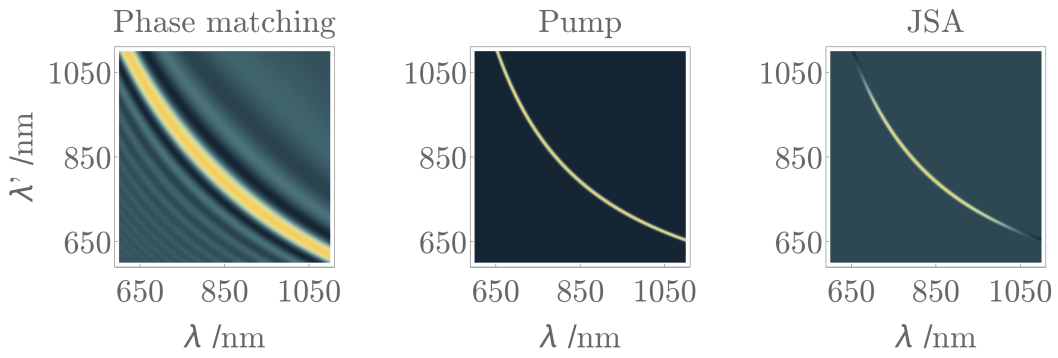


Figure 3.1: Joint spectral amplitude for a 300 μm-long BBO crystal, tilted for degenerate phase matching at $\lambda_{p0} = 410$nm. The pump pulse duration is $\tau_p = 60$ fs (FWHM of wavelength-resolved intensity = 2 nm). The curvature of the pump function is due to the relation between frequency and wavelength.

intensity, ω_{s0} is the seed central frequency and t_0 is the delay with respect to the pump at the center of the crystal.

Optimum pulse lengths

The relatively simple model that we have laid out already allows us to test a number of relevant physical situations. Let us begin by considering again a question that we introduced in section 2.5.3: what is the effect of having pump and seed pulses with different durations? Using the very simple model introduced in section 2.5.3 (see equation (2.39)) we concluded that, if the seed pulse is longer than the pump, a large intensity squeezing is unachievable due to the unsqueezed temporal wings of the seed. Now we can use the tools that we have developed in this section to provide a more rigorous answer.

We set simulation parameters closely replicating our experimental setup. The BBO crystal length is $L = 300\,\mu$m and the duration of the pump pulses is $\tau_p = 60$ fs ($\sim$ 2nm bandwidth). As illustrated in Fig. 3.2, we first consider seed pulses longer than the pump ($\tau_s = 100$ fs, bandwidth ~ 5 nm) and then shorter ($\tau_s = 50$ fs, bandwidth ~ 10 nm). The

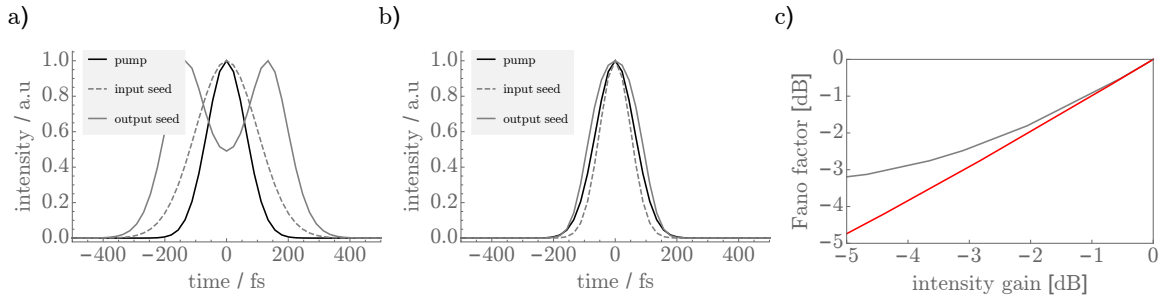


Figure 3.2: a,b) Deamplified seed intensity profile (normalized to unit peak) computed for a seed pulse longer than the pump (a) and shorter (b). We show the input seed pulse and pump pulse for reference. c) Intensity gain (G) and Fano factor (F) for a range of pump mean photon numbers. While G and F are approximately equal for the short seed pulses (red), the Fano factor curbs at high gains for long seed pulses (gray).

crystal length is short enough that temporal walk-off is negligible. In Fig. 3.2.a,b we show that, indeed, the longer seed pulses are deamplified unevenly, while the short seed pulses are uniformly deamplified.

Recalling that the total intensity gain (G) and Fano factor (F) can be calculated from the mean and variance of the time-resolved photon number respectively as

$$G = \frac{\int dt \left\langle n_{\text{out}}(t) \right\rangle}{\int dt \left\langle n_{\text{in}}(t) \right\rangle} \quad , \quad F = \frac{\int \mathrm{d}t \, \mathrm{var}\big(n_{\text{out}}(t)\big)}{\int \mathrm{d}t \left\langle n_{\text{out}}(t) \right\rangle}, \tag{3.52}$$

in Fig. 3.2.c we scan the value of the pump photon number N_{p}, and plot the Fano factor against the mean intensity deamplification. We confirm that the Fano factor of the longer seed pulses curbs at high interaction gains, limiting the amount of achievable intensity squeezing. This effect is not so strong in the shorter seed pulses.

Tolerance to pulse delays

In addition to having different durations, the seed and pump pulses can be slightly delayed from each other due to experimental imperfections. Assuming a crystal shorter than the pulse lengths, we expect that such a delay will reduce the amount of seed deamplification, and therefore its intensity squeezing, due to the imperfect mode overlap. We can test this intuition using our model: taking a short crystal ($L = 10\,\mu$m) and a seed and pump pulses with matched lengths ($\tau_\mathrm{p} = \tau_\mathrm{s} = 60$ fs), we set a pump photon number which yields an intensity deamplification of 3 dB in the absence of delay, and then scan the delay between the pump and seed pulses (t_0 in equation (3.51)). The results are shown in Fig. 3.3. As expected, both the intensity amplification (G) and the Fano factor (F) achieve their minima at zero delay, and go up when the delay between the two pulses is equal to the pulse durations, reaching a value of 1 (0 dB) when the overlap between the pulses is zero. The required spatial resolution to synchronize the arrival time of two sub-picosecond pulses by extending the optical path of one of them is in the order of the tens of micrometers. This is achievable with current linear translation stages, which have a typical spatial resolution of $\sim 1\,\mu$m.

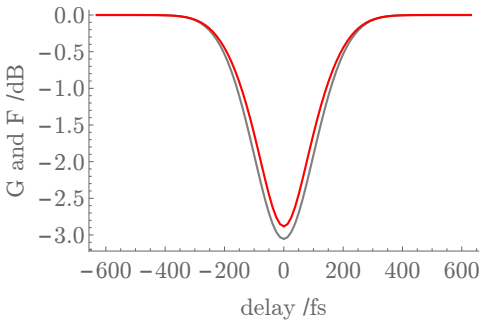


Figure 3.3: Intensity gain, G (gray line), and Fano factor, F (red line), of a pulsed seed ($\tau_\mathrm{s} = 60\mu$m) delayed from the pump ($\tau_\mathrm{p} = 60\mu$m). G and F decay when the two pulses are delayed by a time equal to the pulse lengths.

Maximum crystal length

Let us consider a different question. Given a certain choice of pulse lengths and pump power, it is common to enhance the nonlinear interaction by using longer nonlinear crystals. However, given the group velocity mismatch between the pump and seed pulses, there exists a maximum crystal length after which the two pulses will walk-off and stop "seeing each other". How does this limit squeezing? Moreover, when the crystal is so long that the pulses walk-off from each other as they propagate inside it, some of the points that we made earlier become invalid. For instance, the effect of unequal pulse lengths for the seed and pump might differ from the short crystal case, as now the pulses can effectively walk over each other as they propagate through the crystal.

To test this situation we consider a seed and pump with unequal pulse lengths ($\tau_{\mathrm{p}} = 60$ fs and $\tau_{\mathrm{s}} = 100$ fs), set the pump photon number to achieve an intensity gain of -3 dB for a crystal length of ~ 1 mm, and then proceed to scan the crystal length. In Fig. 3.4 we show our results. As expected, the intensity gain and Fano factor decrease initially due to the higher interaction strength implied by a longer crystal. However, the two begin to plateau for crystal lengths longer than

$$L_{\text{walk-off}} = 2\sqrt{2}(\tau_{\mathrm{s}}^2 + \tau_{\mathrm{p}}^2)/(1/v_{\mathrm{s}} - 1/v_{\mathrm{p}})^2, \tag{3.53}$$

which corresponds to the crystal length for which the overlap between the two pulses is reduced by a factor of two after propagation. Interestingly, something else occurs for crystals longer than $L_{\text{walk-off}}$: the initial asymmetry between intensity gain and Fano factor, which arises due to the difference in pulse lengths, begins to decrease. A hint to explain this

behaviour is found in Fig. 3.4.b, where we show the temporally-resolved intensity of the deamplified pulses for different crystal lengths. While for $L < L_{\text{walk-off}}$ the pulses are deamplified unevenly (more in the center, less in the wings), this is not the case for $L > L_{\text{walk-off}}$. In the later case, the pump pulse walks over the seed as it propagates through the crystal, ensuring that there are no "temporal wings" which do not experience the nonlinear interaction.

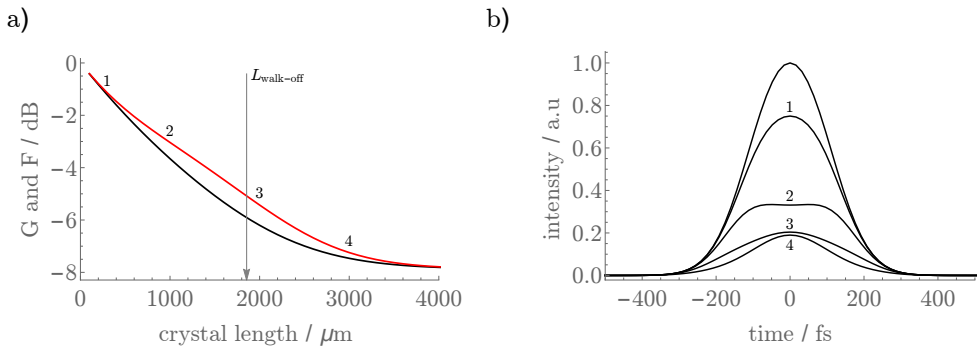


Figure 3.4: Scanning the crystal length. a) Shows the intensity gain, G (black line), and Fano factor, F (red line) of a pulsed seed ($\tau_s = 100$ fs) after interacting with a temporally shorter pulsed pump ($\tau_p = 60$ fs) over a varying crystal length. The magnitude of G and F initially grow due to the longer interaction length, but begin to saturate after $L_{\text{walk-off}}$. The asymmetry between G and F becomes smaller for long crystals, as the pump pulse walks over the seed pulse. b) Temporal envelope of the deamplified pulse intensities. The indices 1-4 label pulses with the corresponding G and F values in a). For short crystal lengths, the seed pulses are deamplified unevenly (e.g. pulse 2), whereas this is not the case for longer crystal lengths (e.g. pulse 4) due to the pump walking over the seed.

The experimental insight that we obtain is the following: in pulsed OPA we can use crystals longer than the walk-off length without further implications than limiting the effective interaction length to the walk-off length. In fact, employing a longer crystal can compensate for the detrimental effect of using unequal pulse lengths.

3.4 Heisenberg spatial input-output relations

The tools that we have developed to analyze the spectral structure of squeezing can be used, with very few modifications, to study its transverse spatial structure. Let us now neglect the spectral degrees of freedom in the OPA transformation, considering positive-frequency monochromatic input and output signal fields of the form

$$\tilde{D}^{(+)}_{\mathrm{in/out}}(\mathbf{r}) = \tilde{D}^{(+)}_{\mathrm{s}}(z_{\mathrm{in/out}},\, \boldsymbol{\rho},\, \omega_{\mathrm{s}0}) \tag{3.54}$$

$$= \gamma_o \int \mathrm{d}^2\mathbf{q}\, \exp\Big(i\,[\mathbf{q}\cdot\boldsymbol{\rho} + k_{o,z}(\mathbf{q})\, z_{\mathrm{in/out}}]\Big)\, \hat{a}(\mathbf{q}) \tag{3.55}$$

where now we are implying that the frequency at which we evaluate the bosonic operators, as well as the longitudinal wavenumbers (recall (3.7)), is the seed central frequency $\omega_{\mathrm{s}0}$. The positions at which these fields are defined are again $z_{\mathrm{in}} = -L/2$ and $z_{\mathrm{out}} = L/2$. We express the OPA unitary in a simplified notation, omitting its frequency dependence

$$\hat{U} = \exp\Big(g \int \mathrm{d}\mathbf{q}\, \mathrm{d}\mathbf{q}'\, h(\mathbf{q},\mathbf{q}')\, \hat{a}^\dagger(\mathbf{q})\, \hat{a}^\dagger(\mathbf{q}') + \mathrm{h.c}\Big) \tag{3.56}$$

where we have defined a function $h(\mathbf{q},\mathbf{q}')$ which, analogously to the joint spectral amplitude, corresponds to the particular case of the six-dimensional joint amplitude (3.14)

$$h(\mathbf{q},\mathbf{q}') = \Psi(\omega = \omega_{\mathrm{s}0},\, \mathbf{q},\, \omega' = \omega_{\mathrm{s}0},\, \mathbf{q}') \tag{3.57}$$

This function, which couples mode operators with different transverse wavevectors, will be referred to as the *joint angular amplitude* (JAA). In the spontaneous regime, this function determines the correlation between transverse wavenumber (propagation angle) of the emit-

ted photon pairs. Analogously to the joint spectral amplitude, the JAA can be expressed as a product of a pump function and a phase matching function (recall equation (3.14))

$$h(\mathbf{q},\mathbf{q}') = \alpha_{\mathrm{p}}(\mathbf{q}+\mathbf{q}')\,\mathrm{sinc}\Big(\frac{L}{2}\Delta k_z(\mathbf{q},\mathbf{q}')\Big) \tag{3.58}$$

where we omit the spectral dependence in equations (3.2) and (3.15) by using the shorthand notation $\alpha_{\mathrm{p}}(\mathbf{q}) = \alpha_{\mathrm{p}}(\omega_{\mathrm{p}} = 2\omega_{\mathrm{s}0}\,,\,\mathbf{q}_{\mathrm{p}})$ for the pump coherent amplitude and

$$\Delta k_z(\mathbf{q},\mathbf{q}') = k_{e,z}(2\omega_{\mathrm{s}0},\mathbf{q}+\mathbf{q}') - k_{o,z}(\omega_{\mathrm{s}0},\mathbf{q}) - k_{o,z}(\omega_{\mathrm{s}0},\mathbf{q}') \tag{3.59}$$

for the transverse momentum mismatch. The momentum mismatch can be conveniently expanded in a power series in $\mathbf{q}$ and $\mathbf{q}'$, keeping only low-order terms. Recalling the dispersion relations experienced by the pump and signal beams (equations (3.11) and (3.7)), we approximate the transverse momentum mismatch as (see Appendix B)

$$\Delta k_z(\mathbf{q},\mathbf{q}') \approx -\frac{|\mathbf{q}-\mathbf{q}'|^2}{4k_{\mathrm{s}0}} + \rho_{\mathrm{wo}}\,(q_y + q_y') \tag{3.60}$$

where we recall that q_y and q_y' are respectively the y projections of $\mathbf{q}$ and $\mathbf{q}'$, and we have defined the signal central wavenumber $k_{\mathrm{s}0} = k_o(\omega_{\mathrm{s}0})$ and the pump walk-off angle (recall section 1.2.2)

$$\rho_{\mathrm{wo}} = \frac{\partial n_{\mathrm{ext}}(\omega_{\mathrm{p}},\theta)}{\partial\theta}\Big|_{\theta_0}\frac{1}{n_{\mathrm{ext}}(\omega_{\mathrm{p}},\theta_0)} \tag{3.61}$$

3.4.1 Separation of transverse directions

Let us begin by assuming that the input mode operators $\hat{a}(\mathbf{q})$ evolve independently along the two transverse directions, q_x and q_y. Thus, we will transform bosonic operators labelled by a single transverse wavenumber, $\hat{a}(q_{x/y})$, assuming that the value of the orthogonal wavenumber is set to zero. This is a valid approximation whenever the JAA can be factored into a product of two functions coupling only mode operators with the same transverse direction

$$h(\mathbf{q},\, \mathbf{q}') = h_x(q_x, q_x')\, h_y(q_y\, q_y') \tag{3.62}$$

such that we can treat each direction independently, solving two independent unitary transformations

$$\hat{U} = \exp\left(g \int \mathrm{d}q_j\, \mathrm{d}q_j'\, h_j(q_j,\, q_j')\, \hat{a}^\dagger(q_j)\, \hat{a}^\dagger(q_j') + \mathrm{h.c}\right) \tag{3.63}$$

for $j \in \{x, y\}$. Let us from here on drop the explicit dependence on j to avoid cluttering, as in this section the transverse direction that we are considering (independently) will always be clear from the context. Under these circumstances, the structure of (3.63) is identical to that of the spectral unitary transformation analyzed in the previous section (3.17). This unitary generates a Bogoliubov transformation analogous to (3.19b) and can also be decomposed using a Takagi factorization (again, note the symmetry of the JA (3.14)).

Let us present the notation that we will use to describe these transformations very briefly, directing the reader to the previous section for a more complete discussion of the parallel frequency transformations. The OPA transforms the mode operators according to

$$\hat{a}_{\mathrm{out}}(q) = \int \mathrm{d}q'\, C(q, q')\, \hat{a}_{\mathrm{in}}(q') + \int \mathrm{d}q'\, S(q, q')\, \hat{a}_{\mathrm{in}}^\dagger(q') \tag{3.64}$$

where the transfer functions $C(q,q')$ and $S(q,q')$ can be expressed in terms of the "broadband modes" and squeezing parameters obtained by performing a Takagi factorization of the joint angular amplitude,

$$h_j(q,q') = \sum_k r_k \, \phi^{(k)}(q) \, \phi^{(k)}(q') \tag{3.65}$$

such that

$$C(q,q') = \textstyle\sum_k \phi^{(k)}(q) \, \phi^{(k)}(q') \;\; \cosh(g\, r_k) \tag{3.66}$$

$$S(q,q') = \textstyle\sum_k \phi^{(k)}(q) \, \phi^{(k)}(q') \;\; \sinh(g\, r_k) \tag{3.67}$$

We consider a seeded OPA where the seed is described as a displaced vacuum

$$\hat{a}_{\mathrm{in}}(\mathbf{q}) = \hat{a}_{\mathrm{v}}(\mathbf{q}) + \alpha_{\mathrm{in}}(\mathbf{q}) \tag{3.68}$$

where a_{v} are annihilation operators referred to the vacuum state and α_{in} is the seed transverse wavevector coherent amplitude, which we assume can be factorized as

$$\alpha_{\mathrm{in}}(\mathbf{q}) = \alpha_{\mathrm{in,y}}(q_x) \, \alpha_{\mathrm{in,y}}(q_y), \tag{3.69}$$

where $\alpha_{\mathrm{in,x}}$ and $\alpha_{\mathrm{in,y}}$ are in general different, but from now on we will denote them with the shorthand notation $\alpha_{\mathrm{in}}(q)$ for either. Now we can decompose these coherent amplitudes in the basis of broadband modes that diagonalize the OPA transformation, finding the input amplitudes

$$c_{\mathrm{in}}^{(k)} = \int dq \, [\phi^{(k)}(q)]^* \alpha_{\mathrm{in}}(q) \tag{3.70}$$

which evolve independently under the OPA transformation into the output coherent amplitudes

$$c_{\text{out}}^{(k)} = \exp(-g\, r_k)\, \text{Re}\{c_{\text{in}}^{(k)}\} + i\, \exp(g\, r_k)\, \text{Im}\{c_{\text{in}}^{(k)}\} \tag{3.71}$$

Analogously, we can express $\hat{a}_{\text{v}}$ in the basis that diagonalizes the OPA transformation, and find that the mean of the momentum-resolved photon number at the input/output is

$$\langle \hat{n}_{\text{in/out}}(q) \rangle = \langle \hat{a}_{\text{in/out}}^{\dagger}(q)\, \hat{a}_{\text{in/out}}(q) \rangle = \Big| \sum_k c_{\text{in/out}}^{(k)}\, \phi^{(k)}(q) \Big|^2 \tag{3.72}$$

and the variance of the momentum-resolved photon number at the output is

$$\text{var}\big(\hat{n}_{\text{out}}(q)\big) = \Big| \sum_k \phi^{(k)}(q) \Big(\exp(-\,g\, r_k)\, \text{Re}\{c_{\text{out}}^{(k)}\} + i\, \exp(\,g\, r_k)\, \text{Im}\{c_{\text{out}}^{(k)}\} \Big) \Big|^2 \tag{3.73}$$

We will often find it useful to work with the spatial representation of the input-output seed beams, which are described by the Fourier transforms of the transverse-momentum mode operators

$$\hat{a}_{\text{in/out}}(x) = \int \text{d}q_x \exp(i\, xq)\, \hat{a}_{\text{in/out}}(q) \tag{3.74}$$

and analogously for the y coordinate. The mean of the spatially-resolved photon number at the input/output are thus

$$\langle \hat{n}_{\text{in/out}}(x) \rangle = \langle \hat{a}_{\text{in/out}}^{\dagger}(x)\, \hat{a}_{\text{in/out}}(x) \rangle = \Big| \sum_k c_{\text{in/out}}^{(k)}\, \phi^{(k)}(x) \Big|^2 \tag{3.75}$$

and the variance of the spatially-resolved photon number at the output is

$$\mathrm{var}\big(n_{\mathrm{out}}(x)\big) = \Big| \sum_k \phi^{(k)}(x) \left(\exp(-\,g\,r_k)\,\mathrm{Re}\{c_{\mathrm{out}}^{(k)}\} + i\,\exp(\,g\,r_k)\,\mathrm{Im}\{c_{\mathrm{out}}^{(k)}\}\right)\Big|^2 \tag{3.76}$$

where we have defined the spatial brodband mode functions

$$\phi^{(k)}(x) = \int \mathrm{d}\omega\, \phi^{(k)}(q)\, \exp(i\,qx) \tag{3.77}$$

3.4.2 Ordinary axis input-output relations: no walk-off

We will first analyze the transformation of the mode operators describing the transverse field along the direction of the ordinary axis (in our convention, the x direction), where no spatial walk-off occurs. The JAA along this direction is simply

$$h_x(q,q') = \alpha_{\mathrm{p}}(q+q')\,\mathrm{sinc}\Big(-\frac{L}{2}\frac{|q-q'|^2}{4k_{\mathrm{s0}}}\Big) \tag{3.78}$$

We assume a pump with a Gaussian profile, focused at the center of the crystal

$$\alpha_{\mathrm{p}}(q) = \sqrt{\frac{2N_{\mathrm{p}}\,W_{\mathrm{p}}^2}{\pi}}\,\exp\Big(-W_{\mathrm{p}}^2\,|q|^2\Big) \tag{3.79}$$

where W_{p} is the standard deviation of the spatial intensity profile and N_{p} is the number of photons in a pump pulse. Under these assumptions, we can compute $h_x(q,q')$ for BBO crystals of different lengths, using pump beams of different widths (see Fig. 3.5)

Similarly to the pump beam, we assume an input seed beam with a Gaussian profile, but allow for its focus to be offset from that of the pump both in the transverse and longitudinal

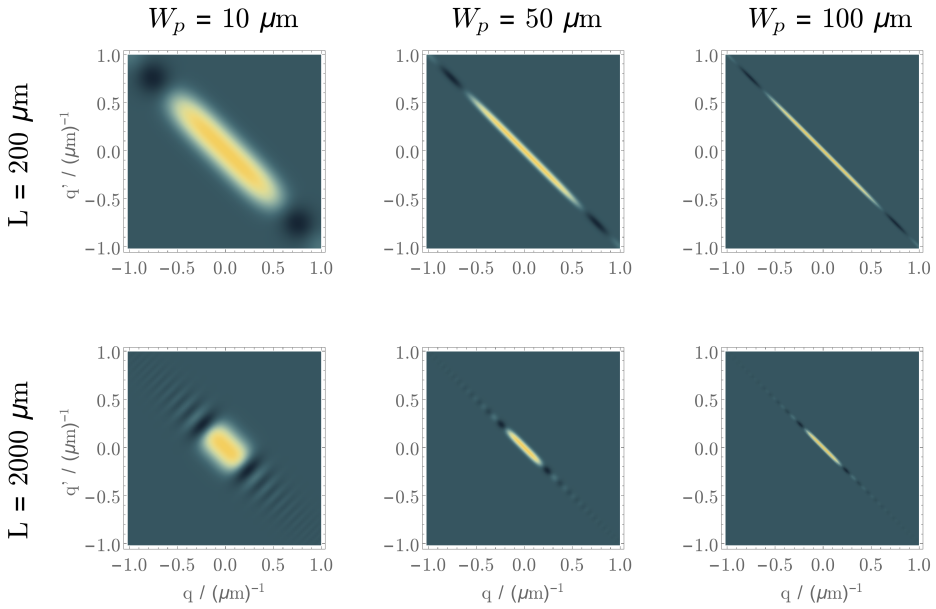


Figure 3.5: Joint angular amplitude along the ordinary axis ($h_x(q, q')$) for BBO crystals of different lengths, using pump beams of different widths. Crystals are tilted for degenerate phase matching at $\lambda_{\mathrm{p0}} = 410\mathrm{nm}$.

directions. The coherent amplitude of the input seed beam is then

$$\alpha_{\mathrm{in}}(q) = \sqrt{\frac{2N_{\mathrm{s}}\,W_{\mathrm{s}}^2}{\pi}}\,\exp\Big(-W_{\mathrm{s}}^2\;q^2\Big)\;\exp\Big(i\,(x_0\,q + \frac{z_0}{2k_{\mathrm{s0}}}q^2)\Big) \tag{3.80}$$

where N_{s} is the photon number in a seed pulse, W_{s} is the standard deviation of the seed spatial intensity profile, x_0 is the transverse spatial offset from the center of the pump beam, and z_0 is the longitudinal offset (along z) of the seed focus. In the following, we will assume that the intensity gain and the Fano factor are defined respectively as

$$G = \frac{\int \mathrm{d}x\,\langle \hat{n}_{\mathrm{out}}(x)\rangle}{\int \mathrm{d}x\,\langle \hat{n}_{\mathrm{in}}(x)\rangle} \quad , \quad F = \frac{\int \mathrm{d}x\,\mathrm{var}\big(\hat{n}_{\mathrm{out}}(x)\big)}{\int \mathrm{d}x\,\langle \hat{n}_{\mathrm{out}}(x)\rangle} \tag{3.81}$$

Beam waists: overlap vs beam divergence

With this notation in place, we can begin to simulate a number of physical scenarios of interest. We start by looking into the influence of the choice of beam waists on the achievable intensity deamplification and squeezing. In section 2.5.4 we noted that previous studies have mentioned a tradeoff between using a seed waist larger or smaller than that of the pump. While the first can be used to fulfill the Boyd-Kleinman condition, the later seems to be required to obtain a complete overlap between the pump and seed beams. Here we show that our simulations indeed reflect this tradeoff.

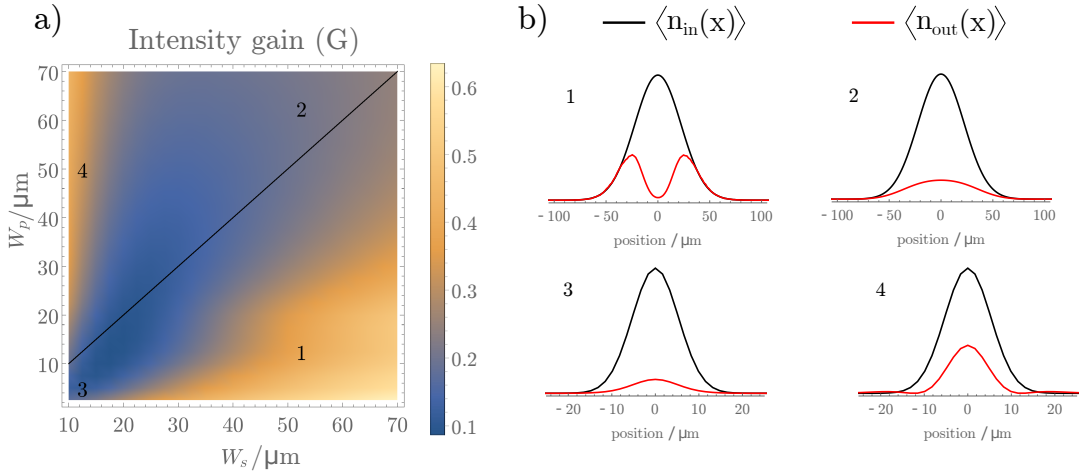


Figure 3.6: a) Intensity gain, G (linear scale), for a range of pump and seed beam waists (W_p and W_s). The black line indicates $W_p = W_s$. Recall that smaller values of G correspond to larger deamplification. b) Samples of the deamplified spatially-resolved intensity (red line) compared with the input intensity (black line). The labels 1-4 correspond to those points marked in a), and reflect distinct regimes of the OPA.

In Fig. 3.6.a we present the intensity gain, G, obtained for a range of pump and seed beam waists (W_p and W_s), using the same pump photon number. In Fig. 3.7.a we present the Fano factor, F, obtained in the same simulations. These simulations assume a seed focus is not offset from that of the pump ($x_0 = z_0 = 0$). The crystal length has been chosen to be long

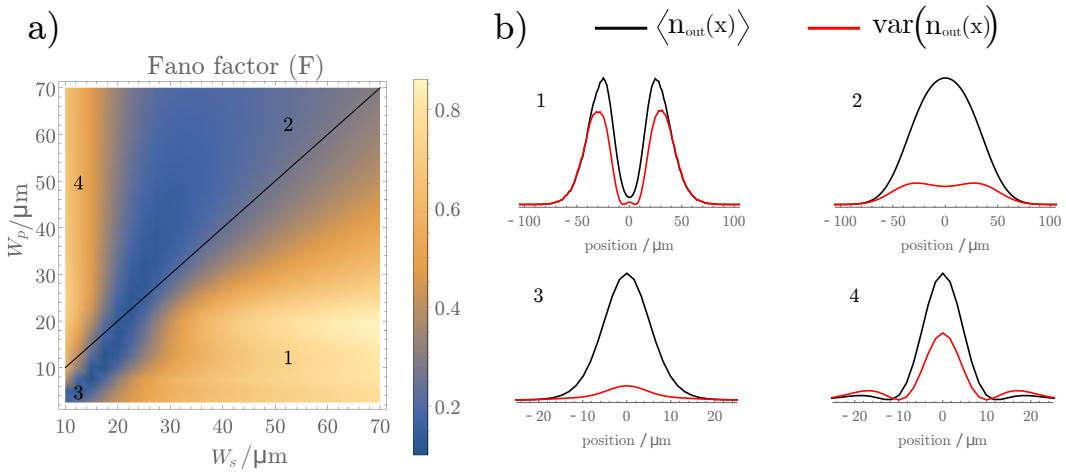


Figure 3.7: a) Fano factor, F (linear scale), for a range of pump and seed beam waists (W_p and W_s). The black line indicates $W_\mathrm{p} = W_\mathrm{s}$. b) Samples of the deamplified spatially-resolved intensity variance (red line) compared with the output intensity mean (black line). The labels 1-4 correspond to those points marked in a), and reflect distinct regimes of the OPA.

($L = 5$mm) in order to observe beam divergence. Significant divergence within the crystal occurs when its length is longer than the Rayleigh range of the beams, which is the case for $W_\mathrm{p} < 20\mu$m and $W_\mathrm{s} < 28\mu$m. We observe that for small beam waists of the pump and seed (e.g. point 3), where divergence is the strongest, maximum deamplification occurs when the seed waist is bigger ($\sim$ by a factor of $\sqrt{2}$) than that of the pump, fulfilling the Boyd-Kleinman condition. In contrast, for large beam waists (e.g. point 2) beam divergence becomes negligible, and more deamplification is obtained by using $W_\mathrm{p} > W_\mathrm{s}$. Our interpretation of these phenomena is supported by the samples of the spatially-resolved output intensity shown in Fig. 3.6.b and the samples of the spatially-resolved output intensity variance shown in Fig. 3.7.b. Samples 2 and 3 correspond to optimum beam waists for the large and small waist regimes respectively. Sample 1 corresponds to $W_\mathrm{p} < W_\mathrm{s}$ in the small-divergence regime, where the characteristic uneven deamplification is observed. Sample 4 corresponds to a scenario where the seed diverges considerably throughout the crystal but the pump

does not. Note that the spatial wings are amplified instead of deamplified, as a result of the non-flat spatial phase that the seed accumulates as it propagates through the crystal, which reverses the direction of the parametric gain in the wings.

In our experiment, we encounter a situation closest to point 2, where divergence is negligible and therefore we set the pump beam width to be larger than the seed beam width in order to maximize the overlap. The scenario is the same in the experiment of Wenger et al.[71], where they find that the optimal pump waist is a factor of $\sqrt{2}$ bigger than the waist of the seed. Given that they use a very short crystal where divergence is negligible, their conclusion agrees with our results.

Maximum crystal length

A question that arises naturally is: what is the maximum crystal length that we can employ efficiently given the limits imposed by beam divergence? This is coupled with a second consideration: what is the optimal choice of beam waists given a particular crystal length? Luckily, we can use the insights from last section to answer that. As the crystal becomes longer than the Rayleigh range of the beams, the optimal beam waist for the seed will be $\sqrt{2}$ larger than that of the pump. In Fig. 3.8 we show both the intensity gain (G) and the Fano factor (F) obtained for a range of crystal lengths and seed beam waists. We have fixed the pump waist to $W_{\mathrm{p}} = 17\,\mu$m in order to observe beam divergence for reasonably short crystal lengths ($<$ 1cm). We find that it is possible to increase both G and F monotonically with L for crystal lengths up to and beyond 8 mm, which is much longer than the maximum crystal length allowed by temporal walk-off. Optimum deamplification and squeezing at such long crystal lengths occurs using seed beams larger than the pump ($W_{\mathrm{s}} > 20\mu$m), which is not a

technical limitation.

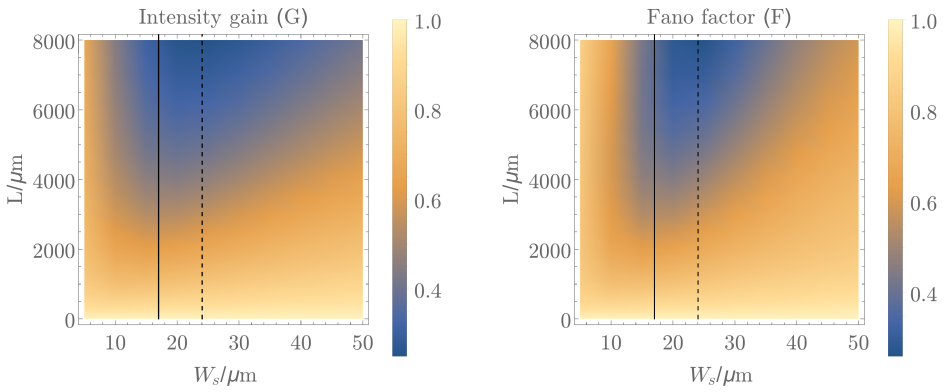


Figure 3.8: Intensity gain and Fano factor obtained for a range of crystal lengths and seed beam waists. The solid vertical line marks the pump waist ($W_\mathrm{p} = 17\mu$m), whereas the dashed vertical line denotes $\sqrt{2}W_\mathrm{p}$

Tolerance to focal point offset

The next question that we can tackle is: what is the effect of a misalignment between the foccii of the pump and seed beams? While the consequences of a transverse misalignment seem straightforward (reduction in G and F due to imperfect overlap), the effect of a longitudinal misalignment is less intuitive. In figures 3.9.a and 3.10.a we show respectively the intensity gain, G, and the Fano factor, F, considering a seed with a range of transverse (x_0) and longitudinal (z_0) spatial offsets between the foccii of the pump and the seed. In figures 3.9.b and 3.10.b we show a representative selection of the mean and variance of the output spatially resolved photon number. These simulations assume a short crystal ($L = 300\,\mu$m), and a pump waist equal to the seed waist ($W_\mathrm{p} = W_\mathrm{s} = 17\,\mu$m). The pump photon number is chosen to obtain a maximum G of $\sim$ -3 dB.

Considering first the effect of a transverse offset ($z_0 = 0$), we oberve that, not too

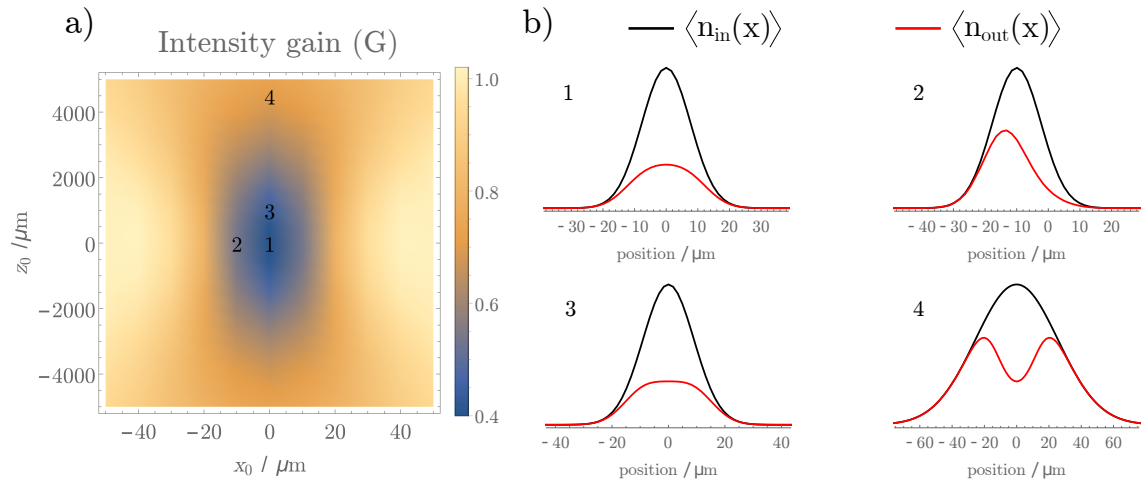


Figure 3.9: a) Intensity gain for a range of transverse (x_0) and longitudinal (z_0) spatial offsets between the foccii of the pump and the seed. b) Samples of the deamplified spatially-resolved intensity (red line) compared with the input intensity (black line). The labels 1-4 correspond to those points marked in a).

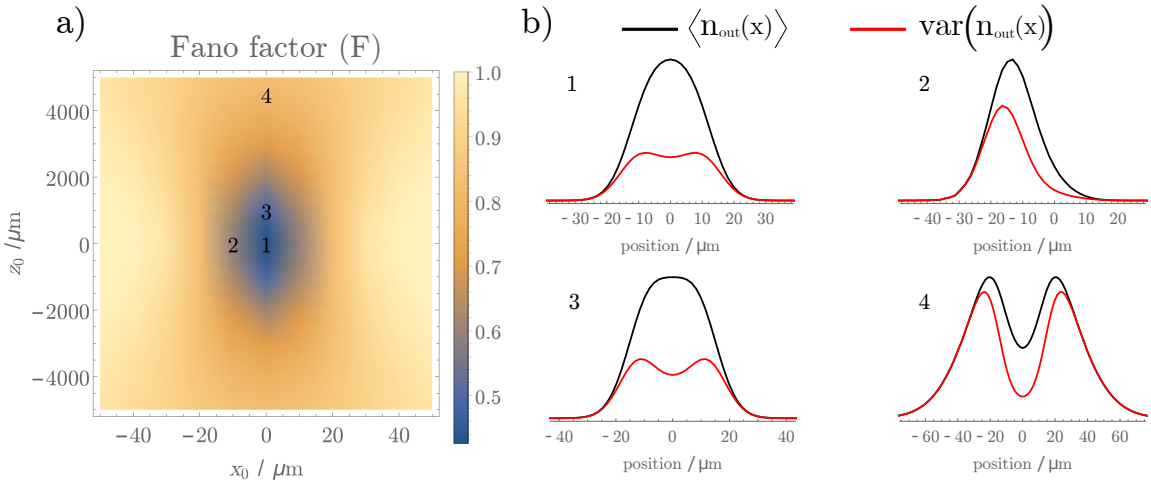


Figure 3.10: a) Fano factor for a range of transverse (x_0) and longitudinal (z_0) spatial offsets between the foccii of the pump and the seed. b) Samples of the deamplified spatially-resolved intensity variance (red line) compared with the output mean intensity (black line). The labels 1-4 correspond to those points marked in a).

surprisingly, both G and F decay when the offset is of the order of the beam waists ($x_0 \sim W_{\mathrm{p/s}}$). Sample 1 corresponds to two centered foccii and shows a uniform deamplification and squeezing of the seed. Sample 2 corresponds to a seed that is laterally offset from the pump by approximately one beam waist, which shows in a skewing of the deamplification

and squeezing. Considering now only a longitudinal offset between the foccii ($x_0 = 0$), we observe that G and F decay for an offset approximately equal to one Rayleigh range of the pump ($z_{\text{Rayleigh}} = 3500\mu\text{m}$). Samples 3 and 4 correspond respectively to $z_0 < z_{\text{Rayleigh}}$ and $z_0 > z_{\text{Rayleigh}}$. The later shows an uneven deamplification and squeezing, both more pronounced at the center of the beam. This is interpreted as due to the non-flat phase of the seed, which causes the wings of the beam to experience parametric amplification with a different phase than the center. Our results for both transverse and longitudinal offsets of the foccii are consistent with common intuition.

3.4.3 Extraordinary axis input-output relations: spatial walk-off

Let us now consider the evolution of the mode operators corresponding to the field transverse direction along the extraordinary axis. Let us recall that we are considering a critically-phase-matched BBO crystal, where the polarization of the pump is not aligned with a principal axis. The angular gradient of the refractive index experienced by the pump causes it to walk-off at an angle ρ_{wo} in the transverse direction as it propagates (recall section 1.2.2). In BBO tilted for degenerate type-I phase-matching at 800 nm, the walk-off angle is $\rho_{\text{wo}} \approx 3°$. It is reasonable to expect that this pump walk-off will influence the spatial structure of the OPA gain. The mode operators $\hat{a}(q_y)$ are transformed by the unitary operation given in Eq. (3.63), with a joint angular amplitude

$$h_y(q, q') = \alpha_{\text{p}}(q + q') \,\text{sinc}\Big(- \frac{L}{2}\big(\frac{|q - q'|^2}{4k_{\text{s0}}} - \rho_{\text{wo}}\,(q + q')\big)\Big) \tag{3.82}$$

which indeed differs from the joint angular amplitude along the ordinary axis (Eq. (3.63)) by the presence of a second argument in the phase-matching function. This difference arises precisely due to the pump walk-off. Again, assuming a pump with the Gaussian spatial profile given in equation (3.79), we can compute the joint angular amplitude in Eq. (3.82). In Fig. 3.11 we show that, while for short crystals (e.g. $L = 200\mu$m) this JAA does

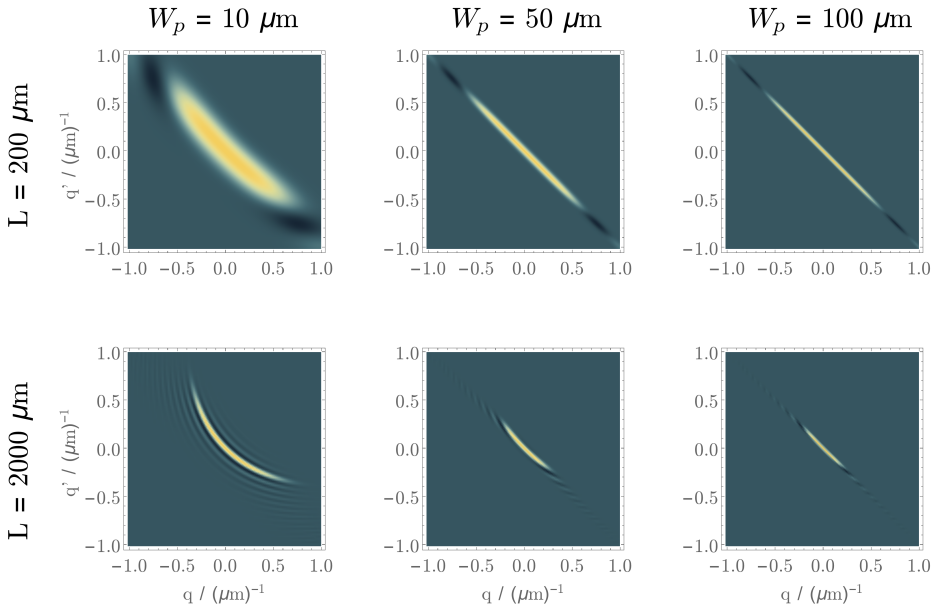


Figure 3.11: Joint angular amplitude along the extraordinary axis ($h_y(q, q')$) for BBO crystals of different lengths, using pump beams of different widths. Crystals are tilted for degenerate phase matching at $\lambda_{\mathrm{p0}} = 410$nm.

not differ much from that corresponding to the ordinary axis (recall figure 3.5), the JAAs corresponding to longer crystals have a distinctive curvature due to the additional walk-off term in the phase matching. In what follows we will analyze the impact that this has on parametric deamplification.

Maximum crystal length

Given that the pump field drifts laterally as it propagates through the crystal, it can be expected that there will be a maximum crystal length beyond which the seed and pump beams will walk-off from each other and stop interacting. Assuming a seed field with the same Gaussian spatial profile given in equation (3.80), and employing the same techniques and definitions used previously, in Fig. 3.12 we compute the intensity gain and Fano factor obtained for a range of crystal lengths and seed beam waists. We fix a pump waist $W_{\mathrm{p}} = 60\mu$m, which corresponds that used in our experimental implementation, and assume no offset between the foccii ($x_0 = z_0 = 0$). We find that the magnitude of both G and F initially increase with crystal length due to the longer interaction region, but eventually saturate. We show that saturation occurs approximately along the curve

$$L_{\text{walk-off}} = \frac{2\sqrt{\log(2)}}{\rho_{\text{wo}}}\sqrt{W_{\mathrm{p}}^2 + W_{\mathrm{s}}^2}, \tag{3.83}$$

which corresponds to the length for which the overlap between the two Gaussian field amplitudes decays by a factor of 2. We observe that given the seed waist that we used in our experiment ($W_{\mathrm{s}} = 40\mu$m), our choice of crystal length ($L = 300\mu$m) was a bit shorter than what could be used efficiently.

3.5 Heisenberg spatio-temporal input-output relations

Until now we have considered the spectral and spatial evolution of the seed field in the OPA independently, assuming constant values of either its frequency or its transverse wavevectors. This is not a complete description of an ultrafast OPA, where the spectral and spatial

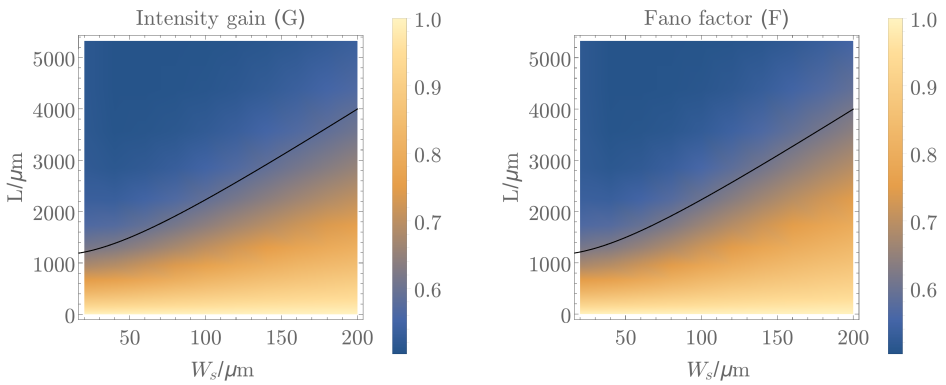


Figure 3.12: Intensity gain and Fano factor for a range of crystal lengths (L) and seed beam waists (W_s). The pump waist is fixed to $W_\mathrm{p} = 60\mu$m. The black line marks $L_{\text{walk-off}}$ beyond which the overlap between the seed and pump amplitudes decays by a factor of 2.

degrees of freedom can be correlated. One way in which such correlation arises is through the angular gradient of the refractive index experienced by the pump, which translates into an angle-dependent phase-matching condition.

3.5.1 The origin of space-time coupling

In order to show from where this spatio-temporal correlation originates, let us now consider a general OPA process where we take into account the frequencies of the interacting fields, as well as their propagation angle (transverse wavevenumber) along the y direction, which corresponds to the spatial walk-off direction. We will introduce the required notation briefly, directing the reader to the previous sections for a detailed explanation of the intermediate steps. The unitary operation that describes such an OPA is (recall (3.12) and (3.14))

$$\hat{U} = g \int \mathrm{d}q\, \mathrm{d}q'\, \mathrm{d}\omega\, \mathrm{d}\omega'\, \psi(\omega, q, \omega', q')\, \hat{a}^\dagger(\omega, q)\, \hat{a}^\dagger(\omega', q') + \mathrm{h.c} \tag{3.84}$$

where we are implying $q = q_y$, and assume that $q_x = 0$. We have defined the 4-dimensional joint amplitude

$$\psi(\omega, q, \omega', q') = \alpha_{\mathrm{p}}(\omega + \omega', q + q') \operatorname{sinc}\Big(\frac{L}{2}\Delta k_z\Big) \tag{3.85}$$

where L is the length of the nonlinear crystal and $\alpha_{\mathrm{p}}(q, \omega)$ is a 2D pump coherent amplitude which describes both its frequency and its transverse momentum (recall (3.2)). The momentum mismatch is

$$\Delta k_z(\omega, q, \omega', q') = k_{e,z}(\omega + \omega', q + q') - k_{o,z}(\omega, q) - k_{o,z}(\omega', q') \tag{3.86}$$

where we recall that $k_{e,z}$ and $k_{o,z}$ are the longitudinal wavenumbers of respectively and e-wave and an o-wave, which depend both on the frequency and transverse wavenumber of the field, as defined in (3.7) and (3.11). We can expand Δk_z as a power series in ω, ω', q and q', keeping only the non-negligible low order terms

$$\Delta k_z \approx (\Omega + \Omega')(\frac{1}{v_e} - \frac{1}{v_o}) + \frac{1}{2}(\Omega + \Omega')^2 \beta_{2,e} - \frac{1}{2}(\Omega^2 + \Omega'^2)\beta_{2,o} \tag{3.87}$$

$$- \frac{|q - q'|^2}{4k_{\mathrm{s0}}} + \rho_{\mathrm{wo}}\,(q_y + q'_y) \tag{3.88}$$

where we recall from previous sections that we have defined the signal central frequency ω_{s0}, the detunings $\Omega = \omega - \omega_{s,0}$ and $\Omega' = \omega' - \omega_{s,0}$, the group velocities v_o and v_e, as well as the group velocity dispersion parameters for an o-wave, $\beta_{2,o}$, and for an e-wave, $\beta_{2,e}$. Propagation of the pump along the z direction occurs at an angle from the optical axis $\theta = \theta_0$, and ρ_{wo} is the pump walk-off angle. For the rest of this section we will assume a pump with factorable Gaussian temporal and spatial profiles, which is described by the

coherent amplitude

$$\alpha_{\mathrm{p}}(\omega, q) = \sqrt{\frac{2N_{\mathrm{p}}W_{\mathrm{p}}\tau_{\mathrm{p}}}{\pi}} \exp\Big(- W_{\mathrm{p}}^2 \ |q|^2 \Big) \ \exp\Big(- \tau_{\mathrm{p}}^2 \ (\omega - \omega_{\mathrm{p},0})^2 \Big) \tag{3.89}$$

The explicit expansion of the momentum mismatch that we have provided makes the coupling between spatial and spectral degrees of freedom apparent: the phase mismatch involved by a large frequency detuning can be cancelled by a phase-mismatch of opposing sign due to angular detuning.

As a sanity check, we show that we can retrieve previous results regarding space-time coupling in PDC. In a series of articles [79,80,83] it was shown that phase-matched PDC emission can occur for both small and large emission angles of the signal and idler photons, provided that their frequencies become more detuned from frequency degeneracy as a function of their propagation angle. An example of this kind of space-time correlation, dubbed X-entanglement in the literature because of the characteristic shape of the phase-matching curve, is shown in Fig. 3.13.a. This figure shows a 2D cut of the 4D joint amplitude, $\psi(\omega_{\mathrm{s}0} + \Omega, q, \omega_{\mathrm{s}0} - \Omega, -q)$, where the frequencies and transverse wavenumbers of the two signal fields are symmetrically detuned from degeneracy. Indeed, we confirm the behaviour described earlier: the value of the joint amplitude, and thus the number of spontaneously emitted photons, remains high for arbitrarily large correlated detunings of the frequency and emission angle. We note, however, that this type of space-time coupling can hardly affect our experiment: the correlations between frequency and propagation angle occur only for wavelength detunings greater than 100 nm, much larger than those involved in our experiment.

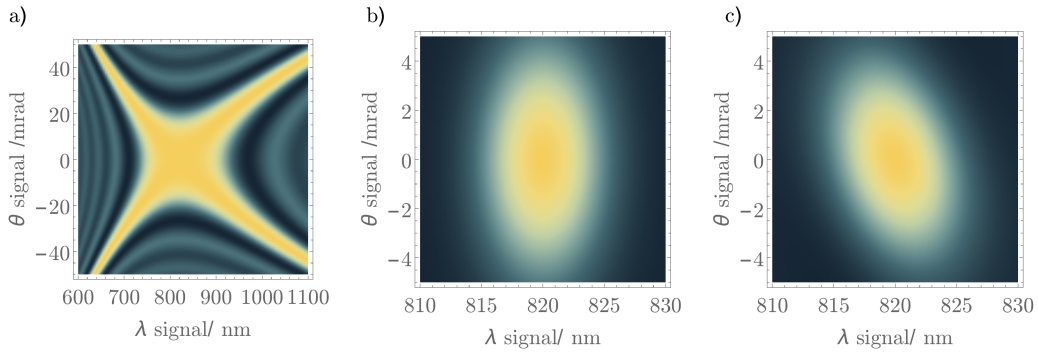


Figure 3.13: Two-dimensional cuts of the four-dimensional joint amplitude $\psi(\omega, q_y, \omega', q'_y)$. For the sake of intuition, frequencies are expressed in terms of wavelengths ($\omega = 2\pi c/\lambda$) and transverse wavenumbers in terms of propagation angles ($q_y = \theta/k_o(\omega_{s0})$). These cuts correspond to a $L = 1$ mm BBO crystal, pumped with a beam with central wavelength $\lambda_{p0} = 410$ nm, pulse duration $\tau_p = 60$fs ($\sim$ 2nm bandwidth) and beam waist $W_p = 60\mu$m . a) Symmetric cut of the joint amplitude, $\psi(\omega_{s0} + \Omega, q_y, \omega_{s0} - \Omega, -q_y)$. b) Asymmetric cut of the joint amplitude, $\psi(\omega_{s0} + \Omega, q_y, \omega_{s0}, 0)$, with no pump walk-off, $\rho_{wo} = 0$. c) Asymmetric cut of the joint amplitude, $\psi(\omega_{s0} + \Omega, q_y, \omega_{s0}, 0)$, with pump walk-off, $\rho_{wo} = 3°$

However, we find that correlation between the spatial and temporal degrees of freedom also occurs over a much smaller frequency bandwidth in a critically phase-matched process. In such a crystal, the first order derivative of the pump refractive index with respect to its propagation angle is non-zero, which produces a strong coupling between the propagations angle and frequencies of the phase-matched SPDC photons. While this correlation does not show in the symmetric 2D cut of ψ presented previously, in Fig. 3.13.b and 3.13.c we consider the asymmetric cut of the joint amplitude, $\psi(\omega, q_y, \omega_{s0}, 0)$, which does reflect this phenomenon. We see that, while in the absence of angular gradient of the pump refractive index ($\rho_{wo} = 0$) the joint amplitude shows no correlations, this changes when we introduce the refractive index gradient corresponding to critically phase-matched BBO ($\rho_{wo} = 3°$). The correlation between emission angle and wavelength occurs over a bandwidth of less than 5 nm, which is much smaller than the correlation bandwidth of X-entanglement and

comparable with the bandwidth of our seed pulses. We expect this feature of the joint amplitude to translate into a correlated spatio-temporal structure of the deamplification (squeezing) generated by the OPA.

3.5.2 Spatio-temporal modal decomposition

Now that we have motivated the need for a joint description of the OPA spatial and spectral degrees of freedom, we proceed to aply such a description to compute the photon statistics of a seed beam after the OPA interaction. To that effect, we evolve the input field bosonic operators analogously to how we proceeded in previous sections

$$\hat{a}_{\mathrm{out}}(\omega, q) = \hat{U}^{\dagger}\, \hat{a}_{\mathrm{in}}(\omega, q)\, \hat{U} \tag{3.90}$$

with $\hat{U}$ defined in (3.84), and where we recall that we are implying the spatial label y in the transverse wavenumber. Computing the evolution of the mode operators $\hat{a}_{\mathrm{in}}$, which depend on a spectral and a spatial variables, appears like a different problem than the single-dimensional cases that we have treated until now. However, we can "flatten" the matrices describing $\hat{a}_{\mathrm{in}}$ and $\hat{a}_{\mathrm{out}}$, writing

$$\hat{a}_j^{(\mathrm{in/out})} = \hat{a}_{\mathrm{in/out}}(\omega_{\mathrm{floor}(j/N_q)},\, q_{j \bmod N_q}) \tag{3.91}$$

$$q_j = \Delta q\ (j - N_q/2) \tag{3.92}$$

$$\omega_j = \omega_{\mathrm{s0}} + \Delta\omega\ (j - N_\omega/2) \tag{3.93}$$

where the subindex j indicates a vector index, 'mod' is the modulo function, 'floor' is the function that returns the greatest integer smaller than its argument. We have defined the discretized frequencies ω_k, and discretized transverse wavenumbers q_k, where $\Delta\omega, \Delta q$ are the discretization steps, and N_ω, N_q are the number of points for each variable. We can discretize and flatten the joint amplitude $\psi(\omega, q, \omega', q')$ analogously, re-casting the 4D tensor as a 2D matrix

$$\psi_{i,j} = \psi(\omega_i, q_i, \omega_j, q_j)\ \Delta q^2\, \Delta\omega^2 \tag{3.94}$$

where the subindices i, j indicate matrix indices and we use the same definition for the discretized frequencies and transverse wavenumber as before.

Using this flattened representation, we can solve for the evolution of the discretized mode operators using the same tools as in previous sections. We find the Takagi decomposition of the flattened joint amplitude

$$\psi_{i,j} = g \sum_k r_k\, \phi_i^{(k)}\, \phi_j^{(k)} \tag{3.95}$$

where we have defined "broadband modes", $\phi_i^{(k)}$, that form a convenient basis where the input seed operators evolve independently under the effect of a single-mode squeezing transformation. These broadband modes can be cast back in the form of 2D matrices (2D functions), where we can visualize their spectral and spatial structure

$$\phi^{(k)}(\omega_i, q_j) = \phi^{(k)}_{i\, N_q + j} \tag{3.96}$$

It is interesting to compare the structure of the broadband modes obtained when we

neglect the pump spatial walk-off (Fig. 3.14) with those obtained when we consider it (Fig. 3.14). While the first can be factored into the tensor product of a spectral and a spatial amplitudes, the second shows a correlated space-time structure and cannot be factored.

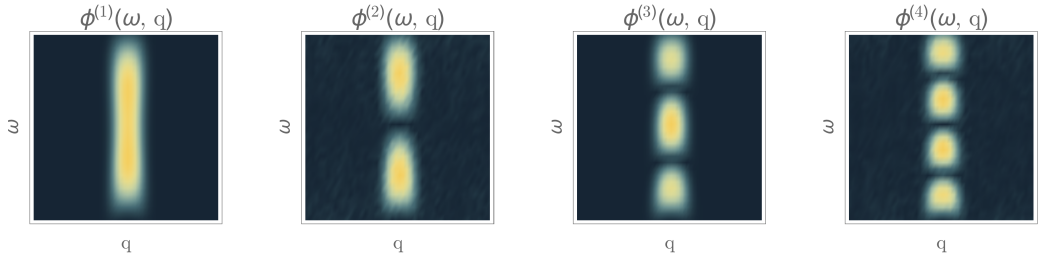


Figure 3.14: First four broadband modes $\phi^{(k)}(\omega, q)$ which diagonalize the 4D joint amplitude $\psi(\omega, q, \omega', q')$ when pump spatial walk-off is omitted. The joint amplitude corresponds to a BBO crystal with $L = 1$mm, pumped by a beam with $\lambda_{\mathrm{p}0} = 410$nm, $\tau_{\mathrm{p}} = 60$ fs, $W_{\mathrm{p}} = 40\mu$m and $\rho_{\mathrm{wo}} = 0$

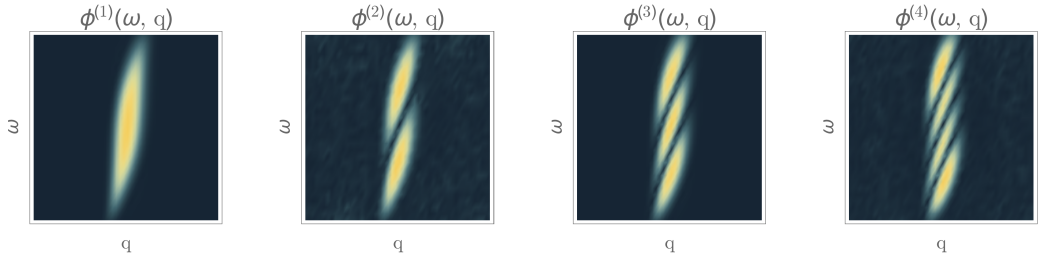


Figure 3.15: First four broadband modes $\phi^{(k)}(\omega, q)$ which diagonalize the 4D joint amplitude $\psi(\omega, q, \omega', q')$ when pump spatial walk-off is included. The joint amplitude corresponds to a BBO crystal with $L = 1$mm, pumped by a beam with $\lambda_{\mathrm{p}0} = 410$nm, $\tau_{\mathrm{p}} = 60$ fs, $W_{\mathrm{p}} = 40\mu$m and $\rho_{\mathrm{wo}} = 3°$

3.5.3 Output photon statistics

Once we have computed the Takagi factorization of the joint amplitude, we can find the output photon statistics for a coherent seed using the same techniques that we employed earlier. We consider input mode operators

$$\hat{a}_{\mathrm{in}}(\omega, q) = \hat{a}_{\mathrm{v}}(\omega, q) + \alpha_{\mathrm{in}}(\omega, q) \tag{3.97}$$

where $\hat{a}_{\rm v}$ are annihilation operators referred to a vacuum state and $\alpha_{\rm in}(\omega,q)$ is the coherent amplitude of the seed. For the remaining of this section we will assume a seed with Gaussian temporal and spatial profiles, propagating collinearly with the pump and with no delay or focus offset from it

$$\alpha_{\rm in}(\omega,q)=\sqrt{\frac{2N_{\rm s}W_{\rm s}\tau_{\rm s}}{\pi}}\exp\Big(-W_{\rm s}^2\ |q_{\rm s}|^2\Big)\ \exp\Big(-\tau_{\rm s}^2\ (\omega_{\rm s}-\omega_{\rm s0})^2\Big) \tag{3.98}$$

We find the seed decomposition in the broadband basis that diagonalizes the OPA interaction

$$c_k^{\rm in}=\int d\omega\, dq\ [\phi_k(\omega,q)]^*\,\alpha_{\rm in}(\omega,q) \tag{3.99}$$

and compute the output coherent amplitudes after the interaction

$$c_k^{\rm out}=\exp(-g\,r_k)\,{\rm Re}\{c_k^{\rm in}\}+i\,\exp(g\,r_k)\,{\rm Im}\{c_k^{\rm in}\} \tag{3.100}$$

The mean and variance of the frequency and momentum resolved photon number after the interaction are respectively

$$\big\langle\hat{n}_{\rm out}(\omega,q)\big\rangle=\big\langle\hat{a}_{\rm out}^\dagger(\omega,q)\,\hat{a}_{\rm out}(\omega,q)\big\rangle=\Big|\sum_k c_k^{\rm out}\,\phi^{(k)}(\omega,q)\Big|^2 \tag{3.101}$$

$${\rm var}\big(\hat{n}_{\rm out}(\omega,q)\big)=\Big|\sum_k \phi^{(k)}(\omega,q)\,\Big(\exp(-\,g\,r_k)\,{\rm Re}\{c_k^{\rm out}\}+i\,\exp(\,g\,r_k)\,{\rm Im}\{c_k^{\rm out}\}\Big)\Big|^2 \tag{3.102}$$

Again, we will find it useful to use the time/space representation of the pulses instead of their frequency/momentum representation. We define the time and space resolved in-

put/output annihilation operators

$$\hat{a}_{\text{in/out}}(t,y) = \int \mathrm{d}\omega\,\mathrm{d}q\,\exp(i(\omega\,t + q\,y))\,\hat{a}_{\text{in/out}}(\omega,q) \tag{3.103}$$

and find the mean and variance of the spatially and temporally resolved output photon number

$$\left\langle \hat{n}_{\text{out}}(t,y)\right\rangle = \left\langle \hat{a}^{\dagger}_{\text{out}}(t,y)\,\hat{a}_{\text{out}}(t,y)\right\rangle = \left|\textstyle\sum_k c_k^{\text{out}}\,\phi^{(k)}(t,y)\right|^2 \tag{3.104}$$

$$\text{var}\big(\hat{n}_{\text{out}}(t,y)\big)) = \left|\textstyle\sum_k \phi^{(k)}(t,y)\left(\exp(-\,g\,r_k)\,\text{Re}\{c_k^{\text{out}}\} + i\,\exp(\,g\,r_k)\,\text{Im}\{c_k^{\text{out}}\}\right)\right|^2 \tag{3.105}$$

where we have defined the space-time broadband functions

$$\phi^{(k)}(t,y) = \int \mathrm{d}\omega\,\mathrm{d}q\,\exp(i(\omega t + qy))\,\phi^{(k)}(\omega,t) \tag{3.106}$$

3.5.4 Space-time coupling limits squeezing

With these definitions in place, we can compute the output photon statistics of a seed undergoing pulsed OPA, where we account for the effect of the space-time correlation of the phase-matching due to the crystal birefringence. In particular, we are interested in finding if there are any limits on the achievable squeezing which we could not capture with the one-dimensional descriptions that we have used until now.

To begin with, let us provide some intuition regarding the effect that phase-matching space-time correlations have on the structure of the OPA process. In Fig. 3.16 we show the output spatio-temporal mean photon number, $\left\langle \hat{n}_{\text{out}}(t,y)\right\rangle$, for a deamplified seed. The pump and seed beam waists have been chosen to optimize squeezing in the short-crystal

regime ($W_\mathrm{p} = 40\mu\mathrm{m} > W_\mathrm{s} = 30\mu\mathrm{m}$), which is justified by the crystal length, $L = 2$ mm. Moreover, the lengths of the seed and pump pulses ($\tau_\mathrm{p} = 60$ fs , $\tau_\mathrm{s} = 50$ fs) have been chosen to prevent inhomogenous temporal deamplification. We observe that, as the intensity gain grows, it becomes apparent that the seed is still being deamplified inhomogeneously, in a correlated space-time manner.

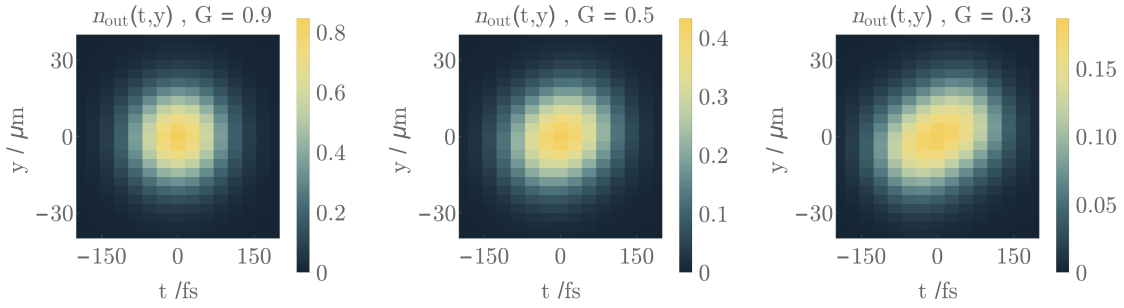


Figure 3.16: Spatio-temporally resolved mean photon number of a deamplified seed with three different values of the intensity gain (G = 0.9, 0.5 and 0.3).

At this point, we are acquainted with the following rule of thumb: an inhomogeneous deamplification of the seed implies a multimode process with a reduced rate of intensity squeezing. In order to quantify the degradation of squeezing due specifically to phase-matching space-time correlations we can compare the Fano factor and intensity gain obtained using either the one-dimensional descriptions presented before or the more general 2D spatio-temporal description presented here (temporal description: (3.44) and (3.46) , spatial description: (3.75) and (3.76), spatio-temporal description: (3.104) and (3.105)).

In Fig 3.17 we perform this comparison for three different crystal lengths, using the same temporal durations and spatial beam waists for the pump and seed as listed above. Computing the Fano factor and intensity deamplification obtained using either description,

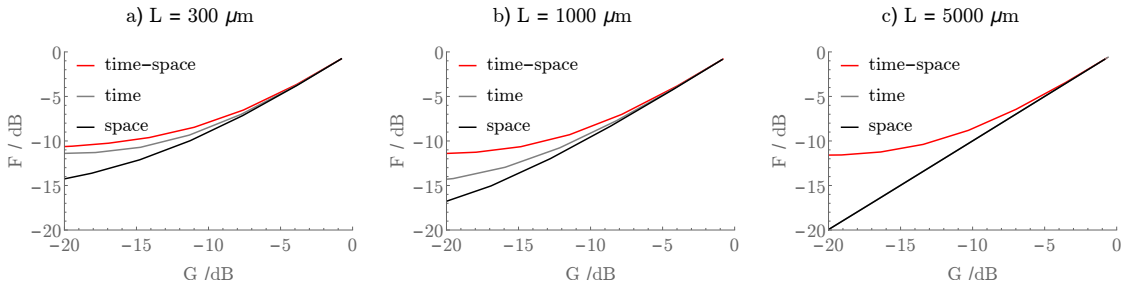


Figure 3.17: Fano factor (F) as a function of intensity gain (G) obtained using a description of the OPA that includes: temporal gain dependence only (black), spatial gain dependence only (gray), spatio-temporal gain dependence (red).

we see that, as expected, the joint spatio-temporal description always yields a lower level of squeezing for the same intensity deamplification. It is interesting to note that, for longer crystal lengths, both the temporal and spatial descriptions predict $F \approx G$, whereas the spatio-temporal description does not. This is explained in the following way: the main reason to have $F < G$ for the temporal and spatial descriptions, in the regime that we are probing, is the imperfect overlap between pump and seed. As explained earlier, this imperfect overlap disappears when the crystal is long enough that the two beams walk over each other as they propagate. However, this mitigation strategy does not apply when we consider the complete spatio-temporal description: the imperfect overlap due to correlated spatio-temporal deamplification is not compensated for by spatial or temporal walk-off.

3.6 An improved design

In this chapter we have developed a framework to simulate the photon statistics of the coherent squeezed states generated by parametric deamplification of pulsed and focused coherent states. Throughout the chapter, we have analyzed the effect that several phenomena have

on the achievable squeezing. Now we will condense the insight that we have gained into an improved design for a sub-Poissonian light source, which will be implemented in a future experiment in order to achieve a greater degree of intensity squeezing.

Avoid critical phase-matching — The OPA used in our experimental implementation (chapter 2) employed a critically phase-matched (angle phase-matched) BBO crystal because of the ease with which this design could be built. However, in this chapter we have shown that the phase-matching condition in critically phase-matched OPAs is modified due to the non-zero first order derivative of the pump refractive index, $n_{\text{ext}}(\omega, \theta)$, with respect to the pump propagation direction. This leads to two main limitations: in first place, we have shown that it is not possible to enhance the degree of deamplification/squeezing by using a crystal longer than the spatial walk-off distance, after which the pump and seed beams stop interacting. Second, we have shown that the angular dependence of the phase-matching condition couples the spatial and angular degrees of freedom of the OPA, in such a way that a seed with a spectrum uncorrelated from its spatial profile cannot be deamplified uniformly. This uneven deamplification leads to a reduction of intensity squeezing which cannot be compensated for.

We suggest to avoid these limitations by employing non-critical phase-matching, where the phase-matching condition is achieved for a pump and seed whose polarizations are aligned with two principal axes of the crystal. In this configuration, the first order derivative of $n_{\text{ext}}(\omega, \theta)$ with respect to the pump propagation angle is zero, avoiding pump walk-off as well as spatio-temporal coupling in the phase-matching condition. This condition can be obtained in certain crystals using temperature tuning[71]. Alternatively, we can achieve quasi-phase-matching by using a periodically poled nonlinear crystal.

Our design for an improved OPA will be based on a periodically poled potassium titanyl phosphate (ppKTP) crystal. The strongest element of the second order susceptibility of KTP is[84] $\chi^{(2)}_{zzz}$, which corresponds to type-0 phase-matching with both pump and seed having the same polarization. We can compute the momentum mismatch for a pump ($\lambda_{\rm p} = 410$nm) and seed ($\lambda_{\rm s} = 820$nm) propagating along this direction of the crystal, and compute the poling period necessary to achieve phase-matching. Using the Sellmeier equations of KTP [85], we compute the pump and seed refractive indices ($n_z(\omega_{\rm p}) = 1.95$ and $n_z(\omega_{\rm s}) = 1.84$), from which we calculate the distance after which the direction of the OPA process is reversed

$$L_{\rm poling} = \left(\frac{n_z(\omega_{\rm p})}{\lambda_{\rm p}} - \frac{2\, n_z(\omega_{\rm s})}{\lambda_{\rm s}}\right)^{-1} = 3.8\ \mu{\rm m} \tag{3.107}$$

This poling period is achievable by commercial crystal manufacturers (e.g. Raicol). However, due to technical fabrication limitations, it is not possible to pole an arbitrarily short crystal. The shortest poled KTP crystal available to us is 1mm long.

Crystal length and beam waists— We realize that temporal walk-off between the pump and seed is the limiting factor in choosing the length of our KTP crystal. Assuming a pump and seed pulses of approximately equal duration, $\tau_{\rm p} \approx \tau_{\rm s} = 150$ fs, their different group velocities ($v_{\rm p} = 0.43\, c$, $v_{\rm s} = 0.53\, c$) cause them to walk-off from each other after only 150 μm of KTP crystal. Currently, periodically poled crystals of such short lenght are not commercially available. However, we have seen in this chapter (see Sec. 3.3.4) that using a crystal longer than the walk-off length is not disadvantageous in principle. In fact, allowing the pump and seed pulses to walk over each other as they propagate along the crystal will reduce the negative impact of pulse length mismatch, allowing us to use the shorter pump

pulses produced in a simple SHG process.

Given that we are fixing the crystal length to $L = 1$ mm, now we would like to compute what pump and seed beam waists will optimize the degree of intensity squeezing. The pump beam waists that yield a Rayleigh range equal to half the crystal length are $W_{\mathrm{p}} \approx 3\mu$m and $W_{\mathrm{s}} \approx 4\mu$m, much smaller than what we can achieve using common lenses. Therefore, we will assume that our design will fall in the short-crystal regime, where beam divergence is negligible. In this chapter we have seen (see Sec. 3.4.2) that in this configuration it is desirable to use a pump beam waist larger than that of the seed, in order to improve mode overlap.

Expected enhancement and risks — We expect that the design provided here will outperform our previous BBO implementation, given that it will not suffer from the deleterious effects derived from angular dispersion in the pump mode. Moreover, the type-0 nonlinear coefficient of KTP is larger than the type-I nonlinear coefficient of BBO by almost an order of magnitude[84,86], which should yield a more efficient parametric amplification process. On the other hand, there is a risk associated with using periodically poled crystals which we should anticipate: an inaccuracy in the poling period will translate into a shift in the frequency where degenerate phase-matching is achieved. This is not a great concern to us, given that the range of tunability of our mode-locked Ti:Saph is larger than the detuning implied by typical fabrication tolerances.

3.7 Summary and outlook

In this section we have developed a framework to simulate the photon statistics of a parametrically amplified/deamplified coherent seed in the low gain regime. Our framework accommodates pulsed and focused pump and seed fields, accounting for the temporal and spatial structure of the parametric amplification. In particular, we can simulate the effect of a correlated spatio-temporal gain, which arises in a critically phase-matched process due to angular dispersion in one of the interacting fields. We have used this framework to analyze the limits on the achievable squeezing imposed by several phenomena such as group velocity mismatch, beam divergence, spatial walk-off and spatio-temporal coupling in the parametric gain, among others. This analysis has allowed us to propose a design for a sub-Poissonian light source which we expect will improve on the performance of the source implemented in Chapter 2. Moreover, the simulations presented in this chapter will provide guidance in the characterization of the future source, as it will be possible to compare measurements (e.g. spatial profile of the deamplified beam) with theory in order to diagnose possible failure modes.

Part II

High gain broadband twin-beam generation

Chapter 4

Simulating twin-beam generation in the high-gain regime

4.1 Motivation

Many pivotal experiments in quantum optics and quantum technologies have relied on twin beams generated by parametric nonlinear optical processes. The emission of photon pairs through spontaneous down conversion (SPDC) was observed as early as the 1970s by Burnham and Weinberg [87], and was later used to produce squeezed light [61], heralded single photons [88] and polarization-entangled photon pairs [89]. Since their inception, twin-beam sources have seen significant progress. The low nonlinearity in naturally occurring crystals has been enhanced either by using optical cavities or by pumping the nonlinear crystal with ultrafast pulses. In addition, higher effective nonlinearities have been achieved by using periodically poled crystals, which enable quasi-phase-matching of stronger elements of the crystal non-linear tensor [90]. Moreover, optical waveguides have been used to increase the

efficiency of SPDC[91], allowing longer interaction lengths and confining the emission of down-converted photons to a single spatial mode.

In this and the next chapter, we will be interested in the design and characterization of pulsed SPDC sources. Using a pump with a short coherence length, photon pairs can be created at well defined times. Together with the development of efficient photon-number-resolving detectors[92], the quantum states of light generated in these sources enable a range of experiments in quantum optics, such as conditional non-Gaussian state preparation[93,94] and sampling experiments[95–97]. However, early pulsed sources could not be described cleanly as the two-mode squeezers required to realize such experiments. The spectral correlation between the emitted signal and idler photons provides information that in principle allows one to distinguish photons emitted at different times[34,36–38,98]: the SPDC emission is in general produced in a product of multiple temporal modes.

Recently, the development of group velocity matching techniques allowed researchers to reduce the number of temporal modes of a source to essentially one[23,99]. Furthermore, the combined use of periodically poled waveguides and spectral engineering techniques allowed two-mode squeezed states to be generated in a single spatio-temporal mode[100], obtaining an unprecedented large brightness and small mode number. In Chapter 5, we will employ a waveguided periodically poled potassium titanyl phosphate (ppKTP) source which has been recently used to report two-mode squeezed states in a single spatio-temporal mode with a mean photon number up to 20[101].

However, alongside the promises offered by these new tehnologies come new challenges. The high optical intensities required to achieve such large parametric interactions can cause collateral effects that have not been systematically accounted for yet. In the first place,

self-phase modulation of the pump (SPM)[90] and cross-phase modulation (XPM) between this and the twin beams[102] can affect the spectral structure of SPDC emission. In addition, the spectral properties of SPDC change at high parametric gains due to the self-seeding of PDC by the spontaneously generated photons. This leads to the so-called time-ordering corrections, which render the perturbative description commonly used to describe twin-beam generation inaccurate[38,103]. The complex interplay between these effects makes the study of pulsed PDC sources in the high gain regime challenging.

Experimental advances call for the development of new experimental and theoretical tools to understand the non-perturbative regime of PDC. In this chapter we will provide a theoretical framework to model the emission of high-gain pulsed PDC sources efficiently. This framework, derived from first principles using a canonical Hamiltonian approach, allows for an arbitrarily high PDC gain to be simulated, and includes parasitic nonlinear phenomena such as SPM and XPM. This theoretical model is motivated by the experiments reported in Chapter 5, where we build on a recently introduced characterization technique called cascaded stimulated emission tomography (SET)[104] to analyze a pulsed high-gain PDC source. Cascaded SET extends the concept of a seeded joint spectral intensity (JSI) measurement[100,105] to the observation of additional cascaded difference-frequency generation (DFG) processes. These cascaded processes provide us with additional information that we use to fit the theoretical model introduced in this chapter. In particular, the ratio between direct and cascaded DFG will be used to obtain a self-referenced measurement of PDC strength. The resulting fitted model describes a situation in which the parasitic nonlinearities (SPM and XPM) play an important role, modifying the spectral structure of PDC. Finally, in Chapter 5 we will propose a design of a PDC source that uses the insight

that we gained to overcome the limitations imposed by these parasitic nonlinearities.

4.2 Efficient modelling of waveguided type-II PDC in the high-gain regime

A number of theoretical descriptions of twin beam generation have been given, each best suited to a certain gain regime, experimental geometry, etc. Amongst these, those models that can describe the high gain regime of pulsed parametric down conversion do so either by following an iterative approach [36,38] or by providing high order perturbative expansions of the SPDC unitary transformation [103]. Here we will provide a model of waveguided high-gain SPDC that can be solved efficiently (non-iteratively) and exactly for an arbitrary value of the parametric gain. The only approximation that we will make is to assume that the interacting fields experience only a linear dispersion over their bandwidth. We follow the approach introduced by M.D. Vidrighin [104], grounding it in a Hamiltonian quantization procedure. We develop this model in order to fit the experimental data that we measure from a ppKTP waveguide, as we detail in Sec. 5.2. Guided by the experiment, we realize that, in addition to the SPDC interaction, we also need to include the effect of SPM of the pump in the model, as well as XPM between the pump and the twin beams.

4.2.1 Field quantization

Let us recall that in our description (see Section 1.2.1) of an optical field in a current-free, non-magnetic medium we take the magnetic ($\mathbf{B}$) and displacement ($\mathbf{D}$) fields as our fundamental fields. Neglecting material dispersion for the moment, we write the polarization

($\mathbf{P}$) as a function of $\mathbf{D}$

$$\mathbf{P}(\mathbf{D}) = \Gamma^{(1)}\mathbf{D} + \Gamma^{(2)}\mathbf{D}^2 + \Gamma^{(3)}\mathbf{D}^3 + \dots \tag{4.1}$$

where we are using a schematic notation that implies the appropriate tensorial form of $\Gamma^{(n)}$ and summation over Cartesian coordinates. The energy density of the system is then

$$\mathcal{H} = \int \mathbf{E}(\mathbf{D}) \cdot \mathrm{d}\mathbf{D} + \int \mathbf{H}(\mathbf{B}) \cdot \mathrm{d}\mathbf{B} \tag{4.2}$$

$$= \frac{\mathbf{B}^2}{2\mu_0} + \frac{1-\Gamma^{(1)}}{2\epsilon_0}\mathbf{D}^2 - \frac{\Gamma^{(2)}\mathbf{D}^3}{3\epsilon_0} - \frac{\Gamma^{(3)}\mathbf{D}^4}{4\epsilon_0} - \dots, \tag{4.3}$$

with the Hamiltonian H given by the integral over space of this density. The commutation relations that retrieve Maxwell's equations from this Hamiltonian are [12,13]

$$[\hat{D}_j(\mathbf{r}), \hat{B}_l(\mathbf{r}')] = i\hbar\varepsilon_{jlm}\frac{\partial}{\partial r_m}\delta(\mathbf{r}-\mathbf{r}'), \tag{4.4a}$$

$$[\hat{D}_j(\mathbf{r}), \hat{D}_l(\mathbf{r}')] = [\hat{B}_j(\mathbf{r}), \hat{B}_l(\mathbf{r}')] = 0, \tag{4.4b}$$

where the indices j, l, m denote Cartesian components, ε_{jlm} is the Levi-Civita symbol and $\delta(\mathbf{r})$ is the Dirac distribution.

4.2.2 Expansion fields in a waveguide

The spatial distribution of the refractive index in an optical waveguide defines a set of solutions of Maxwell's equations that, in the linear propagation regime, travel along the waveguide without changing their spatial profile. We consider solutions that evolve har-

monically in time,

$$\mathbf{B}_{\mu k}(\mathbf{r},t) = \mathbf{B}_{\mu k}(\mathbf{r})\exp(-i\omega_{\mu k}t) + \text{c.c.} \tag{4.5}$$

$$\mathbf{D}_{\mu k}(\mathbf{r},t) = \mathbf{D}_{\mu k}(\mathbf{r})\exp(-i\omega_{\mu k}t) + \text{c.c.} \tag{4.6}$$

where the label k is a wavevector, and we use a "Greek type label" μ to identify which field we are describing, writing $\mu = p$ for the pump and $\mu = s, i$ for the twin beam fields. Assuming that the refractive index is independent of z, the distance along the waveguide, these solutions will have the form

$$\mathbf{D}_{\mu k}(\mathbf{r}) = \frac{\mathbf{d}_{\mu k}(x,y)}{\sqrt{2\pi}}e^{ikz}, \quad \mathbf{B}_{\mu k}(\mathbf{r}) = \frac{\mathbf{b}_{\mu k}(x,y)}{\sqrt{2\pi}}e^{ikz}, \tag{4.7}$$

This is a convenient expansion basis for the field operators $\mathbf{D}(\mathbf{r},t)$ and $\mathbf{B}(\mathbf{r},t)$ even in the presence of material dispersion, under the assumption that at frequencies of interest there is no absorption. If normalization is done according to

$$\int dxdy \frac{\mathbf{d}^*_{\mu k}(x,y)\cdot\mathbf{d}_{\mu k}(x,y)}{\epsilon_0 n^2(x,y;\omega_{\mu k})}\frac{v_{\text{ph}}(x,y;\omega_{\mu k})}{v_{\text{g}}(x,y;\omega_{\mu k})} = 1, \tag{4.8}$$

where $v_{\text{ph}}(x,y;\omega)$ and $v_{\text{g}}(x,y;\omega)$ are respectively the local phase and group velocities at each point in the waveguide[16], then the displacement and magnetic fields can be written

in the following very symmetric form

$$\hat{\mathbf{B}}(\mathbf{r}) = \sum_{\mu} \int \mathrm{d}k \sqrt{\frac{\hbar\omega_{\mu k}}{2}}\, \hat{c}_{\mu k}\, \mathbf{B}_{\mu k}(\mathbf{r}) + \mathrm{H.c.}, \tag{4.9}$$

$$\mathbf{D}(\mathbf{r}) = \sum_{\mu} \int \mathrm{d}k \sqrt{\frac{\hbar\omega_{\mu k}}{2}}\, \hat{c}_{\mu k}\, \mathbf{D}_{\mu k}(\mathbf{r}) + \mathrm{H.c.}, \tag{4.10}$$

and furthermore, the linear part of the Hamiltonian can then be written as

$$\hat{H}_L = \int \mathrm{d}k \sum_{\mu} \hbar\omega_{\mu k}\, \hat{c}^{\dagger}_{\mu k}\, \hat{c}_{\mu k}, \tag{4.11}$$

with the zero-point energy neglected. The creation and destruction operators $\hat{c}^{\dagger}_{\mu k}$ and $\hat{c}_{\mu k}$ satisfy the bosonic commutation relations [16]

$$[\hat{c}_{\mu k}, \hat{c}_{\mu' k'}] = [\hat{c}^{\dagger}_{\mu k}, \hat{c}^{\dagger}_{\mu' k'}] = 0, \tag{4.12}$$

$$[\hat{c}_{\mu k}, \hat{c}^{\dagger}_{\mu' k'}] = \delta_{\mu\mu'}\delta(k - k'). \tag{4.13}$$

We now introduce *field* operators

$$\hat{\psi}_{\mu}(z) = \int \frac{\mathrm{d}k}{\sqrt{2\pi}}\, \hat{c}_{\mu k}\, e^{i(k-\bar{k}_{\mu})z}. \tag{4.14}$$

which are quantum operators analogous to the slowly varying envelope functions in space, since we have removed a central wavevector $\bar{k}_{\mu}$ associated with the central frequency $\bar{\omega}_{\mu}$.

The Schrödinger picture field operators satisfy the commutation relations

$$[\hat{\psi}_\mu(z), \hat{\psi}_{\mu'}(z')] = [\hat{\psi}^\dagger_\mu(z), \hat{\psi}^\dagger_{\mu'}(z')] = 0, \tag{4.15}$$

$$[\hat{\psi}_\mu(z), \hat{\psi}^\dagger_{\mu'}(z')] = \delta_{\mu,\mu'}\,\delta(z - z'), \tag{4.16}$$

again, under the assumptions that the pump, signal, and idler fields span different wavevector and frequency ranges, and thus that for each field operator (4.14) we can formally let k range from $-\infty$ to ∞ when evaluating the commutation relations.

Now we assume that group velocity does not vary significantly over the bandwidths of interest, ignoring group velocity dispersion. Substituting $\omega_{\mu k} = \bar{\omega}_\mu + v_\mu\,(k - \bar{k}_\mu)$, the linear part of the Hamiltonian, given in Eq. (4.11) can be written

$$\hat{H}_\mathrm{L} = \sum_\mu \hbar\bar{\omega}_\mu \int \mathrm{d}k\, \hat{c}^\dagger_{\mu k}\hat{c}_{\mu k} + \hbar\, v_\mu(k - \bar{k}_\mu)\, \hat{c}^\dagger_{\mu k}\hat{c}_{\mu k} \tag{4.17}$$

which, is recast in terms of the field operators as

$$\begin{aligned}\hat{H}_\mathrm{L} = &\sum_\mu \hbar\bar{\omega}_\mu \int \mathrm{d}z\; \hat{\psi}^\dagger_\mu(z)\hat{\psi}_\mu(z) \\ &+ \frac{i}{2}\sum_\mu \hbar v_\mu \int \mathrm{d}z \left(\frac{\partial\hat{\psi}^\dagger_\mu(z)}{\partial z}\hat{\psi}_\mu(z) - \hat{\psi}^\dagger_\mu(z)\frac{\partial\hat{\psi}_\mu(z)}{\partial z}\right),\end{aligned} \tag{4.18}$$

Finally we can write the displacement field $\hat{\mathbf{D}}(\mathbf{r})$ (4.10) in terms of the field operators as

$$\hat{\mathbf{D}}(\mathbf{r}) \approx \sum_\mu e^{i\bar{k}_\mu z}\left[\sqrt{\frac{\hbar\omega_\mu}{2}}\,\mathbf{d}_{\mu k_\mu}(x,y)\right]_{k_\mu=\bar{k}_\mu}\hat{\psi}_\mu(z) + \mathrm{H.c.}, \tag{4.19}$$

where we performed a Taylor expansion of the terms inside the integral around $k_\mu = \bar{k}_\mu$

and assumed any variation in the transverse mode profiles $\mathbf{d}_{\mu k_\mu}$ and the frequencies ω_μ to be negligible; the magnetic field $\hat{\mathbf{B}}(\mathbf{r})$ (4.9) can be written in a similar way.

4.2.3 The nonlinear interaction

We now turn to the nonlinear part of the Hamiltonian, which is given by the integral over space of the third and fourth terms on the right-hand-side of (4.3). Explicitly indicating Cartesian components and with the usual Einstein summation convention we have

$$\begin{aligned}\hat{H}_{\mathrm{NL}} = &-\frac{1}{3\epsilon_0}\int \mathrm{d}\mathbf{r}\ \Gamma^{(2)}_{ijl}(\mathbf{r})\ D_i(\mathbf{r})D_j(\mathbf{r})D_l(\mathbf{r}) \\ &-\frac{1}{4\epsilon_0}\int \mathrm{d}\mathbf{r}\ \Gamma^{(3)}_{ijlm}(\mathbf{r})\ D_i(\mathbf{r})D_j(\mathbf{r})D_l(\mathbf{r})D_m(\mathbf{r}),\end{aligned} \tag{4.20}$$

where we note that the first term will be responsible for SPDC while the second will give rise to SPM and XPM. In terms of the usual nonlinear susceptibilities $\chi^{(2)}_{ijl}(x,y,z)$ and $\chi^{(3)}_{ijlm}(x,y,z)$ characterizing the second and third order optical response, we have

$$\Gamma^{(2)}_{ijl}(x,y,z) = \frac{\chi^{(2)}_{ijl}(x,y,z)}{\epsilon_0\, n_o^6(x,y)}, \tag{4.21}$$

$$\begin{aligned}\Gamma^{(3)}_{ijlm}(x,y,z) = &\frac{\chi^{(3)}_{ijlm}(x,y,z)}{\epsilon_0^2\, n_o^8(x,y)} \\ &-\sum_q \frac{2\,\chi^{(2)}_{ijq}(x,y,z)\,\chi^{(2)}_{qlm}(x,y,z)/n_q^2(x,y)}{\epsilon_0^2\, n_o^8(x,y)},\end{aligned} \tag{4.22}$$

where we neglect the effects of material dispersion on the nonlinear Hamiltonian, and take $n_o(x,y)$ to be an index of refraction at some "typical" wavelength [13] .

We can now write the nonlinear Hamiltonian Eq. (4.20) in terms of the field operators $\psi_\mu(z)$, considering processes in which three beams labelled pump (p), signal (s), and idler (i)

are coupled by the nonlinear interaction. We assume we can choose our center frequencies $\bar{\omega}_\mu$ and the associated wave vectors $\bar{k}_\mu$ such that

$$\bar{\omega}_p - \bar{\omega}_s - \bar{\omega}_i = 0, \tag{4.23}$$

$$\bar{k}_p - \bar{k}_s - \bar{k}_i = 0 \tag{4.24}$$

a condition that will allow for the creation of twin beams via SPDC. Third-order nonlinear processes, such as self- and cross-phase modulation, are automatically phase matched, and can modify the properties of the photons generated in SPDC. Note that if *quasi*-phase matching is used for a second order process, the RHS of Eq. (4.24) should be changed to $\pm 2\pi/\Lambda$ where Λ is the poling period.

Under these assumptions we can write the nonlinear part of the Hamiltonian as

$$\hat{H}_{\mathrm{NL}} = -\hbar \int \mathrm{d}z \Bigg\{ \frac{1}{2}\, \zeta_p(z) \hat{\psi}_p^\dagger(z) \hat{\psi}_p^\dagger(z) \hat{\psi}_p(z) \hat{\psi}_p(z) \tag{4.25a}$$

$$+ \zeta_i(z) \hat{\psi}_p^\dagger(z) \hat{\psi}_p(z) \hat{\psi}_i^\dagger(z) \hat{\psi}_i(z) \tag{4.25b}$$

$$+ \zeta_s(z) \hat{\psi}_p^\dagger(z) \hat{\psi}_p(z) \hat{\psi}_s^\dagger(z) \hat{\psi}_s(z) \tag{4.25c}$$

$$+ \Big(\xi(z) \hat{\psi}_s^\dagger(z) \hat{\psi}_i^\dagger(z)\, \hat{\psi}_p(z) + \mathrm{h.c.} \Big) \Bigg\} \tag{4.25d}$$

where we use the full permutation symmetry of the Γ tensors in their Cartesian indices, and keep the terms that are energy and phase matched consistent with Eq. (4.24); we have also introduced the quantities $\zeta_p, \zeta_i, \zeta_s, \xi$, defined in detail in Appendix C, which capture the strength of the nonlinear interactions corresponding to SPM of the pump (4.25a), XPM

between the pump and the idler (4.25b), XPM between the pump the signal (4.25c) and twin-beam generation via SPDC. We take these quantities to be nonzero only in a region $\ell_{\min} \leq z \leq \ell_{\max}$ where the nonlinear coupling occurs. Notice that in the last set of equations we have only included SPM of the pump, since the intensities of the signal and idler field are small enough for SPM to be negligible.

4.2.4 Dynamics of the fields

With the full Hamiltonian of the system in place we can find the evolution of the field operators in the Heisenberg picture by applying the Heisenberg equation of motion.

Pump dynamics

We first look at the Heisenberg equation of motion for the pump field, which follows from using the commutation relations (4.15) with a Hamiltonian that is the sum of the linear (4.18) and nonlinear (4.25) contributions,

$$\left(\frac{\partial}{\partial t} + v_p \frac{\partial}{\partial z} + i\bar{\omega}_p\right) \hat{\psi}_p(z,t) = \tag{4.26}$$
$$i\zeta_p(z)\hat{\psi}_p^\dagger(z,t)\hat{\psi}_p(z,t)\hat{\psi}_p(z,t) + \text{back-action terms},$$

where the "back-action terms" are contributions that contain the operators $\hat{\psi}_s(z,t)$ and $\hat{\psi}_i(z,t)$. We assume that the pump field is prepared in a strong coherent state with a large number of photons, and we assume that this number remains unchanged during the SPDC process; we may then ignore the back-action terms, which are all proportional to the first power of $\hat{\psi}_p(z,t)$ and second powers of $\hat{\psi}_s(z,t)$ and $\hat{\psi}_i(z,t)$, and have a much smaller effect than the self-phase modulation term appearing in the right hand side of Eq. (4.26).

Furthermore, because of the undepleted pump approximation just described we replace $\hat{\psi}_p(z,t) \to \langle\hat{\psi}_p(z,t)\rangle$. The solution to the equation of motion for the pump mean field is

$$\langle\hat{\psi}_p(z,t)\rangle = \beta(z - v_p(t-t_0))e^{-i\bar{\omega}_p(t-t_0)+i\varphi(z,t)}, \tag{4.27}$$

where the nonlinear phase accumulated due to SPM is

$$\varphi(z,t) = |\beta(z - v_p(t-t_0))|^2 \int_{t_0}^{t} \mathrm{d}t' \zeta_p(z - v_p(t-t')), \tag{4.28}$$

and where we introduced

$$\langle\hat{\psi}_p(z,t_0)\rangle = \beta(z). \tag{4.29}$$

Note that the intensity of the field will not be affected by SPM,

$$|\langle\hat{\psi}_p(z,t)\rangle|^2 = |\beta(z - v_p(t-t_0))|^2, \tag{4.30}$$

Twin-beam dynamics

We can now calculate the Heisenberg equations of motion for the signal (analogously for the idler) field operators ψ_s,

$$\left(\frac{\partial}{\partial t} + v_s\frac{\partial}{\partial z} + i\bar{\omega}_s\right)\hat{\psi}_s(z,t) = i\xi(z)\langle\hat{\psi}_p(z,t)\rangle\,\hat{\psi}_i^\dagger(z,t) + i\zeta_s(z)|\langle\hat{\psi}_p(z,t)\rangle|^2\,\hat{\psi}_s(z,t), \tag{4.31}$$

The right hand side of Eq. (4.31) accounts for photon generation via SPDC, and for cross-phase modulation of the pump on the signal and idler fields . Its left hand side accounts for propagation at group velocity v_j, and oscillation at frequency $\bar{\omega}_j$.

The solution of these coupled equations of motion (Eq. 4.31 and signal analog) is not obvious in their current form. We can eliminate the temporal derivatives by moving to the frequency domain. Defining the (t,ω) Fourier transform of the field operators,

$$\tilde{\psi}_\mu(z,\omega) = \sqrt{v_\mu}\int\frac{\mathrm{d}t}{\sqrt{2\pi}}\,e^{i\omega t}\,\hat{\psi}_\mu(z,t), \tag{4.32}$$

where we ommit the hat to avoid clutter, we obtain the equivalent equation of motion for the frequency-domain signal (analogously for idler)

$$\frac{\partial}{\partial z}\tilde{\psi}_s(z,\omega) = i\left(\frac{\omega-\bar{\omega}_s}{v_s}\right)\tilde{\psi}_s(z,\omega) \tag{4.33}$$

$$+ i\int\frac{\mathrm{d}\omega'}{\sqrt{2\pi v_p v_s v_i}}\xi(z)\;\langle\tilde{\psi}_p(z,\omega+\omega')\rangle\;\tilde{\psi}_i^\dagger(z,\omega') \tag{4.34}$$

$$+ i\int\frac{\mathrm{d}\omega'}{\sqrt{2\pi}v_s}\zeta_s(z)\;I_0(z,\omega-\omega')\;\psi_s(z,\omega'), \tag{4.35}$$

where we have defined the (t,ω) Fourier transform of the pump intensity

$$I_0(z,\omega) = v_p\int\mathrm{d}t\;e^{i\omega t}\;|\langle\hat{\psi}_p(z,t)\rangle|^2 = e^{i\omega t_0}e^{i\omega z/v_p}\int\mathrm{d}z'\;e^{-i\omega z'/v_p}\;|\beta(z)|^2. \tag{4.36}$$

These equations of motion are still not analytically integrable due to the spatial dependece of the rhs. We can do a final change of variables, first introduced in [104], moving to a frame of reference that propagates at the pump group velocity, which yields the transformed operators

$$\tilde{\psi}_j(z,\omega) = e^{i\frac{\omega-\bar{\omega}_j}{v_p}z}\,\hat{a}_j(z,\omega) \quad j \in \{s,i\}, \tag{4.37}$$

$$\langle\tilde{\psi}_p(z,\omega)\rangle = e^{i\frac{\omega-\bar{\omega}_p}{v_p}z}\alpha_p(z,\omega). \tag{4.38}$$

The equations for the spatial evolution of the $\hat{a}_j(z,\omega)$ are then found to be

$$\begin{aligned}
\frac{\partial}{\partial z}\hat{a}_s(z,\omega) &= i\Delta k_s(\omega)\hat{a}_s(z,\omega) \qquad (4.39a)\\
&+ i\frac{\gamma_{\mathrm{XPM},s}\,h_s(z)}{2\pi}\int \mathrm{d}\omega' I(\omega-\omega')\hat{a}_s(z,\omega')\\
&+ i\frac{\gamma\,g(z)}{\sqrt{2\pi}}\int \mathrm{d}\omega'\alpha_p(z,\omega+\omega')\hat{a}_i^\dagger(z,\omega'),\\
\frac{\partial}{\partial z}a_i^\dagger(z,\omega) &= -i\Delta k_i(\omega)\hat{a}_i(z,\omega) \qquad (4.39b)\\
&- i\frac{\gamma_{\mathrm{XPM},i}\,h_i(z)}{2\pi}\int \mathrm{d}\omega' I^*(\omega-\omega')\hat{a}_i^\dagger(z,\omega')\\
&- i\frac{\gamma^*\,g(z)}{\sqrt{2\pi}}\int \mathrm{d}\omega'\alpha_p^*(z,\omega+\omega')\hat{a}_s^\dagger(z,\omega'),
\end{aligned}$$

The first term on the right hand side of these equations describes the pulse walk-off between the pump and the signal/idler; we have defined

$$\Delta k_j(\omega) = \left(\frac{1}{v_j}-\frac{1}{v_p}\right)(\omega-\bar{\omega}_j)\ . \tag{4.40}$$

The second term, accounting for cross-phase modulation, contains a coupling strength pro-

file,

$$\gamma_{\mathrm{XPM},j}\, h_j(z) = \frac{\zeta_j(z)}{v_p\, v_j\, \hbar\, \bar{\omega}_p}\,, \tag{4.41}$$

where we take $h_j(z) = 1, 0$ respectively in the region where the nonlinearity is present or absent, and the (t, ω) Fourier transform of the pump intensity in the moving frame does not depend on z:

$$I(\omega) = I^*(-\omega) = e^{i\omega t_0}\hbar\bar{\omega}_p \int \mathrm{d}z |\beta(z)|^2 e^{-i\omega z/v_p}. \tag{4.42}$$

The last term is responsible for twin-beam generation, and contains a coupling strength profile

$$\gamma\, g(z) = \frac{\xi(z)}{\sqrt{v_p v_s v_i \hbar\bar{\omega}_p}} \tag{4.43}$$

with $g(z) = 0$ where the nonlinearity is absent and either 1 or -1 (the latter to describe quasi-phase matching) where the nonlinearity is present, and the (t, ω) Fourier transform of the pump amplitude in the moving frame is

$$\begin{aligned}\alpha_p(z,\omega) &= \frac{(\hbar\bar{\omega}_p)^{1/2}}{\sqrt{2\pi/v_p}} \int \mathrm{d}t\; e^{i(\omega t - z(\omega-\bar{\omega}_p)/v_p)} \langle \psi_p(z,t)\rangle \\ &= e^{i\omega t_0} \frac{(\hbar\bar{\omega}_p)^{1/2}}{\sqrt{2\pi v_p}} \int \mathrm{d}z' e^{-iz'\frac{(\omega-\bar{\omega}_p)}{v_p}} \big(\beta(z')\big)\, e^{i\;\theta(z,z'))}\end{aligned} \tag{4.44}$$

with a nonlinear phase

$$\theta(z,z') \equiv \varphi\left(z, t_0 + \tfrac{z-z'}{v_p}\right) = |\beta(z')|^2 \int_{z'}^{z} \frac{\mathrm{d}z''}{v_p} \zeta_p(z''). \tag{4.45}$$

In the limit of negligible SPM of the pump $\theta(z,q) \ll 1$, the pump spectral function $\alpha_p(z,\omega)$ becomes independent of z and the right hand side of equations of motion (4.39) depends only on z via the prefactors $\gamma_{\mathrm{SPM},s}$, $\gamma_{\mathrm{SPM},i}$,γ. However, as soon as SPM becomes important this simple translational dependence is lost.

4.2.5 Solving the equations of motion

We will now address the solution of the coupled equations of motion for $\hat{a}_s(z,\omega)$ and $\hat{a}_i^\dagger(z,\omega)$ (4.39), which will allow us to connect the states of the twin-beams at positions before and after the nonlinear interaction. For computational purposes and notational simplicity we discretize the operators $\hat{a}_j(z,\omega)$ on a grid of N points according to $\omega_n = \omega_0 + n\Delta\omega|_{n=0}^{N-1}$. We introduce the column vectors $\mathbf{u}$ and $\mathbf{v}^\dagger$ with components

$$\mathbf{u}_n(z) = \hat{a}_s(z,\omega_n), \tag{4.46}$$

$$\mathbf{v}_n^\dagger(z) = \hat{a}_i^\dagger(z,\omega_n), \tag{4.47}$$

and then, using Eq. (4.39) we can write

$$\frac{\partial}{\partial z}\begin{pmatrix}\mathbf{u}(z)\\ \mathbf{v}^\dagger(z)\end{pmatrix} = i\underbrace{\left[\begin{array}{c|c}\mathbf{G}(z) & \mathbf{F}(z)\\ \hline -\mathbf{F}^\dagger(z) & -\mathbf{H}^\dagger(z)\end{array}\right]}_{:=\mathbf{Q}(z)}\begin{pmatrix}\mathbf{u}(z)\\ \mathbf{v}^\dagger(z)\end{pmatrix}, \tag{4.48}$$

where we have defined the following matrices

$$\mathbf{F}_{n,m}(z) = \frac{\gamma\, g(z)}{\sqrt{2\pi}} \alpha_p(z, \omega_n + \omega_m)\Delta\omega, \tag{4.49a}$$

$$\mathbf{G}_{n,m}(z) = \Delta k_s(\omega_n)\delta_{m,n} + \frac{\gamma_{\mathrm{XPM},s}\, h_s(z)}{2\pi} I(\omega_n - \omega_m)\Delta\omega, \tag{4.49b}$$

$$\mathbf{H}_{n,m}(z) = \Delta k_i(\omega_n)\delta_{m,n} + \frac{\gamma_{\mathrm{XPM},i}\, h_i(z)}{2\pi} I^*(\omega_n - \omega_m)\Delta\omega. \tag{4.49c}$$

In general, the dependence of $\mathbf{Q}(z)$ on the waveguide position, z, forbids a simple analytical solution of this system of coupled differential equations. Nevertheless, we can formally integrate it using the Trotter-Suzuki expansion, obtaining

$$\begin{pmatrix} \mathbf{u}(z) \\ \mathbf{v}^\dagger(z) \end{pmatrix} = \mathbf{U}(z, z_0) \begin{pmatrix} \mathbf{u}(z_0) \\ \mathbf{v}^\dagger(z_0) \end{pmatrix} \tag{4.50}$$

$$= \left[\begin{array}{c|c} \mathbf{U}^{s,s}(z, z_0) & \mathbf{U}^{s,i}(z, z_0) \\ \hline (\mathbf{U}^{i,s}(z, z_0))^* & (\mathbf{U}^{i,i}(z, z_0))^* \end{array}\right] \begin{pmatrix} \mathbf{u}(z_0) \\ \mathbf{v}^\dagger(z_0) \end{pmatrix}, \tag{4.51}$$

where the propagator $\mathbf{U}(z, z_0)$ is defined by the limit

$$\mathbf{U}(z, z_0) = \lim_{n\to\infty} \prod_{p=1}^{n} \exp\left(i\, \Delta z\, \mathbf{Q}(z_p)\right), \tag{4.52}$$

and $\Delta z = (z - z_0)/n$ and $z_p = z_0 + p\Delta z$. The intuition behind the Trotter-Suzuki expansion used in the last equation is that for sufficiently thin "slices" of propagation in z one can approximate the matrix $\mathbf{Q}(z)$ as a constant in that region; thus one can simply compound the propagation over all the small regions to get the net propagator.

If $\mathbf{Q}$ is independent of z, as is the case when SPM can be neglected, then the solution

of the equations of motion can be found through a single matrix exponentiation

$$\mathbf{U}(z, z_0) = \lim_{n\to\infty} \prod_{p=1}^{n} \exp\left(i\,\Delta z\,\mathbf{Q}\right) = \exp(i(z - z_0)\mathbf{Q}). \tag{4.53}$$

The undiscretized form of Eq. (4.50) yields the linear transformation of the continuous-frequency (z, ω) operators

$$\begin{aligned} \hat{a}_s(z,\omega) = &\int \mathrm{d}\omega' U^{s,s}(\omega,\omega'; z, z_0)\hat{a}_s(z_0,\omega') \\ &+ \int \mathrm{d}\omega' U^{s,i}(\omega,\omega'; z, z_0)\hat{a}_i^\dagger(z_0,\omega'), \end{aligned} \tag{4.54a}$$

$$\begin{aligned} \hat{a}_i^\dagger(z,\omega) = &\int \mathrm{d}\omega' (U^{i,s}(\omega,\omega'; z, z_0))^*\hat{a}_s(z_0,\omega') \\ &+ \int \mathrm{d}\omega' (U^{i,i}(\omega,\omega'; z, z_0))^*\hat{a}_i^\dagger(z_0,\omega'), \end{aligned} \tag{4.54b}$$

where the blocks of the propagator $\mathbf{U}(z, z_0)$ are related to the continuous-frequency transfer functions (TFs) as follows:

$$U^{j,k}(\omega_n, \omega_m; z, z_0) = \mathbf{U}^{j,k}_{n,m}(z, z_0)/\Delta\omega. \tag{4.55}$$

For notational simplicity, we omit the spatial dependence when we write the TFs connecting the input and output operators at the facets of the nonlinear medium. In addition, to simplify the form of the transfer functions, we make a change of basis of the input and

output operators that corresponds to linear propagation to the center of the waveguide:

$$\hat{a}_j^{(\mathrm{in})}(\omega) = \hat{a}_j(\ell_{\min}, \omega) \exp(-i\,\Delta k_j(\omega)\,\ell_{\min}) \tag{4.56a}$$

$$\hat{a}_j^{(\mathrm{out})}(\omega) = \hat{a}_j(\ell_{\max}, \omega) \exp(-i\,\Delta k_j(\omega)\,\ell_{\max}) \tag{4.56b}$$

These operators are connected by a propagator suscinctly expressed in its discretized form as

$$\mathbf{U} = \mathbf{V}(0, \ell_{\max})\mathbf{U}(\ell_{\max}, \ell_{\min})\mathbf{V}(\ell_{\min}, 0) \tag{4.57}$$

with

$$\mathbf{V}(z, z') = \exp\left(i(z - z') \left[\begin{array}{c|c} \mathbf{L} & 0 \\ \hline 0 & -\mathbf{P}^\dagger \end{array}\right] \right) \tag{4.58}$$

$$\mathbf{L}_{m,n} = \Delta k_s(\omega_m)\delta_{m,n}, \qquad \mathbf{P}_{m,n} = \Delta k_s(\omega_m)\delta_{m,n} \tag{4.59}$$

Identitying the transfer functions $U^{m,n}(\omega, \omega')$ as the continuous-frequency version of the appropriate block of the propagator $\mathbf{U}$, we write

$$\begin{aligned} \hat{a}_s^{(\mathrm{out})}(\omega) = &\int \mathrm{d}\omega' U^{s,s}(\omega, \omega')\ \hat{a}_s^{(\mathrm{in})}(\omega') \\ &+ \int \mathrm{d}\omega' U^{s,i}(\omega, \omega')\ \hat{a}_i^{\dagger(\mathrm{in})}(\omega'), \end{aligned} \tag{4.60}$$

and an equivalent expression for the idler. We will often refer to the TFs that couple the signal and idler fields ($U_{s,i}, U_{i,s}$) as cross-mode transfer functions. The TFs that couple a mode to itself ($U_{s,s}, U_{i,i}$) will be called same-mode transfer functions.

4.2.6 Commutation relations and modal structure

We now analyze the equal-position commutation relations obeyed by our transformed operators, $\hat{a}_s(z,\omega)$ and $\hat{a}_i^\dagger(z,\omega')$. At a position z_0 before the nonlinear region, the twin-beams are decoupled and the relevant commutation relations are simply

$$[\hat{a}_j(z_0,\omega),\hat{a}_{j'}^\dagger(z_0,\omega')] = \delta_{j,j'}\,\delta(\omega-\omega'), \tag{4.61a}$$

$$[\hat{a}_j(z_0,\omega),\hat{a}_{j'}(z_0,\omega')] = 0, \tag{4.61b}$$

These bosonic commutation relations should be maintained after the nonlinear interaction. Upon using the solutions in Eq. (4.54) and these initial position commutators, we find the commutators at any position in he waveguide to be

$$\begin{aligned}[\hat{a}_s(z,\omega),&\hat{a}_s^\dagger(z,\omega')] = \\ &\int \mathrm{d}\omega'' U^{s,s}(\omega,\omega'';z,z_0)(U^{s,s}(\omega',\omega'';z,z_0))^* \\ &- \int \mathrm{d}\omega'' U^{s,i}(\omega,\omega'';z,z_0)(U^{s,i}(\omega',\omega'';z,z_0))^*,\end{aligned} \tag{4.62a}$$

$$\begin{aligned}[\hat{a}_i(z,\omega),&\hat{a}_i^\dagger(z,\omega')] = \\ &\int \mathrm{d}\omega'' U^{i,i}(\omega,\omega'';z,z_0)(U^{i,i}(\omega',\omega'';z,z_0))^* \\ &- \int \mathrm{d}\omega'' U^{i,s}(\omega,\omega'';z,z_0)(U^{i,s}(\omega',\omega'';z,z_0))^*,\end{aligned} \tag{4.62b}$$

$$\begin{aligned}[\hat{a}_s(z,\omega),&\hat{a}_i(z,\omega')] = \\ &\int \mathrm{d}\omega'' U^{s,s}(\omega,\omega'';z,z_0)U^{i,s}(\omega',\omega'';z,z_0) \\ &- \int \mathrm{d}\omega'' U^{s,i}(\omega,\omega'';z,z_0)U^{i,i}(\omega',\omega'';z,z_0),\end{aligned} \tag{4.62c}$$

and $[\hat{a}_s(z,\omega), \hat{a}_i^\dagger(z,\omega')] = 0$. To show that the right hand sides of Eqs. (4.62 a,b,c) are $\delta(\omega-\omega')$, $\delta(\omega-\omega')$, and 0 respectively, we note that the matrix discretized versions of these putative commutations relations would be

$$\mathbf{U}^{s,s}(z,z_0)(\mathbf{U}^{s,s}(z,z_0))^\dagger - \mathbf{U}^{s,i}(z,z_0)(\mathbf{U}^{s,i}(z,z_0))^\dagger = \mathbb{I}_N, \tag{4.63a}$$

$$\mathbf{U}^{i,i}(z,z_0)(\mathbf{U}^{i,i}(z,z_0))^\dagger - \mathbf{U}^{i,s}(z,z_0)(\mathbf{U}^{i,s}(z,z_0))^\dagger = \mathbb{I}_N, \tag{4.63b}$$

$$\mathbf{U}^{s,s}(z,z_0)(\mathbf{U}^{i,s}(z,z_0))^T - \mathbf{U}^{s,i}(z,z_0)(\mathbf{U}^{i,i}(z,z_0))^T = 0, \tag{4.63c}$$

with $\mathbb{I}_N$ being the N dimensional identity matrix. Note that the last set of equations can be written more compactly in terms of the following equation for the propagator $\mathbf{U}(z,z_0)$

$$\mathbf{U}(z,z_0)\ \mathbf{S}\ \mathbf{U}^\dagger(z,z_0) = \mathbf{S}, \tag{4.64}$$

with

$$\mathbf{S} = \begin{bmatrix} \mathbb{I}_N & 0 \\ 0 & -\mathbb{I}_N \end{bmatrix}. \tag{4.65}$$

Mathematically, Eq. (4.64) states that $\mathbf{U}(z,z_0)$ is an element of the $SU(1,1)$ Lie group (cf. Appendix 11.1.4. of Klimov and Chumakov[106]). To show that $\mathbf{U}(z,z_0) \in SU(1,1)$ it is sufficient to show that its generators, the matrices $\mathbf{Q}(z)$ belong to the algebra of this group, $\mathfrak{su}(1,1)$, thus they need to satisfy

$$\mathbf{Q}(z)\ \mathbf{S} = \mathbf{S}\ \mathbf{Q}^\dagger(z). \tag{4.66}$$

But this is trivial to show using the Hermiticity of the matrices **G** and **H** that, together with **F**, define **Q** in Eq. (4.48). Thus, the bonafide commutation relations of the $\hat{a}_j(z,\omega)$ are guaranteed by the algebraic structure of the equations of motion it satisfies, together with the initial conditions for the commutators derived (Eq. (4.61)). Because of the Lie group constraints, the transfer functions can be *jointly* decomposed as follows

$$U^{s,s}(\omega,\omega';z,z_0) = \sum_l \cosh(r_l)[\rho_s^{(l)}(\omega)][\tau_s^{(l)}(\omega')]^*, \tag{4.67a}$$

$$U^{s,i}(\omega,\omega';z,z_0) = \sum_l \sinh(r_l)[\rho_s^{(l)}(\omega)][\tau_i^{(l)}(\omega')], \tag{4.67b}$$

$$(U^{i,i}(\omega,\omega';z,z_0))^* = \sum_l \cosh(r_l)[\rho_i^{(l)}(\omega)]^*[\tau_i^{(l)}(\omega')], \tag{4.67c}$$

$$(U^{i,s}(\omega,\omega';z,z_0))^* = \sum_l \sinh(r_l)[\rho_i^{(l)}(\omega)]^*[\tau_s^{(l)}(\omega')]^*, \tag{4.67d}$$

where the quantities r_l are the squeezing parameter of the Schmidt mode l and the sets of functions $\left\{\rho_{s,i}^{(l)}\right\}$, $\left\{\tau_{s,i}^{(l)}\right\}$ are complete and orthonormal, and thus for example

$$\int d\omega\ \rho_s^{(l)}(\omega)\ [\rho_s^{(l')}(\omega)]^* = \delta_{l,l'}, \tag{4.68a}$$

$$\sum_l \rho_s^{(l)}(\omega)\ [\rho_s^{(l)}(\omega')]^* = \delta(\omega-\omega'). \tag{4.68b}$$

4.3 A simple example

We can use these results to study what is perhaps the simplest case of twin-beams generation: a $\chi^{(2)}$ process in which the nonlinearity has a flat top-hat profile and we ignore any effect of cross- and self-phase modulation. With the modification of the pump function by SPM neglected and the nonlinearity function $\xi(z)$ a top-hat function extending from $\ell_{\min} = -\frac{\ell}{2}$ to

$\ell_{\max} = \frac{\ell}{2}$, the matrix $\mathbf{Q}$ in Eq. (4.48) is independent of z in the region where the nonlinearity is present. Because of this we can write (recall Eq. (4.53))

$$\mathbf{U}\left(-\tfrac{\ell}{2}, \tfrac{\ell}{2}\right) = \exp(i\mathbf{Q}\ell),$$

and the calculation of the matrix propagator $\mathbf{U}$ is reduced to a single exponentiation, which is one the main advantages of working with the $a(z,\omega)$ operators instead of the $\psi(z,t)$ operators. This matrix exponentiation can be efficiently computed using standard functions in Mathematica.

For illustration, we study a Gaussian pump

$$\langle \psi_p(z,t_0)\rangle = \sqrt{\frac{N_p}{\sqrt{\pi}v_p/\sigma}}\exp\left(-\frac{(z-z_0+v_p(t-t_0))^2}{2(v_p/\sigma)^2}\right),$$

localized around $z = z_0$ at time $t = t_0$, and with bandwidth σ and mean number of photons $N_p = \int dz|\langle\psi(z,t_0)\rangle|^2$. We will work in the symmetric group velocity matched regime[107], in which the argument of the sinc function becomes

$$\tfrac{\ell}{2}\left\{\Delta k_s(\omega) + \Delta k_i(\omega')\right\} = \kappa\left\{(\omega-\bar{\omega}_s) - (\omega'-\bar{\omega}_i)\right\}, \tag{4.69}$$

and furthermore pick the parameter $\kappa = 1.61/\sigma$, which matches the bandwidths of the pump and phase-matching functions.

Cross-mode transfer functions and joint spectral amplitude

We can use the input-output relations established for the signal and idler bosonic operators (4.60) to compute the joint spectral amplitude (JSA) of this SPDC process. The two-mode squeezed vacuum generated in SPDC has the form

$$|\text{TMSV}\rangle = \exp\left(\int d\omega d\omega' J(\omega,\omega') a_s^{(\text{in})\dagger}(\omega) a_i^{(\text{in})\dagger}(\omega') + \text{h.c}\right)|\text{vac}\rangle. \tag{4.70}$$

where $J(\omega,\omega')$ is called the JSA. This state is described univocally by its first and second moments. Matching the moments obtained from the Schrödinger-picture TMSV state and those obtained using the Heisenberg-picture propagator $\mathbf{U}$, we connect the two descriptions. We find that the JSA is conveniently expressed in terms of the Schmidt modes and squeezing parameters of the Heisenberg-picture transfer functions (4.67) [108]

$$J(\omega,\omega') = \sum_l r_l \; \rho_s^{(l)}(\omega)\rho_i^{(l)}(\omega'). \tag{4.71}$$

In the low-gain regime, the JSA is equal to the cross-mode transfer function [104,108], and its first-order perturbative expansion is simply [98]

$$J(\omega,\omega') = \xi^{(0)}\sqrt{\frac{N_p}{2\pi v_s v_i v_p \sigma\sqrt{\pi}}}\exp\left(-\frac{(\omega+\omega'-\bar{\omega}_p)^2}{2\sigma^2}\right) \times \ell \; \text{sinc}\left(\tfrac{\ell}{2}\left\{\Delta k_s(\omega)+\Delta k_i(\omega')\right\}\right), \tag{4.72}$$

where $\xi^{(0)}$ is the nonzero value the nonlinearity function $\xi(z)$ takes in the the region $-\ell/2 < z < \ell/2$. In Fig. 4.1 we show that the absolute value of the JSA obtained with our model

agrees with the low-gain analytical solution (4.72) for small values of the interaction strength but not in the high-gain regime. This is because of so-called time-ordering corrections (TOC), which modify the spectral structure of the SPDC emission. Indeed, our results agree with the TOC described in [33]. Unlike in iterative approaches, the computation times for each JSA on a desktop computer, using a grid of 150 frequencies, takes seconds regardless of the value of N_p. The mean number of photons spontaneously generated in the signal/idler is

$$\langle N_j \rangle = \int \mathrm{d}\omega \langle \hat{a}_j^{(\mathrm{out})\dagger}(\omega)\, \hat{a}_j^{(\mathrm{out})}(\omega) \rangle = \sum_l \sinh^2(r_l). \tag{4.73}$$

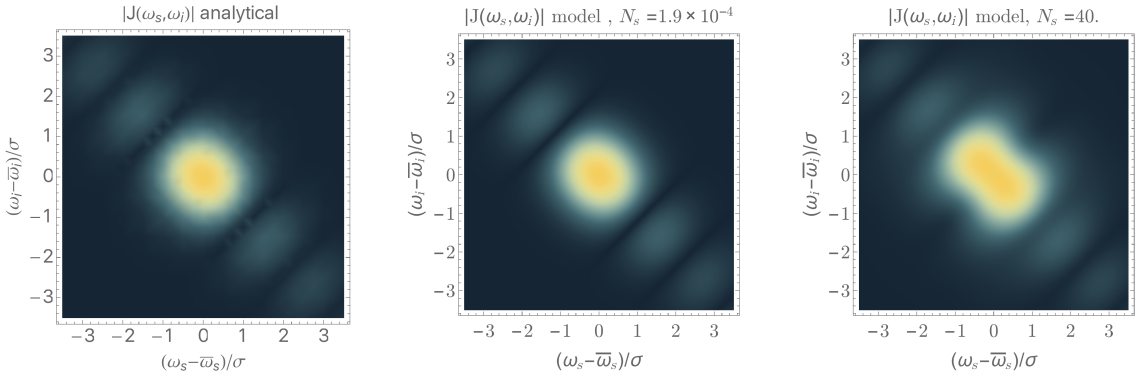


Figure 4.1: Absolute values of the joint spectral amplitude in the symmetric group velocity matched regime. The low-gain analytical solution (left) agrees with of our model at low interaction strengths (middle), but not in the high gain regime (right).

In the non-perturbative regime, the brightness of SPDC also deviates from the low-gain description. While in the low gain regime the amplitude of the JSA (4.72), and therefore the derived squeezing parameters r_k, are proportional to $\sqrt{N_p}$, this is not so in the high-gain regime. In Fig. 4.2 we show the evolution of the squeezing parameters of the JSA from the low-gain regime to the high-gain regime as the pump intensity N_p is increased. As predicted using the Magnus expansion [33,103], the squeezing parameters behave in a nonlinear way as

a function of $\sqrt{N_p}$.

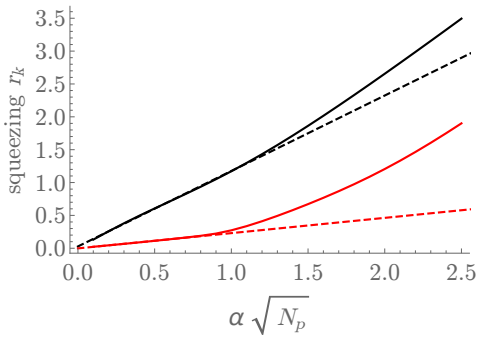


Figure 4.2: We plot the squeezing parameters $\{r_k\}$ of the first two Schmidt modes obtained with our model for a range of $\sqrt{N_p}$(solid lines). For low gain, the squeezing parameters r_k agree with a linear fit to $\sqrt{N_p}$ (dashed lines), but this linearity is lost at high gains.

The same-mode transfer function

While the JSA and the closely related cross-mode TFs have become standard objects to characterize a SPDC source, less attention has been paid to the same-mode TFs. Neglecting the effect of SPM and XPM, the differential equations that describe SPDC (4.39) contain a first term that describes linear propagation of the signal and idler and a second term that describes their nonlinear coupling. Solving these equations perturbatively to first order in the nonlinear interaction strength[36,104] yields that the same-mode transfer functions are simply

$$U_{s,s}(z, z_0, \omega, \omega') \approx \delta(\omega - \omega') \exp(i\,(z - z_0)\Delta k_s(\omega)), \tag{4.74}$$

$$U_{i,i}(z, z_0, \omega, \omega') \approx \delta(\omega - \omega') \exp(i\,(z - z_0)\Delta k_i(\omega)), \tag{4.75}$$

which simply describe the linear propagation in the medium, without involving any nonlinear interaction. However, it has been shown [104] that including higher order terms in this expansion yields a same-mode transfer function with a more complex structure. In Fig. 4.3 we show the absolute value of the same-mode transfer functions corresponding to the twin-beam generation cases analyzed previously. While in the low-gain regime we obtain the expected diagonal TF, in the high-gain case we observe a broadband "pedestal" that induces coupling between different frequencies. As will be seen later, this coupling is interpreted as a cascaded nonlinear process between the twin beams and the pulsed pump [104].

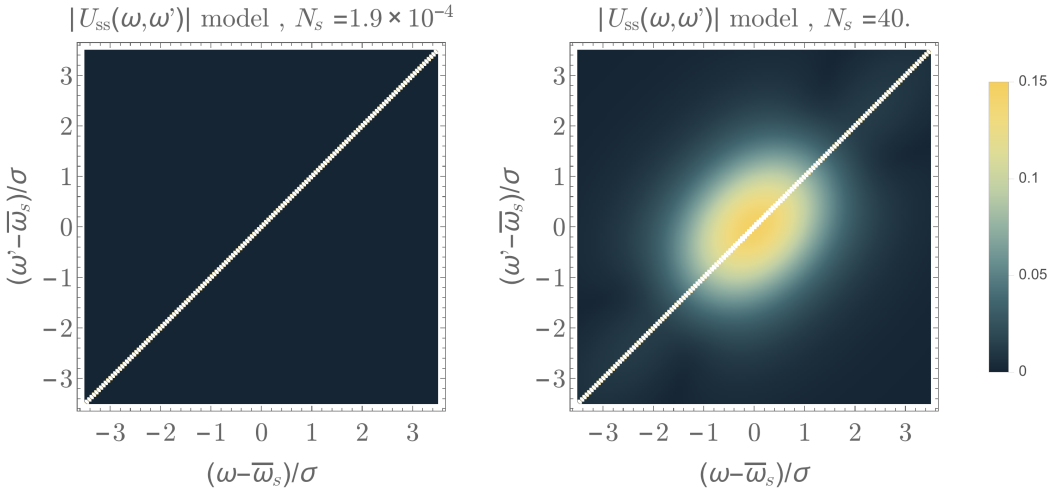


Figure 4.3: Same mode transfer function. Left: the low gain same-mode transfer function is a diagonal delta function. Right: in the high-gain, the same-mode transfer function has a broadband "pedestal".

4.4 Summary and outlook

In this chapter we have introduced new theoretical tools to study parametric twin-beam generation in the high gain regime. We have provided a framework to efficiently simulate a waveguided and pulsed SPDC process for an arbitrarily high nonlinear gain, including the

effect of parasitic nonlinearities such as SPM of the pump and XPM between the pump and the twin beams. The development of this theoretical framework was motivated by the experimental results presented in Chapter 5, where we characterize a twin-beam source in the high gain regime. Our observation of spectral features which could not be accounted for by a simple perturbative model prompted us to develop the theoretical tools presented in this chapter. Besides its generality, our theoretical framework also has the virtue of being efficient: in the scenario where SPM of the pump is negligible, we require a single matrix exponentiation operation to compute all the transfer functions that describe the broadband PDC unitary operation. This contrasts with previous approaches, which required a longer iterative computation to account for the high-gain corrections to the PDC transformation.

3

Chapter 5

Understanding high-gain twin-beam generation through cascaded stimulated emission tomography

5.1 Cascaded stimulated emission tomography

A large body of work has been devoted to characterizing pulsed SPDC sources. Initially, the joint spectral intensity of a source (absolute square of the JSA) was measured by scanning monochromators to select a pair of wavelengths for the signal and idler, and detecting photon coincidences with avalanche photodiodes (APDs) [23]. Subsequently, a more efficient measurement scheme was realized using time-of-flight measurements and dispersive optical fibers [109].

In 2013, Liscidini and Sipe introduced stimulated emission tomography (SET) [105], a general approach used to infer the quantum properties of a spontaneous nonlinear process,

e.g. spontaneous PDC, from an intensity measurement of its corresponding stimulated process, e.g. difference frequency generation (DFG). This approach, which has been the basis of many experiments[110–115], provides a detailed description of the spectral mode structure of a PDC process, but often fails to yield a reliable estimation of the degree of squeezing. It is in principle possible to derive the squeezing strength in a type-II PDC process from the brightness of the DFG signal produced when this is stimulated with a coherent seed. However, this approach is in practice hindered by the uncertainty in the amount of overlap between the seeding and amplified modes (e.g. spatial or polarization overlap), as well as the optical loss in the experiment. An alternative characterization technique consists in using higher order photon correlation functions of the down-converted field to estimate the number of modes in the source[116–118]. This approach has the advantage of being insensitive to loss, but provides little information about the physical mechanisms that degrade the performance of the source.

Here we demonstrate a method that provides complete spectral information about a PDC process, including the absolute value of its squeezing parameters, and which is applicable to the high gain regime. We extend SET to the measurement of all the stimulated emission processes (including cascaded processes) implied by the quadratic nonlinear interaction, as illustrated in figure 5.1. We will show that the measured spectra are interpreted in terms of the transfer functions introduced in the last section (Eq. (4.54)). To our knowledge these aditional measurements have not been reported to date.

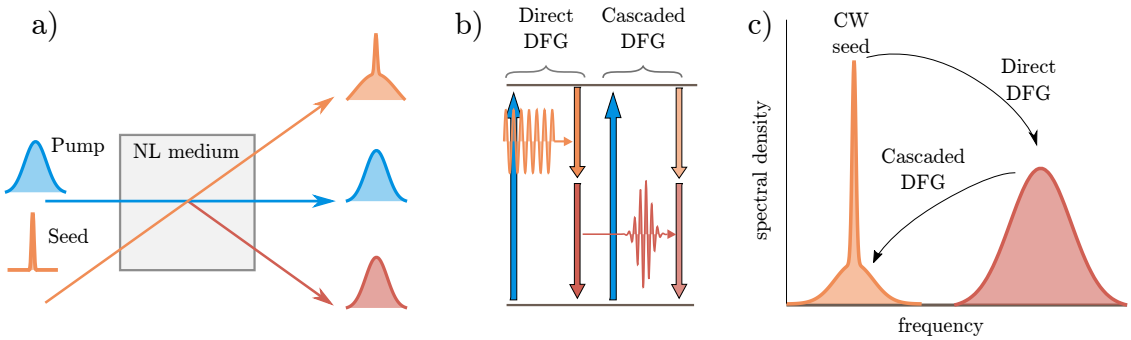


Figure 5.1: a) Schematic of an extended SET experiment, including the broadband light generated in the seeding beam through a cascaded DFG process. b) Cascaded stimulated emission in a PDC crystal. Seeding one of the two down-conversion modes with a continuous wave (CW) field (represented in orange), bright light is generated through DFG between the pump (represented in blue) and the seed. The DFG signal (represented in red) acts as seed for a second DFG interaction with the pump field, leading to broadband light generation in the mode that was originally seeded. The process is repeated with decreasing strength. c) Spectra of cascaded stimulated emission. Seeding with a CW laser, broadband light is generated in the opposite polarization (red) as well as in the same polarization as the seed (orange).

5.1.1 All spectral transfer functions from cascaded stimulated emission

In SET experiments, a monochromatic coherent seed field is coupled to one of the down-conversion modes. The seed stimulates the generation of coherent light in the conjugate mode, which is also known as classical DFG. The stimulated emission is mapped over a range of seed frequencies, resulting in a joint spectral distribution [105]. There is a simple, general correspondence between seeded and unseeded processes, as the input-output relations in Eq. (4.54) remain valid when the creation/annihilation operators are replaced by classical field amplitudes $\alpha_{s(i)}(\omega)$. A broadband coherent seed in the signal mode can be described as a displaced vacuum, which in the Heisenberg picture is simply represented by adding a frequency dependent constant to the annihilation operators.

$$a_s^{(in)}(\omega) = a_s^{(vac)}(\omega) + \alpha_s(\omega). \tag{5.1}$$

Starting with a coherent state in the signal mode, and vacuum in the idler, the bosonic operators after the PDC transformation (4.54) will be

$$\begin{aligned} a_{\mathrm{s}}^{(\mathrm{out})}(\omega) &= \int d\omega'\, U^{\mathrm{s,s}}(\omega,\omega')\,[a_{\mathrm{s}}^{(\mathrm{vac})}(\omega') + \alpha_s(\omega')] + \int d\omega'\, U^{\mathrm{s,i}}(\omega,\omega')\, a_{\mathrm{i}}^{\dagger(\mathrm{vac})}(\omega'), \\ a_{\mathrm{i}}^{(\mathrm{out})}(\omega) &= \int d\omega'\, U^{\mathrm{i,s}}(\omega,\omega')\,[a_{\mathrm{s}}^{\dagger(\mathrm{vac})}(\omega') + \alpha_s^*(\omega')] + \int d\omega'\, U^{\mathrm{i,i}}(\omega,\omega')\, a_{\mathrm{i}}^{(\mathrm{vac})}(\omega'), \end{aligned} \tag{5.2}$$

Then a spectrally resolved measurement of the output idler intensity will yield

$$\begin{aligned} I_i(\omega) &= \langle [a_i^{(\mathrm{out})}(\omega)]^\dagger a_i^{(\mathrm{out})}(\omega)\rangle \\ &= |\int d\omega'\, U^{\mathrm{i,s}}(\omega,\omega')\,\alpha_{\mathrm{s}}^*(\omega')|^2 + |\int d\omega'\, U^{\mathrm{i,s}}(\omega,\omega')|^2 \end{aligned} \tag{5.3}$$

where we identify that the first term corresponds to DFG between the pump and the seed beams, while the second term describes SPDC. This spontaneous term can be made negligible for strong enough seed fields. For a narrowband seed of frequency ω_0, the measured intensity at the output will be

$$I_{i,s}(\omega,\omega_0) = |U^{\mathrm{i,s}}(\omega,\omega_0)|^2, \tag{5.4}$$

This has been previously used to characterize the joint spectral probability of photon pair emission in the low squeezing regime [110].

In addition to stimulating emission in the conjugate idler mode, the coherent seed in the signal mode can also be modified by the PDC interaction. A spectrally resolved measurement

of the ouput signal intensity will yield

$$\begin{aligned} I_{s,}(\omega) &= \langle [a_s^{(\mathrm{out})}(\omega)]^\dagger a_s^{(\mathrm{out})}(\omega)\rangle \\ &= |\int d\omega' \, U^{\mathrm{s,s}}(\omega,\omega')\alpha_{\mathrm{s}}(\omega')|^2 + |\int d\omega' \, U^{\mathrm{s,i}}(\omega,\omega')|^2, \end{aligned} \tag{5.5}$$

where we identify that for a strong, narrowband seed field we can measure the absolute value square of the same-mode transfer function

$$I_{s,s}(\omega,\omega_0) = |U^{\mathrm{s,s}}(\omega,\omega_0)|^2, \tag{5.6}$$

While for low gain $U^{\mathrm{s,s}}(\omega,\omega') \approx \delta(\omega-\omega')$, as the squeezing strength increases, a broadband "pedestal" is generated around the seed frequency. We can interpret this as cascaded stimulated emission. A simple physical picture is that the direct DFG emitted in the signal mode (Eq. (5.5)) stimulates the generation of new frequencies in the idler mode. The broadband part of the same-mode TFs is difficult to measure, because it is much weaker than the seed field. In what follows we will denote the broadband part of the same-mode TF, which we associate with a cascaded nonlinear process, as

$$U_{(\mathrm{b})}^{\mathrm{s,s}}(\omega,\omega') = U^{\mathrm{s,s}}(\omega,\omega') - \delta(\omega-\omega'), \tag{5.7}$$

and analogously for the signal.

5.1.2 Self-referenced measurement of squeezing strength

The imperfect overlap between the seeding beam and the PDC modes, e.g. due to polarization or spatial mismatch, as well as the imperfect coupling/detection efficiency, introduces

a rescaling of the DFG intensity which is difficult to calibrate accurately. In a realistic experiment, equations (5.4) and (5.6) must be replaced with

$$I_{(b)}^{s,s}(\omega,\omega_0) = \eta_{s,s}\,|U_{(b)}^{s,s}(\omega,\omega_0)|^2 \qquad I_{i,s}(\omega,\omega_0) = \eta_{i,s}\,|U^{\mathrm{i,s}}(\omega,\omega_0)|^2, \tag{5.8}$$

where the proportionality constants $\eta_{s,s}$ and $\eta_{i,s}$ describe the imperfect detection and mode-matching with the seed. We have assumed that we measure only the broadband part of the same-mode TF, which contains information about the nonlinear process. We will refer to these signals as same-mode and cross-mode DFG signals, in analogy with the transfer functions that they contain. The unknown rescaling in the DFG emission prevents us from estimating the squeezing strength directly from the cross-mode DFG signal.

Here we will show that, if we can assume that the TFs are real (i.e. their spectral phases are negligible), we can retrieve the squeezing strength directly from relative intensity measurements. This assumption holds when the pump pulse is Fourier limited and the effect of self-phase modulation is negligible. Assuming that all TFs are real, the square root of the same and cross-mode DFG signals correspond directly to the TFs rescaled by the unknowns proportionality constants $\eta_{s,s}$ and $\eta_{i,s}$. The singular value decomposition of these signals is then (recall Eq.(4.67))

$$\sqrt{I_{(b)}^{s,s}(\omega,\omega')} = \sqrt{\eta_{s,s}}\,\Big(\sum_l \cosh(r_l)\,\rho_s^{(l)}(\omega)\,\tau_s^{(l)}(\omega') - \delta(\omega-\omega')\Big), \tag{5.9a}$$

$$\sqrt{I^{i,s}(\omega,\omega')} = \sqrt{\eta_{i,s}}\,\sum_l \sinh(r_l)\,\rho_i^{(l)}(\omega)\,\tau_s^{(l)}(\omega'), \tag{5.9b}$$

where $\rho_s^{(l)}, \rho_i^{(l)}, \tau_s^{(l)}, \tau_i^{(l)}$ are the Schmidt mode functions of the TFs, and r_l are their corres-

ponding squeezing parameters. For a low parametric gain and with a Fourier-limited pump, the input and output eigenmodes of the source are identical[36], $\rho^{(l)}_{\mathrm{s(i)}}(\omega) = \tau^{(l)}_{\mathrm{s(i)}}(\omega)$, allowing us to use the completeness relation of the eigenbasis and write

$$\sqrt{I^{s,s}_{(b)}(\omega,\omega')} = \sqrt{\eta_{s,s}}\ \sum_{l}(\cosh(r_l)-1)\,\rho^{(l)}_{\mathrm{s}}(\omega)\rho^{(l)}_{\mathrm{s}}(\omega'). \tag{5.10}$$

We can compute the decompositions in Eq. (5.9b) and (5.10) directly from intensity measurements, and extract from them the rescaled Schmitd coefficients

$$\lambda^{(l)}_{s,s} = \sqrt{\eta_{s,s}}\ (\cosh(r_l)-1) \approx \sqrt{\eta_{s,s}}\ r_l^2/2 \tag{5.11}$$

$$\lambda^{(l)}_{i,s} = \sqrt{\eta_{i,s}}\ \sinh(r_l) \approx \sqrt{\eta_{i,s}}\ r_l \tag{5.12}$$

where we have used a Taylor expansion in the squeezing coefficients r_l. If we assume that the rescalings for both measurements are equal, $\eta_{s,s} = \eta_{i,s}$, the squeezing coefficients are computed directly from the ratio $\lambda^{(l)}_{s,s}/\lambda^{(l)}_{i,s}$, regardless of the detection efficiency and mode overlap. This illustrates the the potential for self-referencing offered by the simultaneous measurement of the cross-mode and same-mode DFG signals

5.1.3 The need for a model-based approach

In the last section we made a number of simplifications in order to provide some initial intuition on the self-referencing potential of the technique that we introduced. In the first place, we made the important assumption that the TFs describing PDC are real, which is often invalid in real experiments: for instance, the pump field may have a non-flat spectral phase (e.g. chirp) which is transferred to the joint spectral amplitude of SDPC emission

(4.72). The existence of a non-factorable spectral phase is a cause of spectral multimodeness that cannot be detected using traditional measurements of the joint spectral intensity [114]. In addition, we made the assumption that the input and output eigenmodes of the source are identical, $\rho^{(l)}_{\mathrm{s(i)}}(\omega) = \tau^{(l)}_{\mathrm{s(i)}}(\omega)$, which is only the case in the low-gain regime.

In the next section we will take a model-based approach to interpreting direct and cascaded DFG measurements. We will use the model of PDC that we introduced in Sec. 4.2 and fit all of its parameters using a combination of SET data and complementary additional measurements. The self-referencing character of the measurement is preserved by the fact that our model needs to yield both the same and cross-mode TFs, with appropriate amplitudes. We obtain a single physical model that correctly predicts the measured direct and cascaded DFG data ($I_{s,s}, I_{s,i}, I_{i,i}, I_{i,s}$) for a range of pump powers, reaching well into the high-gain regime. The simplicity and physical likelihood of the resulting model, together with its agreement with the complex experimental data in the high gain regime, gives us assurance about its correctness. In consequence, we can use this model (which includes spectral phase, high-gain effects, etc.) to compute the complex TFs that describe the PDC process. The picture that we obtain describes a process where not only high-gain PDC, but also SPM of the pump and XPM between the pump and the downconverted fields, determine the spectral characteristics of the light emission.

5.2 Experimental demonstration

5.2.1 Parametric down-conversion source

Here we apply our method to perform a measurement of all spectral TFs of a bright PDC source. The PDC source used in this work consists of a waveguided ppKTP crystal pumped

by a pulsed Ti:sapphire laser with a center wavelength of 783 nm. The phase-matching of the type-II PDC process has been engineered to obtain signal and idler fields at telecom wavelengths with an almost separable joint spectrum. In the weak squeezing regime the joint spectrum of a PDC source can be expressed as a product of two factors: a pump function and a phase matching function. As illustrated in figure 1.2, the pump function, which enforces energy conservation, introduces anti-correlation of the frequencies of photons generated in the PDC process. The phase matching function, which enforces momentum conservation, depends on the dispersion relation of the guided modes. In a medium with normal dispersion, both signal and idler commonly have higher group velocity than the pump, resulting in frequency anti-correlations[23]. In the wave-guided ppKTP, due to the birefringence of the material, the group velocity of a pump field at 783 nm in the ordinary polarization falls in-between the group velocities of the signal and idler fields centered around 1560 nm in orthogonal polarizations. This results in a phase-matching function with positive frequency correlations[100] which, as illustrated in figure 1.2, can produce an almost separable joint spectrum, with the correct balance of pump and phase matching bandwidths. The KTP is periodically poled in order to attain quasi-phase matching for signal and idler around 1560 nm.

The nonlinear crystal in our experiment is an 8mm ppKTP chip manufactured by Advanced Research (AdvR), made from a z-cut wafer, with a set of waveguides written using a proton exchange process. The waveguides are roughly $4\mu m \times 4\mu m$ in cross section. The chip output is anti-reflection (AR) coated for 1550 nm. We pump the source with a pulsed Ti:Sapphire laser (Coherent Chameleon) with central wavelength 783 nm and 8nm bandwidth, which we filter using two bandpass thin-film filters (Semrock LL01-785-12.5) to a

bandwidth of 1.9 nm. Using an ordinarily polarized pump (H polarization), we obtain a signal (H polarization) and idler (V polarization) beams with respective central wavelengths of 1563 nm and 1569 nm. The periodic poling has a spatial period of 104μm.

This design [100] has previously been used in the high-gain regime, measuring spontaneous PDC with mean photon numbers as high as 20 per pulse [101], giving this device unprecedented performance for its squeezing achieved on a small number of spectral modes. However, the limits of this system are still unclear. For instance, the effect of high gain phenomena on the joint spectral properties of this source has not been systematically considered.

5.2.2 Stimulated emission measurements

The cascaded stimulated emission setup is depicted in figure 5.2. We send the pump pulses with center wavelength of 783nm in the ordinary axis of the crystal (H polarization), generating a signal field with the central wavelength at 1563 nm in the H polarization and an idler field at 1569 nm in the V polarization. To measure the direct and cascaded DFG signals we seed one of the downconverted fields with a continuous wave laser with wavelength tunable between 1500nm and 1680nm (Yenista Tunics T100S-HP), filter in polarization using birefringent waveplates and a Glan-Taylor polarizer, and measure the generated stimulated emission using an optical spectrum analyzer (Yokogawa AQ6370D).

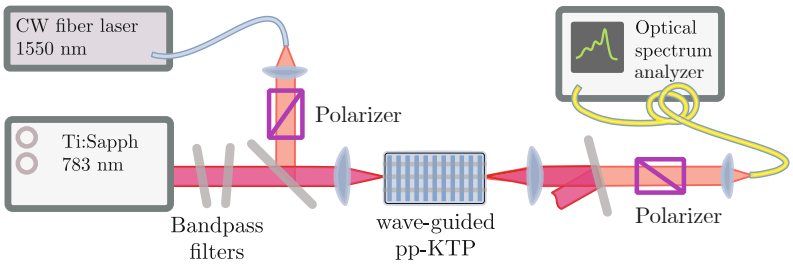


Figure 5.2: Experimental setup.

The laser has a very high spontaneous noise suppression (>100 dB over a bandwidth of 1 nm), and the OSA has a high dynamic range (78 dB over 1nm), allowing us to distinguish the weak broadband cascaded DFG signal (<1nW) from the narrowband seed ($\approx 600\mu$W). While the linewidth of the seed laser is many orders of magnitude smaller than the broadband cascaded DFG emission, the finite resolution of the OSA (0.2 nm) broadens the width of the narrowband component of the spectra, hindering the retrieval of the broadband pedestal. To remove the CW seed from the data we first subtract a background trace from it, where we send the seed beam but not the pump through the crystal. Fluctuations of the seed power between the moment when the data and the background are measured lead to an imperfect extinction of the narrowband component. We eliminate this CW remnant by masking the frequency range occupied by it and interpolating the remaining spectrum, as illustrated in figure 5.3.

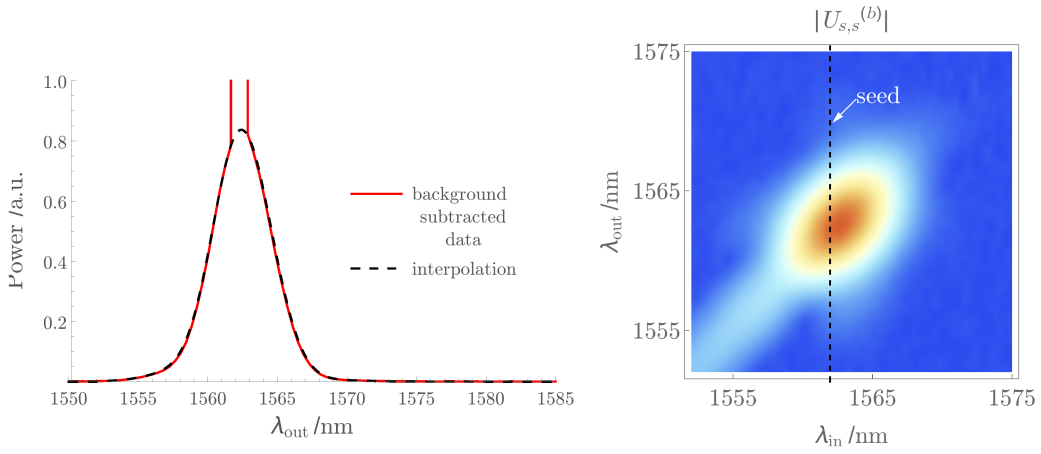


Figure 5.3: a). Reconstruction of the stimulated emission spectrum as a function of seeding wavelength, measured in the seed polarization; color indicates the absolute value of the field (square root of the measured spectral power density) b). One "slice" of the background subtracted data (red), showing a noisy measurement around the seed wavelength, where the OSA detector is blinded by the seed; reconstructed spectrum obtained by interpolating over the noisy region (dashed black).

5.2.3 Results

We performed measurements for pump pulse energies ranging from 125 pJ to 600 pJ. For each pump power, we obtained all four TFs (absolute value) as explained above. In what follows, we will detail how we used the SET data, together with some additional measurements, to fit the model presented in equation (4.39). Remarkably, a single model is able to very accurately account for all the experimental data in the pump energy range that we probed.

Low squeezing cross-mode TFs

We first measured the cross-mode stimulated emission as a function of seeding wavelength, using a relatively low pump power (125 pJ), which reproduces a standard SET experiment. The results correspond to the $U^{\mathrm{s,i}}$ and $U^{\mathrm{i,s}}$ TFs shown in figure 5.4. The measured spectral distribution may be interpreted as the joint spectrum of photon pairs generated in the source. To obtain the fits shown in Figure 5.4 we independently measured the pump spectral intensity and phase, as well as the width and orientation of the phase-matching profile. In what follows, we provide some detail about these measurements.

Pump spectral intensity The pump spectral amplitude, $\alpha_{\mathrm{p}}(z,\omega)$, is generally a complex-valued function describing the spectral density of the pump beam at position z in the crystal. In our experiment, we measure the absolute value of $\alpha_{\mathrm{p}}(z=0,\omega)$ in two ways: on the one hand, we perform a direct measurement of the pump spectrum using an OSA, which provides the modulus square of the pump function (see figure 5.5). On the other hand, we compare this to the projection of a low gain joint spectral intensity along the 45° direction (the pump function). These two measurements agree well , as is expected from the perturbative solution of the PDC interaction.

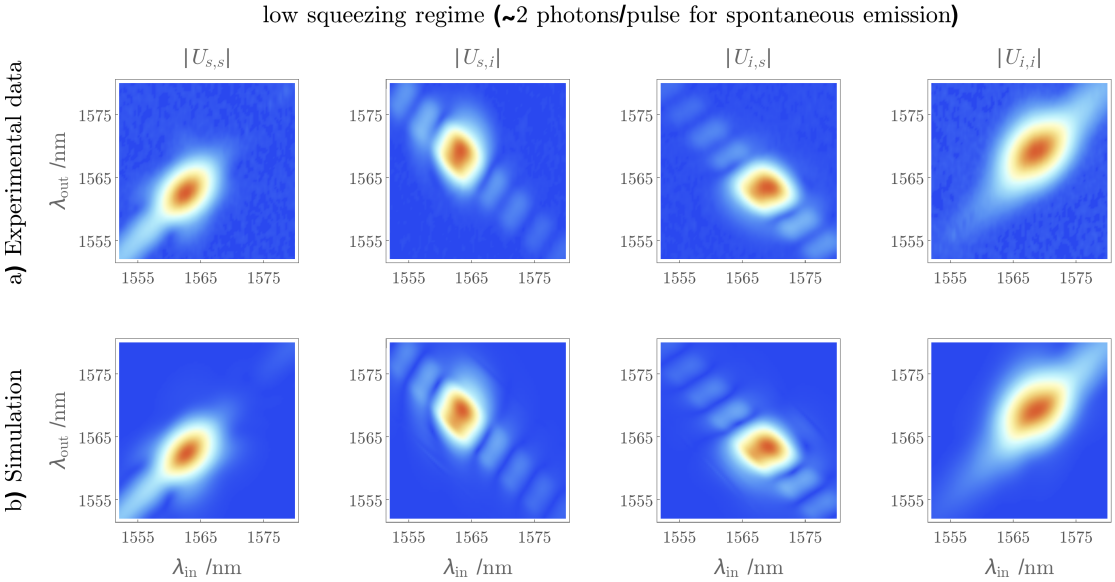


Figure 5.4: All measured and modeled TFs, in the low squeezing regime. The color scale is normalized separately for each density plot. The TFs are plotted as a function of wavelength instead of angular frequency, where these are connected by $\lambda = 2\pi c/\omega$.

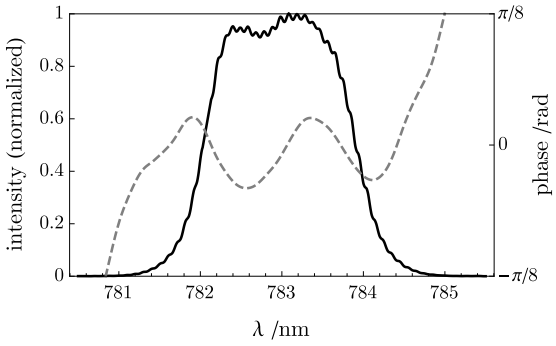


Figure 5.5: Spectral intensity and phase of the filtered pump. Intensity measured with an OSA. Phase measured using Spider and spectral interference with a reference pulse.

Pump spectral phase In addition to knowing the pump spectral intensity, our model requires us to estimate its spectral phase. In our experiment we used an APE LX-Spider (wavelength range between 750 and 900 nm), to characterize the spectral phase of the Ti:Sapphire pump laser, but could not extend that measurement to the filtered pump (1.9 nm

bandwidth) because of the limit in the spectral resolution of the apparatus. We characterized the spectral phase added by the filters using a spectral self-interference measurement: the filtered pump was interfered with a delayed sample of the unfiltered pump, thus revealing their differential spectral phase.

Let us briefly sketch the procedure to recover the phase added by the optical filters. Assuming that the spectrum of the unfiltered sample is much broader than that of the filtered pump, such that it can be treated as a constant spectral density, the complex spectral amplitude of the sum of the fields is

$$A(\omega) = E_f(\omega)\, e^{i\phi(\omega)} + E_r\, e^{i\Delta t\, \omega} \tag{5.13}$$

where $E_f(\omega)$ is the spectral envelope of the filtered pump, E_r is the constant amplitude of the unfiltered pump, $\phi(\omega)$ is the spectral phase of the filtered pump and Δt is the delay between the two pulses. The measured intensity is therefore

$$I(\omega) = |A(\omega)|^2 = E_f^2(\omega) + E_r^2 + E_r E_f(\omega) \cos(\phi(\omega) - \Delta t\, \omega) \tag{5.14}$$

where we recognize that the last term describes spectral fringes with a period of approximately $1/\Delta t$, modulated by the spectral phase added by the optical filters. This modulation can be retrieved by keeping only positive frequencies above the bandwidth of the base-band component of $I(\omega)$, which retains only the complex signal

$$I_{\mathrm{HF}}(\omega) = E_r\, E_f(\omega)\, e^{i(\Delta t\, \omega + \phi(\omega)} \tag{5.15}$$

whose argument contains the spectral phase added by the filters.

The total spectral phase of the pump is obtained by adding the spectral phase of the reference beam, measured using Spider, and the phase added by the optical filters. Our measurement is shown in figure 5.5.

Phase-matching In our model we have assumed that the dispersion experienced by the interacting fields is locally linear. Under this approximation only the group velocities of the three fields, but not their group velocity dispersion coefficients, determine the linear propagation of the fields in the crystal. In this situation, we only need to obtain the two group velocity mismatch parameters, $\Delta\beta_{\mathrm{s(i)}} = 1/v_{\mathrm{s(i)}} - 1/v_{\mathrm{p}}$, to fit our model.

We recall (equation (4.72)) that in this situation the phase matching (PM) function of a low gain joint spectral amplitude has the simple form

$$\phi_{\mathrm{PM}}(\Omega_s, \Omega_i) = \mathrm{sinc}\Big(\frac{\ell}{2}(\Delta\beta_s\Omega_s + \Delta\beta_i\Omega_i)\Big) \tag{5.16}$$

where $\Omega_j = \omega_j - \bar{\omega}_j$ are the detunings from the central phase-matching frequencies. Due to the neglect of group velocity dispersion, perfect phase-matching occurs for frequencies $\Omega_i = \Omega_s \tan(\theta_{\mathrm{PM}})$, with $\tan(\theta_{\mathrm{PM}}) = -\Delta\beta_{\mathrm{s}}/\Delta\beta_{\mathrm{i}}$. Moving to a frequency frame of reference rotated by the phase matching angle, θ_{PM},

$$\Omega_{||} = \cos(\theta_{\mathrm{PM}})\Omega_s + \sin(\theta_{\mathrm{PM}})\Omega_i \tag{5.17}$$

$$\Omega_{\perp} = \cos(\theta_{\mathrm{PM}})\Omega_i - \sin(\theta_{\mathrm{PM}})\Omega_s, \tag{5.18}$$

the phase-matching function depends only on the perpendicular component:

$$\phi_{\mathrm{PM}}(\Omega_{\perp}) = \mathrm{sinc}(\frac{1}{2}\Omega_{\perp}\frac{\Delta\mu}{\cos(\theta_{\mathrm{PM}}) + \sin(\theta_{\mathrm{PM}})}) \tag{5.19}$$

where we have introduced the quantity $\Delta\mu = L(\Delta\beta_{\mathrm{s}} - \Delta\beta_{\mathrm{i}}) = L(1/v_{\mathrm{s}} - 1/v_{\mathrm{i}})$, which corresponds to the delay between the signal and idler over the crystal length. This parametrization makes it clear that, in the symmetric group velocity matching case, the phase-matching bandwidth is inversely proportional to the walk-off between the signal and idler pulses in the crystal. We can use these quantities to retrieve the group velocity mismatch parameters, $\Delta\beta_{s(i)}$, through

$$\Delta\beta_{\mathrm{s}} = \frac{\Delta\mu}{L}\frac{\tan(\theta_{\mathrm{PM}})}{\tan(\theta_{\mathrm{PM}})+1} \quad , \quad \Delta\beta_{\mathrm{i}} = -\frac{\Delta\mu}{L}\frac{1}{\tan(\theta_{\mathrm{PM}})+1} \tag{5.20}$$

To obtain the phase matching angle, θ_{PM}, we reconstruct a broad section of the phase matching function by measuring the cross-mode TF as we scan the pump frequency, thus moving the pump function along the diagonal direction, and then joining the resulting emission profiles as seen in figure 5.6.a . The phase-matching angle can be accurately measured to be $\theta_{\mathrm{PM}} = 59.2°$.

We measure the second parameter, $\Delta\mu$, in two independent ways. The first method consists in fitting the bandwidth of the phase matching function of a low-gain JSA (equation 5.19). This approach is only valid if we asume a homogeneous periodic poling in the waveguide, as an inhomogeneity in the poling would distort the phase matching function [30]. While our chip contained a number of waveguides with a distorted phase-matching (see figure 5.6.d), the measurements that we report in this work were done in the waveguide that

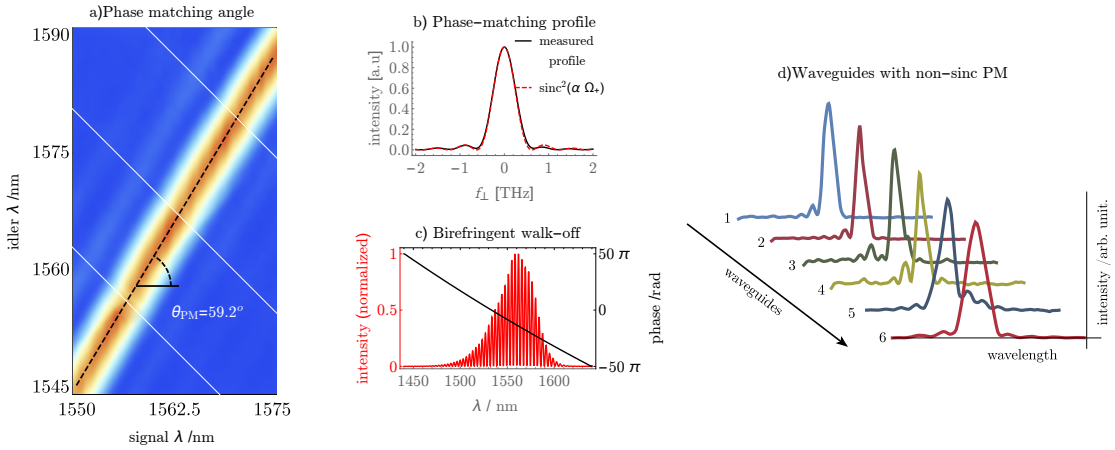


Figure 5.6: Phase-matching characterization. a) Four cross-mode TFs with different pump central frequencies are joined into a long reconstruction of the phase-matching function. The slope of the maxima of this reconstructed function gives the phase-matching angle. b) The projection of the cross-mode TF along the direction perpendicular to the PM angle angle yields the absolute square of the phase-matching profile, $|\phi_{\mathrm{PM}}(\Omega_\perp)|^2$. The measured PM profile agrees with a "sinc" function and its bandwidth is proportional to $\Delta\mu$. c) Signal-idler walk-off measurement: two orthogonal polarizations of a broadband superluminiscent LED traverse the crystal and walk-off from each other. We back off their relative delay from the spectral interference fringes measured in an OSA.

showed a phase-matching profile most closely approximating a 'sinc' function. The good agreement that we observe between our measurement and a theoretical "sinc" profile (figure 5.6.b) allows us to make the assumption that the periodic poling is homogeneous. Fitting the bandwidth of the phase-matching function, we obtain a value of $\Delta\mu = 2.2$ ps.

An alternative way of obtaining $\Delta\mu$ is by directly measuring the walk-off between the signal and idler through spectral interference. We propagate a diagonally polarized broadband field (in our case a superluminiscent LED with a bandwidth of $\sim$ 100nm) through the birefringent crystal, and send the output to a single mode fiber and into an OSA. The measured spectrum shows fringes caused by the interference between the two walked-off

polarizations. Neglecting GVD, the intensity measured in the OSA is

$$I(\omega) = |\frac{1}{2}\alpha_0(\omega)(1 + \exp(i\,\omega\Delta\mu))|^2 = \frac{|\alpha_0(\omega)|^2}{2}(1 + \cos(\omega\Delta\mu)), \tag{5.21}$$

where $\alpha_0(\omega)$ is its spectral amplitude of the broadband field and the walk-off $\Delta\mu$ induces a differential linear spectral phase on one polarization. Figure 5.6.c shows our measurement of these spectral fringes, also yielding an inferred delay between signal and idler of $\Delta\mu = 2.2$ ps.

Low-squeezing same-mode TFs

In the same setup, we succeeded in resolving a broadband stimulated emission signal in the same polarization as the CW seed, centered around the seed wavelength. We found that the intensity of this signal is maximized for the seeding wavelength that maximizes the direct DFG intensity, which identifies it as cascaded stimulated emission. By scanning the seed wavelength, we reconstruct a 2D spectral distribution, analogously to a SET measurement. As discussed in previous sections, this corresponds to absolute value squared of the same mode TFs $U^{\mathrm{s,s}}$ and $U^{\mathrm{i,i}}$, which are shown in figure 5.4 (the narrowband seed diagonal contribution has been subtracted). We compared the measured spectral distributions with the TFs calculated using the model parametrized to match the low power cross-mode TFs just mentioned. We found very good agreement between the central wavelengths and bandwidths of the measured and simulated spectra.

Cross-phase modulation However, we noticed a significant departure from the model in the tails of the measured spectral distributions: the intensity is stronger than predicted

at lower(higher) wavelengths, when seeding in the signal(idler) mode (see figure 5.7). We found that this asymmetry is explained by the presence of cross phase modulation induced by the pump pulse on the down-converted modes. In the same mode TFs, the effect of XPM appears as a constant background along the $\omega = \omega'$ contour, which in the stimulated emission process is interpreted as broadening of the CW seed spectrum due to XPM with the broadband pump. This XPM background interferes with the resonant PDC process, resulting in a Fano resonance[119]: the phase of the PDC signal has a π jump around the central frequency, which results in asymmetric interference.

We assume a constant $\chi^{(3)}$ nonlinearity along the waveguide, setting $h_{s(i)} = \Pi(z/\ell)$ in the equations of motion of the twin-beams (4.39), where $\Pi(z)$ is a normalized rectangular function. The characteristic Fano shape can be observed, in contrast to the symmetric emission predicted by a model that does not include XPM, in figure 5.7. We note that the degree of asymmetry of the same-mode TF does not depend on the interaction strength, as both cascaded PDC and XPM scale quadratically with the pump power in the low gain regime. This makes it a robust feature that can be used to estimate the ratio between $\chi^{(2)}$ and $\chi^{(3)}$ interaction strengths.

We found that the asymmetry of the Fano shape, and thus the strength of XPM, that best fits the measurement, was not equal for the signal and idler modes: the signal (with the same polarization as the pump) has a XPM interaction strength of $\gamma_{\mathrm{XPM,s}} = 0.16\,\mathrm{W}^{-1}\,\mathrm{m}^{-1}$, roughly three times greater than the idler, $\gamma_{\mathrm{XPM,i}} = 0.059\,\mathrm{W}^{-1}\,\mathrm{m}^{-1}$, which has a polarization orthogonal to that of the pump.

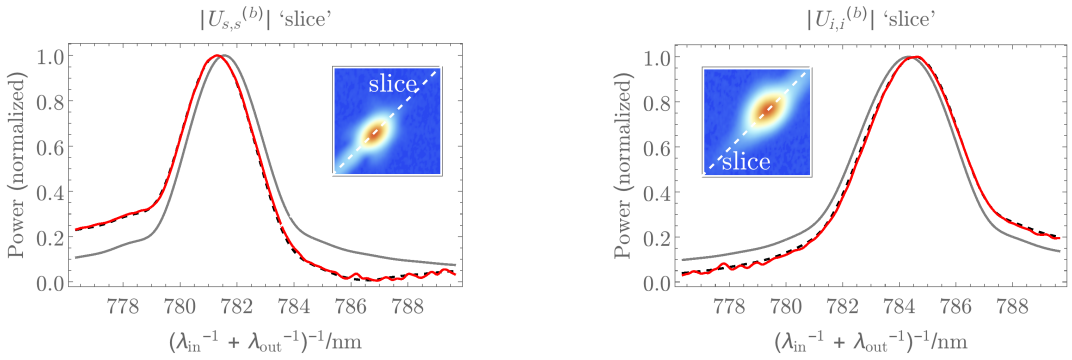


Figure 5.7: Same-mode TF slices showing effect of XPM. The plots show $\left|U^{s,s(i,i)}_{(b)}(\lambda_{in}, \lambda_{out})\right|$ for $\lambda_{in} = \lambda_{out}$. Red: Measurement (background subtracted). Black dashed: model prediction. Gray: prediction of a model that does not include XPM. The asymmetry arises from superposing the signals generated by cascaded stimulated PDC and XPM.

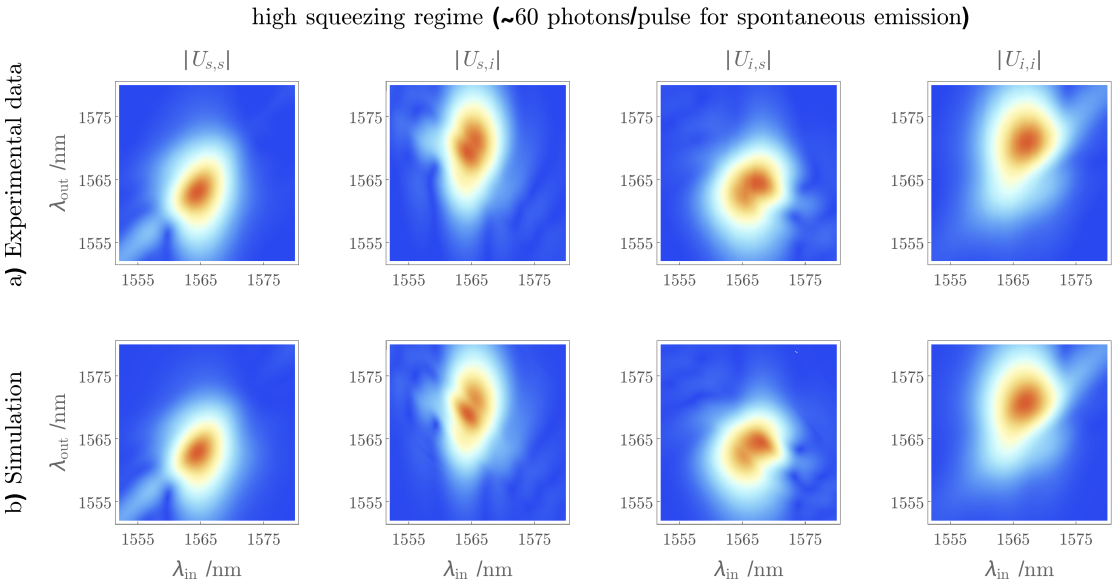


Figure 5.8: All measured and modeled TFs, in the high squeezing regime. The color scale is normalized separately for each density plot. The TFs are plotted as a function of wavelength instead of angular frequency, where these are connected by $\lambda = 2\pi c/\omega$.

High squeezing regime

Increasing the pump power, we observed additional deviations from a simple PDC model.

The experimental results in figure 5.8 contain the cross mode TFs ($U^{s,i}$ and $U^{i,s}$) measured

with a pump pulse energy of 600 pJ. The phase matching side lobes have been suppressed as expected in the high squeezing regime [116]. Simultaneously, the spectra have been broadened in a way that the simple PDC model does not account for. This observation is complemented by the measurement of the same-mode TFs ($U^{\mathrm{s,s}}$ and $U^{\mathrm{i,i}}$) in the same figure, which appears significantly shifted with respect to the diagonal.

Self-phase modulation of the pump — We were able to explain these features by including the effect of self-phase modulation in the model. The effect of SPM on the broadband pump is to induce a characteristic broadening and splitting of its spectrum [120]. This is visible in the pump function of the high-gain regime TFs, which shows a clear broadening and splitting. In addition, SPM induces a chirp in the broadband pump [120]. This spectral phase cannot be seen in the intensity of the cross-mode TFs, but it does leave a measurable trace in the same-mode TFs. As illustrated in figure 5.9, the spectral phase of the pump is mapped onto the absolute value of the same-mode TFs, as different pump frequencies interfere in the cascaded frequency generation process. In our measurement, the same-mode TFs lose their symmetry, which is consistent with a chirped pump.

To include the effect of SPM in our model, we solve for the pump pulse evolution through the crystal independently (equation 4.27) and then introduce the solution as $\alpha_{\mathrm{p}}(z,\omega)$ in the equations of motion of the twin-beams (equation 4.39). We assume a constant $\chi^{(3)}$ along the waveguide, setting the nonlinear interaction strength of equation (4.27) to be $\zeta_p(z) = \gamma_{\mathrm{SPM}}\Pi(z/\ell)$, where $\Pi(z)$ is a rectangular function, $\gamma_{\mathrm{SPM}} = \frac{2\pi}{\lambda}\frac{n_2}{A_{\mathrm{eff}}}$, with $n_2 = \frac{3\chi^{(3)}}{4\,\varepsilon_0\,c\,n(\omega)^2}$ (the material nonlinear refractive index) and A_{eff} is the effective wave-guided mode area. Given that we verified that linear dispersion does not play a significant role in the pump pulse evolution, the pump solution contains γ_{SPM} as its only free parameter. Including this

solution in the equations of motion of the twin-beams, we choose the γ_{SPM} for which the resulting TFs fit our measurements best. In particular, we use the broadening of the pump function in the cross-mode TF, as well as the shift of the same-mode TF from the diagonal, as the most relevant features to fit. The best fit is obtained for $\gamma_{\mathrm{SPM}} = 0.56\,\mathrm{W}^{-1}\,\mathrm{m}^{-1}$.

Our extended model correctly captures the features of the high gain data, as illustrated in the fitted model shown in figure 5.8. There is, therefore, clear evidence that SPM becomes relevant at this pump pulse energy.

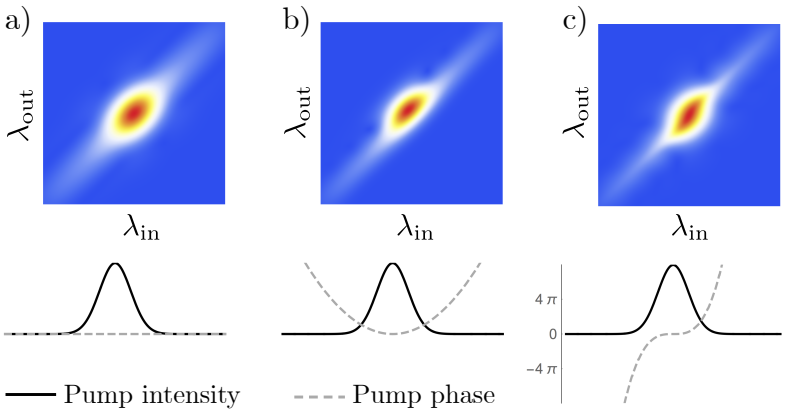


Figure 5.9: The absolute value of the same-mode TFs, $U_{(\mathrm{b})}^{\mathrm{s,s(i,i)}}(\omega,\omega'))$ is affected by the pump spectral phase. Same-mode TF for a) Fourier limited, b) chirped, and c) higher-order chirped Gaussian pump pulses (intensity and bandwidth in arbitrary units).

Self-referenced measurement of the PDC interaction strength

In section 5.1.2 we provided some intuition as to how the different scaling of the same- and cross-mode TFs allows us to obtain the squeezing parameters of the source. Here we show that the broadband part of the signal (unseeded) and idler (seeded) experimental data indeed exhibit a different scaling, which our model correctly predicts. This unequal scaling has been used to fit the strength of the PDC interaction.

In first place, we will show that we can construct a metric based on the ratio of the amplitudes of the same and cross-mode TFs, which is monotonically increasing with PDC strength and which is independent of detection efficiency and mode overlap. Defining a seeding efficiency for the signal (idler), $\eta^{\text{seed}}_{\text{s(i)}}$, and also a detection efficiency $\eta^{\text{det}}_{\text{s(i)}}$, the measured intensity distributions are related to the optical transfer functions via

$$I_{\text{s,s}}(\omega,\omega') = \eta^{\text{seed}}_{\text{s}}\,\eta^{\text{det}}_{\text{s}}\,U^{\text{s,s}}(\omega,\omega') \quad , \quad I_{\text{i,s}}(\omega,\omega') = \eta^{\text{seed}}_{\text{s}}\,\eta^{\text{det}}_{\text{i}}\,U^{i,s}(\omega,\omega') \tag{5.22}$$

and equivalently for the signal. Assuming that these efficiencies remain constant between measurements, we can construct the following quantity

$$\kappa = \frac{\max[|U^{\text{s,s}}_{\text{(b)}}(\omega,\omega')|]}{\max[|U^{\text{s,i}}(\omega,\omega')|]}\frac{\max[|U^{\text{i,i}}_{\text{(b)}}(\omega,\omega')|]}{\max[|U^{\text{i,s}}(\omega,\omega')|]}. \tag{5.23}$$

which can be obtained by dividing the respective measured intensity distributions. All the seeding and detection efficiencies are cancelled in the division. In order to mitigate the effect of measurement noise, we smooth the spectral distributions using a Gaussian kernel with a standard deviation of 0.35 nm before taking their maxima.

Assuming a homogeneous periodic poling, $g(z) = \Pi(z/\ell)$ in equation (4.39), we use the scaling of the metric κ with pump pulse energy to fit the PDC interaction strength in the equations of motion of the twin-beams (4.39), as illustrated in figure 5.10. Using the fit parameter $\gamma = 28\,\text{W}^{-1/2}\,\text{m}^{-1}$, our model correctly predicts the ratio between the amplitudes of the self and cross-mode TFs for all the pump pulse energies that we use.

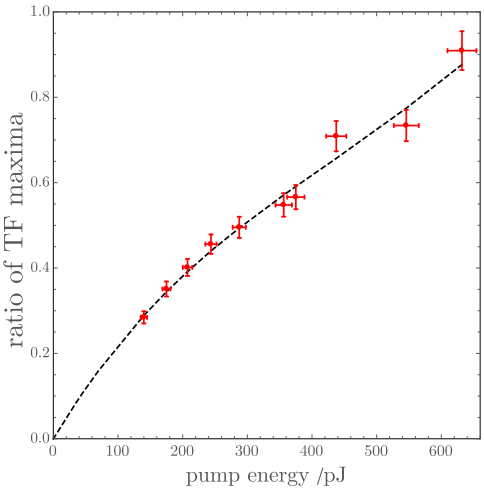


Figure 5.10: Ratio between the self and cross-mode transfer functions (κ) for different pump powers.

Validation of the model — fitting error

Using the features that we have introduced in this section, we have achieved a complete fit of the twin-beams equations of motion (4.39). Keeping the parameters of the fit constant except for the pump pulse energy, which sets the PDC, XPM and SPM interaction strengths, we achieve a very good agreement between our fits and the experimental data at all the pump pulse energies that we have probed. Figure 5.11 shows the error between the measured TFs and the fitted model, computed as

$$\text{error} = \int \mathrm{d}\omega\, \mathrm{d}\omega' \left| |U_{\text{sim}}^{\text{norm}}(\omega,\omega')| - |U_{\text{meas}}^{\text{norm}}(\omega,\omega')| \right|^2 \tag{5.24}$$

where we have defined the absolute value of the normalized simulated transfer functions

$$|U_{\text{sim}}^{\text{norm}}(\omega,\omega')| = \left| \frac{U_{\text{sim}}(\omega,\omega')}{\int \mathrm{d}\omega\, \mathrm{d}\omega' |U_{\text{sim}}(\omega,\omega')|^2} \right| \tag{5.25}$$

where $U_{\mathrm{sim}}(\omega,\omega')$ is the simulated transfer function. We have also defined the absolute value of the normalized measured TFs

$$|U^{\mathrm{norm}}_{\mathrm{meas}}(\omega,\omega')| = \frac{\sqrt{I_{\mathrm{sim}}(\omega,\omega')}}{\int \mathrm{d}\omega\, \mathrm{d}\omega' I_{\mathrm{sim}}(\omega,\omega')} \tag{5.26}$$

where $I_{\mathrm{meas}}(\omega,\omega')$ is the measured DFG signal.

The fitting error remains very low for all pump pulse energies if we use a model that incorporates XPM and SPM (solid lines). On the contrary, we see that if we do not incorporate these effects (dashed lines) the error grows at as the pump pulse energy increases.

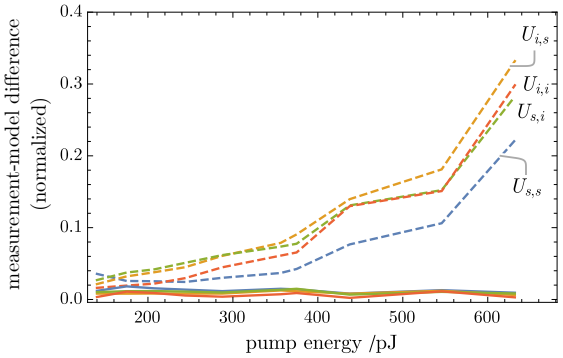


Figure 5.11: Mean-squared error between measured and modeled TFs (details in the Methods section). Solid lines – our complete model; dashed lines – PDC model not including SPM and XPM.

5.2.4 Discussion

Benefits of cascaded SET — It has been known for some time that the high-gain regime of PDC involves nonlinear phenomena that depart from the perturbative approximations usually made in ultrafast quantum optics. However, our work provides one of the first attempts to experimentally quantify these effects. We have shown that our extension of SET to all cascaded stimulated processes greatly simplifies this task: besides providing a

self-referenced measurement of PDC strength, the information obtained from cascaded DFG has been key to identifying and quantifying other relevant nonlinear processes (i.e. SPM and XPM). These additional phenomena have been clarified through our approach based on fitting physical equations of motion: features of the data that could not be explained initially have prompted the extension of our model. Moreover, by requiring that all four TFs be generated from the same EOM, we have imposed a connection between the phase of $U^{\mathrm{s,i(i,s)}}$ and the absolute value of $U^{\mathrm{s,s(i,i)}}$. We have leveraged this connection to infer phase information of the cross-mode TFs from intensity measurements of the same-mode TFs.

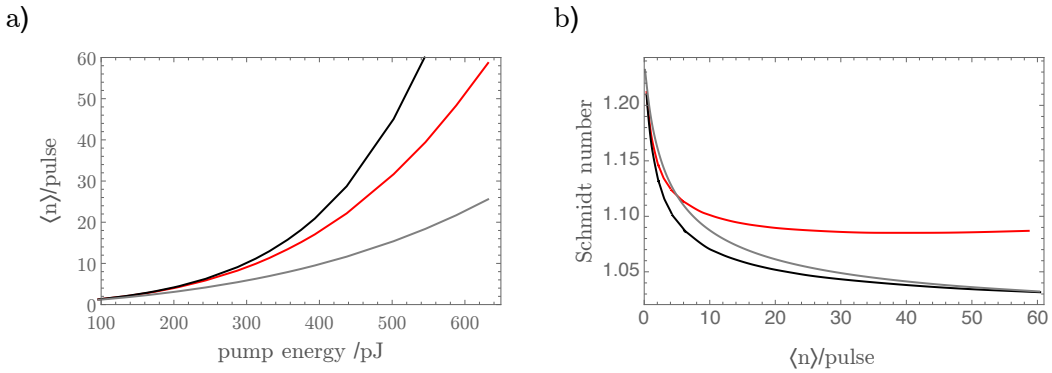


Figure 5.12: a) Average number of photons generated per pump pulse as a function of pump pulse energy. b) Spectral Schmidt number as a function of the average number of photons generated per pulse. Red – our complete model; black – PDC model not including SPM and XPM; gray – simple model assuming the average number of photons in mode k simply scales like $\sinh^2(c_k\sqrt{P})$ where P is pump power and c_k is determined from the low-gain perturbative calculation.

We have analyzed a source that aims at providing a high EPR squeezing (mean photon number) in a small number of spectral modes. Having developed a model that agrees with our experiments, we can use it to characterize the performance of the source, including the high squeezing regime, where conventional measurements become difficult to interpret. Moreover, once the model is fitted, it is easy to vary individual parameters to witness their influence on the source performance. In particular, we will determine the effect of third-

order nonlinear processes on the brightness and purity of our source. These metrics can be extracted from the Schmidt decomposition of the fitted TFs (equation 4.67).

Spontaneous mean photon number — We can calculate the mean number of spontaneously generated photons by adding the squares of the Schmidt coefficients of the cross-mode TF[38]. In the low squeezing regime, the mean number of photons generated by SPDC is linearly proportional to the pump power, whereas in the high squeezing regime it is nonlinear. It has been pointed out before[108] that for mean photon numbers higher than 2, the dependence of the mean photon number on pump power departs from the $\langle N \rangle \propto \sinh^2(c\sqrt{P})$ scaling predicted by a perturbative model of PDC[38,103], where c is a fitting parameter. Figure 5.12.a shows our results: indeed, the photon number that we infer from the fitted transfer functions (red) grows nonlinarly, at a rate faster than predicted by a perturbative model (gray). We find that the SPM affecting the pump pulse leads to a lower mean photon number than that predicted by our model in the absence of SPM (black). On the contrary, our numerical simulations show that the effect of XPM on the mean photon number is negligible.

Spectral purity — Next, we consider the Schmidt number of the fitted TFs, defined as[116,121]

$$K = \frac{(\sum_l \sinh(r_l)^2)^2}{\sum_l \sinh(r_l)^4}. \tag{5.27}$$

This quantifies the number of spectral modes in which the spontaneously generated photons are emitted. A low Schmidt number leads to high purity of heralded single photons generated in the low squeezing regime. More generally, the Schmidt number quantifies the maximum visibility of the interference between the generated light and another optical mode[122]. It

has been shown that the Schmidt number of a PDC source is reduced in the high-gain regime, due to the dominance of strongly populated modes[38,123]. We find that the pump SPM causes an opposing effect: the Schmidt number saturates at a moderate pump power and then grows due to increased spectral correlations. Again, in this regime XPM does not impact the Schmidt number of the source. Figure 5.12.b shows the calculated Schmidt number of our source as a function of pump power.

Improved design by pre-chirping the pump — It becomes evident that the SPM caused by the residual $\chi^{(3)}$ nonlinearity is impacting the performance of our source in the regime where tens of photons are generated in each pulse. We can suggest a simple way to counteract this effect: pre-chirping the pump pulses will reduce the strength of third-order nonlinear processes, which is proportional to the pump field intensity. If the sign and magnitude of the chirp are appropriately chosen, it is possible to counter the reduction in purity and brightness due to SPM. In figure 5.13 we show a comparison of the mean photon number and Schmidt number predicted by our model of the source, contrasted with what could be achieved using chirped pump pulses. The dispersion parameter needed to optimize the performance of the source is $D = 178$ fs/nm. While it is difficult to obtain anomalous dispersion in the visible by means of material dispersion, it is easy to achieve it using a comercial pulse compressor.

5.2.5 Summary and outlook

In this chapter we have introduced new experimental tools to study parametric twin-beam generation in the high gain regime. We have characterized a waveguided ppKTP source using a new technique based on stimulated frequency generation, which we call *cascaded*

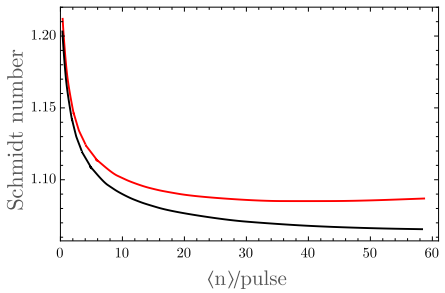


Figure 5.13: Effect of pre-chirping pump pulses on the spectral Schmidt number of a PDC source as a function of the average number of photons generated. Red – Fourier-limited pump pulses; black – pre-chirped pump pulses.

stimulated emission tomography. Measuring the DFG generated in the same and orthogonal polarization of the seeding beam, we estimated the absolute value of all the transfer functions describing a spontaneous frequency conversion process. We overcome the lack of phase information by fitting these data, together with additional complementary measurements, to the theoretical model that we developed initially. A single fitted model correctly predicts all the spectral transfer functions even for high pump powers, where the spectral structure of the emission changes. The modified spectrum at high-gains arises not only due to non-perturbative corrections of PDC, but also due to the distortion of the pump spectrum through SPM. Using this insight, we are able to propose a strategy to enhance the purity of this SPDC source in the high-gain regime: by introducing a small pre-chirping of the pump, the SPM process is mitigated and the spectral factorability of the source is enhanced.

Part III

Conclusions and outlook

Chapter 6

Conclusions and outlook

In the course of this thesis we have reported results concerning two different research projects, both sharing a strong component of design and characterization of sources of pulsed non-classical light.

In Part 1 we have presented work towards improving stimulated emission microscopy (SEM), a label-free nonlinear microscopy technique, by using a bright intensity-squeezed probe.

In Chapter 2 we have presented the requirements of such a quantum-enhanced measurement, and described our implementation of a SEM setup and a suitable pulsed sub-Poissonian light source. With this source, we have demonstrated intensity squeezing of bright, ultrashort laser pulses, achieving a minimum Fano factor of - 0.4 dB. We have used this squeezed probe as the stimulation beam in a SEM experiment, observing that, while the measurement noise is indeed sub-Poissonian, we simultaneously obtained a systematic reduction of the signal amplitude of unknown origin. The modest degree of intensity squeezing achieved, together with the presence of this yet-unexplained signal reduction, prevented us

from achieving a measurable quantum advantage. We concluded the chapter by recognizing that future work is required in two directions: in the first place, a systematic study of SEM with a sub-Poissonian probe must be carried out in order to identify the origin of the signal reduction. In the second place, a more detailed understanding of pulsed sub-Poissonian sources was needed in order to design an improved source, capable of achieving a larger degree of intensity squeezing.

In Chapter 3 we have developed a theoretical framework capable of simulating the photon statistics corresponding the squeezed probe used in the previous chapter. Our framework allows for the simulation of single-pass type-I OPA under a variety of conditions of the pump and seed fields, as well as of the nonlinear material. We study the effect of temporal and spatial propagation of the interacting beams, including phenomena such as material dispersion, birefringent walk-off, or spatio-temporal coupling of the parametric gain, amongs others. Using the insight obtained from these simulations, we have proposed a design for an improved sub-Poissonian light source: we propose to use a long, non-critically phase-matched ppKTP crystal, where a larger parametric gain and no deleterious effects are expected. This design is currently being implemented in our laboratory.

In Part 2 we have presented work concerning the simulation, characterization and design of pulsed PDC twin-beam sources in the high-gain regime.

In Chapter 4 we have introduced a novel theoretical framework to simulate the quantum states generated in a pulsed, waveguided PDC process in the high-gain regime. Unlike previous approaches to high gain PDC, our theoretical model can be solved very efficiently and exactly, requiring a single matrix exponentiation step to compute the special but relevant scenario of a uniform quadratic nonlinearity. The solutions that we find are exact, as

opposed to those arising from perturbative calculations, and correctly replicate high-gain spectral features presented in other works (i.e. time-ordering corrections). Our framework also includes the effect that parasitic nonlinearities, such as SPM of the pump and XPM of the downconverted light by the pump, have on the spectral structure of the twin beams. This model, which describes a complex interplay between different nonlinearities, is key to explaining the data presented in Chapter 5.

In Chapter 5 we have presented an experimental framework to characterize a waveguided, pulsed PDC twin-beam source in the high-gain regime. We have introduced cascaded stimulated emission tomography (SET), a seeded measurement which generalizes direct SET, and applied it to characterize a waveguided ppKTP source producing tens of spontaneously generated photons per pulse. We have used a characterization approach based on employing the cascaded SET data, together with complementary measurements, to fit the equations of motion of the model presented in Chapter 4. This approach has allowed us to show that the redundancy offered by cascaded SET allows for a self-referenced measurement of the PDC interaction strength, independently of the seeding and detection efficiency. We have also revealed that, because of the connection between the direct and cascaded DFG data, a measurement of the magnitude of the cascaded DFG signal provides information about the spectral phase of the biphoton joint spectral amplitude. Moreover, the cascaded SET data has allowed us to recognize the unexpected role of parasitic nonlinearities (SPM and XPM) in the spectral structure of the twin-beams. We believe that this framework will forward the study and design of twin-beam sources in the high-gain regime, a task currently hindered by the presence and complex interplay of different nonlinear optical phenomena in the process.

Bibliography

[1] Albert Einstein. Concerning an heuristic point of view towards the emission and transformation of light. *Ann. Phys.*, 17:132–148, 1905.

[2] S.J Freedman and J.F. Clauser. Experimental test of local hidden-variable theories. *Phys. Rev. Lett.*, 28:938, 1972.

[3] A Aspect, P Grangier, and R Gerard. Experimental tests of realistic local theories via Bell's theorem. *Phys. Rev. Lett.*, 47(7):460–463, 1981.

[4] Y. Huang, C. Li, Y. Zhang, J. Pan, and G. Guo. Experimental test of the Kochen-Specker theorem with single photons. *Phys. Rev. Lett.*, 90(25), 2003.

[5] H Zhong, Y Li, and Et al. 12-Photon Entanglement and Scalable Scattershot Boson Sampling with Optimal Entangled-Photon Pairs from Parametric Down-Conversion. *Phys. Rev. Lett.*, 121(250505), 2018.

[6] C Abellan, W Amaya, D Domenech, P Muñoz, J Capmany, S Longhi, M.W. Mitchell, and V Pruneri. Quantum entropy source on an InP photonic integrated circuit for random number generation. *Optica*, 3(9):989–994, 2016.

[7] N Walenta, A Burg, D Caselunghe, J Constantin, N Gisin, O Guinnard, R Houlmann, P Junod, B Korzh, N Kulesza, and Et al. A fast and versatile quantum key distribution system with hardware key distillation and wavelength multiplexing. *New J. Phys.*, 16(013047), 2014.

[8] Joni Aasi, Joan Abadie, and Et al. Enhanced sensitivity of the ligo gravitational wave detector by using squeezed states of light. *Nat. Photonics*, 7(613-619), 2013.

[9] Mark Hillery and Leonard D Mlodinow. Quantization of electrodynamics in nonlinear dielectric media. *Phys. Rev. A*, 30(4), 1984.

[10] Nicolás Quesada and J. E. Sipe. Why you should not use the electric field to quantize in nonlinear optics. *Opt. Lett.*, 42(17):1–4, 2017.

[11] J. D. Jackson. *Classical electrodynamics*. Wiley, 2007 edition.

[12] M Born and L Infeld. On the Quantization of the New Field Equations. I. *Proc. R. Soc. London. Ser. A*, 147(8):522–546, 1934.

[13] S. N. Volkov and J. E. Sipe. Nonlinear optical interactions of wave packets in photonic crystals: Hamiltonian dynamics of effective fields. *Phys. Rev. E - Stat. Physics, Plasmas, Fluids, Relat. Interdiscip. Top.*, 70(6):14, 2004.

[14] I Abram. Quantum theory of light propagation: Linear medium. *Phys. Rev. A*, 35(11):4661–4672, 1987.

[15] J. E. Sipe, Navin A.R. Bhat, Philip Chak, and Suresh Pereira. Effective field theory for the nonlinear optical properties of photonic crystals. *Phys. Rev. E - Stat. Physics, Plasmas, Fluids, Relat. Interdiscip. Top.*, 69(1):20, 2004.

[16] Navin A.R. Bhat and J. E. Sipe. Hamiltonian treatment of the electromagnetic field in dispersive and absorptive structured media. *Phys. Rev. A - At. Mol. Opt. Phys.*, 73(6):1–25, 2006.

[17] T. A. B Kennedy and E. M. Wrigh. Quantization and phase-space methods for slowly varying optical fields in a dispersive nonlinear medium. *Phys. Rev. A*, 38(1), 1988.

[18] Bruno Huttner and Stephen M Barnett. Quantization of the electromagnetic field in dielectrics. *Phys. Rev.*, 46(7), 1992.

[19] Benjamin Brecht. Engineering ultrafast quantum frequency conversion. *Univ. Paderborn PhD Thesis*, pages 1–144, 2014.

[20] Joshua Nunn. *Quantum memory in atomic ensembles.* PhD thesis, University of Oxford, 2008.

[21] A. Einstein, B. Podolsky, and N. Rosen. Can quantum-mechanical description of physical reality be considered complete? *Phys. Rev.*, 47:777 – 780, 1935.

[22] C. Gerry and P. Knight. *Introductory quantum optics.* Cambridge University Press, 2005.

[23] PJ Mosley. *Generation of heralded single photons in pure quantum states.* PhD thesis, University of Oxford, 2007.

[24] Andrew Weiner. *Ultrafast Optics.* 2009.

[25] A Yariv. Quantum electronics, 1989.

[26] Grant R Fowles. *Introduction to modern optics.* Second edition.

[27] N. Boeuf. Calculating characteristics of noncollinear phase matching in uniaxial and biaxial crystals. *Opt. Eng.*, 39(4):1016, 2000.

[28] M Bass, P A Franken, F Ward, and G Weinreich. Opical Rectification. *Phys. Rev. Lett.*, 9(11):28–31, 1962.

[29] P. A. Franken, A. E. Hill, C. W. Peters, and G. Weinreich. Generation of Optical Harmonics. *Phys. Rev. Lett.*, 7(4):118–119, 1961.

[30] M.M. Fejer, G.A. Magel, D.H. Jundt, and R.L. Byer. Quasi-phase-matched second harmonic generation: tuning and tolerances. *J. quantum Electron.*, 28(11), 1992.

[31] Agata M. Brańczyk. *Non-classical states of light.* PhD thesis, University of Queensland, 2010.

[32] Wilhelm Magnus. On the Exponential Solution of Differential Equations for a linear operator. *Commun. pure Appl. Math.*, VII:649–673, 1954.

[33] Nicolás Quesada and J. E. Sipe. Time-ordering effects in the generation of entangled photons using nonlinear optical processes. *Phys. Rev. Lett.*, 114(9):1–5, 2015.

[34] C. K. Law, I. A. Walmsley, and J. H. Eberly. Continuous frequency entanglement: Effective finite hilbert space and entropy control. *Phys. Rev. Lett.*, 84(23):5304–5307, 2000.

[35] Samuel L. Braunstein. Squeezing as an irreducible resource. *Phys. Rev. A - At. Mol. Opt. Phys.*, 71(5):1–4, 2005.

[36] Wojciech Wasilewski, A. I. Lvovsky, Konrad Banaszek, and Czesław Radzewicz. Pulsed squeezed light: Simultaneous squeezing of multiple modes. *Phys. Rev. A - At. Mol. Opt. Phys.*, 73(6):1–12, 2006.

[37] A. I. Lvovsky, Wojciech Wasilewski, and Konrad Banaszek. Decomposing a pulsed optical parametric amplifier into independent squeezers. *J. Mod. Opt.*, 54(5):721–733, 2007.

[38] Andreas Christ, Benjamin Brecht, Wolfgang Mauerer, and Christine Silberhorn. Theory of quantum frequency conversion and type-II parametric down-conversion in the high-gain regime. *New J. Phys.*, 15(053038), 2013.

[39] Alexander M. Chebotarev and Alexander E. Teretenkov. Singular value decomposition for the Takagi factorization of symmetric matrices. *Appl. Math. Comput.*, 234:380–384, 2014.

[40] Carlton M. Caves. Quantum-mechanical noise in an interferometer. *Phys. Rev. D*, 23(8):1693–1708, 1981.

[41] Vittorio Giovannetti, Seth Lloyd, and Lorenzo Maccone. Quantum-Enhanced Measurements : Beating the Standard Quantum Limit. *Science (80-.).*, 306(5700):1330–1336, 2016.

[42] D. J Wineland, J. J Bollinger, W. M. Itano, and F. L Moore. Spin squeezing and reduced quantum noise in spectroscopy. *Phys. Rev. A*, 46(11), 1992.

[43] M. Auzinsh, D. Budker, D. F. Kimball, S. M. Rochester, J. E. Stalnaker, A. O. Sushkov, and V. V. Yashchuk. Can a quantum nondemolition measurement improve the sensitivity of an atomic magnetometer? *Phys. Rev. Lett.*, 93(17):1–4, 2004.

[44] Mikhail Kolovob. The spatial behavior of nonclassical light. *Rev. Mod. Phys.*, 71(5):1587–1629, 1999.

[45] Michael A. Taylor and Warwick P. Bowen. Quantum metrology and its application in biology. *Phys. Rep.*, 615:1–59, 2016.

[46] Magued B. Nasr, Darryl P. Goode, Nam Nguyen, Guoxin Rong, Linglu Yang, Björn M. Reinhard, Bahaa E.A. Saleh, and Malvin C. Teich. Quantum optical coherence tomography of a biological sample. *Opt. Commun.*, 282(6):1154–1159, 2009.

[47] Andrea Crespi, Mirko Lobino, Jonathan C.F. Matthews, Alberto Politi, Chris R. Neal, Roberta Ramponi, Roberto Osellame, and Jeremy L. O'Brien. Measuring protein concentration with entangled photons. *Appl. Phys. Lett.*, 100(23), 2012.

[48] Hans-A. Bachor, Boris Hage, Vincent Daria, Michael A. Taylor, Warwick P. Bowen, Jiri Janousek, and Joachim Knittel. Biological measurement beyond the quantum limit. *Nat. Photonics*, 7(3):229–233, 2013.

[49] Michael A. Taylor, Jiri Janousek, Vincent Daria, Joachim Knittel, Boris Hage, Hans-A. Bachor, and Warwick P. Bowen. Subdiffraction-Limited Quantum Imaging within a Living Cell. *Phys. Rev. X*, 4(1):1–7, 2014.

[50] Nigam Samantaray, Ivano Ruo-Berchera, Alice Meda, and Marco Genovese. Realization of the first sub-shot-noise wide field microscope. *Light Sci. Appl.*, 6(7):1–7, 2017.

[51] Wei Min, Sijia Lu, Shasha Chong, Rahul Roy, Gary R. Holtom, and X. Sunney Xie. Imaging chromophores with undetectable fluorescence by stimulated emission microscopy. *Nature*, 461(7267):1105–1109, 2009.

[52] Valérian Thiel, Jonathan Roslund, Syamsundar De, Claude Fabre, and Nicolas Treps. Recovering the dynamics of optical frequency combs from phase-amplitude noise correlations measurements. *arXiv1806.02198v1 [physics.ins-det] 5 Jun 2018.*

[53] Carlton M. Caves. Quantum limits on noise in linear amplifiers. *Phys. Rev. D*, 26(8):1817–1839, 1982.

[54] D. F. Walls. Squeezed states of light. *Nature*, 306(5939):141–146, 1983.

[55] Horace P Yuen. Two-photon coherent states of the radiation field. *Phys. Rev. A*, 13(6), 1976.

[56] B Yurke. Optical back-action-evading amplifiers. 2(5):732–738, 1985.

[57] Marlan O. Scully and M. Suhail Zubairy. Quantum optics, 2001.

[58] Rodney Loudon. The Quantum Theory of Light. *Am. J. Phys.*, 42(11):1041–1042, 2005.

[59] Ulf Leonhardt. *Measuring of Quantum State of Light.* Cambridge University Press, 1997.

[60] K. J. Blow, Rodney Loudon, Simon J D Phoenix, and T. J. Shepherd. Continuum fields in quantum optics. *Phys. Rev. A*, 42(7):4102–4114, 1990.

[61] R. E. Slusher, P. Grangier, A. Laporta, B. Yurke, and M. J. Potasek. Pulsed squeezed light. *Phys. Rev. Lett.*, 59(22):2566–2569, 1987.

[62] Takuya Hirano and Masahiro Matsuoka. Broadband squeezing of light by pulse excitation. *Opt. Lett.*, 15(20):1153, 1990.

[63] Paul D. Townsend and Rodney Loudon. Quantum-noise reduction at frequencies up to 0.5 GHz using pulsed parametric amplification. *Phys. Rev. A*, 45(1):458–467, 1992.

[64] Orhan Aytür and Prem Kumar. Squeezed-light generation with a mode-locked Q-switched laser and detection by using a matched local oscillator. *Opt. Lett.*, 17(7):529, 1992.

[65] B. Yurke, P. Grangier, R. E. Slusher, and M. J. Potasek. Generating and detecting short-duration pulses of squeezed light. *Phys. Rev. A*, 35(8):3586–3589, 1987.

[66] Arthur La Porta and Richart E. Slusher. Squeezing limits at high parametric gains. *Phys. Rev. A*, 44(3):2013–2022, 1991.

[67] Chonghoon Kim, Ruo-Ding Li, and Prem Kumar. Deamplification response of a traveling-wave phase-sensitive optical parametric amplifier. *Opt. Lett.*, 19(2):132, 1994.

[68] Ruo Ding Li, Sang Kyung Choi, Chonghoon Kim, and Prem Kumar. Generation of sub-Poissonian pulses of light. *Phys. Rev. A*, 51(5), 1995.

[69] G. D. Boyd and D. A. Kleinman. Parametric interaction of focused Gaussian light beams. *J. Appl. Phys.*, 39(8):3597–3639, 1968.

[70] Jérôme Wenger. *Dispositifs Impulsionnels Pour La Communication Quantique À Variables Continues.* PhD thesis, Universite Paris XI, 2004.

[71] J. Wenger, Rosa Tualle-Brouri, and Philippe Grangier. Pulsed homodyne measurements of femtosecond squeezed pulses generated by single-pass parametric deamplification. *Opt. Lett.*, 29(11):1267, 2004.

[72] R. Akbari and A. Major. Optical, spectral and phase-matching properties of BIBO, BBO and LBO crystals for optical parametric oscillation in the visible and near-infrared wavelength ranges. *Laser Phys.*, 23(3), 2013.

[73] T. Hirano, K. Kotani, T. Ishibashi, S. Okude, and T. Kuwamoto. 3 dB squeezing by single-pass parametric amplification in a periodically poled KTiOPO_4 crystal. *Opt. Lett.*, 30(13):1722, 2005.

[74] L. Song, E. J. Hennink, I. T. Young, and H. J. Tanke. Photobleaching kinetics of fluorescein in quantitative fluorescence microscopy. *Biophys. J.*, 68(6):2588–2600, 1995.

[75] M. J. Werner, M. G. Raymer, M. Beck, and P. D. Drummond. Ultrashort pulsed squeezing by optical parametric amplification. *Phys. Rev. A*, 52(5):4202–4213, 1995.

[76] Ryan S. Bennink and Robert W. Boyd. Improved measurement of multimode squeezed light via an eigenmode approach. *Phys. Rev. A - At. Mol. Opt. Phys.*, 66(5):5, 2002.

[77] R. Ramírez-Alarcón, H. Cruz-Ramírez, and A. B. U'Ren. Effects of crystal length on the angular spectrum of spontaneous parametric downconversion photon pairs. *Laser Phys.*, 23(5), 2013.

[78] P. Sharapova, A. M. Pérez, O. V. Tikhonova, and M. V. Chekhova. Schmidt modes in the angular spectrum of bright squeezed vacuum. *Phys. Rev. A - At. Mol. Opt. Phys.*, 91(4):1–9, 2015.

[79] A. Gatti, E. Brambilla, L. Caspani, O. Jedrkiewicz, and L. A. Lugiato. X entanglement: The nonfactorable spatiotemporal structure of biphoton correlation. *Phys. Rev. Lett.*, 102(22):5–8, 2009.

[80] A. Gatti, T. Corti, E. Brambilla, and D. B. Horoshko. Dimensionality of the spatiotemporal entanglement of parametric down-conversion photon pairs. *Phys. Rev. A - At. Mol. Opt. Phys.*, 86(5):1–12, 2012.

[81] D. J. Lovering, J. A. Levenson, P. Vidakovic, J. Webjörn, and P. St. J. Russell. Noiseless optical amplification in quasi-phase-matched bulk lithium niobate. *Opt. Lett.*, 21(18):1439–1441, Sep 1996.

[82] J.J Sakurai and J. Napolitano. *Modern quantum mechanics*. Cambridge University Press, 2nd edition, 2018.

[83] E. Brambilla, L. Caspani, L. A. Lugiato, and A. Gatti. Spatiotemporal structure of biphoton entanglement in type-II parametric down-conversion. *Phys. Rev. A - At. Mol. Opt. Phys.*, 82(1):1–14, 2010.

[84] H Vanherzeele and J.D Bierlein. Magnitude of the nonlinear optical coefficients of KTiOPO4. *Opt. Lett.*, 17(14):982–984, 1992.

[85] K Kato and E Takaoka. Sellmeier and thermo-optic dispersion formulas for KTP. *Appl. Opt.*, 41(24):5040–5044, 2002.

[86] D.J. Armstrong, W.J. Alford, T.D. Raymond, and A.V. Smith. Absolute measurement of the effective nonlinearities of KTP and BBO crystals by optical parametric amplification. *Appl. Opt.*, 35(12):2032–2040, 1996.

[87] David C. Burnham and Donald L. Weinberg. Observation of simultaneity in parametric production of optical photon pairs. *Phys. Rev. Lett.*, 25(2):84–87, 1970.

[88] C. K Hong and L. Mandel. Realization of a Localized One-Photon State ' X ,. *Phys. Rev. Lett.*, 56, 1985.

[89] Y. H. Shih and C. O. Alley. New type of einstein-podolsky-rosen-bohm experiment using pairs of light quanta produced by optical parametric down conversion. *Phys. Rev. Lett.*, 61(26):2921–2924, 1988.

[90] M. L. Sundheimer, J. D. Bierlein, Ch. Bosshard, E. W. Van Stryland, and G. I. Stegeman. Large nonlinear phase modulation in quasi-phase-matched KTP waveguides as a result of cascaded second-order processes. *Opt. Lett.*, 18(17):1397, 1993.

[91] Matthew E. Anderson, J. D. Bierlein, M. Beck, and M. G. Raymer. Quadrature squeezing with ultrashort pulses in nonlinear-optical waveguides. *Opt. Lett.*, 20(6):620, 2008.

[92] Daiji Fukuda, Go Fujii, Takayuki Numata, Kuniaki Amemiya, Akio Yoshizawa, Hidemi Tsuchida, Hidetoshi Fujino, Hiroyuki Ishii, Taro Itatani, Shuichiro Inoue, and Tatsuya Zama. Titanium-based transition-edge photon number resolving detector with 98% detection efficiency with index-matched small-gap fiber coupling. *Opt. Express*, 19(2):870–5, 2011.

[93] A Zavatta, S Viciani, and M Bellini. Quantum-to-Classical Transition with Single-PhotonAdded Coherent States of Light. *Science (80-.).*, 306:660–662, 2004.

[94] Jérôme Wenger, Rosa Tualle-Brouri, and Philippe Grangier. Non-Gaussian Statistics from Individual Pulses of Squeezed Light. *Phys. Rev. Lett.*, 92(15):153601, 2004.

[95] A. P. Lund, A. Laing, S. Rahimi-Keshari, T. Rudolph, J. L. O'Brien, and T. C. Ralph. Boson sampling from a Gaussian state. *Phys. Rev. Lett.*, 113(10):1–5, 2014.

[96] Craig S. Hamilton, Regina Kruse, Linda Sansoni, Sonja Barkhofen, Christine Silberhorn, and Igor Jex. Gaussian Boson Sampling. *Phys. Rev. Lett.*, 119(17):1–5, 2017.

[97] Joonsuk Huh, Gian Giacomo Guerreschi, Borja Peropadre, Jarrod R. Mcclean, and Alán Aspuru-Guzik. Boson sampling for molecular vibronic spectra. *Nat. Photonics*, 9(9):615–620, 2015.

[98] W. P. Grice and I. A. Walmsley. Spectral information and distinguishability in type-II down-conversion with a broadband pump. *Phys. Rev. A - At. Mol. Opt. Phys.*, 56(2):1627–1634, 1997.

[99] M.M Weston, H.M. Chrzanowski, S. Wollman, A. Boston, J. Ho, L.K. Shalm, V.B Verma, M.S. Allman, S.W. Nam, R.B Patel, S Slussarenko, and G.J Pryde. Efficient and pure femtosecond-pulse-length source of polarization-entangled photons. *Opt. Express*, 24 (10):10869–10879, 2016.

[100] Andreas Eckstein, Andreas Christ, Peter J. Mosley, and Christine Silberhorn. Highly Efficient Single-Pass Source of Pulsed Single-Mode Twin Beams of Light. *Phys. Rev. Lett.*, 106(1):013603, jan 2011.

[101] Georg Harder, Tim J. Bartley, Adriana E. Lita, Sae Woo Nam, Thomas Gerrits, and Christine Silberhorn. Single-Mode Parametric-Down-Conversion States with 50 Photons as a Source for Mesoscopic Quantum Optics. *Phys. Rev. Lett.*, 116(14):1–5, 2016.

[102] Carlo Liberale, Ilaria Cristiani, Vittorio Degiorgio, Marco Marangoni, Gianluca Galzerano, and Roberta Ramponi. Cross-phase modulation due to a cascade of quadratic interactions in a PPLN waveguide. *IEEE J. Sel. Top. Quantum Electron.*, 12(3):405–410, 2006.

[103] Nicolás Quesada and J. E. Sipe. Effects of time ordering in quantum nonlinear optics. *Phys. Rev. A - At. Mol. Opt. Phys.*, 90(6):1–13, 2014.

[104] Mihai D Vidrighin, Ian A Walmsley, and Myungshik Kim. *Quantum Optical Measurements for Practical Estimation and Information Thermodynamics*. PhD thesis, Imperial College London, 2016.

[105] M Liscidini and J E Sipe. Stimulated Emission Tomography. *Phys. Rev. Lett.*, 111(193602), 2013.

[106] A.B Klimov and S.M Chumakov. *A group theoretical approach to quantum optics: models of atom-field interactions*. John Wiley & Sons, 2009.

[107] Andreas Eckstein. *Mastering quantum light pulses with nonlinear waveguide interactions*. PhD thesis, Friedrich-Alexander-Universit\"at Erlangen-N\"urnberg, 2012.

[108] Nicolás Quesada. *Very Nonlinear Quantum Optics*. PhD thesis, University of Toronto, 2015.

[109] M. Avenhaus, A. Eckstein, P.J. Mosley, and C. Silberhorn. Fiber-assisted single-photon spectrograph. *Opt. Lett.*, 34(18):2873–2875, 2009.

[110] Andreas Eckstein, Guillaume Boucher, Aristide Lema, Pascal Filloux, Ivan Favero, Giuseppe Leo, John E Sipe, Marco Liscidini, and Sara Ducci. High-resolution spectral characterization of two photon states via classical measurements. *Laser Photonics Rev.*, 8(5):76–80, 2014.

[111] B. Fang, O. Cohen, M. Liscidini, J Sipe, and V. O. Lorenz. Fast and highly resolved capture of the joint spectral density of photon pairs. *Optica*, 1 (5):281–284, 2014.

[112] B. Fang, M. Liscidini, J.E. Sipe, and V.O. Lorenz. Multidimensional characterization of an entangled photon-pair source via stimulated emission tomography. *Opt. Express*, 24 (9):10013–10019, 2016.

[113] L.A. Rozema, C. Wang, D.H. Mahler, A. Hayat, A.M. Steinberg, J. Sipe, and M. Liscidini. Characterizing an entangled-photon source with classical detectors and measurements. *Optica*, 2(5):430–433, 2015.

[114] I Jizan, Bryn Bell, L.G. Helt, A. Casas Bedoya, C. Xiong, and B.J. Eggleton. Phase-sensitive tomography of the joint spectral amplitude of photon pair sources. *Opt. Lett.*, 41(20):4803–4806, 2016.

[115] V. Ansari. Temporal-mode measurement tomography of a quantum pulse gate. *Phys. Rev. A*, 96(063817), 2017.

[116] A. Christ, K. Laiho, A. Eckstein, K.N. Cassemiro, and C. Silberhorn. Probing multimode squeezing with correlation functions. *New J. Phys.*, 13(033027), 2011.

[117] E.A Goldschmidt, , and A more. Mode reconstruction of a light field by multiphoton statistics. *Phys. Rev. A*, 88(013822), 2013.

[118] I.A. Burenkov and Al Et al. Full statistical mode reconstruction of a light field via a photon-number-resolved measurement. *Phys. Rev. A*, 95(053806), 2017.

[119] U. Fano. Effects of configuration interaction on itensities and phase shifts. *Phys. Rev.*, 124:1866–1878, 1961.

[120] Govind Agrawal and Govind P. Agrawal. *Nonlinear Fiber Optics*. Third edit edition.

[121] J.H Eberly. Schmidt analysis of pure-state entanglement. *Laser Phys.*, 16(6):921–926, 2006.

[122] T. Iskhakov, K. Spasibko, M. V. Chekhova, and G. Leuchs. Macroscopic Hong-Ou-Mandel interference. *New J. Phys.*, 15, 2013.

[123] I. V. Dyakonov, P. R. Sharapova, T. Sh Iskhakov, and G. Leuchs. Direct Schmidt number measurement of high-gain parametric down conversion. *Laser Phys. Lett.*, 12(6):0–4, 2015.

Appendix A

Locking on deamplification: generating the error signal

Here we show that an estimation of the gradient of the amplified/deamplified signal power $\mathrm{P}_{\mathrm{s,out}}(\phi_0)$ can be done by applying a small sinusoidal modulation of the signal phase and then demodulating at the modulation frequency. Let us consider the modulated signal power $\mathrm{P}_{\mathrm{s,out}}(\phi_0 + s(t)) = \mathrm{P}_{\mathrm{s,out}}(\phi_0 + \delta \sin(\omega_0 t))$. The demodulation is performed by multiplying this signal by a sinusoidal voltage of frequency f_{mod} and then low-pass filtering. A simple model of this process is

$$\mathrm{P}_{f_{\mathrm{mod}}} = \int_0^T dt\, \mathrm{P}_{\mathrm{s,out}}(\phi_0 + s(t)) \sin(2\pi f_{\mathrm{mod}} t) \tag{A.1}$$

Considering that $s(t)$ is a small perturbation, we can do a Taylor expansion of $P_{\mathrm{s,out}}$ around $s = 0$, yielding

$$\mathrm{P}_{2\pi f_{\mathrm{mod}}} \approx \int_0^T dt \left(\mathrm{P}_{\mathrm{s,out}}(\phi_0) + \frac{\partial \mathrm{P}_{\mathrm{s,out}}(\phi_0 + s)}{\partial s}\, s(t) \right) \sin(2\pi f_{\mathrm{mod}} t) \tag{A.2}$$

Now, writing the explicit sinusoidal modulation and integrating over t we obtain

$$\mathrm{P}_{f_{\mathrm{mod}}} \approx \frac{T}{2} \frac{\partial \mathrm{P}_{\mathrm{s,out}}(\phi_0 + s)}{\partial s} \tag{A.3}$$

Appendix B

Taylor expansion of the transverse momentum mismatch

The transverse momentum mismatch in equation (3.15) can be re-written as

$$\Delta k_z(\mathbf{q},\mathbf{q}') = \sqrt{k_e^2(2\omega_{\mathrm{s}0},\theta) - |\mathbf{q}_{\mathrm{p}}|^2} - \sqrt{k_o^2(\omega_{\mathrm{s}0}) - |\mathbf{q}|^2} - \sqrt{k_o^2(\omega_{\mathrm{s}0}) - |\mathbf{q}'|^2} \tag{B.1}$$

where we recall that due to energy conservation

$$\mathbf{q}_{\mathrm{p}} = \mathbf{q} + \mathbf{q}'. \tag{B.2}$$

The signal field is an o-wave with wavenumber $k_{\mathrm{s}0} = k_o(\omega_{\mathrm{s}0}) = \omega_{\mathrm{s}0}\, n_o(\omega_{\mathrm{s}0})/c$ and the pump field is an e-wave with wavenumber $k_{\mathrm{p}}(\theta) = k_e(2\omega_{\mathrm{s}0},\theta) = 2\omega_{\mathrm{s}0}\, n_{\mathrm{ext}}(2\omega_{\mathrm{s}0},\theta)/c$ with

$$n_{\mathrm{ext}}(\omega,\theta) = \Big(\frac{\sin^2\theta}{n_e^2(\omega)} + \frac{\cos^2\theta}{n_o^2(\omega)}\Big)^{-1} \tag{B.3}$$

where n_e and n_o are the two principal refractive indices of a uniaxial crystal, and θ is the angle with respect to the optical axis that the pump plane waves propagate at (see Fig 1.1). The angle θ has been defined as contained in the y-z plane and is equal to θ_0 for propagation along z. Defining the pump collinear wavenumber as $k_{\mathrm{p}0} = k_{\mathrm{p}}(\theta_0)$, we assume that

$$k_{\mathrm{p}0} - 2k_{\mathrm{s}0} = 0 \tag{B.4}$$

In the paraxial approximation, the pump propagation angle can be expressed as

$$\theta \approx \theta_0 + \frac{q_{p,y}}{k_{\mathrm{p}0}} \tag{B.5}$$

where $q_{p,y}$ is the projection of $\mathbf{q}_{\mathrm{p}}$ along the y direction (the direction of gradient of n_{ext}). The pump wavenumber can then be written

$$k_{\mathrm{p}}(\theta) = k_{\mathrm{p}0} + \partial_\theta\, k_{\mathrm{p}}(\theta)|_{\theta_0}(\theta - \theta_0) = k_{\mathrm{p}0} + \rho_{\mathrm{wo}}\, q_{\mathrm{p},y} \tag{B.6}$$

where

$$\rho_{\mathrm{wo}} = \frac{\partial n_{\mathrm{ext}}(2\omega_{\mathrm{s}0},\theta)}{\partial\theta}\Big|_{\theta_0} \frac{1}{n_{\mathrm{ext}}(2\omega_{\mathrm{s}0},\theta_0)} \tag{B.7}$$

Given the paraxial approximation, we can assume small transverse wavevectors and write

$$\sqrt{k^2 - |\mathbf{q}|^2} \approx k - \frac{|\mathbf{q}|^2}{2k} \tag{B.8}$$

for all the fields involved in equation (B.1). Together with equation (B.6), this allows us to re-write the transverse momentum mismatch as

$$\Delta k_z(\mathbf{q}, \mathbf{q}') \approx k_{\mathrm{p}0} + \rho_{\mathrm{wo}}\, q_{\mathrm{p},y} - \frac{|\mathbf{q}_{\mathrm{p}}|^2}{2k_{\mathrm{p}0}} - k_{\mathrm{s}0} + \frac{|\mathbf{q}|^2}{2k_{\mathrm{s}0}} - k_{\mathrm{s}0} + \frac{|\mathbf{q}'|^2}{2k_{\mathrm{s}0}} \tag{B.9}$$

Substituting equations (B.2) and (B.4) we arrive at

$$\Delta k_z(\mathbf{q}, \mathbf{q}') = -\frac{|\mathbf{q} + \mathbf{q}'|^2}{2k_{\mathrm{p}0}} + \frac{|\mathbf{q}|^2 + |\mathbf{q}'|^2}{2k_{\mathrm{s}0}} + \rho_{\mathrm{wo}}\,(q_y + q'_y) \tag{B.10}$$

where q_y and q'_y are respectively the projections along the y direction of $\mathbf{q}$ and $\mathbf{q}'$. The last step is to substitute again (B.4) and recast this equation as

$$\Delta k_z(\mathbf{q}, \mathbf{q}') = -\frac{|\mathbf{q} - \mathbf{q}'|^2}{4k_{\mathrm{s}0}} + \rho_{\mathrm{wo}}\,(q_y + q'_y) \tag{B.11}$$

Appendix C

The nonlinear coefficients

The nonlinear coefficients describing the nonlinear interaction between the pump, signal and idler modes are defined as follows

$$\zeta_p(z) = \frac{3}{\epsilon_0\hbar}\left(\frac{\hbar\bar{\omega}_p}{2}\right)^2 \int dxdy\ \Gamma_3^{ijlm}(\mathbf{r})\left(d^i_{p\bar{k}_p}(x,y)\right)^*\left(d^j_{p\bar{k}_p}(x,y)\right)^* d^l_{p\bar{k}_p}(x,y)d^m_{p\bar{k}_p}(x,y) \tag{C.1a}$$

$$= \frac{3}{\epsilon_0\hbar}\left(\frac{\hbar\bar{\omega}_p}{2}\right)^2 \int dxdy\ \frac{\chi_3^{ijlm}(\mathbf{r})}{\epsilon_0 n_i^2 n_j^2 n_l^2 n_m^2}\left(d^i_{p\bar{k}_p}(x,y)\right)^*\left(d^j_{p\bar{k}_p}(x,y)\right)^* d^l_{p\bar{k}_p}(x,y)d^m_{p\bar{k}_p}(x,y), \tag{C.1b}$$

$$\zeta_{i/s}(z) = 2\frac{3}{\epsilon_0\hbar}\left(\frac{\hbar\bar{\omega}_{i/s}}{2}\right)\left(\frac{\hbar\bar{\omega}_p}{2}\right)\int dxdy\ \Gamma_3^{ijlm}(\mathbf{r})\left(d^i_{p\bar{k}_p}(x,y)\right)^*\left(d^j_{i,s\bar{k}_{i,s}}(x,y)\right)^* d^l_{i,s\bar{k}_{i,s}}(x,y)d^m_{p\bar{k}_p}(x,y) \tag{C.1c}$$

$$= 2\frac{3}{\epsilon_0\hbar}\left(\frac{\hbar\bar{\omega}_{i/s}}{2}\right)\left(\frac{\hbar\bar{\omega}_p}{2}\right)\int dxdy\ \frac{\chi_3^{ijlm}(\mathbf{r})}{\epsilon_0 n_i^2 n_j^2 n_l^2 n_m^2}\left(d^i_{p\bar{k}_p}(x,y)\right)^*\left(d^j_{i,s\bar{k}_{i,s}}(x,y)\right)^* d^l_{i,s\bar{k}_{i,s}}(x,y)d^m_{p\bar{k}_p}(x,y), \tag{C.1d}$$

$$\xi(z) = \frac{2}{\epsilon_0\hbar}\sqrt{\frac{\hbar^3\bar{\omega}_i\bar{\omega}_s\bar{\omega}_p}{(2)^3}}\int dxdy\ \Gamma_2^{ijl}(\mathbf{r})\left(d^i_{i\bar{k}_i}(x,y)\right)^*\left(d^j_{s\bar{k}_s}(x,y)\right)^* d^l_{p\bar{k}_p}(x,y) \tag{C.1e}$$

$$= \frac{2}{\epsilon_0\hbar}\sqrt{\frac{\hbar^3\bar{\omega}_i\bar{\omega}_s\bar{\omega}_p}{(2)^3}}\int dxdy\ \frac{\chi_2^{ijl}(\mathbf{r})}{\epsilon_0^2 n_i^2 n_j^2 n_l^2}\left(d^i_{i\bar{k}_i}(x,y)\right)^*\left(d^j_{s\bar{k}_s}(x,y)\right)^* d^l_{p\bar{k}_p}(x,y). \tag{C.1f}$$

Note the extra factor of two in the definition of $\zeta_{s/i}(z)$ that comes about because of the permutation symmetry of the Γ coefficients. In the last equations we ignored the χ_2 contributions to Γ_3, but they can be easily added.